Exciton Dynamics and Interfacial Engineering in Semiconducting Nanomaterials: Role of Ionic Liquids and Organic Hybrids

By

DEBABRATA CHAKRABORTY
CHEM11201804014

National Institute of Science Education and Research
Bhubaneswar, Odisha

A thesis submitted to the
Board of Studies in Chemical Sciences
In partial fulfilment of requirements
For the degree of

DOCTOR OF PHILOSOPHY
of
HOMI BHABHA NATIONAL INSTITUTE

December, 2025

Homi Bhabha National Institute

Recommendations of the Viva Voce Committee

As members of the Viva Voce Committee, we certify that we have read the dissertation prepared by Mr. Debabrata Chakraborty entitled "*Exciton Dynamics and Interfacial Engineering in Semiconducting Nanomaterials: Role of Ionic Liquids and Organic Hybrids*" and recommend that it may be accepted as fulfilling the thesis requirement for the award of Degree of Doctor of Philosophy.

Chairman – (Name: Prof. A Srinivasan) Date: 08.04.2026

Guide / Convener – (Name: Prof. Moloy Sarkar) Date: 08/04/2026

Co-guide –

Examiner – (Prof. Saptarshi Mukherjee) Date: April 08, 2026

Member 1 – (Name: Prof. Shankappa Nembenna) Date: 08.04.2026

Member 2 – (Name: Prof. Bhargava B L) Date: 08.04.2026

Member 3 – (Name: Prof. Yatendra Singh Chaudhary) Date: 08.04.2026

Final approval and acceptance of this thesis is contingent upon the candidate's submission of the final thesis copies to HBNI. I/We hereby certify that I/we have read this thesis prepared under my/our direction and recommend that it may be accepted as fulfilling the thesis requirement.

Date : 08/04/2026 Signature Co-guide (if any)

Place: NISER Bhubaneswar Jatni campus

Signature Guide

STATEMENT BY AUTHOR

This dissertation has been submitted in partial fulfilment of requirements for an advanced degree at Homi Bhabha National Institute (HBNI) and is deposited in the library to be made available to borrowers under rules of the HBNI. Brief quotations from this dissertation are allowable without special permission, provided that accurate acknowledgement of source is made. Requests for permission for extended quotation from or reproduction of this manuscript in whole or in part may be granted by the Competent Authority of HBNI when in his or her judgment the proposed use of the material is in the interests of scholarship. In all other instances, however, permission must be obtained from the author.

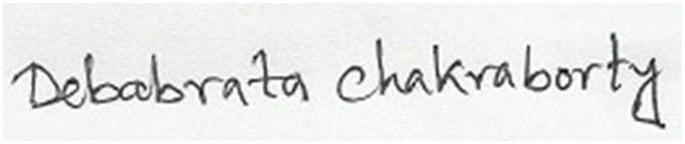

Debabrata Chakraborty

DECLARATION

I, hereby declare that the investigation presented in the thesis has been carried out by me. The work is original and has not been submitted earlier as a whole or in part for a degree/diploma at this or any other Institution / University.

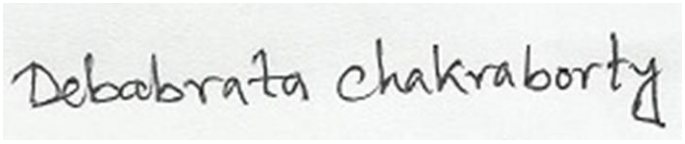

Debabrata Chakraborty

LIST OF PUBLICATIONS

1. **# Chakraborty, D.**; Preeyanka, N.; Akhuli, A.; Sarkar, M. Enhancing the Stability and Photoluminescence Quantum Yield of $CsPbX_3$ (X = Cl and Br) Perovskite Nanocrystals by Treatment with Imidazolium-Based Ionic Liquids through Surface Modification. *J. Phys. Chem. C* **2021**, *125*, 48, 26652–26660.
2. **# Chakraborty, D.**; Akhuli, A.; Preeyanka, N.; Sarkar, M. Energy-Transfer-Induced Enhanced Valley Splitting of Excitonic Emission of Inorganic CdTe@ZnS QDs in the Presence of Organic J-Aggregates: A Spectroscopic Insight into the Efficient Exciton (Inorganic)–Exciton (Organic) Coupling. *J. Phys. Chem. C* **2023**, *127*, 10, 5082–5089.
3. **# Chakraborty, D.**; Akhuli, A.; Sarkar, M. Ionic Liquid Engineered Defect-Driven Green Emitting Zero-Dimensional Cs_4PbBr_6 Microdisks. *J. Phys. Chem. Lett.* **2025**, 16, 9646−9655.
4. **# Chakraborty, D.**; Barik, S.; Sarkar, M. Probing Charge-Transfer Dynamics between CdTe@ZnS Quantum Dots and Pyridinium-Based Ionic Liquids (Manuscript Communicated).
5. Akhuli, A.; **Chakraborty, D.**; Agarwal, A. K.; Sarkar, M. Probing the Interaction of Bovine Serum Albumin with Copper Nanoclusters: Realization of Binding Pathway Different from Protein Corona. *Langmuir*, **2021**, *37*, 1823-1837.
6. Banerjee, S.; **Chakraborty, D.**; Preeyanka, N.; Sarkar, M. Understanding the Interaction between Inorganic and Organic Excitonic Components of an Inorganic-Organic Nanohybrid Associate. *ChemNanoMat* **2022**, e202200117.
7. Preeyanka, N.; Akhuli, A.; Dey, H.; **Chakraborty, D.** Rahaman, A.; Sarkar, M. Realization of a Model-Free Pathway for Quantum Dot–Protein Interaction Beyond Classical Protein Corona or Protein Complex. *Langmuir* **2022**, 38, 34, 10704–10715.
8. Akhuli, A.; Preeyanka, N.; **Chakraborty, D.**; Sarkar, M. Turn-Off Detection of Reactive Oxidative Species and Turn-On Detection of Antioxidants Using Fluorescent Copper Nanoclusters. *ACS Appl. Nano Mater.* **2022**, *5*, 4, 5826–5837.
9. Akhuli, A.; **Chakraborty, D.**; Preeyanka, N. Dora, A. S.; Sarkar, M. Copper Nanoclusters as an Effective Enzyme Inhibitor on the Activity Modulation of α-Chymotrypsin. *ACS Appl. Nano Mater.* **2023**, *6*, 6, 4910–4924.

10. Akhuli, A.; Preeyanka, N.; **Chakraborty, D.**; Sarkar, M. Understanding the Mechanism of Energy Transfer Process from Non-Plasmonic Fluorescence Bimetallic Nanoparticle to Plasmonic Gold Nanoparticle. *Phys. Chem. Chem. Phys.* **2023**, *25*, 17470–17481.
11. Sethi, N. M.; Nayak, A.; Khator, K. R.; Preeyanka, N.; **Chakraborty, D.**; Senanayak, S. P.; Sarkar, M. Chitosan Mediated FAPbBr3 Nanocrystal Thin-Films with High Color Purity and Enhanced Hole Mobility. *ChemNanoMat.* **2024**, e202400355.
12. Akhuli, A.; Mahanty, A.; **Chakraborty, D.**; Biswal, J. R.; Sarkar, M. Ligand-Mediated Surface Restructuring of Copper Nanoclusters and Its Impact on the Reduction of 4-Nitrophenol to 4-Aminophenol. *J. Phys. Chem. C* **2024**, *128*, 37, 15380–15392.
13. Akhuli, A.; Mahanty, A.; Barik, S.; Mahapatra, A.; **Chakraborty, D.**; Sarkar, M. Understanding the Resonance Energy Transfer between Fluorescent Bimetallic Nanoparticles and Organic Dye molecules. ISRAPS Bulletin At: BARC Mumbai, India. **2024**, 34, 1&2, page:24-34.
14. Ghosh, J.; Patra, C.; **Chakraborty, D.**; Koiri, D.; Pradhan, S. K.; Sarkar, M. Role of Surface-Controlled Modulation of Copper Nanocluster−DNA Interaction and Its Implication for Targeted Biological Applications. *ACS Appl. Nano Mater.* **2025**, *8*, 21, 11150–11165.

List of publications pertaining to the thesis.

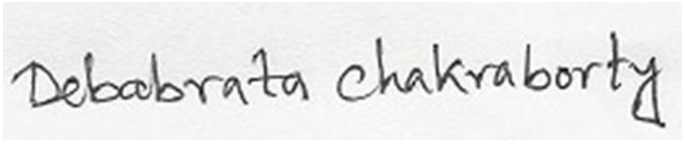

Debabrata Chakraborty

CONFERENCE/SYMPOSIUM

1. Participate in FCS 2020 National Workshop on Fluorescence and Raman Spectroscopy, organized by IIT Bombay, Mumbai, India, 7th -12th, December 2020.
2. Presented poster in International Conference on “Aggregation-Induced Emission-from Fundamentals to Applications, Department of BITS Pilani, Goa Campus,16th-18th December, 2022
3. Presented poster in14th National Symposium on Radiation & Photochemistry (NSRP-2021), organized by Indian Institute of Technology Gandhinagar, Gandhinagar, India via virtual meet,25th -26th, June 2021.
4. Presented poster in International Conference on Metal Halide Perovskites, HyPe 24, organized by NISER Bhubaneswar, 19th-22nd December 2024.

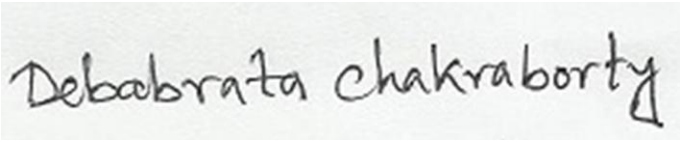

Debabrata Chakraborty

Dedicated to……..

My Beloved Parents, Wife, and Son

ACKNOWLEDGEMENTS

It is with profound gratitude that I express my sincere appreciation to my supervisor, Dr. Moloy Sarkar, whose exceptional guidance, unwavering support, and inspiring mentorship have shaped every phase of this thesis. His insightful advice, constant encouragement, and faith in my abilities have been invaluable, not only in the successful completion of this work but also in my personal and professional growth throughout this Ph.D. journey. I remain deeply indebted to him.

I extend my heartfelt thanks to Prof. Hirendra Nath Ghosh (Director, NISER), Prof. Sudhakar Panda (Former Director, NISER), and Prof. T. K. Chandrasekhar (Founder Director, NISER) for their vision and tireless efforts in establishing state-of-the-art research facilities at NISER, which significantly enriched my research experience. My sincere appreciation goes to Dr. Pranay Swain, Dean of Academic Affairs, for his understanding, support, and timely assistance in navigating various academic matters. I am equally grateful to my thesis committee members—Prof. Alagar Srinivasan, Dr. Bhargava B. L, Dr. Sharanappa Nembenna, and Dr. Yatendra Singh Chaudhary—for their valuable suggestions, constructive feedback, and continuous encouragement during my doctoral research. I would also like to acknowledge my course instructors—Dr. Upakara Samy Louderaj, Dr. A. Srinivasan, Dr. Himanshu Sekhar Biswal, Dr. Bidraha Bag, and Dr. Sudip Barman—whose dedication to teaching provided me with a strong academic foundation. My gratitude extends to the current Chairperson, Dr. Chidambaram Gunanathan, and the former Chairpersons—Dr. Sharanappa Nembenna, Dr. Himansu S. Biswal, and Dr. A. Srinivasan—of the School of Chemical Sciences (SCS) for their leadership and support during the course of my research. I am thankful to all the esteemed faculty members, scientific officers (Dr. Arun Kumar and Dr. Priyanka Pandey), and the ever-helpful non-teaching staff of SCS for cultivating a warm, collaborative, and stimulating academic environment.

My heartfelt gratitude also goes to NISER, Bhubaneswar, for providing world-class infrastructure and resources that enabled the smooth progress of my research work. I gratefully acknowledge the Council of Scientific and Industrial Research (CSIR) for their generous financial support, without which this work would not have been possible.

I extend my warmest and most heartfelt thanks to all my former lab members, whose presence transformed this journey into an experience filled with learning, joy, and cherished memories. I am profoundly grateful to Dr. Muhaiminul Islam, and Dr. Lakkoji Satish for their invaluable guidance, thoughtful suggestions, and constructive feedback, all of which played a pivotal role in shaping the quality and direction of my research. My sincere appreciation goes to Somnath da, whose personal kindness added immense value to my life at NISER. My Ph.D. years would feel incomplete without acknowledging Preeyanka di, to whom I owe countless moments of intellectual clarity and emotional comfort. Our discussions—whether about experimental techniques, data analysis, or fundamental research concepts—enriched my understanding immensely. I am equally grateful to Manjari di for her steadfast support in both my academic pursuits and personal life. I feel fortunate to have Sahadev Bhaina as both a senior and a true friend. His constant encouragement, readiness to help, and companionship

through every difficult moment have left a lasting impression on me. The friendship I share with Amit and Amita holds a special place in my life. Amit, like an elder brother, has been someone with whom I could share every aspect of my life without hesitation. Amita's kindness, warmth, and ever-helpful nature have touched me deeply. The playful banter among us added a refreshing and joyful rhythm to my days at NISER—moments I will always treasure. My heartfelt thanks go to my wonderful juniors—Joyoti, Jyoti, Chinmayee, Sumit, Samarth, Yash, Anup, Bibhudutta, Anirudh, Priyanka, and Priyaranjan—for filling the final stretch of my Ph.D. with laughter, enthusiasm, and positivity. I will fondly remember the time spent with Aman, Ramya, Dinesh, Aditya, Biswa, Aradhana, Nilesh, Rashmita, Subhakant, Yashaswini, and Aditi, whose companionship added warmth and color to this journey.

I would also like to express my heartfelt thanks to Rakesh, whose help across various academic tasks and personal situations proved invaluable.

My hostel days remain among the brightest chapters of my life, filled with fun, camaraderie, and endless conversations. The countless parties, late-night discussions, and memorable travels with the DAT'S group (Debu, Amit, Tanmoy, and Sahadev) have become unforgettable stories I will carry with me always. A special note of appreciation goes to our Hi For Chai group—Rakesh, Himanshu, Swaraj, and Debabrata—for the never-ending discussions that ranged across science, philosophy, life, and everything in between. This Ph.D. journey has also been enriched by the meaningful connections I built with Sushanta, Nachiketa, Pradeep, and Unmesh, whose presence added depth and warmth to my days at NISER. Finally, I express my heartfelt gratitude to my dear friends Narayan, Madhai, Tubun, and Nityananda for their unwavering support, kindness, and encouragement, personally.

Finally, I extend my deepest and most heartfelt gratitude to my family, whose unconditional love and support have made this journey both peaceful and memorable. My father and my mother have stood by every decision I made, offering strength, trust, and encouragement at every step. Their unwavering belief in me has been a constant source of motivation, and I remain forever grateful for the values and resilience they instilled in me.

I owe a special and profound thanks to my wife, Surobita, whose companionship has been my greatest blessing throughout this Ph.D. journey. Her steady support—academically, emotionally, and mentally—has carried me through the most challenging phases. From discussing research problems together to sharing moments of doubt and joy, she has been both a pillar of strength and a true partner in every sense. I am equally grateful to my little son, Sourabrata, whose innocent smiles and presence brought joy, comfort, and balance into my life during demanding times.

My journey would also be incomplete without acknowledging my beloved sisters—Kakoli, Barnali, and Mitali—along with my nieces and nephews. Their affection, encouragement, and constant prayers have always reminded me that I am surrounded by a family that cares deeply about my happiness and success.

I extend my sincere gratitude to my father-in-law, mother-in-law, grandmother-in-law, and brother-in-law for their constant support, encouragement, and blessings throughout my research journey. Their presence has been a true source of strength and motivation.

Lastly, I wish to thank every single person I have met along the way. Each interaction—no matter how small—has contributed in some way to shaping me into a better individual. For all the kindness, inspiration, and lessons I received, I am truly grateful.

With utmost reverence, I express my heartfelt gratitude to Lord Radha–Krishna. Their divine grace, ever-flowing compassion, and spiritual guidance have sustained me through every step of this journey, filling my heart with peace, clarity, and unwavering hope.

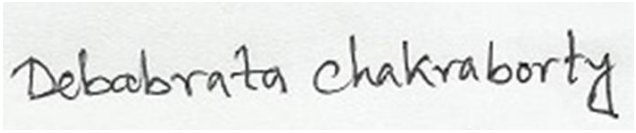

Debabrata

CONTENTS

		Page
Thesis Synopsis		XVI-XXVI
List of Scheme		XXVII
List of Figures		XVIII-XXXII
List of Charts		XXXIII
List of Tables		XXXIV
Glossary of Acronyms		XXXV-XXXVI
Chapter 1		
Introduction		
1.1.	**Introduction to Semiconducting Nanomaterials**	2
1.2	**Perovskite Nanocrystals**	5
1.2.1	**Synthesis of Lead halides Perovskite Nanocrystal**	8
1.3	**Quantum Dots**	9
1.3.1	**Synthesis of Quantum Dots**	14
1.4	**Challenges and Opportunities**	15
1.5	**Interfacial Modulation**	16
1.5.1	**Ionic Liquids**	16
1.5.2	**Organic Aggregates**	18
1.5.2.1	**Fabrication Methods**	20

1.6	**Inorganic-Organic Nanohybrid Assemblies**	20
1.7	**Photophysical Processes in Molecules/Materials**	22
1.7.1	**Photoinduced Energy and Charge Transfer**	22
1.7.1.1	**Energy Transfer**	22
1.7.1.2	**Electron and Hole Transfer**	25
1.8	**Scope and Objectives of the Thesis**	27
1.8.1	**Limitations of Current Nanomaterials**	27
1.8.2	**Rationale for Using Ionic Liquids (ILs)**	27
1.8.3	**Rationale for Using Organic J-Aggregates**	28
1.8.4	**Overall Motivation**	28
1.9	**Chapterwise Organization of the Thesis**	28
1.10	**References**	30
Chapter 2		
Materials, Experimental Techniques, and Methods		
2.1	**Materials**	45
2.1.1	**For $CsPbBr_3$ Nanocrystal Synthesis and ILs Interaction**	45
2.1.2	**For Cs_4PbBr_6 microdisks Synthesis**	46
2.1.3	**For CdTe@ZnS QDs Synthesis**	46
2.1.4	**For ILs Synthesis**	46
2.2	**Synthesis and Purification**	46
2.2.1	**Synthesis and Purification of $CsPbX_3$ NCs**	46
2.2.2	**Synthesis and Purification of Cs_4PbBr_6 microdisks MDs**	47
2.2.3	**Synthesis of ILs**	47
2.2.4	**Synthesis and Purification of CdTe@ZnS QDs**	47
2.3	**Sample Preparation:**	48

2.3.1	**Preparation of CdTe@ZnS QDs_J-aggregate nanohybrid**	48
2.3.2	**Preparation of SEM Sample**	48
2.3.3	**Preparation of TEM Samples**	48
2.4	**Instrumentations**	49
2.4.1	**Instrument for Microscopic Characterization**	49
2.4.2	**Instrumentation Steady-State optical measurements**	49
2.4.2.1	**Absorption Spectroscopy**	49
2.4.2.2	**Fluorescence Spectroscopy**	50
2.4.3	**Instruments for Time-Resolved Study**	50
2.4.3.1	**Fluorescence Lifetime Measurements**	50
2.4.3.1.1	**Basic Principle of TCSPC**	51
2.4.3.1.2	**Major Components of a TCSPC System**	52
2.4.3.1.3	**Working Overview**	53
2.4.3.2	**Broadband Pump-Probe Femtosecond Transient Absorption Spectroscopy**	54
2.4.3.2.1	**Components of the TAS Setup**	55
2.4.3.2.2	**Origin of Transient Signals in a TA Spectrometer**	57
2.4.3.2.3	**Types of TA Signals**	58
2.4.3.2.4	**Data Analysis in Our Setup**	59
2.4.3.3	**Time-Resolved Confocal Fluorescence Microscopy**	60
2.4.3.3.1	**Fluorescence Correlation Spectroscopy (FCS)**	61
2.4.3.3.2	**Fluorescence Lifetime Imaging (FLIM)**	63
2.4.4	**Nuclear Magnetic Resonance (NMR) spectroscopy**	64
2.4.5	**Dynamic Light Scattering**	64

2.4.6	**X-ray Diffraction (XRD)**	64
2.5	**Standard Error Limit**	66
2.6	**References**	66
Chapter 3		
Surface Modification of $CsPbX_3$ (X = Cl and Br) Nanocrystals by Treatment with Imidazolium-Based Ionic Liquids in Enhancing the Stability and Photoluminescence Quantum Yield		
3.1	**Introduction**	69
3.2	**Results and Discussion**	72
3.3	**Conclusion**	85
3.4	**Appendix**	86
3.5	**References**	93
Chapter 4		
Ionic Liquid Engineered Defect-Driven Green Emitting Zero Dimensional Cs_4PbBr_6 Microdisks		
4.1	**Introduction**	103
4.2	**Results and Discussion**	105
4.3	**Conclusion**	120
4.4	**Appendix**	121
4.5	**References**	127
Chapter 5		
Energy Transfer Induced Enhanced Valley Splitting of Emission of Inorganic CdTe@ZnS QDs in Presence of Organic J-Aggregates		
5.1	**Introduction**	136
5.2	**Results and Discussion**	139
5.3	**Conclusion**	150
5.4	**Appendix**	151
5.5	**References**	164
Chapter 6		

Charge-Transfer Dynamics between CdTe@ZnS Quantum Dots and Pyridinium-Based Ionic Liquids		
6.1	**Introduction**	172
6.2	**Results and Discussion**	176
6.3	**Conclusion**	188
6.4	**Appendix**	189
6.5	**References**	194
Thesis Summary and Future Perspective		201

SYNOPSIS

Semiconducting nanomaterials have attracted significant attention owing to their tunable excitonic properties and promise for next-generation optoelectronic and photonic devices.[1-7] Among these, halide perovskite nanocrystals (PNCs) are particularly attractive because of their high absorption coefficients, bright emission, and facile solution processability.[8-10] However, their practical deployment remains limited by poor stability, and the presence of surface defects.[11-15] In this thesis, imidazolium-based ionic liquids (ILs) are explored as versatile interfacial modulators to overcome these limitations. Post-synthetic treatment of PNCs with imidazolium ILs markedly enhances PLQY by effectively removing excess lead ions from their surfaces while simultaneously improving both chemical and photostability, even at the single-particle level. Additionally, imidazolium IL-assisted synthesis enables the controlled preparation of phase-pure zero-dimensional Cs_4PbBr_6 microdisks, with tunable morphology and strong intrinsic green emission. Temperature-dependent photoluminescence studies have further revealed high exciton-binding energy and strong exciton–phonon coupling, affirming the intrinsic excitonic origin of emission in these IL-modulated systems. These findings have clearly established the importance of imidazolium-based ILs for tailoring the stability and optical response of perovskite nanomaterials.

In addition to perovskites, colloidal quantum dots (QDs) represent another important class of semiconducting nanomaterials, known for their size-dependent emission, high photostability, and wide-ranging applicability in optoelectronics, sensing, and bioimaging.[1-2,16] In this work, CdTe@ZnS quantum dots (QDs) have been investigated to explore exciton dynamics and interfacial charge-transfer processes. A hybrid system of CdTe@ZnS QDs and organic J-aggregates exhibit highly efficient Förster resonance energy transfer (FRET) and a

remarkable valley splitting in QD emission even without external fields. This splitting, tunable by FRET efficiency and chemical modification of the aggregates, introduces a new pathway toward valleytronic applications. Furthermore, interactions of QDs with pyridinium-based ILs have revealed distinct fluorescence quenching behavior of QDs in presence of ILs driven by photoinduced electron transfer (PET). The quenching efficiency is found to be strongly dependent on IL structure, viscosity, and interfacial interactions, offering valuable mechanistic insight into charge-transfer processes at QDs–ILs interfaces.

Overall, this thesis demonstrates how imidazolium- and pyridinium-based ILs, along with organic moieties, can act as powerful modulators of their properties for semiconducting nanomaterials. By facilitating surface modification, control over morphology, improved stability, and tunable excitonic or charge-transfer processes, such strategies are expected to facilitate the design of long-lasting nanohybrids for optoelectronic and valleytronic applications.

Organisation of thesis

The current thesis has been divided into six chapters. The contents of all the chapters of the present thesis are briefly described below.

Chapter 1: Introduction

This chapter provides the background and motivation for the thesis. It introduces semiconducting nanomaterials, with a focus on perovskite nanocrystals (PNCs) and quantum dots (QDs), highlighting their unique excitonic properties. The photophysical properties of these materials and their importance for various applications, including optoelectronic, photonic, and energy-related devices, are discussed. Major challenges pertaining to these materials, such as surface defects, instability, and limited control over interfacial charge and exciton dynamics, are presented. The role of ionic liquids (ILs) and organic moieties as interfacial modulators in overcoming these challenges is introduced. Additionally, some

general synthetic approaches for preparing and modifying these nanomaterials are briefly described. Finally, the objectives and scope of the thesis are outlined.

Chapter 2: Experimental Techniques and Methods

This chapter describes the experimental techniques, instrumentation, and methodologies employed throughout the thesis. It includes a detailed overview of the synthesis methods used for perovskite nanocrystals (PNCs) and CdTe@ZnS quantum dots (QDs), as well as postsynthetic modifications using ionic liquids (ILs) and organic moieties. The characterization techniques discussed include structural analysis tools such as transmission electron microscopy (TEM), selected area electron diffraction (SAED), scanning electron microscopy (SEM), and energy-dispersive X-ray spectroscopy (EDX), powder X-ray diffraction (PXRD), and spectroscopic methods such as steady-state and time-resolved photoluminescence (PL), fluorescence lifetime imaging microscopy (FLIM), infrared spectroscopy (FTIR), X-ray photoelectron spectroscopy (XPS), and Transient Absorption Spectroscopy (TAS) for probing ultrafast exciton and charge-transfer dynamics. The chapter also outlines procedures for studying photophysical properties, charge transfer, and exciton dynamics, both at ensemble and single-particle levels. FLIM and Fluorescence Correlation Spectroscopy (FCS) are highlighted as key techniques for single-particle/single-molecule investigations, enabling analysis of diffusion dynamics, emission fluctuations, and interfacial interactions of individual nanomaterials. Finally, the rationale for selecting specific ionic liquids and organic modifiers, along with their preparation and handling, is presented.

Chapter 3: Surface Modification of $CsPbX_3$ (X = Cl and Br) Nanocrystals by Treatment with Imidazolium-Based Ionic Liquids in Enhancing the Stability and Photoluminescence Quantum Yield

This chapter focuses on the role of imidazolium-based ionic liquids (ILs) in enhancing the stability and photophysical performance of perovskite nanocrystals (PNCs), which are

otherwise limited by poor photoluminescence quantum yield (PLQY) and low chemical stability (Figure 1).[11-15,17] The study explores how postsynthetic treatment with ILs can efficiently passivate surface defects, diminish nonradiative recombination, and remove excess lead adatoms from the nanocrystal surface.

A combination of structural and spectroscopic tools has been employed to probe these improvements. TEM and PXRD confirm the retention of crystalline integrity, while XPS provides evidence for the removal of surface Pb adatoms upon IL treatment. Optical investigations, including steady-state and time-resolved PL, reveal a substantial increase in PLQY and extended exciton lifetimes, indicating suppressed trap-assisted recombination pathways.

Furthermore, the effect of ionic liquid passivation is evident not only at the ensemble level but also during single-particle measurements, where enhanced emission stability is observed. The presence of ionic liquids improves the chemical robustness of PNCs, maintaining their luminescence properties even under conditions where untreated PNCs undergo rapid degradation.

Overall, this chapter demonstrates that ionic liquids can act as effective surface modulators for perovskite nanocrystals, offering a dual advantage of defect passivation and chemical stabilization. These findings highlight the potential of IL-assisted strategies for advancing the practical deployment of PNCs in optoelectronic and photonic applications.

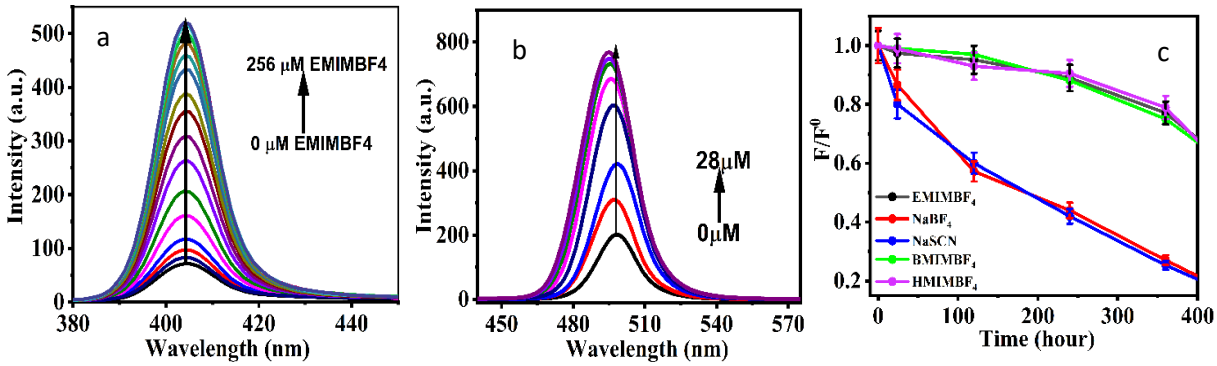

Figure 1. (a) and (b) emission spectra of $CsPbCl_3$ and $CsPbBr_3$ PNCs respectively with gradual addition of $EMIMBF_4$ (c) Plot of relative fluorescence intensity versus time showing the stability of $CsPbBr_3$ PNCs in presence of $EMIMBF_4$, $BMIMBF_4$, $HMIMBF_4$, $NaBF_4$, and NaSCN.

Chapter 4: Ionic Liquid Engineered Defect-Driven Green Emitting Zero Dimensional Cs_4PbBr_6 Microdisks

This chapter presents the synthesis and photophysical investigation of zero-dimensional (0D) cesium lead bromide (Cs_4PbBr_6) microdisks (MDs) using an ionic liquid (IL)-mediated antisolvent precipitation method at room temperature. The motivation arises from the unique excitonic properties of 0D perovskites and the challenges in obtaining phase-pure, defect-controlled materials with tunable morphology and stable optical response.[18-19]

The role of imidazolium-based ionic liquids in the synthesis of 0D MDs has been systematically explored by varying alkyl chain length, cationic type, and IL concentration. Such variations enable control over crystal morphology and surface environment, thereby tailoring the optical properties of the resulting microdisks. Structural characterizations using TEM, SAED, PXRD, and EDX have confirmed the formation of highly crystalline and phase-pure Cs_4PbBr_6 MDs, free from $CsPbBr_3$ impurities.

Photophysical investigations, including steady-state PL, time-resolved PL, temperature-dependent PL, and FLIM have also established the origin of strong intrinsic green emission in Cs_4PbBr_6. The emission mechanism is attributed to defect-mediated midgap recombination, supported by the observation of a large exciton-binding energy (~222 meV) and strong exciton–phonon coupling. Importantly, FLIM studies reveal heterogeneity in PL intensity and lifetime, which can be linked to spatial variations in trap-state distributions across the MDs (Figure 2).

The results have demonstrated the effectiveness of ionic liquids as functional ligands in directing crystal growth, improving optical stability, and tuning excitonic emission in 0D

perovskites. This chapter highlights the potential of IL-assisted approaches for designing next-generation perovskite-based materials with tailored morphology and photophysical properties.

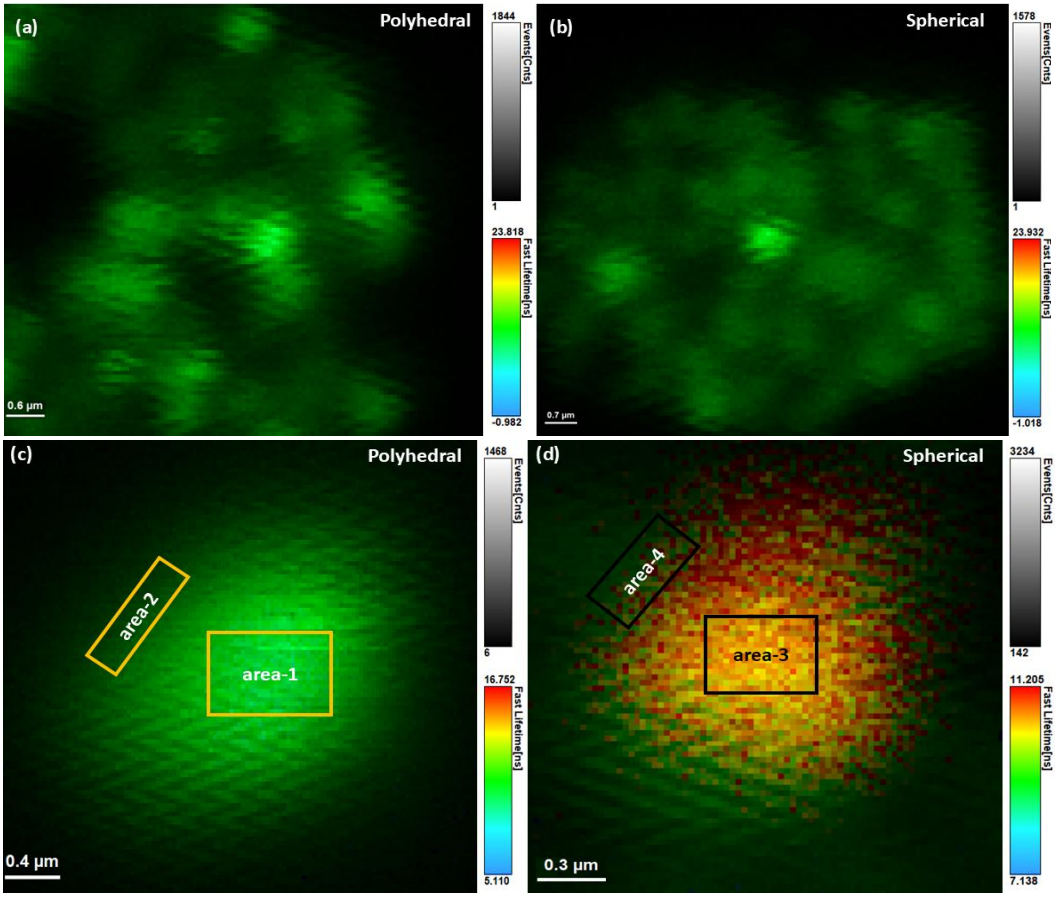

Figure 2: Fluorescence intensity and lifetime images (FLIM) of Cs_4PbBr_6 MDs highlighting spatial variation: (a) polyhedral particle, (b) spherical particles; (c, d) corresponding fluorescence intensity and lifetime images of single polyhedral and spherical MDs respectively.

Chapter 5: Energy Transfer Induced Enhanced Valley Splitting of Emission of Inorganic CdTe@ZnS QDs in Presence of Organic J-Aggregates

This chapter explores the design and photophysical behavior of inorganic–organic hybrid nanomaterials comprising cadmium telluride/zinc sulfide (CdTe@ZnS) quantum dots (QDs) and organic J-aggregates. The motivation lies in the prospect of engineering strong exciton–exciton interactions for next-generation optoelectronic and valleytronic applications.

Nanohybrid materials QDs with J-aggregates results in highly efficient Förster resonance energy transfer (FRET) from QDs (donors) to J-aggregates (acceptors) (Figure 3a

and b). A unique and significant finding is the clear valley splitting of the QD emission band during the FRET process, even in the absence of an external field. The energy separation associated with valley splitting is shown to have a linear relationship with FRET efficiency (Figure 3c), establishing a direct link between exciton coupling and energy transfer dynamics.

The coupling can be tuned by modifying the organic moieties of the J-aggregates, offering chemical control over exciton interactions. This flexibility demonstrates the advantage of hybrid systems, where organic components can act not only as energy acceptors but also as regulators of inorganic exciton behavior.

Spectroscopic analyses, including steady-state and time-resolved PL, have been employed to probe exciton transfer pathways and recombination dynamics. Together, these measurements have provided a detailed understanding of interfacial exciton coupling and its impact on emission properties of the nanohybrid systems.

Overall, this chapter highlights how QD–J-aggregate hybrids represent a promising class of materials for manipulating valley physics and exciton–exciton interactions under ambient conditions. The findings have established a new platform for tailoring excitonic processes through nanoscale hybridization, with strong implications for the development of valleytronic and optoelectronic devices.

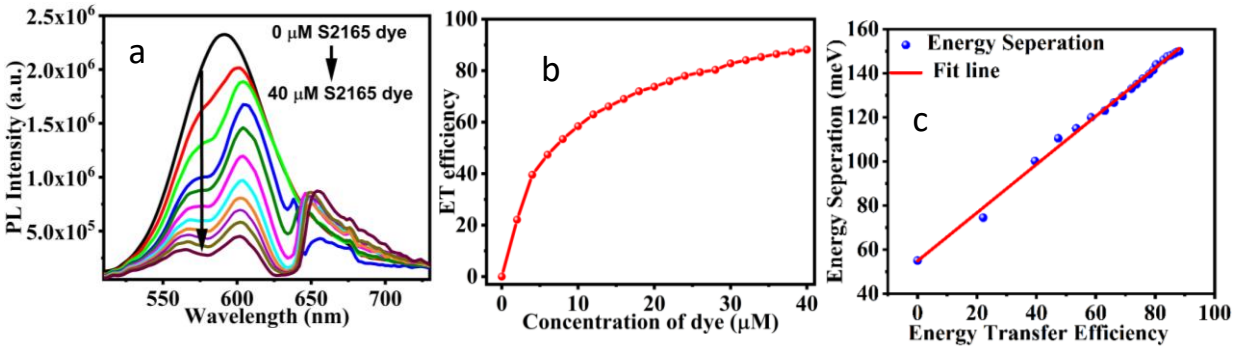

Figure 3: PL spectra of CdTe@ZnS QD with increasing concentration of S2165 dye (λ_{ex} = 405 nm). (b) Change in ET efficiency from CdTe ZnS QDs to J-aggregate as a function of J-aggregate(acceptor) concentration and (c) plot of energy separation between two emission peaks versus ET efficiency.

Chapter 6: Charge-Transfer Dynamics between CdTe@ZnS Quantum Dots and Pyridinium-Based Ionic Liquids

This chapter investigates interfacial charge-transfer processes in hybrid systems comprising cadmium telluride/zinc sulfide (CdTe@ZnS) quantum dots (QDs) and pyridinium-based ionic liquids (ILs). The motivation stems from the facts that ionic liquids have unique ability to stabilize charged species, provide tunable microenvironments, and can act as effective electron acceptors, making them suitable candidates for regulating quantum dot photophysics.[20]

In this work, systematic studies have been carried out using both monocationic (C_3PyrBr, C_6PyrBr) and dicationic ([C_6Pyr_2]Br_2) pyridinium-based ILs to explore how structural variations in ILs influence electron-transfer dynamics. The QD–IL hybrids are examined using steady-state and time-resolved PL to monitor fluorescence quenching and charge-transfer efficiency. These measurements have revealed that interfacial electron transfer strongly depends on the cationic structure, viscosity, and microenvironment of the IL, as well as the nature of QD–IL interactions.

Advanced spectroscopic techniques, particularly Transient Absorption Spectroscopy (TAS), have been employed to directly probe ultrafast excited-state dynamics (Figure 4). It is well known that TAS measurements can efficiently capture charge-transfer events occurring at femtosecond to nanosecond timescales, offering mechanistic insights into how electron-transfer pathways evolve in different QD–IL environments. Scheme 1 illustrates the photoinduced electron transfer (PET) process from CdTe@ZnS quantum dots (QDs) to pyridinium-based ionic liquids (ILs). Upon photoexcitation, it has been observed that the QDs generate excitons, where the excited electron can be transferred to the electron-accepting pyridinium cation of the ILs. This interfacial process in turn results in fluorescence quenching of the QDs and facilitates charge separation, the efficiency of which depends on the structural features of the ILs.

The results demonstrate that ionic liquid structure can be judiciously tuned to control the extent and rate of electron transfer from quantum dots (Scheme 1). This chapter underscores the importance of molecular-level interface engineering in QD–IL systems and highlights their potential in designing functional hybrid nanomaterials for optoelectronic, sensing, and energy-harvesting applications.

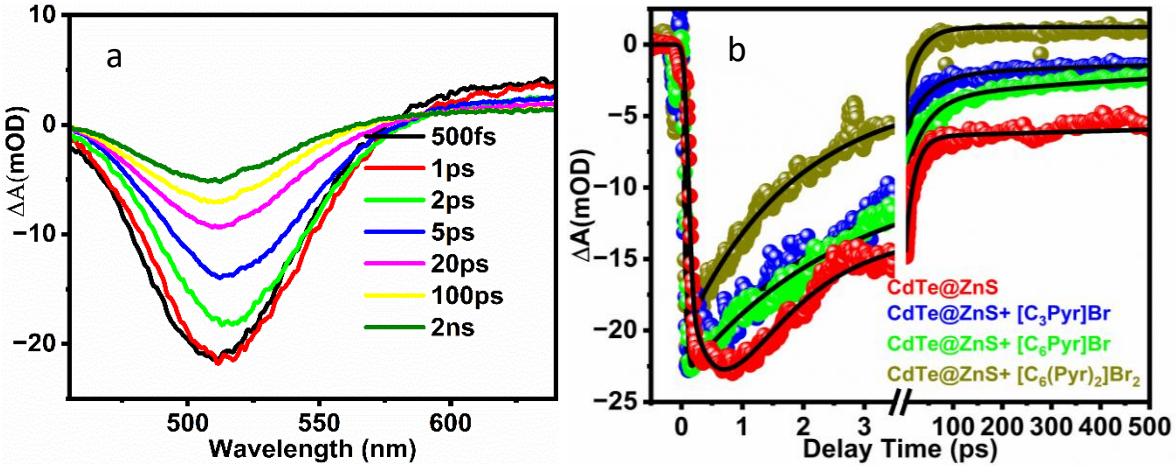

Figure 4: (a) Transient absorption spectra of CdTe@ZnS QDs plotted at different pump-probe delay times after the photoexcitation of 420 nm (2.95 eV) (b) TA kinetics of CdTe@ZnS QDs in absent and present of various pyridinium based ILs probed at 520 nm after the photoexcitation of 420 nm.

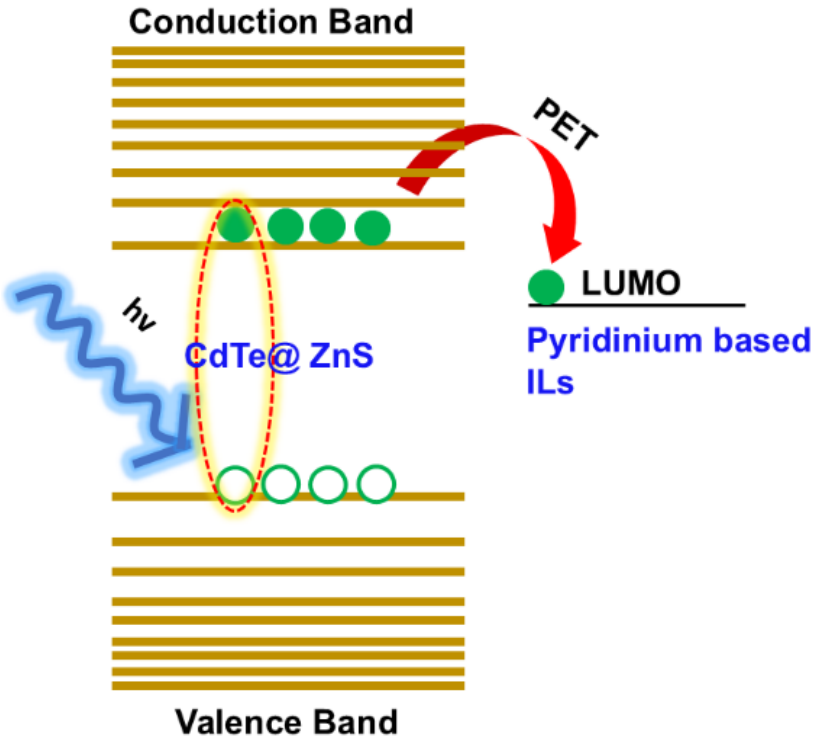

Scheme 1: The schematic representation of photoinduced charge transfer dynamics from CdTe@ZnS QDs to Pyridinium based ILs.

References

1. Kundu, S.; Patra, A. *Chem. Rev.* **2017**, *117*, 712–757.
2. Thomas, A.; Sandeep, K.; Somasundaran, S. M.; Thomas, K. G. *ACS Energy Lett*. **2018**, *3*, 2368−2375.
3. Wang, Y.; Li, X.; Song, J.; Xiao, L.; Zeng, H.; Sun, H. *Adv. Mater.* **2015**, *27*, 7101−7108.
4. Jeon, N. J.; Noh, J. H.; Yang, W. S.; Kim, Y. C.; Ryu, S.; Seo, J.; Seok, S. *Nature* **2015**, *517*, 476-480.
5. Ramasamy, P.; Lim, D.H.; Kim, B.; Lee, S.-H.; Lee, M.-S.; Lee, J. S. *Chem. Commun.* **2016**, *52*, 2067−2070.
6. Wang, J.; Wang, N.; Jin, Y.; Si, J.; Tan, Z.; Du, H.; Cheng, L.; Dai, X.; Bai, S.; He, H.; Ye, Z.; Lai, M. L.; Friend, R. H.; Huang, W. *Adv. Mater.* **2015**, *27*, 2311-2316.
7. Jaramillo-Quintero, O. A.; Sanchez, R. S.; Rincon, M.; Mora-Sero, I. Bright *J. Phys. Chem. Lett.* **2015**, *6*, 1883-1890.
8. Aldakov, D.; Reiss, P. *J. Phys. Chem. C* **2019**, *123*, 12527−12541.
9. Roo, J. D.; Ibanez, M.; Geiregat, P.; Nedelcu, G.; Walravens, W.; Maes, J.; Martins, J. C.; Van Driessche, I.; Kovalenko, M. V.; Hens, Z. *ACS Nano* **2016**, *10*, 2071−2081.
10. Dutta, A.; Behera, R. K.; Pal, P.; Baitalik, S.; Pradhan, N. *Angew. Chem. Int. Ed.* **2019**, *58*, 5552−5556.
11. Yang, D.; Li, X.; Zeng, H. *Adv. Mater. Interfaces* **2018**, *5*, 1701662.
12. Grisorio, R.; Di Clemente, M. E.; Fanizza, E.; Allegretta, I.; Altamura, D.; Striccoli, M.; Terzano, R.; Giannini, C.; Irimia-Vladu, M.; Suranna, G.P. *Nanoscale* **2019**, *11*, 986– 999.
13. Kovalenko, V. M.; Protesescu, L.; Bodnarchuk, M. I. *Science* **2017**, *358*, 745−750.
14. Swarnkar, A.; Ravi, V. K.; Nag, A. *ACS Energy Lett.* **2017**, *2*, 1089−1098.

15. Giansante, C.; Infante, I. *J. Phys. Chem. Lett.* **2017**, *8*, 5209−5215.

16. Almeida, G.; Poll, L. V.; Evers, W. H.; Szoboszlai, E.; Vonk, S. J. W.; Rabouw, F. T.; Houtepen, A. J. *Nano Lett.* **2023**, *23*, 18, 8697–8703.

17. Behera, R. K.; Adhikari, S. D.; Dutta, S. K.; Dutta, A.; Pradhan, N. *J. Phys. Chem. Lett.* **2018**, 9, 23, 6884–6891.

18. Zhang, Y.; Saidaminov, M. I.; Dursun, I.; Yang, H.; Murali, B.; Alarousu, E.; Yengel, E.; Alshankiti, B. A.; Bakr, O. M.; Mohammed, O. F. *J. Phys. Chem. Lett.* **2017**, *8* (5), 961– 965.

19. Seth, S.; Samanta, A. *J. Phys. Chem. Lett.* **2018**, *9*, 176– 183.

20. Saladin, M.; Maroncelli, M. *J. Phys. Chem. B* **2020**, *124*, 50, 11431–11445.

List of Schemes

Sl. No.	Scheme No	Scheme Title	Page No.
1	Scheme 1.1	Schematic of halide perovskite nanocrystals	6
2	Scheme 1.2	Schematic of halide perovskite nanocrystals illustrating dimensional classification (0D, 1D, 2D, 3D)	7
3	Scheme 1.3	Schematic illustration depicting how particle size influences energy levels and bandgap in semiconductor materials	10
4	Scheme 1.4	Schematic showing the differences in electronic energy levels between a molecule, quantum dot, and bulk semiconductor; EQD and Ebulk correspond to the quantum dot and bulk band gaps	11
5	Scheme 1.5	Schematic illustration of the electronic structure and trap-state formation in perovskite nanocrystals and comparison with conventional semiconductor systems.	13
6	Scheme 1.6	Schematic illustration of the permitted electronic transitions in J- and H-aggregates, where 'm' denotes the transition dipole moment integral (with allowed transitions corresponding to $m > 0$)	19
7	Scheme 1.7	Schematic of singlet-singlet Dexter and Forster energy transfer	23
8	Scheme 1.8	Schematic of oxidative and reductive pathways involved in a photoinduced electron-transfer (PET) process.	26
9	Scheme 2.1	Schematic diagram for the working principle of the TCSPC setup	52
10	Scheme 2.2	Schematic diagram of basic pump-probe interaction in TAS	54
11	Scheme 2.3	Basic schematic of TA Spectrometer	57
12	Scheme 2.4	Schematic of different types of signals produced in TAS	59
13	Scheme 2.5	Schematic of Time-resolved confocal fluorescence microscope setup	61
14	Scheme 2.6	Scheme illustrates the diffusion of a fluorophore through the ellipsoidal confocal volume	63
15	Scheme 2.7	Schematic depiction of the Bragg condition. The incident X-ray beam strikes the lattice plane at an angle θ, and the reflected beam emerges at the same angle, producing constructive interference when the Bragg equation is satisfied	65
16	Scheme 3.1	Schematic representation of surface passivation of ILs on the perovskite surface	85
17	Scheme 5.1	Schematic representation of the interaction of CdTe@ZnS QDs with J-aggregate	144

18	Scheme 6.1	The schematic representation of photoinduced charge transfer dynamics from CdTe@ZnS QDs to Pyridinium-based ILs	180

List of Figures

Sl. No.	Figure No	Figure Title	Page No.
1	Figure 1.1	Global primary energy consumption	3
2	Figure 1.2	Global semiconductor market	4
3	Figure 3.1	TEM image of $CsPbBr_3$ PNCs (a) before and (b) after treatment of ILs. (c) Powder X- ray diffraction patterns of $CsPbBr_3$ PNCs before and after treatment of ILs (Inset of (a) and (b) shows the HRTEM image of their respective samples)	74
4	Figure 3.2	(a) Absorption and (b) emission spectra of $CsPbCl_3$ PNCs with gradual addition of $EMIMBF_4$ (c) Absorption and (d) emission spectra of $CsPbBr_3$ PNCs with gradual addition of $EMIMBF_4$ (e) Photographs of colloidal solutions of PNCs (blue-$CsPbCl_3$, green-$CsPbBr_3$, and red-$CsPbI_3$ NCs solution) before and after treatment with ILs.	75
5	Figure 3.3	PL decay curve of $CsPbBr_3$ NCs before and after treatment with $EMIMBF_4$.	79
6	Figure 3.4	(a) XPS spectra of Pb 4f7/2 and 4f7/2 of $CsPbBr_3$ before and after the treatment with $[EMIM][BF_4]$.(b) Fourier transformed infrared spectroscopy (FTIR) transmission spectra of $[EMIM][BF_4]$ in hexane, $CsPbBr_3$ NCs before and after treatment with $[EMIM][BF_4]$. Region of interest is (900 – 2000) cm^{-1}. After treatment a broad peak around 1080 cm^{-1} corresponds to B-F stretching of BF^{4-} bound to lead and another peak arises at around 1560 cm^{-1} corresponds to the C=O bond stretching of oleate	81
7	Figure 3.5	(a) Plot of relative fluorescence intensity (F/F0) versus time showing the stability of $CsPbBr_3$ PNCs in presence of $EMIMBF_4$, $BMIMBF_4$, $HMIMBF_4$, $NaBF_4$, and NaSCN. (b) Relative fluorescence intensity, (c) relative PL lifetime of $CsPbBr_3$ NCs before and after the treatment with $EMIMBF_4$ with time under the continuous irradiation of light of $CsPbBr_3$ NCs	83

8	Figure 3.6	Normalized fitted Fluorescence correlation curves of the $CsPbBr_3$ NCs before and after the treatment with $EMIMBF_4$	85
9	Figure APX3.1	a) TEM, (b) HRTEM and (c) SAED images of $CsPbCl_3$ PNCs (d) TEM, (e) HRTEM and (f) SAED images of $CsPbBr_3$ NCs.	87
10	Figure APX3.2	Powder X-ray diffraction patterns of (a) $CsPbCl_3$ (b) $CsPbBr_3$ and (c) $CsPbI_3$ NCs	87
11	Figure APX3.3	UV−vis absorption (black line) and PL (red line) spectra of (a) the $CsPbCl_3$, (b) $CsPbBr_3$ and (c) $CsPbI_3$ Perovskite NCs	88
12	Figure APX3.4	PL Decay curves of a-e) $CsPbCl_3$ f-i) $CsPbBr_3$ j) $CsPbI_3$ in absence and presence of selected ILs	88-89
13	Figure APX3.5	SEM image, EDX and elemental composition of precipitated (of Pb(0)-BF_4 mixture) solid after several wash and centrifugation of $CsPbBr_3$ NC solution after treatment with $EMIMBF_4$. Presence of excess lead is observed as Br:Pb=12:13	90
14	Figure APX3.6	XPS survey spectra of $CsPbBr_3$ NCs before and after treatment. No peak for F could be seen at around 685 eV after treatment	90
15	Figure APX3.7	Fourior transformed infrared spectroscopy (FTIR) transmission spectra of (a) [EMIM][OAc] in hexane, $CsPbBr_3$ NCs before and after treatment with [EMIM][OAc], (b) EMS in hexane, $CsPbBr_3$ NCs before and after treatment with EMS	91
16	Figure APX3.8	Relative fluorescence intensity of $CsPbBr_3$ NCs film before and after the treatment with $EMIMBF_4$ with time (a) under normal atmospheric conditions and (b) under the continuous irradiation of light.	91
17	Figure 4.1	(a) TEM image of the Cs_4PbBr_6 MDs. (b) Elemental mapping confirms the uniform distribution of N, Cs, Pb, and Br elements across the MDs (c) HRTEM image showing lattice fringes of the (110) and (300) planes. (d) SAED pattern of a single MD indicating multiple crystallographic planes. (e) EDX spectrum and elemental composition of Cs_4PbBr_6. (f) Powder X-ray diffraction patterns of Cs_4PbBr_6 perovskite microstructure with different ILs and its different concentrations	108
18	Figure 4.2	FESEM images showing the concentration-dependent morphological evolution of Cs_4PbBr_6 MDs synthesized using varying concentrations of $[C_{16}mim]Br$ ionic liquid: (a) 0.05 mM, (b) 0.1 mM, (c) 0.15 mM, and (d) 0.20 mM	110
19	Figure 4.3	(a) Absorption, excitation (λ_{em}=515 nm), and PL spectra (λex=405 nm) of Polyhedron Cs_4PbBr_6 MDs (b) PL spectra of $[C_{12}mim]Br$, $[C_{14}mim]Br$, $[C_{16}mim]Br$, and	112

		$[C_{12}(mim)_2]Br_2$ ILs mediated Cs_4PbBr_6 MDs (C) PL spectra of Cs_4PbBr_6 MDs for various concentration of $[C_{16}mim]Br$ ILs as ligand during synthesis	
20	Figure 4.4	Fluorescence intensity and lifetime images (FLIM) of Cs_4PbBr_6 MDs highlighting spatial variation: (a) polyhedral particle, (b) spherical particles; (c, d) corresponding fluorescence intensity and lifetime images of single polyhedral and spherical MDs respectively. (e, f) PL decay curves from selected regions of the polyhedral (e) and spherical (f) MDs	115
21	Figure 4.5	(a) Temperature-dependent PL spectra of Cs_4PbBr_6 MDs. (b) Integrated PL intensity, (c) plot of FWHM with temperature of Cs_4PbBr_6 MDs, and (d) plot of FWHM with 1/T of Cs_4PbBr_6 MDs (e) Raman spectrum of Cs_4PbBr_6 MDs sample	120
22	Figure APX4.1	FESEM image of polyhedron MDs showing thickness	122
23	Figure APX4.2	FTIR spectra of a) $[C_{16}mim]Br$ and $[C_{16}mim]Br$ IL mediated Cs_4PbBr_6 MDs, b) $[C_{12}(mim)_2]Br_2$ and $[C_{12}(mim)_2]Br_2$ mediated Cs_4PbBr_6 MDs	122
24	Figure APX4.3	FESEM image of (a) $[C_{12}mim]Br$, (b) $[C_{14}mim]Br$, (c) $[C_{16}mim]Br$ and (d) $[C_{12}(mim)_2]Br_2$ ILs mediated of Cs_4PbBr_6 perovskite MDs	123
25	Figure APX4.4	(a) FESEM image of Spherical microdisks. (b) EDX spectrum confirms Cs_4PbBr_6 composition. (c) Elemental mapping of constituent elements shows their even distribution in the MDs.	124
26	Figure APX4.5	FESEM image of the microwires particles	124
27	Figure APX4.6	Absorption, excitation and emission spectra of spherical Cs_4PbBr_6 MDs	125
28	Figure APX4.7	FLIM images of (a) collective and (b, c) single Cs_4PbBr_6 MDs	125
29	Figure APX4.8	(a) Digital image of PL (under UV light) of Cs_4PbBr_6 and $CsPbBr_3$ perovskite sample after adding PbI_2. (b) FLIM image of a mixture of microwire and MDs sample.	125
30	Figure APX4.9	(a) FESEM image of $PbBr_2$ solution added sample of Cs_4PbBr_6. (b) and (c) EDX spectra of different region as marked in panel a. (d) Change in emission spectrum (λ_{exc} = 405 nm) with time of adding DMF solution of $PbBr_2$ to a toluene dispersion of Cs_4PbBr_6 MDs	126
31	Figure 5.1	(a) Normalized absorption (black) and emission (red) spectra of QD. (b) Absorption spectra of QD (black), dye molecule (red), dye J-aggregate (blue dash), and QD/dye aggregate hybrid system (green). (c) Spectral overlap between the emission spectrum of QD (red) and absorption spectrum of S2165 dye aggregate (black). (d) Steady-state PL spectra of QD and QD J-aggregate nanohybrid (red) at 405 nm excitation	142
32	Figure 5.2	PL spectra of CdTe@ZnS QD with increasing concentration of S2165 dye (λ_{ex} = 405 nm)	143

33	Figure 5.3	(a) CdTe ZnS QDs PL spectra with gradual addition of j-aggregated dye (b) change in ET efficiency as a function of dye (acceptor) concentration and (c) plot of energy separation between two emission peaks versus ET efficiency	146
34	Figure 5.4	Deconvoluation of PL spectra of CdTe@ZnS QDs (a) without addition of dye aggregate, (b) at low concentration of dye aggregate, (c) at moderate concentration and (d) at high concentration of dye aggregate	147
35	Figure 5.5	Time resolved PL decay curves of CdTe@ZnS QD alone and in presence of J-aggregate (monitored at 585 nm) at λ_{exc}= 405 nm (inset given ultra-fast PL decay).	149
36	Figure 5.6	Normalized FCS curve of QD alone (black) and in presence of dye aggregate (red)	150
37	Figure APX5.1	EDS elemental mapping of CdTe@ZnS QD (a) image and (b) overlay elemental mapping of Cd, Te, Zn, and S elements and right corner atom% of elements. (c) area EDS spectrum of CdTe@ZnS QD	152
38	Figure APX5.2	a) TEM image and Inset HRTEM image b) size distribution of TEM of CdTe@ZnS QDs and c) XRD of CdTe@ZnS QDs	153
39	Figure APX5.3	Absorption spectra of QD-J aggregate which is deconvoluted by multiple fit analysis.	153
40	Figure APX5.4	Zeta potential graphs for the (a) CdTe@ZnS QDs, (b) CdTe@ZnS QDs+ S2165 dye, and (c) hybrid system of CdTe@ZnS QDs+ S2165 dye aggregate	155
41	Figure APX5.5	(a) The Stern–Volmer plot of relative fluorescence intensity vs. quencher concentration. (b) Plot of F0/(F0 – F) versus 1/[Q] at various temperatures. (c) van't Hoff plot (ln Ka vs. 1000//T) corresponding to the quenching event	156
42	Figure APX5.6	TEM image of CdTe@ZnS QD-J-aggregate nanocomposite.	158
43	Figure APX5.7	Emission spectra of S2165 dye and it's J-aggregate	159
44	Figure APX5.8	Spectral overlap between the emission spectrum of QD (red for 560nm peak and blue for 605nm peak) and absorption spectrum of S2165 dye aggregate (black)	159
45	Figure APX5.9	PL Spectra of CdTe@ZnS QDs with increasing concentration of the same QD	151
46	Figure APX5.10	Time resolved PL decay curves of CdTe@ZnS QD alone and in presence of J-aggregate monitored at (a) λem = 560nm and (b) λem = 605nm with λexc= 405 nm	162
47	Figure APX5.11	Change in ET efficiency as a function of dye (acceptor) concentration (a) and (c) for 560nm peak and 605nm peak respectively. Plot of energy separation between two emission peaks versus ET efficiency (b), (d) for 560nm peak and 605nm peak respectively	163
48	Figure APX5.12	(a) FRET-FLIM image of QD in presence of J-aggregate (b) plot of occurrence of events against FRET.	163

49	Figure 6.1	Normalized absorption (black) and emission (red) spectra of CdTe@ ZnS QD	177
50	Figure 6.2	(a–c) Emission spectra of the CdTe@ZnS QDs recorded with successive additions of C_3PyBr, C_6PyBr, and $C_6(Py)_2Br_2$. (d–f) Corresponding Stern–Volmer plots illustrating the fluorescence quenching behaviour of the CdTe@ZnS QDs in the presence of increasing concentrations of C_3PyBr, C_6PyBr, and $C_6(Py)_2$Br2 ILs	180
51	Figure 6.3	(a–c) Fluorescence decay profiles of the CdTe@ZnS QDs recorded with successive additions of C_3PyBr, C_6PyBr, and $C_6(Py)_2Br_2$. (d–f) Corresponds plots of τ_0/τ versus of concentrations of C_3PyBr, C_6PyBr, and $C_6(Py)_2Br_2$ ILs.	182
52	Figure 6.4	Transient absorption spectra of CdTe@ZnS QDs in (a) absence ILs and in presence of (b) C_3PyBr, (c) C6PyBr, and (d)$[C_6Py_2]Br_2$ ILs plotted at different pump-probe delay times after the photoexcitation of 420 nm.	186
53	Figure 6.5	(a) Normalized TA kinetics of CdTe@ZnS QDs in the absence and presence of various pyridinium-based ILs probed at 516 nm after the photoexcitation of 420 nm. (b) Comparative kinetics for CdTe@ZnS QDs in the absence and presence of C_3PyBr, C_6PyBr, and $[C_6Py_2]Br_2$ at their bleach maxima (516 nm).	186
54	Figure APX6.1	EDS spectrum of CdTe@ZnS QD	190
55	Figure APX6.2	a) TEM image and Inset HRTEM image b) size distribution of TEM of CdTe@ZnS QDs and c) XRD of CdTe@ZnS QDs.	190
56	Figure APX6.3	Spectral overlap between absorbance of ILs and PL of CdTe@ZnS QDs.	191
57	Figure APX6.4	TEM image of CdTe@ZnS QDs in (a) absence and presence of (b)$C_3(Py)]Br$, (c)$[C_6(Py)]Br$, and (d)$[C_6(Py)_2]Br_2$ ILs.	181
58	Figure APX6.5	Zeta potential graphs for the CdTe@ZnS QDs in (a) absence of ILs and in the presence of (b)C_3PyBr, (c) C_6PyBr, and (d)$[C_6Py_2]Br_2$ ILs.	192
59	Figure APX6.6	FCS spectra of CdTe@ZnS QDs in the absence and presence of ILs.	193

List of Charts

Sl. No.	Charts No	Charts Title	Page No.
1	Chart 3.1.	Molecular structures of ILs	72
2	Chart APX4.1	Structure of MILs and DILs	121
3	Chart APX5.1	Molecular structure of S2165 dye.	151
4	Chart APX6.1	Molecular structure of $[C_3(Py)]Br$, $[C_6(Py)]Br$, and $[C_6(Py)_2]Br_2$ ILs	189

List of Tables

Sl. No.	Table No	Table Title	Page No.
1	Table 2.1	Standard error limits involved in the experimental results	65
2	Table 3.1	PL peak and QY of the perovskite NCs before and after treatment	76
3	Table 3.2	PL Decay Parameters of $CsPbBr_3$ With addition of $EMIMBF_4$	78
4	Table APX3.1	PL Decay Parameters of the PNCs in presence and absence of various ILs	91
5	Table APX3.2	Estimated Translational Diffusion Coefficient of [EMIM][BF_4] in presence and absence of $CsPbBr_3$ NCs	92
6	Table APX3.3	Translational diffusion time of $CsPbBr_3$ NCs in absent and the presence (recorded after 0 hour, 5 hour, 10 hour) of $EMIMBF_4$	92
7	Table 4.1	Photoluminescence decay parameters of various regions of different MDs	116
8	Table APX4.1	PLQY of different IL mediated Cs_4PbBr_6 MDs	126
9	Table APX4.2	Average lifetime components along with their mean deviations of centre and edge areas on 10 individual MDs	127
10	Table APX5.1	Zeta potential of CdTe@ZnS QD with and without dye and dye aggregate.	155
11	Table APX5.2	Stern-Volmer quenching constant and thermodynamic parameters for the interaction between CdTe@ZnS QD and S2165 dye at various temperatures	156
12	Table APX5.3	FRET parameters of CdTe@ZnS QD_S2165 J-aggregate nanohybrid associate.	160
13	Table APX5.4	PL decay parameters of CdTe@ZnS QD alone and in presence of S2165 dye aggregate	160
14	Table APX5.5	Ultra-fast PL decay parameters of CdTe@ZnS QD alone and in presence of S2165 dye aggregate	161
15	Table APX5.6	PL decay parameters of CdTe@ZnS QD alone and in presence of S2165 dye aggregate at λ_{em} = 560 nm and λ_{em} = 605 nm with λ_{exc}= 405 nm and their ET efficiency	162
16	Table 6.1	Kinetic Fitting Parameters for the Probe Monitored at the Bleach Position (516 nm)	187

17	Table APX6.1	Zeta potential of CdTe@ZnS QDs in absence of ILs and in the presence of C_3PyBr, C6PyBr, and $[C_6Py_2]Br_2$ ILs.	193
18	Table APX6.2	PL decay parameters of CdTe@ZnS QD alone and in presence of ILs.	193

Glossary of Acronyms

NPs	Nanoparticles
QDs	Quantum Dots
LHPNCs	Lead Halide Perovskite Nanocrystals
UV	Ultra-Violet
PL	Photoluminescence
FRET	Förster resonance energy transfer
DET	Dexter Energy Transfer
EET	Excitation energy transfer
PET	Photoinduced Electron Transfer
$J(\lambda)$	Overlap integral
R_{DA}	Donor to acceptor distance
θ_D	Quantum yield of donor
R_0	Förster distance
FLIM	Fluorescence lifetime imaging
TEM	Transmission electron microscopy
EDX	Energy dispersive X-ray analysis
XPS	X-ray photoelectron spectroscopy
DLS	Dynamic light scattering
DLS	Cyclic Voltammetry
TCSPC	Time-Correlated Single Photon Counting
PMT	Photo multiplier tube
CFD	Constant fraction discriminator
TAC	Time to amplitude converter
PGA	Programmable gain amplifier
ADC	Analog to digital converter
WD	Window discriminator
MCA	Multichannel analyzer
MCP	Microchannel plate
IRF	Instrument response function
CCD	Charged coupled device
SPADs	single-photon avalanche photodiodes
NLLS	Nonlinear least squares
TTTR	time-tagged time-resolved

FCS	Fluorescence Correlation Spectroscopy
D	Diffusion coefficient
η	Refractive index
τ_f	Fluorescence lifetime
$\emptyset_f$	Fluorescence quantum yield
k_{nr}	Non-radiative rate constan
k_r	Radiative rate constant
λ_{exc}	Excitation wavelength
VB	Valence Band
CB	Conduction Band
HOMO	Highest Occupied Molecular Orbital
LUMO	Lowest Unoccupied Molecular Orbital
ILs	Ionic liquids
RTILs	Room temperature ionic liquids
DILs	Dicationic ionic liquids
MILs	Monocationic ionic liquids
APX	Appendix

CHAPTER 1

Introduction

Abstract

This chapter introduces the fundamental concepts and materials central to this thesis. It focuses on halide perovskite nanocrystals (PNCs), chalcogenide quantum dots (QDs), and organic nano/microparticles such as J-aggregates. Their key photophysical properties, bandgap tunability, exciton dynamics, emission characteristics, and surface-defect sensitivity have been outlined along with the major challenges that limit their performance in optoelectronic and energy-related applications. The potential of inorganic–organic hybrid assemblies has been highlighted, in order to depict the fact that coupling between Wannier–Mott excitons in PNCs/QDs and Frenkel excitons in organic aggregates can yield emergent optical behavior and improved light-harvesting efficiency. The role of ionic liquids (ILs) as interfacial modulators, capable of passivating defects, stabilizing nanocrystals, and regulating energy or electron transfer, has also been introduced. Fundamentals associated with some important photophysical processes such as fluorescence, Förster and Dexter energy transfer, and photoinduced electron transfer (PET) have been outlined to establish the mechanistic framework for the thesis. Overall, this chapter provides the scientific basis, motivation, and objectives for the detailed studies on exciton dynamics and interfacial engineering presented in the subsequent chapters.

1.1. Introduction to Semiconducting Nanomaterials

The rapid industrialization and exponential growth in global energy consumption have intensified the demand for sustainable and renewable energy technologies (Figure 1.1).[1] Traditional fossil fuels, while still dominant, pose severe environmental challenges due to greenhouse gas emissions and finite reserves. Consequently, the transition toward a clean-energy economy necessitates the development of advanced materials capable of efficiently

harvesting, converting, and storing solar energy, which remains the most abundant and inexhaustible natural resource.[1]

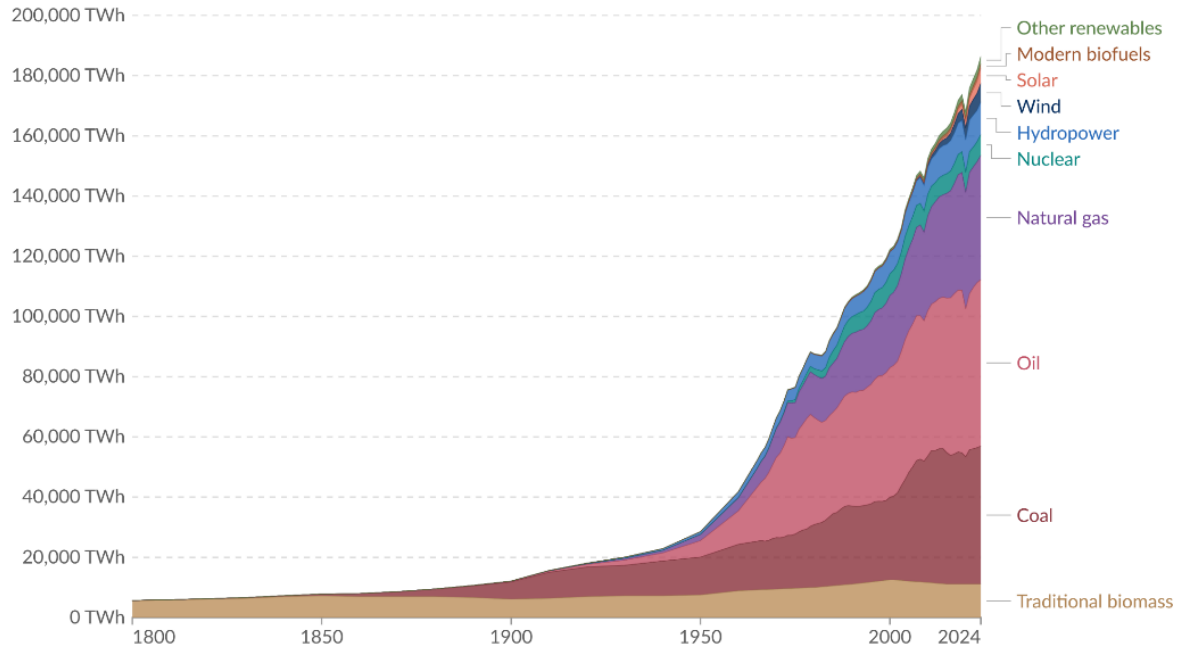

Figure 1.1. Global primary energy consumption.[1]

Semiconducting materials occupy a central role in this global energy transition. The global semiconductor market is growing steadily and is expected to expand even more rapidly in the near future (Figure 1.2).[2] Their unique capacity to absorb light and convert it into electrical or chemical energy underpins the operation of solar cells, photodetectors, light-emitting diodes (LEDs), photocatalysts, and other optoelectronic systems.[3-5] For example, high-efficiency solar cells depend on semiconductors that generate excitons (electron–hole pairs) and facilitate their rapid separation and transport to produce electrical current. Likewise, in LEDs, semiconductors with tunable bandgaps are crucial for efficient light emission across the visible spectrum.[3-5]

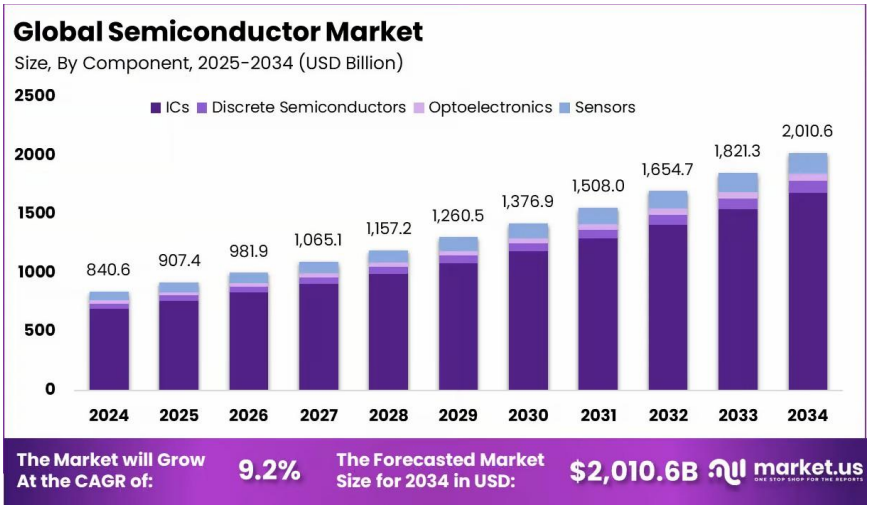

Figure 1.2. Global semiconductor market.[2]

Although silicon-based semiconductors dominate commercial photovoltaic and electronic technologies, they are expensive and require high-temperature, energy-intensive processing.[6-8] This cost limitation has prompted extensive research into alternative semiconducting materials that are not only low-cost but also solution-processable, tunable, and compatible with flexible device architectures.

In recent years, nanostructured semiconductors such as halide perovskite nanocrystals (PNCs), quantum dots (QDs), and nanohybrid materials have emerged as next-generation materials for renewable energy and light-harvesting applications.[9-17] These nanoscale systems enable precise control over optical and electronic properties, offering unprecedented design flexibility for solar-energy conversion, photon management, and photochemical transformations.[12-16] Furthermore, their solution processability and compatibility with flexible substrates enable scalable, low-cost, and energy-efficient device fabrication.[15] However, despite these advantages, challenges such as instability under ambient conditions, surface trap states, and inefficient exciton or charge-transfer dynamics limit their widespread adoption.[18-21] Addressing these issues requires a deeper understanding of the fundamental processes governing exciton generation, recombination, and interfacial interactions. In order to

understand these aspects of the materials, steady-state and time-resolved spectroscopic investigations are often employed. Additionally, this has motivated the exploration of specialized materials such as ionic liquids (ILs) and organic molecular assemblies as soft-matter components capable of stabilizing semiconductor interfaces and modulating their photophysical behavior.[22-31]

1.2. Perovskite Nanocrystals

The mineral now known as perovskite was first discovered in 1839 by Gustav Rose during his examination of geological samples from the Ural Mountains in Russia. He named the mineral in honor of the Russian mineralogist Lev Aleksevich von Perovski. Although the term perovskite originally referred specifically to the oxide $LaFeO_3$, it has since expanded to encompass a broader class of materials with the general formula ABO_3 that share a common crystal structure.[32]

In recent years, lead halide perovskite nanocrystals (LHPNCs) have emerged as a particularly important subset of perovskite materials owing to their exceptional optoelectronic characteristics, including tunable band gaps, high photoluminescence quantum yields (PLQY), and low trap-state densities.[33-38] Their general chemical formula, ABX_3, analogous to the ABO_3 oxide perovskites, consists of a monovalent cation ($A = Cs^+$, MA^+, FA^+), a divalent metal cation ($B = Pb^{2+}$, Sn^{2+}), and a halide anion ($X = Cl^-$, Br^-, I^-) (shown in Scheme 1.1). The crystal structure, formed by corner-sharing $[BX_6]^{4-}$ octahedra arranged in a three-dimensional framework or isolated in low-dimensional architectures, plays a crucial role in determining their band structure, excitonic behavior, and overall optoelectronic performance.[39-47]

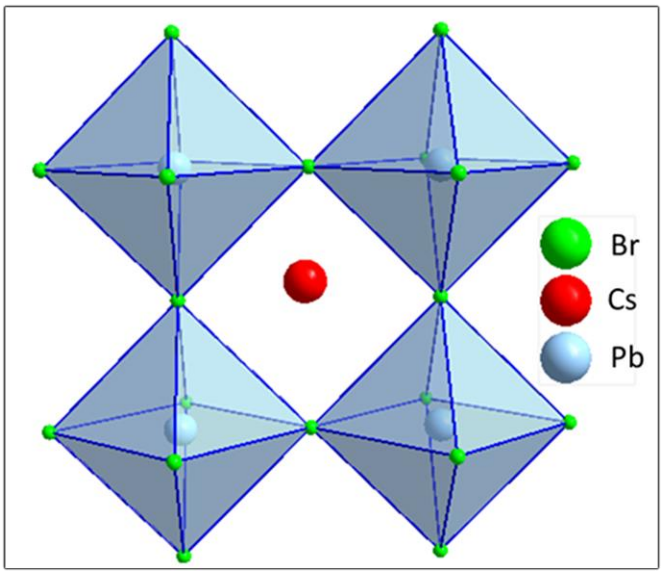

Scheme 1.1. Schematic of cubic structure of lead halide perovskite nanocrystals.

Halide perovskites can be broadly categorized according to their structural dimensionality (Scheme 1.2), which plays a decisive role in dictating their optical and electronic behavior. The conventional three-dimensional (3D) perovskites, with the general formula ABX_3, comprise corner-sharing $[BX_6]^{4-}$ octahedra arranged into an extended 3D network (Scheme 1.2). This structural connectivity facilitates efficient charge transport, resulting in high carrier mobilities, long diffusion lengths, and bandgap tunability through halide substitution.[41-43,47] However, these materials often exhibit limited stability under ambient conditions.[48] For example, reducing the dimensionality leads to the formation of two-dimensional (2D) or layered perovskites, typically represented by $(RNH_3)_2BX_4$, in which inorganic octahedral sheets are separated by bulky organic spacer cations (Scheme 1.2).[49-50] Such layered architectures show pronounced exciton confinement, improved environmental stability, and anisotropic charge-transport characteristics.[51-52] Interestingly, further lowering the dimensionality, material yields one-dimensional (1D) perovskites, composed of linear chains of corner- or edge-sharing $[BX_6]^{4-}$ octahedra (Scheme 1.2). These systems display strongly localized excitonic states and exhibit significant low-dimensional quantum confinement effects, often accompanied by

intense photoluminescence.[47] At the extreme end of the dimensional spectrum lie zero-dimensional (0D) perovskites, exemplified by materials with the formula A_4BX_6, where the $[BX_6]^{4-}$ octahedra are fully isolated and electronically decoupled from one another (Scheme 1.2). Zero-dimensional perovskites are particularly noteworthy for their intense green photoluminescence, attributed to highly localized excitons.[53-56] The origin of this green emission has been debated extensively.[53-59] Some studies argue that it arises intrinsically from the 0D perovskite lattice, while others suggest that trace $CsPbBr_3$ nanocrystal impurities or defect-assisted radiative recombination are responsible.[57] Regardless of the exact origin, the combination of high PLQY, sharp emission, and solution processability makes 0D perovskites attractive for LEDs, display technologies, and photonic applications. Careful synthetic control and surface passivation are essential to enhance emission efficiency and resolve the debate over intrinsic versus extrinsic emission.[56,59,60]

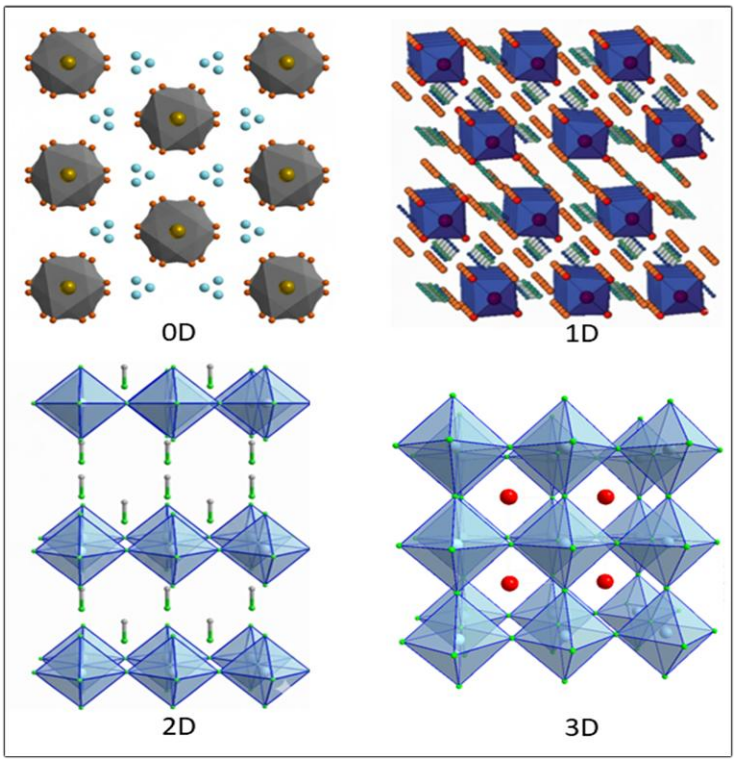

Scheme 1.2. Schematic of halide perovskite nanocrystals illustrating dimensional classification (0D, 1D, 2D, 3D).

Halide perovskites exhibit highly tunable photophysical properties, with bandgap modulation primarily governed by the halide composition in the ABX_3 framework. Substitution of Br^- with Cl^- in $CsPbBr_3$ typically induces a blue shift in the optical absorption and photoluminescence spectra, while partial or full replacement of Br^- with I^- results in a pronounced red shift.[61-62] This compositional flexibility enables continuous tuning of emission across the visible spectrum without significantly altering the underlying crystal structure.[61-62] In addition to bandgap tunability, halide perovskite nanocrystals possess several intrinsic photophysical advantages, including exceptionally high absorption coefficients, which allow efficient harvesting of incident photons over a broad spectral window.[33-35,37] Three-dimensional (3D) perovskites are characterized by long carrier diffusion lengths, promoting efficient charge transport and separation, a property that has contributed to their rapid adoption in optoelectronic devices such as solar cells and LEDs.[22-24,26,34,63] These materials also display rapid radiative recombination rates, contributing to their high photoluminescence quantum yields (PLQYs).[35-37] Importantly, halide perovskite nanocrystals typically contain shallow trap states rather than the deep defect levels commonly found in chalcogenide quantum dots (e.g., CdSe, CdTe).[61] The presence of shallow traps facilitates facile passivation and minimizes nonradiative recombination losses, thereby enabling superior luminescence efficiency and more favorable exciton dynamics.[61] Furthermore, size-dependent quantum confinement in perovskite nanocrystals and microstructures provides an additional mechanism for fine-tuning optical responses, enabling precise control of emission linewidth, energy, and carrier dynamics.[64]

1.2.1. Synthesis of Lead halides Perovskite Nanocrystal

Halide perovskite nanocrystals (PNCs) can be prepared through a variety of synthetic strategies that operate across both high-temperature and ambient-condition regimes. Among these, the

hot-injection approach is widely used, wherein a preformed Cs-oleate solution is swiftly introduced into a heated mixture containing lead halide and coordinating ligands, producing uniform and highly emissive nanocrystals.[9-10,34,61-62] In contrast, the ligand-assisted reprecipitation (LARP) technique enables nanocrystal formation at room temperature by driving rapid nucleation when precursor solutions in polar media are mixed with a nonpolar antisolvent.[65] Several alternative low-energy methods, such as ultrasonication, which relies on acoustic cavitation, and microwave irradiation, which provides fast volumetric heating, also facilitate PNC formation.[66] Additionally, mechanochemical (solid-state) synthesis offers a solvent-free route, while microfluidic flow synthesis ensures precise mixing and excellent reproducibility for scalable production.[66] In this work, we have primarily employed the hot-injection and LARP methods to prepare the desired perovskite nanocrystals.

1.3. Quantum Dots

Another class of semiconductor nanocrystals is quantum Dots. Quantum dots (QDs) have been a central topic of research for decades. Their discovery dates back to the early 1980s, when Louis E. Brus identified them in colloidal solutions and Alexei Ekimov reported similar size-dependent effects in glass matrices.[67-68] The term “quantum dot” was later introduced by Mark Reed to describe these nanoscale semiconductor materials.[69] Quantum dots are typically composed of metal chalcogenides (such as Zn, Cd, Hg, or Pb compounds) and generally fall within a size range of 2–10 nm. Semiconductors possess electrical conductivities intermediate between conductors and insulators, with band gaps typically between 0.5 and 3 eV and low intrinsic carrier concentrations in their bulk crystalline form. In contrast to their bulk counterparts, QDs exhibit striking size-dependent optical and electronic characteristics because of the quantum confinement of excitons generated upon thermal or photoexcitation.[70-71] Excitons (electron–hole) pairs play a crucial role in the photophysics of QDs. Their

characteristic separation distance, known as the exciton Bohr radius (aB), is given by Equation 1.1[72]

$$a_B = \frac{\varepsilon \hbar^2}{e^2}\left(\frac{1}{m_e^*} + \frac{1}{m_h^*}\right) \quad (1.1)$$

where ε is the dielectric constant, ħ is the reduced Planck constant, e is the electron charge, and m_e^* and m_h^* are the effective masses of the electron and hole, respectively. When a nanoparticle's size approaches or falls below the exciton Bohr radius, exciton motion becomes spatially restricted, leading to quantum confinement.[73-75] This phenomenon results in discrete, quantized energy levels. As the particle size decreases, the energy spacing increases and the band gap widens (Scheme 1.3), in contrast to bulk semiconductors where the valence and conduction bands are continuous.[76]

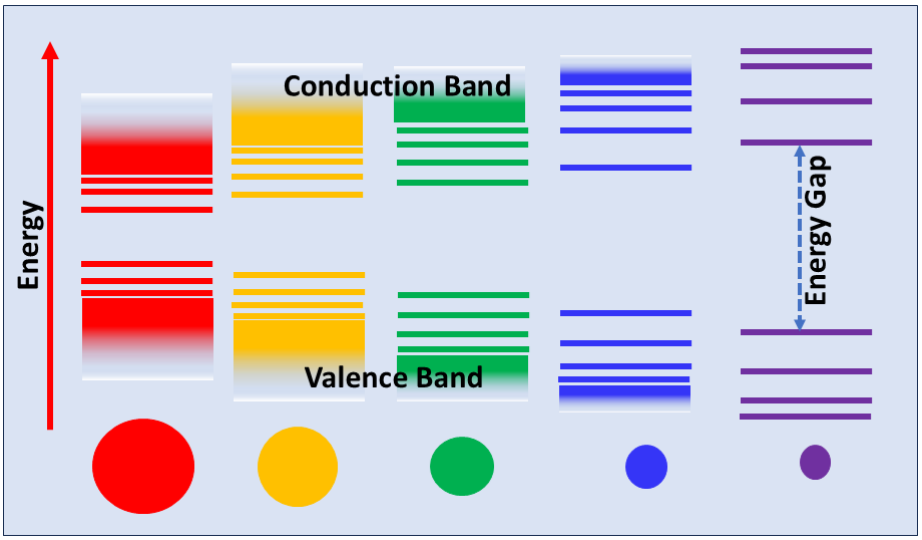

Scheme 1.3. Schematic illustration depicting how particle size influences energy levels and bandgap in semiconductor materials.

Because of their discretized energy levels, QDs resemble individual atoms or small molecules, although they also retain features typical of extended semiconductor materials. They are often regarded as intermediates between molecular species and bulk crystals (Scheme 1.4).[70] Unlike

bulk semiconductors, which have a fixed band gap (E_{bulk}), QDs exhibit a tunable band gap (E_{QD}) dependent on particle size. Their optical behavior, broad absorption spectra with high extinction coefficients and bright fluorescence, arises from their dense electronic states and efficient radiative recombination processes.[70,77]

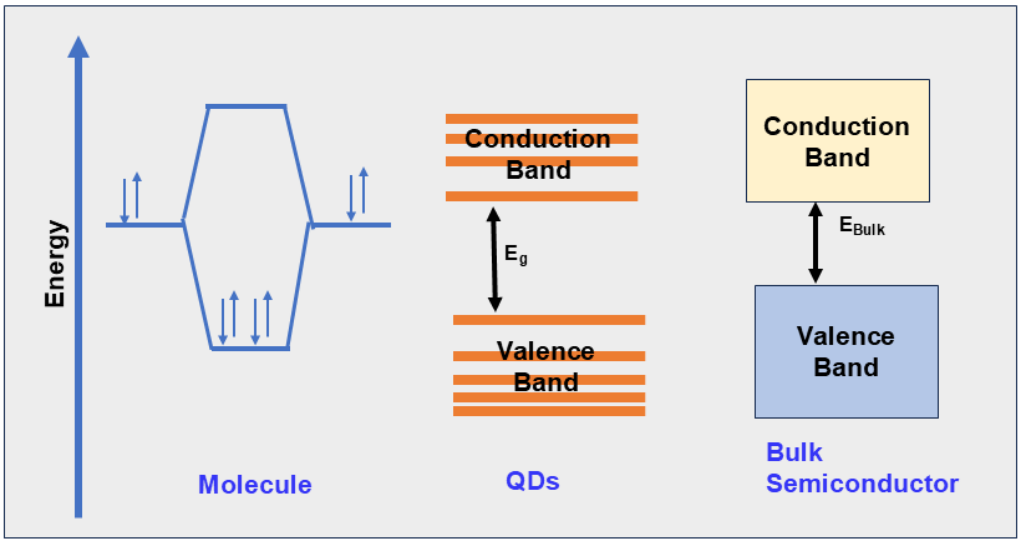

Scheme 1.4. Schematic showing the differences in electronic energy levels between a molecule, quantum dot, and bulk semiconductor; E_{QD} and E_{bulk} correspond to the quantum dot and bulk band gaps.

The size-dependent shift in band gap energy relative to bulk semiconductors can be described by Equation 1.2[71,78]

$$E_{QD} = E_{Bulk} + \frac{\hbar^2\pi^2}{2m_e^* R^2} + \frac{\hbar^2\pi^2}{2m_h^* R^2} - \frac{1.786e^2}{\varepsilon R} - 0.248E_{Ry}^* \qquad (1.2)$$

where R is the QD radius, the second and third terms correspond to electron and hole confinement energies, the fourth term represents the Coulomb attraction between the electron and hole, and E_{Ry}^* is the exciton Rydberg energy. Although often negligible, this last term becomes significant in semiconductors with low dielectric constants.[79]

Quantum dots are generally composed of cations from groups IIIA, IVA, and IIB combined with anions from groups VA and VIA.[80-81] Their elemental composition contributes to exceptional resistance to photodegradation.[82] Compared with conventional organic fluorophores, QDs offer numerous advantages, including high surface-to-volume ratios, broad absorption profiles, narrow and size-tunable emission bands, and outstanding photostability, making them highly attractive for a range of optical and optoelectronic applications.[83-84] The optical properties of QDs are strongly influenced by surface states and lattice defects, which can create localized energy levels, called trap states, within the bandgap.[61] To further elucidate the origin and impact of these defect states, a schematic representation of the electronic structure and trap-state formation in semiconductor nanocrystals is shown in Figure 1.5. In conventional chalcogenide quantum dots, such as CdSe and CdTe, the valence band is primarily derived from bonding states of chalcogenide orbitals, while the conduction band originates from antibonding metal orbitals.[61] Structural imperfections, including dangling bonds, vacancies, and undercoordinated surface atoms, introduce localized energy levels within the bandgap. These defect states can be broadly classified into shallow surface traps, located near the band edges, and deep trap states positioned energetically far from both the conduction and valence bands. Deep traps act as efficient nonradiative recombination centers, significantly reducing photoluminescence quantum yield and carrier mobility.

In contrast, lead halide perovskite nanocrystals exhibit a fundamentally different electronic structure, wherein the valence band maximum possesses antibonding character arising from the interaction between Pb 6s and halide p orbitals, while the conduction band is dominated by Pb 6p orbitals.[61] As a result, most intrinsic defects, such as halide vacancies, tend to introduce shallow states close to the band edges rather than deep mid-gap levels. This unique defect-tolerant electronic structure minimizes trap-assisted nonradiative recombination and enables high photoluminescence efficiency.[61] Such distinctions in trap-state distribution

between chalcogenide quantum dots and perovskite nanocrystals play a crucial role in governing their exciton dynamics and interfacial charge-transfer behavior, which are central to the investigations presented in this thesis. Thus, while QDs are structurally stable but defect-sensitive, PNCs are highly emissive yet prone to environmental degradation.[61] To minimize trap-assisted nonradiative losses, core–shell QDs have been developed, where a narrow-bandgap core is coated by a wider-bandgap shell (e.g., CdTe@ZnS, PbSe@ZnS).[70,85] The shell effectively passivates surface defects, confines carriers, and protects the core from photooxidation, leading to improved PL intensity and long-term stability.[85]

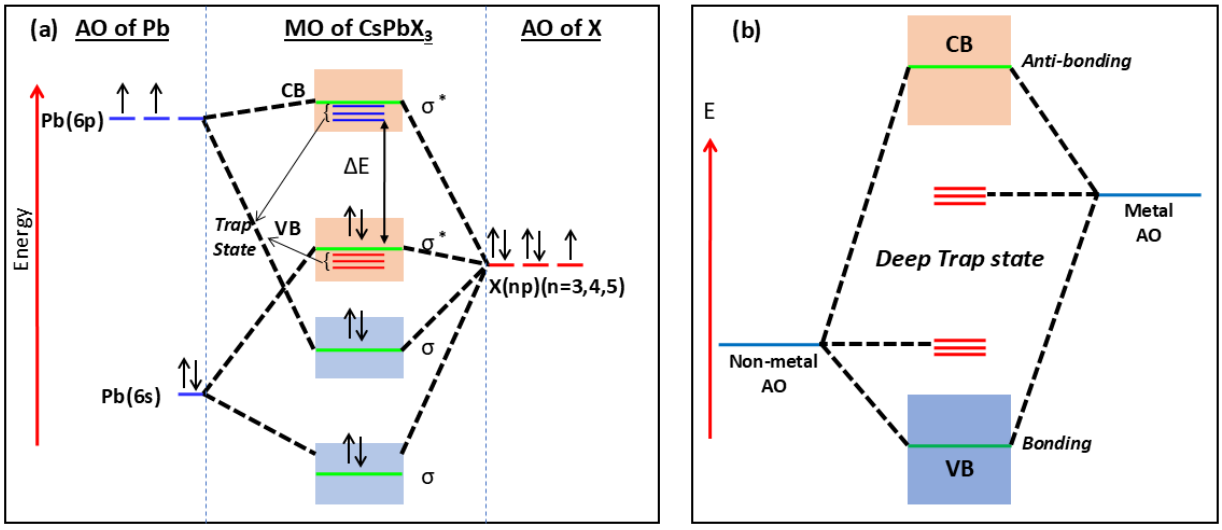

Scheme 1.5. Schematic illustration of the electronic structure and trap-state formation in (a) perovskite nanocrystals and comparison with (b) conventional semiconductor systems.

Among the core-shell QDs, CdTe@ZnS QDs represent a well-studied Type I heterostructure, where both electrons and holes are confined within the CdTe core while the ZnS shell serves as a high-bandgap barrier.[86-87] This design leads to high PL quantum yield, enhanced photostability, and reduced environmental sensitivity. Importantly, due to the strong lattice mismatch between CdTe (a = 6.48 Å) and ZnS (a = 5.41 Å), careful control of shell thickness is crucial to minimize interfacial strain and preserve emission efficiency.[87]

CdTe@ZnS QDs are widely utilized in biolabeling, sensors, and light-harvesting devices, demonstrating the power of surface engineering in tailoring optical response and chemical stability.

Quantum dots (QDs) are widely used in various technologies owing to their distinctive photophysical properties, such as strong absorption, size-tunable emission, long exciton lifetimes, and high photostability.[74-80] These features enable applications in QLEDs, photocatalysis, solar cells, bioimaging, biosensing, and energy-transfer processes.[13,15] Moreover, their ability to generate multiple excitons from a single photon, along with low fabrication costs, positions QDs as promising candidates for next-generation photovoltaic devices.[13,15,25-26]

1.3.1. Synthesis of Quantum Dots

Quantum dots are usually prepared using two main strategies: top-down and bottom-up approaches.

- **Top-Down Approach:** In this method, bulk semiconductor materials are reduced to the nanoscale using physical or lithographic techniques. Common examples include milling, grinding, electron-beam lithography, ion or laser-beam lithography, and wet chemical etching, all of which break down larger structures into nanocrystalline QDs.[14]
- **Bottom-Up Approach:** This route builds nanomaterials from molecular precursors through various wet-chemical or gas-phase processes. Wet-chemical methods include microemulsion, hot-solution decomposition, sol–gel, electrochemical, hydrothermal, ultrasonic, and microwave-assisted synthesis, where particles grow from atoms or molecules to nanoscale dimensions.[14]

1.4. Challenges and Opportunities

Although halide perovskite nanocrystals (PNCs) and chalcogenide quantum dots (QDs) exhibit excellent size-dependent optical properties and strong excitonic behavior, both systems possess intrinsic limitations that restrict their standalone performance.[88-89] Furthermore, PNCs, despite their high photoluminescence quantum yield (PLQY), defect-tolerant electronic structure, and tunable bandgap, remain highly unstable under ambient conditions. They undergo halide loss, surface reconstruction, moisture-induced degradation, and ion migration, all of which reduce PL intensity and long-term usability.[88] QDs, in contrast, offer high structural robustness and chemical durability, owing to their covalent lattice, but suffer from deep trap states, complex surface chemistry, and nonradiative recombination pathways, which diminish exciton mobility and charge-transfer efficiency.[89] Furthermore, both PNCs and QDs face surface-induced recombination, inefficient exciton transport, and interfacial energy losses, limiting their performance in optoelectronic or photonic applications.

Despite these challenges, both nanomaterials present significant opportunities. In the case of PNCs, they allow rapid exciton formation, shallow trap states, and straightforward bandgap tuning, making them ideal candidates for light-emitting devices by improving their stability. Moreover, QDs provide broad spectral tunability, aqueous compatibility, and suitability for donor–acceptor assemblies, enabling advanced photonic and energy-transfer studies. These inherent advantages have motivated us to use the functional molecular additives and interfacial modifiers that can stabilize the nanocrystals, passivate surface traps, and modulate exciton dynamics.

1.5. Interfacial Modulation

While both halide perovskite nanocrystals (PNCs) and chalcogenide QDs have exhibited size-tunable optical properties, exciton dynamics, and surface-sensitive photophysics, their full potential in optoelectronic and energy applications has been realized only when interfacial interactions have been carefully engineered.[22-30] Integration with ionic liquids (ILs) or organic molecular assemblies enables nano-hybrid architectures that combine the high luminescence and defect-tolerance of PNCs with the stability and surface tunability of QDs.[22-26] In these hybrid systems, ILs serve as surface passivators, charge-transfer mediators, and interfacial stabilizers, while organic J-aggregates or π-conjugated molecules facilitate strong excitonic coupling and directional energy transfer.[27-30] Such synergistic combinations provide a versatile platform to study and control photoinduced charge and energy transfer, bridging the intrinsic photophysics of nanocrystals with the functional capabilities of soft-matter components. This sets the stage for the detailed exploration of IL- and organic-assisted exciton modulation in semiconducting nano-hybrids, as discussed below.

1.5.1. Ionic Liquids

Ionic liquids (ILs) are salts composed entirely of ions that remain liquid below 100 °C. Their negligible vapor pressure, high ionic conductivity, tunable viscosity, and wide electrochemical window make them attractive not only as unconventional solvents but also as functional surface modifiers in nanomaterial research.[22-26] Owing to their structural tunability, the physicochemical properties of ILs can be precisely adjusted by selecting appropriate cation–anion combinations, enabling tailored interactions with semiconductor surfaces and allowing modulation of charge transport, exciton recombination, and interfacial energetics.

ILs can be broadly categorized into monocationic ionic liquids (MILs) and dicationic ionic liquids (DILs). MILs consist of a single cation–anion pair, where the cation may be

imidazolium, pyridinium, ammonium, or phosphonium, and the anion can be chosen to tune polarity, hydrophobicity, and coordinating ability. Imidazolium-based MILs have been employed for PNC and QD surface passivation due to their capacity for π–π, cation–π, and hydrogen-bonding interactions, whereas pyridinium-based ILs offer enhanced chemical stability and can function as mild electron acceptors, subtly influencing charge-transfer behavior.[24,90-91] In contrast, DILs contain two cationic centers connected by a flexible or rigid spacer, allowing multisite coordination to nanocrystal surfaces. This "di"cationic architecture is expected to help in stronger interfacial binding, more effective suppression of trap states, and improved thermal and structural stability, which together help to reduce ion migration and exciton quenching in both PNCs and QDs.[92-94] A distinct subclass of ILs, known as surface-active ionic liquids (SAILs), incorporates long alkyl chains that impart amphiphilic character. These systems can self-assemble into micelles, bilayers, or ordered ion layers at nanocrystal interfaces, thereby enabling colloidal stabilization, surface passivation, and controlled exciton interactions.[95]

At the semiconductor–IL interface, IL ions can interact strongly with surface sites and defects. Cations typically bind to electron-rich regions, such as halide vacancies on PNCs or chalcogen vacancies on QDs, while anions can stabilize undercoordinated cationic centers, such as Pb-adatom. This dual-passivation mechanism is expected to reduce trap-state density, suppress nonradiative recombination pathways, and improve both photoluminescence and charge-transport properties. In PNCs, ILs are also expected to inhibit halide migration and moisture-induced degradation, resulting in improved environmental stability. Moreover, ILs may provide templates for nanocrystal growth in a particular direction to form different shapes and sizes of nanocrystals. It is also expected that in CdTe@ZnS QDs, ILs can help mitigate deep trap states, thereby facilitating more efficient photoinduced charge separation and electron-transfer processes.

1.5.2. Organic Aggregates

Organic nano- and microparticles, commonly termed organic aggregates, have emerged as a growing class of functional materials with distinctive and attractive optical properties. Compared with the long-established research on metal and semiconductor nanoparticles, studies on organic aggregates are relatively new, yet they have revealed rich and unconventional photophysical behavior.[27-30] These systems often display optical and electronic responses that differ markedly from those of their individual molecular constituents or their corresponding bulk phases.[27-30] The design and exploration of fluorescent organic nano/microparticles have attracted considerable attention, as the vast chemical versatility of organic molecules and the adaptability of synthetic routes provide exceptional opportunities for tailoring their structures and properties.[27-30] Organic nanoparticles typically occupy a size regime spanning from the nanometer to the micrometer range, often exceeding the dimensions characteristic of many inorganic nanomaterials.[27-30] In these systems, the constituent molecules organize into aggregates through a combination of weak, noncovalent interactions, including van der Waals forces, hydrogen bonding, π–π stacking, electrostatic effects, and charge-transfer interactions.[96] The nature of these interactions is fundamentally different from those dictating the formation of inorganic nanoparticles, providing unique opportunities to tune the architecture and properties of the aggregates by controlling the underlying molecular self-assembly processes.

Organic aggregates are commonly classified as H-aggregates and J-aggregates, and their optical behavior is well explained by Kasha's molecular exciton model.[97-98] As depicted in Scheme 1.6, coupling between the transition dipole moments of closely packed dye molecules splits the excited state into two levels. In J-aggregates, where molecules align in a head-to-tail fashion, the lower-energy transition becomes optically allowed. Conversely, in H-

aggregates, the dipoles align in a parallel configuration, making the higher-energy transition allowed.[97-98] As a result, J-aggregates typically display bathochromic (red) shifts, while H-aggregates exhibit hypsochromic (blue) shifts in their absorption and emission spectra. Many cyanine dyes are known to favor J-aggregation upon self-assembly.[99-101] J-aggregates are especially attractive for optoelectronic applications due to their strong absorption and emission, narrow spectral features, very small Stokes shifts (often ~200 cm^{-1} or less), and high fluorescence quantum yields.[99-101]

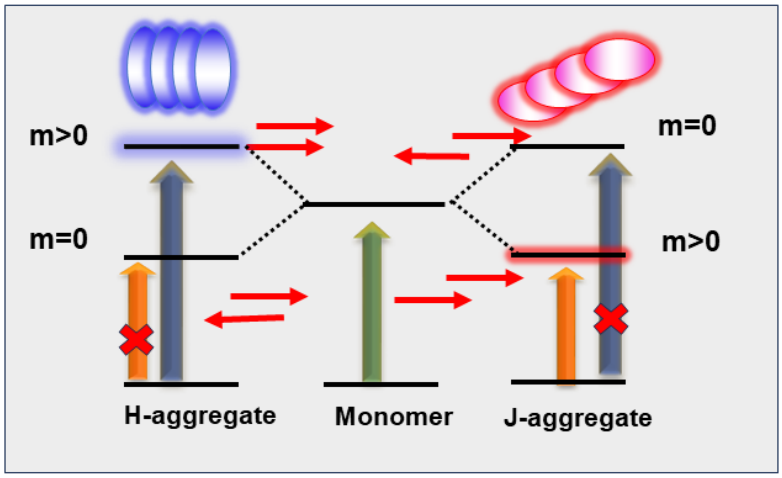

Scheme 1.6. Schematic illustration of the permitted electronic transitions in J- and H-aggregates, where 'm' denotes the transition dipole moment integral (with allowed transitions corresponding to $m > 0$).

Unlike semiconductor quantum dots, these size-dependent behaviors have not arisen from conventional quantum confinement. Such effects were first reported by Nakanishi and co-workers in perylene nanocrystalsr[102-103] and have been explored extensively for pyrazoline derivatives by Yao and coworkers.[104] Organic microcrystals have also demonstrated notable nonlinear optical (NLO) responses, making them attractive for advanced photonic applications.[105-106] Moreover, J-aggregates have emerged as particularly significant. These self-assembled π-conjugated dye systems, typically cyanine, squaraine, or perylene derivatives

have adopted a head-to-tail packing arrangement that has produced a sharp delocalized exciton band with red-shifte.[27-30,99] This supramolecular organization has enabled coherent exciton delocalization and efficient energy transfer across nanoscale distances, features highly beneficial for hybrid optoelectronic applications.

Because of their unique optical properties, organic aggregates have found utility in a broad range of technologies. Initially, they were used as photographic sensitizers[107] and in fluorescent fibers,[108] but they have since become important in modern optoelectronic devices such as organic light-emitting diodes (OLEDs), organic photovoltaic devices (OPVs), and organic field-effect transistors (OFETs).[109-114] Organic nanoparticles have also shown potential in affordable light-harvesting materials for organic solar cells.[111,113]

1.5.2.1. Fabrication Methods

The synthesis of organic nano- and microparticles has differed markedly from the conventional methods used for inorganic or semiconductor nanomaterials. A variety of approaches has been developed to produce organic aggregates of different sizes and morphologies. Common techniques have included reprecipitation,[115] chemical reaction-based methods, thermal evaporation, microemulsion protocols,[116] and laser ablation.[117] Moreover, numerous one-dimensional (1D) organic structures—such as nanorods, nanotubes, and nanowires—have been obtained through physical vapor deposition (PVD), templated routes, and self-assembly-driven strategies.[118-120]

1.6. Inorganic-Organic Nanohybrid Assemblies

In the earlier sections of this chapter, the important features of semiconductor nanomaterials, particularly halide perovskite nanocrystals (PNCs) and chalcogenide quantum dots (QDs), and organic nano/microparticles have been described independently. Although these inorganic and organic materials have been utilized in a variety of optoelectronic, sensing, and light-harvesting applications, each class has exhibited intrinsic limitations.[61] Organic assemblies have offered

excellent structural tunability through synthetic modification, yet their high exciton binding energies and tendency toward photobleaching have reduced their operational stability.[99-101,107,110] In contrast, inorganic nanocrystals have provided strong photochemical stability and well-defined electronic structures, but their surface functionalization has often remained challenging. These contrasting features have raised an important question: what type of material system has been capable of combining facile functionalization, broad absorption, tunable bandgap, long exciton diffusion lengths, and high stability, properties essential for efficient optoelectronic operation?

Hybrid nanoscale systems composed of inorganic nanocrystals and organic aggregates have emerged as a promising solution. By bringing together the robustness of the inorganic component with the structural flexibility of the organic counterpart, such hybrids have been expected to exhibit enhanced optical and electronic behavior. When strong coupling between Wannier–Mott excitons in PNCs or QDs and Frenkel excitons in organic aggregates has occurred, these assemblies have displayed photophysical responses distinct from either constituent alone.[22-26,27-30] As a result, inorganic–organic nanohybrids have shown potential in applications such as photodetectors, LEDs, display technologies, photocatalysis, quantum information systems, and biosensing.[24-26,28-30]

Despite this promise, relatively few studies have focused on understanding how the inorganic and organic excitonic components interact within a single hybrid structure. These limitations have motivated efforts to design hybrids involving less toxic and more environmentally friendly semiconductor nanomaterials, enabling the study of exciton interactions while minimizing ecological impact. Such systems have provided valuable platforms for probing the interplay between Wannier–Mott and Frenkel excitons and have contributed to progress in fields ranging from photovoltaics and optoelectronics to sensing, catalysis, nanomedicine, and molecular electronics.

1.7. Photophysical Processes in Molecules/Materials

Light–matter interactions, in particular, semiconductor materials, have long intrigued spectroscopists, because photoexcitation has promoted electrons from the valence band to the conduction band, creating electron–hole pairs that have undergone diverse radiative and non-radiative recombination pathways. In general, after excitation, fluorophores have experienced competing processes such as energy transfer, electron or hole transfer, proton transfer, conformational rearrangements, and solvent relaxation, which have modulated intrinsic deactivation and have led to fluorescence quenching or enhancement.[121] These behaviors have been probed using both steady-state and time-resolved fluorescence methods, including steady-state emission spectroscopy, time-correlated single-photon counting (TCSPC), fluorescence correlation spectroscopy (FCS), fluorescence lifetime imaging microscopy (FLIM), and transient absorption (TA)spectroscopy (detail provided in Chapter 2). Within this thesis, particular attention has been devoted to energy-transfer processes, electron-transfer pathways.

1.7.1. Photoinduced Energy and Charge Transfer

Photoinduced charge and energy transfer processes are crucial to the function of semiconducting nanocrystals, ionic liquid interfaces, and organic excitonic assemblies. Upon light absorption, nanocrystals generate Wannier–Mott excitons (electron–hole pairs) that can either recombine radiatively or participate in charge/energy transfer to nearby acceptors. Efficient control of these processes is essential for maximizing photoluminescence, photocurrent generation, and photocatalytic efficiency.[121]

1.7.1.1. Energy Transfer

Electronic energy transfer (EET) describes the movement of electronic excitation from a donor to an acceptor. Based on the distance between the interacting species and the nature of their coupling, EET has been understood to occur primarily through two pathways: the short-range

Dexter exchange mechanism and the long-range Förster resonance energy transfer (FRET) mechanism (Scheme 1.7).[121] In both mechanisms, the donor loses its excitation nonradiatively while the acceptor becomes electronically excited. The Dexter pathway is effective only when the donor and acceptor are in very close proximity (on the order of 1–10 Å), since it relies on a direct electron exchange between the two species. Whereas FRET operates over much larger separations (typically 10–100 Å) and proceeds through long-range dipole–dipole coupling between the transition dipoles of the donor and acceptor.[121] The overall efficiency of FRET is dictated by several parameters, including the spectral overlap between the donor emission and acceptor absorption profiles, the donor–acceptor distance, the orientation factor describing the relative alignment of the transition dipoles, the refractive index of the surrounding medium, and the intrinsic quantum yield of the donor.[121]

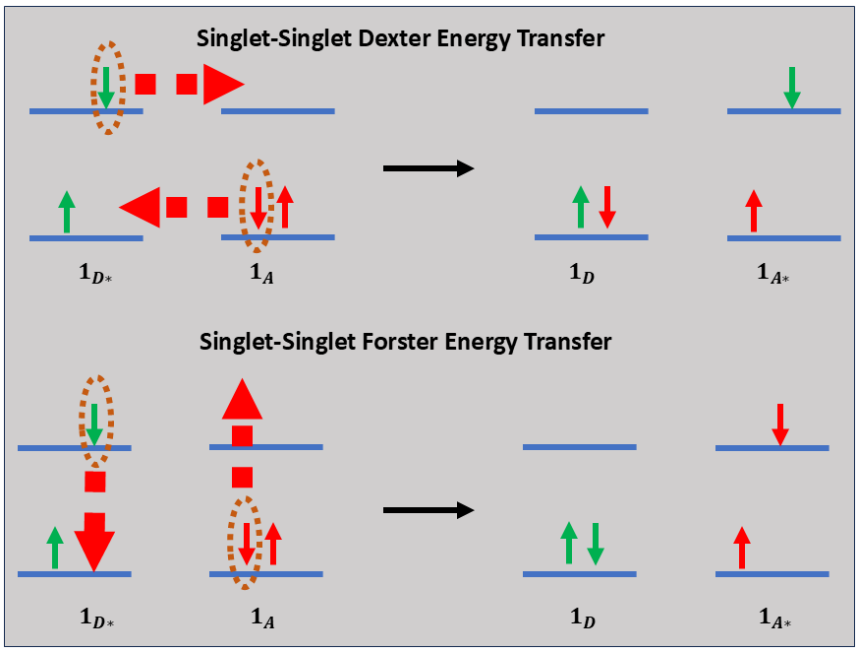

Scheme 1.7. Schematic of singlet-singlet Dexter and Forster energy transfer.

a) Spectral Overlap Integral, J(λ)

The spectral overlap integral quantitatively describes the extent to which the donor's emission spectrum coincides with the acceptor's absorption spectrum. A greater overlap enhances the probability of resonance energy transfer.[121]

$$J(\lambda) = \frac{\int_0^\infty F_D(\lambda)\,\varepsilon_A(\lambda)\,\lambda^4\,d\lambda}{\int_0^\infty F_D(\lambda)\,d\lambda} \quad (1.3)$$

where $F_D(\lambda)$ is the normalized donor emission spectrum and $\varepsilon_A(\lambda)$ is the molar extinction coefficient of the acceptor.

b) Förster Distance, R_0

The Förster distance (R_0) is defined as the donor–acceptor separation at which the efficiency of energy transfer is 50%. It is given by[121]:

$$R_0 = 0.211\,[\kappa^2\,\eta^{-4}\,\phi_D\,J(\lambda)]^{\frac{1}{6}} \quad (1.4)$$

Where κ^2 = orientation factor (commonly assumed to be 2/3 under dynamic averaging), η= refractive index of the medium, ϕ_D = photoluminescence quantum yield of the donor.

c) Quantum Yield of the Donor, ϕ_D

The quantum yield of a fluorophore is generally determined relative to a reference standard using[121]:

$$\phi_s = \frac{A_s}{A_r}\left(\frac{\eta_s}{\eta_r}\right)^2\left(\frac{OD_r}{OD_s}\right)\phi_r \quad (1.5)$$

where A_s and A_r represent the integrated emission areas, η_s and η_r correspond to refractive indices, OD_s and OD_r denote the optical densities of the sample and reference, respectively. And ϕ_r is the quantum yield of the reference fluorophore.

d) FRET Efficiency

Using the parameters above, the efficiency of Förster energy transfer is expressed as:

$$E = \frac{R_0^6}{R_0^6 + R_{DA}^6} \quad (1.6)$$

where R_{DA} is the donor–acceptor separation. Owing to its strong distance dependence, FRET is frequently employed as a spectroscopic ruler, especially in biological and nanoscale systems where precise distance measurements are required.[121]

1.7.1.2. Electron and Hole Transfer

The classical description of charge transfer was established by Marcus, who formulated a theoretical framework in which the reactant and product states are represented by parabolic free-energy surfaces (FESs) along a generalized reaction coordinate.[121] This coordinate encompasses both intramolecular motions and solvent reorganization processes (Figure 1.6). Within this model, the activation energy barrier for ET is given by:

$$\Delta G^* = \frac{(\Delta G^0+\lambda)^2}{4\lambda} \quad (1.7)$$

Where ΔG^0 = standard Gibbs free energy change of the reaction, λ = total reorganization energy.

a) Electron-Transfer (ET) Rate Constant

According to Marcus theory,[121] the ET rate constant is expressed as:

$$k_{ET} = | V_{DA} |^2 \frac{1}{\sqrt{4\pi\lambda k_B T}} \exp\left[-\frac{(\Delta G^0+\lambda)^2}{4\lambda k_B T}\right] \quad (1.8)$$

where V_{DA} denotes the electronic coupling matrix element. Weak coupling results in non-adiabatic ET, whereas strong coupling yields an adiabatic process characterized by a single, smoothly connected FES. The dependence of k_{ET} on ΔG^0 gives rise to the well-known normal and inverted regimes.

b) Photoinduced Electron Transfer (PET)

Photoinduced electron transfer (PET) is a fundamental process in numerous chemical, biological, and optoelectronic systems.[122] Upon absorption of a photon, either the donor or the acceptor may reach an excited state from which electron transfer occurs:

$$D + A + h\nu \rightarrow D^* + A \rightarrow D^+ + A^- \quad (1.9)$$

$$D + A + h\nu \rightarrow D + A^* \rightarrow D^+ + A^- \quad (1.10)$$

Two principal pathways are involved:

- **Oxidative PET**, in which an electron is transferred from the LUMO of the excited donor to the LUMO of an electron-deficient acceptor[121] (Shown in Scheme 1.8).

- **Reductive PET**, in which an electron is transferred from the HOMO of an electron-rich donor to the HOMO of the excited fluorophore[121] (Shown in Scheme 1.8).

The thermodynamic feasibility of PET is governed by the redox potentials of the donor–acceptor pair.

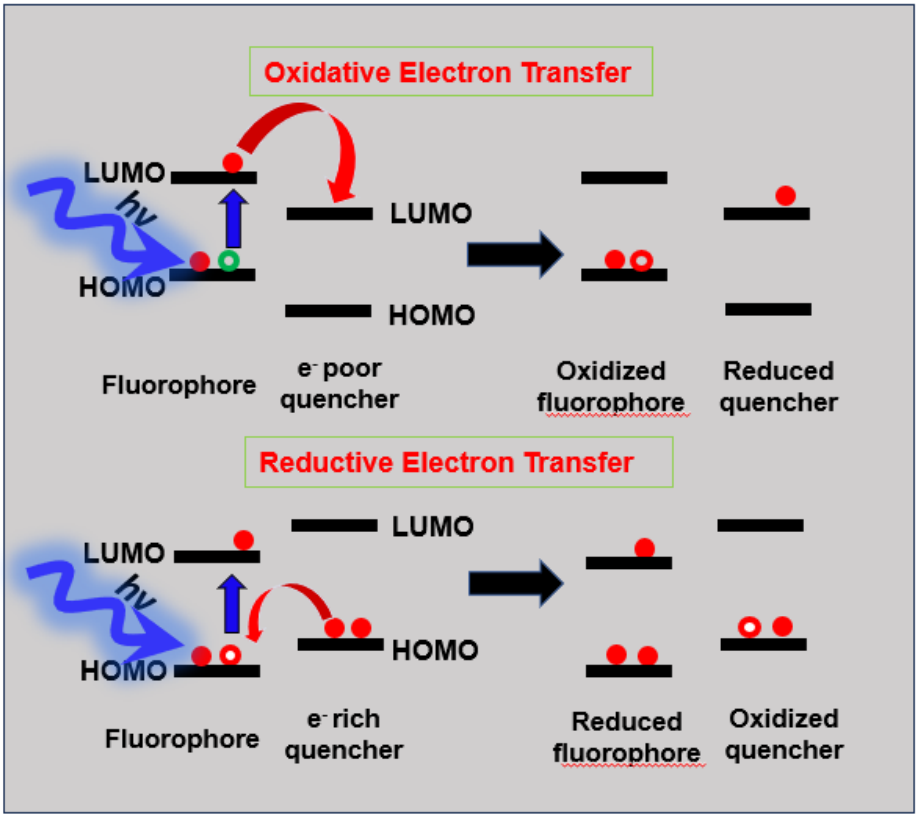

Scheme 1.8. Schematic of oxidative and reductive pathways involved in a photoinduced electron-transfer (PET) process.

c) Rehm–Weller Equation

The driving force for PET is estimated using the Rehm–Weller relationship:[121]

$$\Delta G_{ET} = E(D^+/D) - E(A/A^-) - \Delta E_{00} - \frac{e^2}{\varepsilon d} \qquad (1.11)$$

Where $E(D^+/D)$ is the oxidation potential of the donor, $E(A/A^-)$ is the reduction potential of the acceptor, ΔE_{00} = energy corresponding to the 0-0 transition of the fluorophore, ε = dielectric constant of the solvent, d is the donor-acceptor separation. A negative ΔG_{ET} indicates a thermodynamically favorable PET process.

1.8. Scope and Objectives of the Thesis

Semiconductor nanomaterials, especially halide perovskite nanocrystals (PNCs) and chalcogenide quantum dots (QDs), have shown tremendous potential for next-generation optoelectronic and energy-related technologies. However, their intrinsic limitations have highlighted the need for advanced interfacial engineering. The motivation of this thesis arises from the following considerations:

1.8.1. Limitations of Current Nanomaterials

- PNCs, although highly emissive and defect-tolerant, have suffered from poor environmental stability, rapid halide loss, and strong sensitivity to moisture, oxygen, and heat.
- Also, PNCs have contained surface defects, such as halide vacancies and undercoordinated metal centers, which promote nonradiative recombination.
- Moreover, obtaining phase-pure zero-dimensional perovskites remains challenging, and the fundamental origin of their fluorescence is still a subject of debate.
- QDs have exhibited excellent structural stability but have required precise surface modification to reduce deep trap states and enable efficient exciton and charge transport.
- Both materials have lacked reliable interfacial control, limiting their performance in long-term optoelectronic applications.

1.8.2. Rationale for Using Ionic Liquids (ILs)

- ILs have offered tunable cation–anion structures, allowing selective surface passivation and defect suppression in PNCs and QDs.
- They have improved stability against moisture, oxygen, and light exposure.
- Depending on their electronic structure, ILs have facilitated exciton stabilization or photoinduced electron transfer, enabling controlled charge-transfer pathways.

1.8.3. Rationale for Using Organic J-Aggregates

- Organic J-aggregates have exhibited strong exciton delocalization, sharp and intense spectral bands, and well-defined Frenkel excitons.
- When combined with QDs, they have enabled efficient Förster resonance energy transfer (FRET) and unique modulation of QD emission, including valley splitting.
- These interactions have opened opportunities for designing hybrid excitonic architectures with enhanced light-harvesting efficiency.

1.8.4. Overall Motivation

- There is a strong need to understand and engineer how ILs and organic aggregates interact with semiconductor nanomaterials to tune exciton dynamics, improve stability, and control energy/charge transfer.
- This thesis aims to provide fundamental insights into:
  - IL-assisted stabilization and passivation of PNCs,
  - IL-directed synthesis and defect control in 0D perovskites,
  - Excitonic coupling and FRET in QD–J-aggregate hybrids, and
  - Photoinduced electron transfer (PET) in QD–IL systems.
- Such understanding will support the development of stable, efficient, and environmentally friendly hybrid nanomaterials for applications in LEDs, photodetectors, solar cells, sensing, bioimaging, and emerging excitonic technologies.

1.9 Chapter-wise Organization of the Thesis

The thesis has been structured into six chapters, each addressing a specific scientific component of exciton dynamics and interfacial engineering in semiconducting nanomaterials. A brief overview of the chapters is provided below, following the outline presented in the synopsis.

CHAPTER 1

*Chapter 1*establishes the conceptual foundation of the thesis. It introduces semiconducting nanomaterials, focusing on halide perovskite nanocrystals (PNCs) and chalcogenide quantum dots (QDs), and summarizes their excitonic properties, optoelectronic relevance, and associated challenges such as instability, surface defects, and inefficient exciton/charge transport. The role of ionic liquids (ILs) and organic assemblies as interfacial modifiers is highlighted, and general synthetic concepts relevant to nanocrystal and aggregate preparation are discussed. The chapter concludes with the motivation, scope, and objectives of the work.

Chapter 2 describes the instrumentation, characterization techniques, and synthetic methods used throughout the thesis. It includes preparation of PNCs and CdTe@ZnS QDs, post-synthetic IL treatments, formation of hybrid nanostructures, and procedures for optical and structural characterization. Special emphasis is placed on transient absorption spectroscopy, fluorescence lifetime imaging microscopy (FLIM), and fluorescence correlation spectroscopy (FCS), which are essential for probing exciton dynamics at ensemble and single-particle levels.

Chapter 3 demonstrates how imidazolium-based ILs significantly improve the photophysical properties and stability of $CsPbX_3$ (X = Cl, Br) PNCs. IL treatment effectively removes excess surface Pb-adatoms, suppresses trap-assisted recombination, and enhances photoluminescence quantum yield (PLQY). Structural analyses confirm the preservation of crystallinity, while steady-state and time-resolved PL data reveal prolonged exciton lifetimes and improved emission stability, validated even at the single-particle level.

Chapter 4 explores an IL-mediated antisolvent precipitation route to synthesize phase-pure, highly crystalline Cs_4PbBr_6 microdisks (MDs) at room temperature. By tuning IL structure and concentration, the morphology, crystallinity, and optical response of the MDs are precisely controlled. Photophysical investigations, including temperature-dependent PL and FLIM, show strong intrinsic green emission arising from defect-mediated recombination, supported by large exciton-binding energy and pronounced exciton–phonon coupling. Spatial variations

in emission are correlated with heterogeneous trap-state distribution across individual microdisks.

Chapter 5 investigates exciton–exciton coupling in hybrid assemblies composed of CdTe@ZnS QDs and organic J-aggregates. Highly efficient FRET from QDs to J-aggregates induces a clear and tunable valley splitting in the QD emission, achieved in the absence of external magnetic or electric fields. The magnitude of splitting scales linearly with FRET efficiency, establishing a direct linkage between exciton transfer and valley-selective emission. The findings have established a new platform for tailoring excitonic processes through nanoscale hybridization, with strong implications for the development of valleytronic and optoelectronic devices.

Chapter 6 examines photoinduced electron-transfer processes in QD–IL hybrid systems using pyridinium-based monocationic and dicationic ILs. Fluorescence quenching studies, combined with time-resolved PL and transient absorption spectroscopy, reveal strong dependence of electron-transfer efficiency on IL structure, viscosity, and interfacial microenvironment. Ultrafast measurements capture charge separation events on femtosecond–nanosecond timescales, providing mechanistic insight into how ILs regulate exciton dissociation and charge transport in QD-based assemblies.

At the end of this chapter, the overall conclusion and future perspective of the thesis are also provided.

1.10 References

1. Statistical Review of World Energy, *Energy Institute,* **2025.**
2. Semiconductor Market report, *Market.us,* Report ID: 105940, September **2025**.
3. Sze, S. M.; Ng, K. K. Physics of Semiconductor Devices, 3rd ed.; *Wiley-Interscience: Hoboken*, NJ, **2007**.

4. Pimputkar, S.; Speck, J. S.; DenBaars, S. P.; Nakamura, S. Prospects for LED Lighting. *Nat. Photonics* **2009**, *3*, 4, 180–182.
5. O'Regan, B.; Grätzel, M. A Low Cost, High Efficiency Solar Cell Based on Dye Sensitized Colloidal TiO_2 Films. *Nature* **1991**, *353*, 6346, 737–740.
6. Saga, T. Advances in Crystalline Silicon Solar Cell Technology for Industrial Mass Production. *NPG Asia Materials* **2010**, *2*, 96–102.
7. Machín, A.; Márquez, F. Advancements in Photovoltaic Cell Materials: Silicon, Organic, and Perovskite Solar Cells. *Materials* **2024**, *17*, 1165.
8. Maldonado, S. The Importance of New "Sand to Silicon" Processes for the Rapid Future Increase of Photovoltaics. *ACS Energy Lett.* **2020**, *5*, 11, 3626–3635.
9. Kovalenko, M. V.; Protesescu, L.; Bodnarchuk, M. I. Properties and Potential Optoelectronic Applications of Lead Halide Perovskite Nanocrystals. *Science* **2017**, *358*, 745–750.
10. Akkerman, Q. A.; Rainò, G.; Kovalenko, M. V.; Manna, L. Genesis, challenges and opportunities for Lead Halide Perovskite Nanocrystals for Optoelectronic Applications. *Nat. Mater.* **2018**, *17*, 394–405.
11. Huang, H.; Polavarapu, L.; Sichert, J. A.; Susha, A. S.; Urban, A. S.; Rogach, A. L. Colloidal Lead Halide Perovskite Nanocrystals: Synthesis, Optical Properties and Applications. *NPG Asia Mater.* **2016**, *8*, e328.
12. Kamat, P. V. Quantum Dot Solar Cells. Semiconductor Nanocrystals as Light Harvesters. *J. Phys. Chem. C* **2008**, *112*, 48, 18737–18753.
13. Nozik, A. J.; Beard, M. C.; Luther, J. M.; Law, M.; Ellingson, R. J.; Johnson, J. C. Semiconductor Quantum Dots and Quantum Dot Arrays and Applications of Multiple Exciton Generation to Third Generation Photovoltaic Solar Cells. *Chem. Rev.* **2010**, *110,* 11, 6873–6890.

14. Klimov, V. I. Semiconductor and Metal Nanocrystals: Synthesis and Electronic and Optical Properties; CRC Press: *Boca Raton*, **2003**.

15. Duan, L.; Hu, L.; Guan, X.; Lin, C.-H.; Chu, D.; Huang, S.; Liu, X.; Yuan, J.; Wu, T. Quantum Dots for Photovoltaics: A Tale of Two Materials. *Adv. Energy Mater*. **2021,** *11*, 2100354 (1-23).

16. Peng, X.; Lai, Z.; Shao, H.; Shen, Y.; Meng, Y.; Ho, J. C.; Halide Perovskite Nanostructures: Processing Methods and Optoelectronics Applications. *npj Nanophoton.* **2025**, *2*, 42.

17. Behera, R. K.; Das, R.; Patra, A.; Dutta, S. K.; Pradhan, N. Pt–$CsPbBr_3$ Perovskite Nanocrystal Heterostructures for Enhanced Photocatalysis. *Nano Lett.* **2023**, *23*, 7890–7898.

18. Liu, X.; Zhang, Y.; Lee, E.-C. Advancements in Perovskite Nanocrystal Stability Enhancement: A Comprehensive Review. *Nanomaterials* **2023**, *13*, 1847.

19. Otero-Martínez, C.; Fiuza-Maneiro, N.; Polavarapu, L.; Enhancing the Intrinsic and Extrinsic Stability of Halide Perovskite Nanocrystals for Efficient and Durable Optoelectronics. *ACS Appl. Mater. Interfaces* **2022**, *14,* 30, 34291–34302.

20. du Fossé, I.; Mulder, J. T.; Almeida, G.; Spruit, A. G. M.; Infante, I.; Grozema, F. C.; Houtepen, A. J.; Limits of Defect Tolerance in Perovskite Nanocrystals: Effect of Local Electrostatic Potential on Trap States. *J. Am. Chem. Soc.* **2022**, *144*, 11059−11063.

21. Giansante, C.; I. Infante, Surface Traps in Colloidal Quantum Dots: A Combined Experimental and Theoretical Perspective. *J. Phys. Chem. Lett.* **2017**, *8*, 20, 5209–5215.

22. Wang, S.; Li, Z.; Zhang, Y.; Liu, X.; Han, J.; Li, X.; Liu, Z.; Frank Liu, S.; Choy, W. C. H. Water-Soluble Triazolium Ionic-Liquid-Induced Surface Self-Assembly to Enhance the Stability and Efficiency of Perovskite Solar Cells. *Adv. Funct. Mater.* **2019**, *29*, 1900417.

23. Salado, M.; Ramos, F. J.; Manzanares, V. M.; Gao, P.; Nazeeruddin, K.; Dyson, P. J.; Ahmad, S. Extending the Lifetime of Perovskite Solar Cells using a Perfluorinated Dopant. *Chem. Sus. Chem.* **2016**, *9*, 2708−2714.

24. Dong, W.; Sun, C.; Sun, M.; Ge, H.; Asiri, A. M.; Marwani, H. M.; Ni, R.; Wang, S. Interface Engineering of Imidazolium Ionic Liquids toward Efficient and Stable $CsPbBr_3$ Perovskite Solar Cells. *ACS Appl. Mater. Interfaces* **2020**, *12*, 4540−4548.

25. Shahiduzzaman, Md.; Muslih, E. Y.; Hasan, A. K. M.; Wang, L.; Fukaya, S.; Nakano, M.; Karakawa, M.; Takahashi, K.; Akhtaruzzaman, M.; Nunzi, J. M.; Taima, T. The benefits of ionic liquids for the fabrication of efficient and stable perovskite photovoltaics. *Chem. Eng. J.* **2021**, *411*, 128461.

26. Shahiduzzaman, M.; Yamamoto, K.; Furumoto, Y.; Kuwabara, T.; Takahashi, K.; Taima, T. Ionic Liquid-Assisted Growth of Methylammonium Lead Iodide Spherical Nanoparticles by a Simple Spin-coating Method and Photovoltaic Properties of Perovskite Solar Cells. *RSC Adv.* **2015**, *5*, 77495−77500.

27. Smirnov, M. S.; Ovchinnikov, O. V.; Dedikova, A. O.; Shapiro, B. I.; Vitukhnovsky, A. G.; Shatskikh, T. S. Luminescence Properties of Hybrid Associates of Colloidal CdS Quantum Dots with J-Aggregates of Thiatrimethine Cyanine Dye. *J. Lumin*. **2016**, *176*, 77−85.

28. Hoffman, J. B.; Choi, H.; Kamat, P. V. Size-Dependent Energy Transfer Pathways in CdSe Quantum Dot−Squaraine Light-Harvesting Assemblies: Förster versus Dexter. *J. Phys. Chem. C* **2014**, *118*, 18453–18461.

29. Qiao, Y.; Polzer, F.; Kirmse, H.; Steeg, E.; Kuhn, S.; Friede, S.; Kirstein, S.; Rabe, J. P. Nanotubular J-Aggregates and Quantum Dots Coupled for Efficient Resonance Excitation Energy Transfer. *ACS Nano* **2015**, *9*, 1552–1560.

30. Freyria, F. S.; Cordero, J. M.; Caram, J. R.; Doria, S.; Dodin, A.; Chen, Y.; Willard, A. P.; Bawendi, M. G. Near-Infrared Quantum Dot Emission Enhanced by Stabilized Self-Assembled J-Aggregate Antennas. *Nano Lett.* **2017**, *17*, 7665−7674.

31. Shahar, C.; Tidhar, Y.; Jung, Y.; Weissman, H.; Cohen, S. R.; Bitton, R.; Pinkas, I.; Haran, G.; Rybtchinski, B. Control over size, shape, and photonics of self-assembled organic nanocrystals. *J. Org. Chem.* **2021**, *17,* 42–51.

32. Szuromi, P.; Grocholski, B. Natural and engineered perovskites. *Science* **2017**, *358*, 732-733.

33. Aldakov, D.; Reiss, P. Safer-by-Design Fluorescent Nanocrystals: Metal Halide Perovskites Vs Semiconductor Quantum Dots. *J. Phys. Chem. C* **2019**, *123*, 12527−12541.

34. Roo, J. D.; Ibanez, M.; Geiregat, P.; Nedelcu, G.; Walravens, W.; Maes, J.; Martins, J. C.; Van Driessche, I.; Kovalenko, M. V.; Hens, Z. Highly Dynamic Ligand Binding and Light Absorption Coefficient of Cesium Lead Bromide Perovskite Nanocrystals. *ACS Nano* **2016**, *10*, 2071−2081.

35. Dutta, A.; Behera, R. K.; Pal, P.; Baitalik, S.; Pradhan, N. Near- Unity Photoluminescence Quantum Efficiency for All $CsPbX_3$ (X = Cl, Br, and I) Perovskite Nanocrystals: A Generic Synthesis Approach. *Angew., Chem. Int. Ed.* **2019**, *58*, 5552−5556.

36. Swarnkar, A.; Chulliyil, R.; Ravi, V. K.; Irfanullah, M.; Chowdhury, A.; Nag, A. Colloidal $CsPbBr_3$ Perovskite Nanocrystals: Luminescence beyond Traditional Quantum Dots. *Angew. Chem., Int. Ed.* **2015**, *54*, 15424−15428.

37. Ghosh, S.; Mandal, S.; Mukherjee, S.; De, C. K.; Samanta, T.; Mandal, M.; Roy, D.; Mandal, P. K. Near-Unity Photoluminescence Quantum Yield and Highly Suppressed Blinking in a Toxic-Metal-Free Quantum Dot. *J. Phys. Chem. Lett.* **2021**, *12*, 1426-1431.

38. Tian, Y.; Scheblykin, I. G. Artifacts in Absorption Measurements of Organometal Halide Perovskite Materials: What Are the Real Spectra*? J. Phys. Chem. Lett.* **2015**, *6*, 17, 3466–3470.

39. Goesten, M. G.; Hoffmann, R. Mirrors of Bonding in Metal Halide Perovskites. *J. Am. Chem. Soc.* **2018**, *140*, 40, 12996–13010.

40. Sun, S.; Lu, M.; Gao, X.; Shi, Z.; Bai, X.; Yu, W. W.; Zhang Y. 0D Perovskites: Unique Properties, Synthesis, and Their Applications. *Adv. Sci.* **2021**, 8, 2102689.

41. Simenas, M.; Gagor, A.; Banys, J.; Maczka, M. Phase Transitions and Dynamics in Mixed Three- and Low-Dimensional Lead Halide Perovskites. *Chem. Rev.* **2024**, 124, 2281−2326.

42. Zhu, P.; Zhu, J. Low-dimensional metal halide perovskites and related optoelectronic applications. *InfoMat.* **2020**, *2*, 341–378.

43. Zhang, Y.; Liu, J.; Wang, Z.; Xue, Y.; Ou, Q.; Polavarapu, L.; Zheng, J.; Qiae, X.; Bao, Q. Synthesis, properties, and optical applications of low-dimensional perovskites. *Chem. Commun.*, **2016**, *52*, 13637-13655.

44. Chu, Z.; Chu, X.; Zhao, Y.; Ye, Q.; Jiang, J.; Zhang, X.; You, J. Emerging Low-Dimensional Crystal Structure of Metal Halide Perovskite Optoelectronic Materials and Devices. *Small Struct.* **2021**, 2, 2000133.

45. Wang, H.-P.; Li, S.; Liu, X.; Shi, Z.; Fang, X.; He, J.-H. Low-Dimensional Metal Halide Perovskite Photodetectors. *Adv. Mater.* **2021**, *33*, 2003309.

46. Hoye, R. L. Z.; Hidalgo, J.; Jagt, R. A.; Correa-Baena, J.-P.; Fix, T.; MacManus-Driscol, J. L. The Role of Dimensionality on the Optoelectronic Properties of Oxide and Halide Perovskites, and their Halide Derivatives. *Adv. Energy Mater.* **2022**, 12, 2100499.

47. Manser, J. S.; Christians, J. A.; Kamat, P. V. Intriguing Optoelectronic Properties of Metal Halide Perovskites. *Chem. Rev.* **2016**, *116* (21), 12956–13008.15.

48. Seth, S.; Samanta, A. A facile methodology for engineering the morphology of CsPbX3 perovskite nanocrystals under ambient condition. *Scientific Reports* **2016**, 6 (1), 37693.

49. Akkerman, Q. A.; Motti, S. G.; Srimath Kandada, A. R.; Mosconi, E.; D'Innocenzo, V.; Bertoni, G.; Marras, S.; Kamino, B. A.; Miranda, L.; De Angelis, F. Solution synthesis approach to colloidal cesium lead halide perovskite nanoplatelets with monolayer-level thickness control. *J. Am. Chem. Soc.* **2016**, *138* (3), 1010-1016.

50. Bekenstein, Y.; Koscher, B. A.; Eaton, S. W.; Yang, P.; Alivisatos, A. P. Highly luminescent colloidal nanoplates of perovskite cesium lead halide and their oriented assemblies. *J. Am. Chem. Soc.* **2015**, *137* (51), 16008-16011.

51. Amgar, D.; Stern, A.; Rotem, D.; Porath, D.; Etgar, L. Tunable length and optical properties of CsPbX3 (X= Cl, Br, I) nanowires with a few unit cells. *Nano Lett.* **2017**, 17 (2), 1007-1013.

52. Imran, M.; Di Stasio, F.; Dang, Z.; Canale, C.; Khan, A. H.; Shamsi, J.; Brescia, R.; Prato, M.; Manna, L. Colloidal synthesis of strongly fluorescent CsPbBr3 nanowires with width tunable down to the quantum confinement regime. *Chem. Mater.* **2016**, *28* (18), 6450-6454.

53. Cha, J.-H.; Han, J. H.; Yin, W.; Park, C.; Park, Y.; Ahn, T. K.; Cho, J. H.; Jung, D.-Y. Photoresponse of CsPbBr3 and Cs4PbBr6 perovskite single crystals. *J. Phys. Chem. Lett.* **2017**, *8* (3), 565-570.

54. Saidaminov, M. I.; Almutlaq, J.; Sarmah, S.; Dursun, I.; Zhumekenov, A. A.; Begum, R.; Pan, J.; Cho, N.; Mohammed, O. F.; Bakr, O. M. Pure Cs4PbBr6: highly luminescent zero-dimensional perovskite solids. *ACS Energy Lett.* **2016**, *1* (4), 840-845.

55. Zhang, Y.; Saidaminov, M. I.; Dursun, I.; Yang, H.; Murali, B.; Alarousu, E.; Yengel, E.; Alshankiti, B. A.; Bakr, O. M.; Mohammed, O. F. Zero-dimensional Cs4PbBr6 perovskite nanocrystals. *J. Phys. Chem. Lett.* **2017**, *8* (5), 961-965.

56. Seth, S.; Samanta, A. Photoluminescence of Zero-Dimensional Perovskites and Perovskite-Related Materials. *J. Phys. Chem. Lett.* **2018**, *9*, 176−183.

57. Akkerman, Q. A.; Park, S.; Radicchi, E.; Nunzi, F.; Mosconi, E.; De Angelis, F.; Brescia, R.; Rastogi, P.; Prato, M.; Manna, L. Nearly monodisperse insulator Cs4PbX6 (X= Cl, Br, I) nanocrystals, their mixed halide compositions, and their transformation into CsPbX3 nanocrystals. *Nano Lett.* **2017**, *17* (3), 1924-1930.

58. De Bastiani, M.; Dursun, I.; Zhang, Y.; Alshankiti, B. A.; Miao, X.-H.; Yin, J.; Yengel, E.; Alarousu, E.; Turedi, B.; Almutlaq, J. M.; Saidaminov, M. I.; Mitra, S.; Gereige, I.; AlSaggaf, A.; Zhu, Y.; Han, Y.; Roqan, I. S.; Bredas, J.-L.; Mohammed, O. F.; Bakr, O. M. Inside Perovskites: Quantum Luminescence from Bulk Cs4PbBr6 Single Crystals. *Chem. Mater.* **2017**, *29* (17), 7108-7113.

59. Seth, S.; Samanta, A. Fluorescent Phase-Pure Zero-Dimensional Perovskite-Related Cs4PbBr6 Microdisks: Synthesis and Single-Particle Imaging Study. *J. Phys. Chem. Lett.* **2017**, *8* (18), 4461-4467.

60. Liu, Z.; Bekenstein, Y.; Ye, X.; Nguyen, S. C.; Swabeck, J.; Zhang, D.; Lee, S.-T.; Yang, P.; Ma, W.; Alivisatos, A. P. Ligand mediated transformation of cesium lead bromide perovskite nanocrystals to lead depleted Cs4PbBr6 nanocrystals. *J. Am. Chem. Soc.* **2017**, *139* (15), 5309-5312.

61. Huang, H.; Bodnarchuk, M. I.; Kershaw, S. V.; Kovalenko, M. V.; Rogach, A. L. Lead Halide Perovskite Nanocrystals in the Research Spotlight: Stability and Defect Tolerance. *ACS Energy Lett.* **2017**, 2, 9, 2071–2083.

62. Protesescu, L.; Yakunin, S.; Nazarenko, O.; Dirin, D. N.; Kovalenko, M. V. Low-Cost Synthesis of Highly Luminescent Colloidal Lead Halide Perovskite Nanocrystals by Wet Ball Milling. *ACS Appl. Nano Mater.* **2018**, 1, 1300−1308.

63. Bai, W.; Xuan, T.; Zhao, H.; Dong, H.; Cheng, X.; Wang, L.; Xie, R.-J. Perovskite Light-Emitting Diodes with an External QuantumEfficiency Exceeding 30%. *Adv. Mater.* **2023**, *35*, 2302283.

64. Polavarapu, L.; Nickel, B.; Feldmann, J.; Urban, A. S. Advances in Quantum-Confined Perovskite Nanocrystals for Optoelectronics. *Adv. Energy Mater.* **2017**, *7*, 1700267.

65. C. K.; Ng, Yin, W.; Li, H.; Jasieniak, J. J. Scalable synthesis of colloidal CsPbBr3 perovskite nanocrystals with high reaction yields through solvent and ligand engineering. *Nanoscale*, **2020**, *12*, 4859–4867.

66. Shamsi, J.; Urban, A.; S. Imran, M.; Trizio, L. D.; Manna, L. Metal Halide Perovskite Nanocrystals: Synthesis, Post-Synthesis Modifications, and Their Optical Properties. *Chem. Rev.* **2019**, 119, 5, 3296–3348.

67. Rossetti, R.; Nakahara, S.; Brus, L. E. Quantum size effects in the redox potentials, resonance Raman spectra, and electronic spectra of CdS crystallites in aqueous solution. *J. Chem. Phys.* **1983**, *79*, 1086-1088.

68. Ekimov, A. I.; Efros, A. L.; Onushchenko, A. A. Quantum size effect in semiconductor microcrystals *Solid State Commun.* **1985,** *56*, 921-924.

69. Reed, M. A.; Randall, J. N.; Aggarwal, R. J.; Matyi, R. J.; Moore, T. M.; Wetsel, A. E. Observation of discrete electronic states in a zero-dimensional semiconductor nanostructure *Phys. Rev. Lett.* **1988,** *60*, 535-537.

70. Smith, A. M.; Nie, S. Semiconductor Nanocrystals: Structure, Properties, and Band Gap Engineering *Acc. Chem. Res.* **2010,** *43*, 190-200.

71. Brus, L. E. Electron–electron and electron-hole interactions in small semiconductor crystallites: The size dependence of the lowest excited electronic state. *J. Chem. Phys.* **1984,** *80*, 4403-4409.

72. Trindade, T.; O'Brien, P.; Pickett, N. L., Nanocrystalline Semiconductors: Synthesis, Properties, and Perspectives. *Chem. Mater.* **2001,** *13*, 3843-3858.

73. Alivisatos, A. P.Perspectives on the Physical Chemistry of Semiconductor Nanocrystals *J. Phys. Chem.* **1996,** *100*, 13226-13239.

74. Takagahara, T.; Takeda, K. Theory of the quantum confinement effect on excitons in quantum dots of indirect-gap materials. *Phys. Rev. B* **1992,** *46*, 15578-15581.

75. Nirmal, M.; Brus, L. Luminescence Photophysics in Semiconductor Nanocrystals. *Acc. Chem. Res.* **1999,** *32*, 407-414.

76. Bawendi, M. G.; Steigerwald, M. L.; Brus, L. E. The Quantum Mechanics of Larger Semiconductor Clusters ("Quantum Dots"). *Annu. Rev. Phys. Chem.* **1990,** *41*, 477-496.

77. Yu, W. W.; Qu, L.; Guo, W.; Peng, X. Experimental Determination of the Extinction Coefficient of CdTe, CdSe, and CdS Nanocrystals. *Chem. Mater.* **2003,** *15*, 2854-2860.

78. Brus, L. E. A simple model for the ionization potential, electron affinity, and aqueous redox potentials of small semiconductor crystallites. *J. Chem. Phys.* **1983,** *79*, 5566-5571.

79. Wang, Y.; Herron, N. Nanometer-sized semiconductor clusters: materials synthesis, quantum size effects, and photophysical properties. *J. Phys. Chem.* **1991,** *95*, 525-532.

80. Chen, Z.; O'Brien, S. Structure Direction of II−VI Semiconductor Quantum Dot Binary Nanoparticle Superlattices by Tuning Radius Ratio. *ACS Nano* **2008,** *2*, 1219-1229.

81. Machol, J. L.; Wise, F. W.; Patel, R.; Tanner, D. B. Optical studies of IV-VI quantum dots *Physica A* **1994,** *207*, 427-434.

82. Gao, X.; Nie, S. Molecular profiling of single cells and tissue specimens with quantum dots. *Trends in Biotechnology* **2003,** *21*, 371-373.

83. Hodes, G. Comparison of Dye- and Semiconductor-Sensitized Porous Nanocrystalline Liquid Junction Solar Cells. *J. Phys. Chem. C* **2008,** *112*, 17778-17787.

84. Resch-Genger, U.; Grabolle, M.; Cavaliere-Jaricot, S.; Nitschke, R.; Nann, T. Quantum dots versus organic dyes as fluorescent labels. *Nat Methods* **2008,** *5*, 763-775.

85. Grodzinska, D.; Evers, W. H.; Dorland, R.; Van Rijssel, J.; Van´ Huis, M. A.; Meijerink, A.; De Mello Donegá, C.; Vanmaekelbergh, D. Two-Fold Emission from the S-Shell of PbSe/CdSe Core/Shell Quantum Dots. Small **2011**, *7*, 3493−3501.

86. Sattler, K. D. Handbook of nanophysics: Nanoparticles and Quantum Dots; CRC Press, USA, 2011.

87. Wang, Y.; Si, B.; Lu, S.; Ma, X.; Liu, E.; Fan, J.; Li, X.; Hu, X. Effective improvement in optical properties of colloidal CdTe@ZnS quantum dots synthesized from aqueous solution. *Nanotechnology* **2016**, *27*, 365707.

88. Peighambardoust, N. S.; Sadeghi, E.; Aydemir, U. Lead Halide Perovskite Quantum Dots for Photovoltaics and Photocatalysis: A Review. *ACS Appl. Nano Mater.* **2022**, 5, 10, 14092–14132

89. Kahmann, S.; Loi, M. A. Trap states in lead chalcogenide colloidal quantum dots—origin, impact, and remedies. *Appl. Phys. Rev.* **2020**,*7*, 041305.

90. Santhosh, K.; Samanta, A. Exploring the CdTe Quantum Dots in Ionic Liquids by Employing a Luminescent Hybrid of the Two. *J. Phys. Chem. C* **2012**, *116*, 20643−20650.

91. Saladin, M.; Maroncelli, M. Electron Transfer Kinetics between an Electron-Accepting Ionic Liquid and Coumarin Dyes. *J. Phys. Chem. B* **2020**, 124, 50, 11431–11445.

92. Sahu, P. K.; Das, S. K.; Sarkar, M. Fluorescence response of a dipolar organic solute in a dicationic ionic liquid (IL): is the behavior of di-cationic IL different from that of usual monocationic IL? *Phys. Chem. Chem. Phys.* **2014**, *16*, 12918-12928.

93. Majhi, D.; Seth, S.; Sarkar, M. Differences in the behavior of dicationic and monocationic ionic liquids as revealed by time resolved-fluorescence, NMR and fluorescence correlation spectroscopy. *Phys. Chem. Chem. Phys.*, **2018**, *20*, 7844-7856.

94. Sahu, P. K.; Das, S. K.; Sarkar, M. Toward Understanding Solute−Solvent Interaction in Room-Temperature Mono- and Dicationic Ionic Liquids: A Combined Fluorescence Spectroscopy and Mass Spectrometry Analysis. *J. Phys. Chem. B* **2014**, *118*, 1907−1915.

95. Singh, G.; Kaur, Drechslerb, M. M.; Kang, T. S. Unprecedented self-assembled architectures of surface-active ionic liquids in aqueous medium. *Chem. Commun.* **2018**, *54*, 2432.

96. Xue, P.; Zhang, C.; Wang, K.; Liang, M.; Zhang, T. Alkyl chain-dependent cyano-stilbene derivative's molecular stacking, emission enhancement and fluorescent response to the mechanical force and thermal stimulus. *Dyes and Pigments* **2019,** *163*, 516-524.

97. Takahashi, S.; Miura, H.; Kasai, H.; Okada, S.; Oikawa, H.; Nakanishi, H. Single-Crystal-to-Single-Crystal Transformation of Diolefin Derivatives in Nanocrystals. *J. Am. Chem. Soc.* **2002,** *124*, 10944-10945.

98. Kasha, M.; Rawls, H. R.; Ashraf El-Bayoumi, M. The Exciton Model in Molecular Spectroscopy. *Pure Appl. Chem.* **1965,** *11*, 371-392.

99. Bricks, J. L.; Slominskii, Y. L.; Panas, I. D.; Demchenko, A. P. Fluorescent J-aggregates of cyanine dyes: basic research and applications review. *Methods Appl. Fluoresc.* **2018,** *6*, 012001.

100. Ma, S.; Du, S.; Pan, G.; Dai, S.; Xu, B.; Tian, W., Organic molecular aggregates: From aggregation structure to emission property. *Aggregate* **2021,** *2*, e96.

101. Saikin, S. K.; Eisfeld, A.; Valleau, S.; Aspuru-Guzik, A. Photonics meets excitonics: natural and artificial molecular aggregates. *Nanophotonics* **2013,** *2*, 21-38.

102. Oikawa, H.; Mitsui, T.; Onodera, T.; Kasai, H.; Nakanishi, H.; Sekiguchi, T. Size-effect on Fluorescence Spectrum of Perylene Nanocrystal Studied by Single-particle Microspectroscopy Coupled with Atomic Force Microscope Observation. *Jpn. J. Appl. Phys.* **2003,** *42*, L111-L113.

103. Takahashi, S.; Miura, H.; Kasai, H.; Okada, S.; Oikawa, H.; Nakanishi, H. Functional Organic Nanocrystals. *J. Am. Chem. Soc.* **2002,** *124*, 10944-10945.

104. Fu, H.-B.; Yao, J.-N. Size Effects on the Optical Properties of Organic Nanoparticles. *J. Am. Chem. Soc.* **2001,** *123*, 1434-1439.

105. Zhao, Y. S.; Fu, H.; Peng, A.; Ma, Y.; Xiao, D.; Yao, J. Low-Dimensional Nanomaterials Based on Small Organic Molecules: Preparation and Optoelectronic Properties. *Adv. Mater.* **2008**, *20*, 2859-2876.

106. Sainudeen, Z.; Ray, P. C. First-Order Hyperpolarizabilities of Sulfophthalein Dyes. *J. Phys. Chem. A* **2005,** *109*, 9095-9103.

107. Tani, T. J-Aggregates in Spectral Sensitization of Photographic Materials. In Kobayashi, T., Ed., J-Aggregates. **1996**, *World Scientific, Singapore*, p. 209.

108. Takechi, K.; Sudeep, P. K.; Kamat, P. V. Harvesting Infrared Photons with Tricarbocyanine Dye Clusters. *J. Phys. Chem. B* **2006**, *110*, 16169-16173.

109. Higgins, D. A.; Kerimo, J.; Vanden Bout, D. A.; Barbara, P. F.A Molecular Yarn: Near-Field Optical Studies of Self-Assembled, Flexible, Fluorescent Fibers. *J. Am. Chem. Soc.* **1996**, *118*, 4049-4058.

110. Mei, J.; Wang, J.; Sun, J. Z.; Zhao, H.; Yuan, W.; Deng, C.; Chen, S.; Sung, H. H. Y.; Lu, P.; Qin, A.; *et. al.* Siloles symmetrically substituted on their 2,5-positions with electron-accepting and donating moieties: facile synthesis, aggregation-enhanced emission, solvatochromism, and device application. *Chem. Sci.* **2012**, *3*, 549-558.

111. O'Regan, B.; Grätzel, M. A low-cost, high-efficiency solar cell based on dye-sensitized colloidal TiO2 films. *Nature* **1991**, *353*, 737-740.

112. Zaumseil, J.; Sirringhaus, H. Electron and Ambipolar Transport in Organic Field-Effect Transistors. *Chem. Rev.* **2007**, *107*, 1296-1323.

113. Grimsdale, A. C.; Leok Chan, K.; Martin, R. E.; Jokisz, P. G.; Holmes, A. B. Synthesis of Light-Emitting Conjugated Polymers for Applications in Electroluminescent Devices. *Chem. Rev.* **2009**, *109*, 897-1091.

114. Ng, K. K.; Zheng, G. Molecular Interactions in Organic Nanoparticles for Phototheranostic Applications. *Chem. Rev.* **2015**, *115*, 11012-11042.

115. Jang, J.; Oh, J. H. Facile Fabrication of Photochromic Dye–Conducting Polymer Core–Shell Nanomaterials and Their Photoluminescence. *Adv. Mater.* **2003,** *15*, 977-980.

116. Debuigne, F.; Jeunieau, L.; Wiame, M.; B.Nagy, J. Synthesis of Organic Nanoparticles in Different W/O Microemulsions. *Langmuir* **2000,** *16*, 7605-7611.

117. Tamaki, Y.; Asahi, T.; Masuhara, H. Nanoparticle Formation of Vanadyl Phthalocyanine by Laser Ablation of Its Crystalline Powder in a Poor Solvent. *J. Phys. Chem. A* **2002,** *106*, 2135-2139.

118. Zhao, Y. S.; Xiao, D.; Yang, W.; Peng, A.; Yao, J. 2,4,5-Triphenylimidazole Nanowires with Fluorescence Narrowing Spectra Prepared through the Adsorbent-Assisted Physical Vapor Deposition Method. *Chem. Mater.* **2006,** *18*, 2302-2306.

119. Hou, S.; Harrell, C. C.; Trofin, L.; Kohli, P.; Martin, C. R. Layer-by-Layer Nanotube Template Synthesis. *J. Am. Chem. Soc.* **2004,** *126*, 5674-5675.

120. Huang, Y.; Quan, B.; Wei, Z.; Liu, G.; Sun, L.Organic nanotubes created from mesogenic derivatives. *J. Phys. Chem. C* **2009,** *113*, 3929-3933.

121. Lakowicz, J. R. Principles of Fluorescence Spectroscopy. *Springer* US: Boston, MA, **2006**.

122. Niu, H.; Liu, J.; O'Connor, H. M.; Gunnlaugsson, T.; James, T. D.; Zhang, H. Photoinduced electron transfer (PeT) based fluorescent probes for cellular imaging and disease therapy. *Chem. Soc. Rev.* **2023**, *52*, 2322-2357.

CHAPTER 2

Materials, Experimental Techniques, and Methods

Abstract

This chapter outlines the materials, synthesis protocols, and experimental techniques employed throughout the thesis. It details the preparation and purification of $CsPbX_3$ nanocrystals, Cs_4PbBr_6 microdisks, CdTe@ZnS quantum dots, and various ionic liquids. Standardized sample preparation methods for optical, microscopic, and spectroscopic studies are described. The chapter further summarizes the instrumentation used, including UV–Vis and fluorescence spectroscopy, TCSPC-based lifetime measurements, femtosecond transient absorption spectroscopy, confocal fluorescence microscopy, NMR diffusion studies, DLS, and XRD. Together, these methodologies provide a comprehensive framework for probing structural, optical, and dynamical properties of the studied nanomaterial systems.

2.1. Materials

All chemicals employed for the synthesis, purification, and characterization of the compounds discussed in this thesis were procured from reputed suppliers, including Sigma-Aldrich, TCI Chemicals, Merck, Alfa Aesar, Finar, and NICE Chemicals. Detailed information on these materials is provided below.

2.1.1. For $CsPbBr_3$ Nanocrystal Synthesis and ILs Interaction Cs_2CO_3 (99.9% Aldrich), octadecene (ODE, 90%, Aldrich), oleic acid (OA, 90%, Aldrich), oleylamine (OLA, 70%, Aldrich), trioctylamine (TOP, 97 % Aldrich), $PbCl_2$ (99.999%, Aldrich), $PbBr_2$ (99.999%, Aldrich), PbI_2 (99%, Aldrich), 1-ethyl-3-methylimidazolium tetrafluoroborate ($EMIMBF_4$, 99%, Aldrich), 1-ethyl-3-methylimidazolium acetate (EMIMOAc, 99%, Aldrich), 1-ethyl-3-methylimidazolium methansulphonate (EMIMS, 99%, Aldrich), 1-butyl-3-methylimidazolium tetrafluoroborate (BMIMBF4, 99%, Aldrich), 1-hexyl-3-methylimidazolium tetrafluoroborate (HMIMBF4, 99%, Aldrich), and chloroform (99.8%, Aldrich, anhydrous).

2.1.2. For Cs_4PbBr_6 microdisks Synthesis Lead bromide ($PbBr_2$, >99%), cesium bromide (CsBr, 99.999% trace metals basis) are purchased from Sigma-Aldrich. N, N-dimethyl formamide (DMF) (Sigma-Aldrich), Toluene (Sigma-Aldrich).

2.1.3. For CdTe@ZnS QDs Synthesis Tellurium powder (Te, 99%), Cadmium chloride dehydrates ($CdCl_2.2H_2O$, 99%), Sodium borohydride ($NaBH_4$, 97%), 3-mercapto propionic acid (MPA, 98%), Zinc acetate dihydrate (Zn $(OAc)_2$, $2H_2O$ 99%), sodium sulphide (Na_2S, 98%), and absolute ethanol (analytical reagent were purchased from Sigma). Sodium hydroxide (NaOH, 98%) was purchased from SciChem, and S2165 dye was purchased from FEW chemicals.

2.1.4. For ILs Synthesis 1-methylimidazole, 1-bromohexadecane, 1-bromotetradecane, 1-bromododecane, 1,12-dibromododecane, purchased from Sigma-Aldrich, Pyridine (Sigma), 1-bromohexane, 1-bromopropane, 1,6-dibromohexane, acetonitrile (Finar), and diethyl ether (Finar) were bought and redistilled before use.

2.2. Synthesis and Purification

2.2.1. Synthesis and Purification of $CsPbX_3$ NCs The colloidal $CsPbX_3$ (X= Cl, Br, I) NCs studied in this work were synthesized following the procedure reported by Protesescu et al. [1]with minor modifications. Cs_2CO_3 (0.10175 g), OA (0.3125 mL) and ODE (5 mL) were mixed in a 50 mL double-necked round-bottom (RB) flask and kept at 120 °C in vacuum for 1 hour. Later, the temperature was raised to 160 °C to get a clear solution of cesium oleate (Cs-oleate). The Cs-oleate solution was kept at 100 °C under N_2 atmosphere before injection to avoid precipitation. ODE (5 mL), PbX_2 (0.188 mmol), OA (0.5 mL), and OLA (0.5 mL) were loaded in a 50 mL double-necked RB flask, and the mixture was heated under vacuum at 120°C for 1 hour. Further, the temperature was raised to 170 ºC and kept for 20 minutes, followed by the injection of Cs-oleate solution (0.4 mL). The reaction mixture was rapidly cooled in an ice-water bath. The crude solution was centrifuged at 8000 rpm for 10 min. The supernatant

containing unreacted precursors was discarded, and the obtained precipitate was washed with toluene and centrifuged at 3000 rpm for 5 min to remove trace amounts of unreacted species. Purified PNCs were dispersed in distilled, anhydrous chloroform for further measurements.

2.2.2. Synthesis and Purification of Cs_4PbBr_6 microdisks MDs were synthesized using an anti-solvent precipitation method conducted at room temperature under ambient conditions.[2] In a typical procedure, 0.1 mM each of $PbBr_2$ and CsBr were dissolved in 3 mL of dimethylformamide (DMF). Subsequently, the desired amount of ionic liquids (ILs, 0.05–0.2 mM) was added to the solution, followed by sonication to ensure complete dissolution. The resulting precursor solution was transferred to a 50 mL round-bottom flask, and 0.75 mL of toluene was introduced under vigorous stirring. After 5–10 minutes, a color change to greenish-yellow indicated the formation of MDs. The mixture was then centrifuged at 7000 rpm for 5 minutes, and the precipitate was washed multiple times with toluene to remove residual impurities.

2.2.3. Synthesis of ILs 1-Bromohexadecane, 1-Bromotetradecane, 1-Bromododecane**,** were mixed with 1-methyl imidazole separately in 1 : 1.2 molar ratio in acetonitrile and stirred under heating at 80 °C for 72 hours to obtain C_{16}mimBr, C_{14}mimBr, C_{12}mimBr respectively. 1,12-dibromododecane was mixed with 1-methyl imidazole separately in 1 : 2.5 molar ratio in acetonitrile and stirred under heating at 80 °C for 72 hours to obtain $C_{12}mimBr_2$.[3] The bromide salt was washed repeatedly with diethyl ether to remove the unreacted solvents. The same procedure is applied for the synthesis of pyridinium ILs synthesis.

2.2.4. Synthesis and Purification of CdTe@ZnS QDs The aqueous CdTe@ZnS QDs were prepared by following the procedure of Wang et al[4]with minor modifications. Usually, $CdCl_2 \cdot 2H_2O$ (0.0457 g, 0.2 mmol) and MPA (0.0433 g, 0.4 mmol) (i.e., Cd^{2+}/MPA ratio was of 1:2) were taken in a 250 mL round-bottom flux, and 100mL Millipore water was added. The mixture

was stirred for 30 min at room temperature. To get the Cd^{2+} precursor solution, the pH of the mixture was adjusted to 9 with NaOH solution (1 M). To prepare the sodium hydrogen telluride (NaHTe) as Te^{2-} precursors, $NaBH_4$ (0.0567 g, 1.5 mmol) was used to react with Te powder (0.0638 g, 0.5 mmol) (i.e, by a molar ratio of $NaBH_4$/Te=3:1) in 20 mL of ultrapure water. The Cd^{2+} precursor solution was heated up to 100 °C by that time, 4 ml NaHTe solution was added to it, then the mixture was cooled and refluxed at 90 °C. By varying the refluxing time, we varied the size of the QDs. After that, to obtain CdTe@ZnS QDs 20 ml solution of $Zn(OAc)_2$ (5 mM) and Na_2S (5 mM) solution was added dropwise to the as-prepared CdTe QDs solution, and refluxed for 2 h. The precipitates of CdTe@ZnS QDs could be gained by adding ethanol to the CdTe@ZnS QDs solution and centrifugation. The precipitation was repeatedly washed with ethanol to remove unwanted species like excess capping molecules and ions present in the product. Finally, the products were dried in a vacuum oven at 60 °C for 10 h.

2.3. Sample Preparation:

2.3.1. Preparation of CdTe@ZnS QDs_J-aggregate nanohybrid The target inorganic-organic nanohybrid compound is prepared *insitu*, where dye is gradually added to the QDs solution to form a nanohybrid associate. The formation of the product is monitored by careful observation of optical spectroscopy.

2.3.2. Preparation of SEM Samples For SEM imaging, the nanomaterial dispersion is first diluted to a suitable concentration and sonicated to ensure a well-dispersed suspension. A small volume of this suspension is then drop-cast onto a silicon wafer, dried under vacuum for overnight before imaging.

2.3.3. Preparation of TEM Samples For TEM imaging, the nanomaterial dispersion is first diluted to an appropriate concentration and subsequently sonicated to ensure uniform distribution. A small aliquot of the solution is then drop-cast onto a 300-mesh copper grid. The

coated grid is allowed to dry under a lamp for 10–15 minutes and subsequently placed under vacuum for 4–5 hours before imaging.

2.4. Instrumentations

2.4.1. Instrument for Microscopic Characterization The microscopic characterization was done by scanning electron microscope (SEM) and transmission electron microscope (TEM). The Zeiss Gemini 2 Scanning Electron Microscope has been used for FESEM measurement. The TEM images of the NCs were determined using a JEM-F200 Multi-purpose Electron Microscope (JEOL) at an accelerating voltage of 200 kV.

2.4.2. Instrumentation Steady-State optical measurements To investigate the optical properties of the synthesized nanomaterials, steady-state absorption and fluorescence techniques were primarily employed.

2.4.2.1. Absorption Spectroscopy UV–Vis absorption measurements were carried out using a Cary 100 Bio UV–Vis spectrophotometer, which offers a wavelength resolution of 0.15 nm and uses a xenon lamp as the excitation source. UV–Vis spectroscopy provides insights into the electronic energy levels of a material by analyzing the positions and intensities of its absorption bands. This helps in identifying various chromophoric groups as well as understanding their surrounding chemical environments. In addition, UV–Vis absorption profiles can reveal ground-state interactions such as hydrogen bonding and solvent polarity effects associated with the chromophoric species. The technique follows the Beer–Lambert law, which states that the absorbance A_λ at a particular wavelength λ is directly proportional to the molar extinction coefficient ε_λ, the concentration C, and the optical path length l. Mathematically, it is expressed as:

$$A_\lambda = \log\left(\frac{I_0}{I}\right) = \varepsilon_\lambda C l \qquad (2.1)$$

where I_0 and I represent the intensities of the incident and transmitted light at a wavelength λ, respectively, and l is the cuvette path length.

2.4.2.2 Fluorescence Spectroscopy Fluorescence spectroscopy is an extremely sensitive optical method used to study photophysical and photochemical processes occurring in the excited states of fluorophores. Even minor changes in the energy levels or interactions between fluorophore molecules can alter the emission profile, including variations in spectral shape, intensity, and peak position.[5-7] These sensitivities make fluorescence spectroscopy a powerful tool for probing the microenvironment around the emitting species. In this thesis, fluorescence spectroscopy has been extensively utilized to investigate the photophysical behavior of all the studied systems. For steady-state fluorescence measurement Cary Eclipse Fluorescence Spectrophotometer (Agilent Technologies) has been used. Temperature-dependent PL measurement was carried out using HORIBA Fluorolog QM fluorimeter.

2.4.3. Instruments for Time-Resolved Study

2.4.3.1. Fluorescence Lifetime Measurements Time-resolved fluorescence spectroscopy provides valuable information about the kinetics of photophysical and photochemical processes. When a fluorophore is excited by an ultrafast laser pulse, an initial excited-state population n_0 is produced. The decay of this population follows[5-7]

$$-\frac{dn(t)}{dt} = (k_r + k_{nr})\, n(t) \qquad (2.2)$$

where $n(t)$is the number of excited molecules at time t, $k_r$and k_{nr} are radiative and nonradiative decay rate constants, respectively.

The solution of the above equation gives an exponential decay[5-7]

$$n(t) = n_0 \exp\left(-\frac{t}{\tau}\right) \qquad (2.3)$$

where τ is the excited-state lifetime of the fluorophore. Since fluorescence intensity is directly proportional to the excited-state population, the time-dependent emission intensity can be written as[5-7]

$$I(t) = I_0 \exp\left(-\frac{t}{\tau}\right) \quad (2.4)$$

where $I(t)$ and I_0 fluorescence intensity at time t and intensity immediately after excitation

The fluorescence lifetime is related to the decay rates as[5-7]

$$\tau = \frac{1}{k_r + k_{nr}} \quad (2.5)$$

The fluorescence lifetime of a fluorophore is commonly determined using the time-correlated single photon counting (TCSPC) technique. Because individual fluorophores remain in their various excited states for varying durations, the detected photons exhibit a characteristic time distribution, which manifests as the fluorescence decay profile of the sample. Consequently, the lifetime measured by the TCSPC system represents the statistical average of the time that the ensemble of fluorophore molecules spends in the excited state. Fluorescence lifetime measurements presented in this thesis were carried out with Edinburgh LifeSpec II systems.

2.4.3.1.1 Basic Principle of TCSPC

Time-Correlated Single Photon Counting (TCSPC) detects individual photons emitted after pulsed excitation and constructs a histogram of their arrival times. This histogram reflects the probability distribution of excited-state decay. Because TCSPC is statistical in nature, high repetition-rate excitation sources are required to accumulate sufficient photon counts. A schematic representation of the working principle of TCSPC setup (in reverse mode) is shown in Scheme 2.1. In reverse mode operation, commonly used at high repetition rates, the emission photon generates the STOP signal, while the excitation reference generates the START signal.

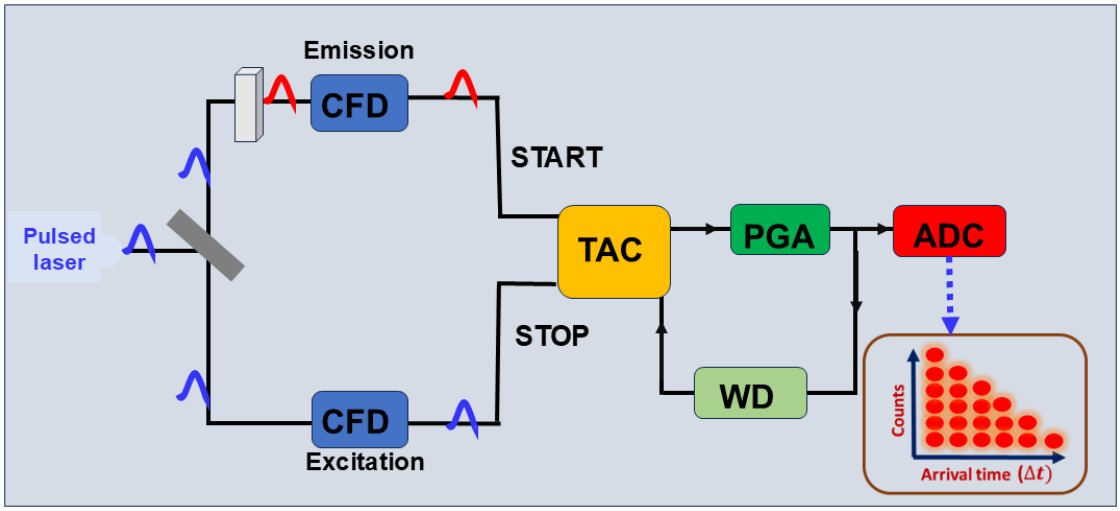

Scheme 2.1. Schematic diagram for the working principle of the TCSPC setup.

2.4.3.1.2. Major Components of a TCSPC System

a) **Pulsed Excitation Source:** Diode lasers (e.g., 375, 405, 445 nm) are used for excitation. The shortest measurable decay corresponds to the Instrument Response Function (IRF), typically ~100 ps FWHM. The IRF is recorded under identical experimental conditions for deconvolution during data analysis.

b) **Constant Fraction Discriminator (CFD)** The CFD enhances timing precision by rejecting low-amplitude noise signals and ensuring accurate determination of photon arrival times for both START and STOP pulses.

c) **Time-to-Amplitude Converter (TAC)** The TAC acts as the core timing unit. Upon receiving a START signal, a timing capacitor charges linearly. When the STOP signal arrives, charging stops and the resulting voltage is proportional to the time difference between the two pulses. The TAC range (50 ns–400 µs) is selected based on the expected fluorescence lifetime.

d) **Multichannel Analyzer (MCA)** The MCA sorts the TAC output pulses into discrete time channels. It operates in Pulse Height Analysis (PHA) mode for decay curves and

Multichannel Scaling (MCS) mode for time-resolved emission spectra. Processed data are transferred to a computer for fitting.

e) **START and STOP Photomultiplier Tubes (PMTs)** In reverse mode, excitation pulses generate the START signal, while emitted photons generate STOP signals, minimizing unnecessary TAC triggering at high repetition rates.

2.4.3.1.3. Working Overview Light from the pulsed excitation source is split into two paths: one produces the START signal via the PMT, while the other excitation pulse excites the sample. Fluorescence photons from the sample provide STOP pulses. The TAC converts the time delay between START and STOP into a voltage signal, which is digitized by an analog-to-digital converter (ADC) and accumulated in the MCA as a histogram. Repeated cycles generate a complete decay profile. Data analysis, including deconvolution with the IRF and lifetime fitting, has been performed using the Edinburgh F980 software package.

2.4.3.2. Broadband Pump-Probe Femtosecond Transient Absorption Spectroscopy

Photoinduced relaxation in molecules generally occurs through both radiative and non-radiative pathways. Techniques such as time-correlated single-photon counting (TCSPC) primarily provide information about radiative decay processes. However, to obtain a complete picture of the excited-state relaxation, it is essential to investigate both radiative and non-radiative channels. Transient absorption (TA) spectroscopy is particularly suitable for this purpose, as it monitors changes in absorption following photoexcitation and therefore provides insight into charge-carrier dynamics. Femtosecond transient absorption (TA) spectroscopy is a widely used technique in modern photochemistry and photophysics. Ultrafast spectroscopy employs extremely short laser pulses to monitor and manipulate the evolution of physical processes in real time. Phenomena such as carrier–carrier scattering, carrier–phonon interactions, charge-carrier relaxation, recombination, and charge separation occur on ultrafast

timescales, and their lifetimes can be determined using time-resolved ultrafast spectroscopic methods.

In a typical transient absorption experiment, an excitation or pump pulse promotes a small fraction of atoms or molecules, generally between 0.1% and a few tens of percent, depending on the material, into an electronically excited state. A second, relatively weak probe pulse then passes through the sample after a controlled time delay (τ) with respect to the pump. The difference between the probe absorption in the presence and absence of the pump, measured over a broad spectral range, reveals information about the structural and electronic changes induced in the sample. By systematically varying the pump–probe delay (Shown in Scheme 2.2) and recording the corresponding changes in absorbance, one can map out the dynamical processes occurring within the material.

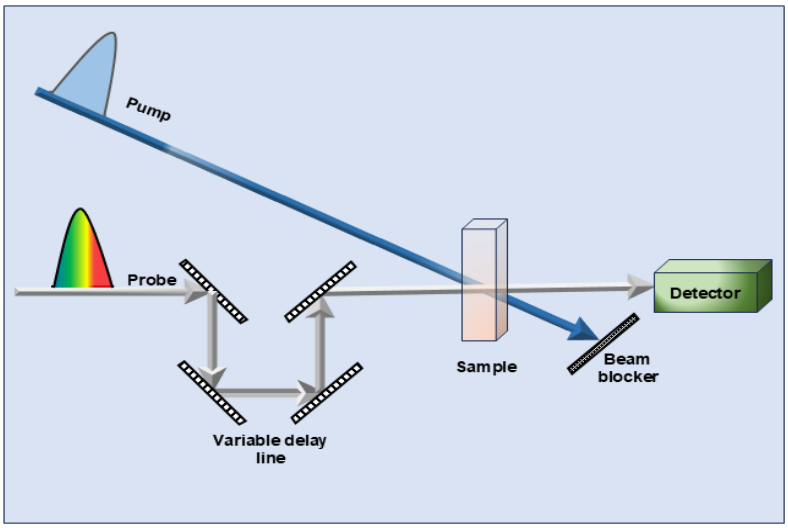

Scheme 2.2. Schematic diagram of basic pump-probe interaction in TAS

2.4.3.2.1. Components of the TAS Setup

In this work, the Astrella amplified laser system is used, which integrates an ultrafast oscillator, regenerative amplifier, Q-switched pump laser, synchronization and delay units, and a stretcher–compressor setup. A closed-loop water chiller (set at 20 °C) cools the Vitara,

Revolution, and amplifier modules to ensure stable long-term operation. Basic schematic of TAS is shown in Scheme 2.3. where all the components have been discussed below-

a) **Ti: Sapphire Oscillator** The Ti: Sapphire (Ti-S) crystal is pumped by a 532 nm VITARA-G diode-pumped solid-state (DPSS) laser operating in continuous wave mode. At high pump intensities, the refractive index of Ti: Sapphire becomes intensity-dependent[8-10]

$$n = n_0 + n_2 I \qquad (2.6)$$

Since n_2 is positive, the medium behaves like a lens, focusing the beam toward its center.

b) **Amplifier** The femtosecond pulses from the oscillator are too weak for TA experiments and must be amplified. To prevent optical damage during amplification, the pulses are first stretched to ~100 ps (chirped pulse amplification) and then amplified.

c) **Multistage Amplification** Amplification occurs in two stages: a regenerative amplifier followed by a multipass amplifier. Both stages use Ti: Sapphire as the gain medium.

d) **Pulse Compressor** After amplification, the pulses are compressed using a pair of diffraction gratings that introduce negative dispersion, shortening the pulse to ~50 fs. The high peak power of the compressed pulse enables nonlinear optical processes, such as second harmonic generation and white-light continuum generation.

e) **Second Harmonic Generation (400 nm Pump)** Second harmonic generation (SHG) of the 800 nm beam is achieved using a β-barium borate (BBO) crystal. SHG arises from the second-order nonlinear polarization[8-10]

$$P = \varepsilon_0 \chi^{(1)} E + \varepsilon_0 \chi^{(2)} E^2 + \cdots \qquad (2.7)$$

The second-order term generates light at twice the frequency (half the wavelength).

Efficient SHG requires phase matching, which is achieved in birefringent crystals such as BBO. Optical Parametric Amplifier (OPA)

After amplification, the Astrella output is split into pump and probe beams. The pump is directed into the OPA-NIRVIS two-stage optical parametric amplifier, which comprises pump-delivery optics, a white-light continuum generator (WLG), and two pre-amplifier stages (PA1, PA2). All translational and rotational stages are computer-controlled, allowing precise wavelength tuning over a broad range (Scheme 2.3).

OPA operation is based on the nonlinear interaction of an intense pump photon ($\hbar\omega_p$) with the crystal, producing signal ($\hbar\omega_s$) and idler ($\hbar\omega_i$) photons from conservation of energy $\omega_p = \omega_s + \omega_i$ and the momentum conservation phase matching is $k_p = k_s + k_i$

A white-light continuum is generated from the 800 nm pump and overlapped with a portion of the pump pulse inside the nonlinear crystal for parametric amplification. After amplification, signal, pump, and idler beams are separated geometrically, and the signal beam is recollimated and passed to the second amplification stage. Moreover, wavelength tuning is achieved by adjusting the delay stage and phase-matching angle. Additional mixers extend the tuning range, enabling second- and fourth-harmonic generation using Type-I BBO crystals. In this work, a LIGHT CONVERSION OPA with a tuning range of 260–2600 nm is used.

The output of the Astrella amplifier is split into pump and probe beams (90:10) using a beam splitter. The probe beam enters the Helios Fire transient absorption spectrometer through an adjustable pinhole. The optical layout of the Helios Fire setup is shown in Scheme 2.3. The system includes a fast delay stage, a broadband probe generation unit, detection modules, and a pump chopper. The probe continuum (350–1600 nm) is generated by focusing the 800 nm pulse onto nonlinear crystals to produce white light (Figure 2.14). The crystal stage holds CaF_2 (UV), Ti:Al_2O_3 (visible), and an IR crystal for NIR generation, all computer-controlled for selecting the probe region. Detection is performed through fiber-coupled spectrographs . Two

detectors are used: a CMOS UV–Vis detector and an InGaAs NIR detector. Data acquisition is handled by Helios Fire software and analysis by Surface Explorer.

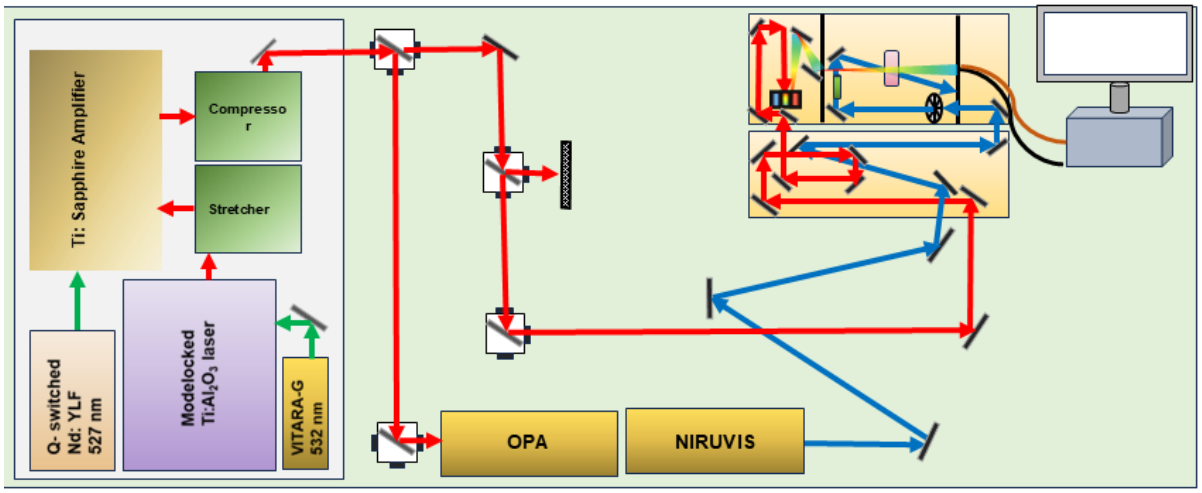

Scheme 2. 3. Basic schematic of TA Spectrometer

2.4.3.2.2. Origin of Transient Signals in a TA Spectrometer When light passes through any absorbing material, its absorption follows the Beer–Lambert law

$$A = \log\left(\frac{I_0}{I}\right) = \varepsilon(\lambda)\, c\, L \qquad (2.8)$$

Where ε(λ) is the molar absorption coefficient, c is the concentration of the sample, and L is the optical path length. In transient absorption spectroscopy, two laser pulses are used: one is a Pump, and the other is a probe pulse. The pump pulse excites the sample to higher energy states, and the probe pulse measures how the excited sample behaves at a certain time. The probe pulse is detected both: without the pump, and with the pump at different time delays (Δt). The difference in probe absorption gives the transient absorption signal (ΔA)[8-11]

$$\Delta A = A_{\text{with pump}} - A_{\text{without pump}} \qquad (2.9)$$

The intensity of the probe pulse at delay time Δt can be written as[8-11]

$$I(\lambda, \Delta t) = I_0(\lambda)\, 10^{-\varepsilon(\lambda)\, N(\Delta t)\, L} \qquad (2.10)$$

Here, N(Δt) is the excited-state population at time Δt. So, the transient signal becomes[8-11]

$$\Delta A(\Delta t) = \varepsilon(\lambda)\, N(\Delta t)\, L \qquad (2.11)$$

And the decay of the excited-state population decreases exponentially according to the equation

$$N(\Delta t) = N_0 e^{-\Delta t/\tau} \qquad (2.12)$$

where N_0 is the initial population and τ is the lifetime, then[8-11]

$$\ln\left[\Delta A(\Delta t)\right] = \ln\left(\varepsilon N_0 L\right) - \frac{\Delta t}{\tau} \qquad (2.13)$$

This shows that the change in ΔA with time directly gives the excited-state decay.

So the basic TA signal expression

The absorbances with pump, $A_{\text{with pump}} = \log\left(\frac{I_0}{I(\Delta t)}\right)$, and without pump $A_{\text{without pump}} = \log\left(\frac{I_0}{I}\right)$. So the transient absorption giving by the equation

$$\Delta A = \log\left(\frac{I}{I(\Delta t)}\right) \qquad (2.14)$$

2.4.3.2.3. Types of TA Signals

Depending on the sign of ΔA, different signals appear shown in Scheme 2.4

- **Negative Signal — Ground-State Bleach (GSB) / Stimulated Emission (SE)**

ΔA < 0 when $I(\lambda, \Delta t) > I(\lambda)$ This means the probe is less absorbed after pump excitation. There are three reason behind the negative signal- (i) Pump empties the ground state (ii)Probe experiences less absorption and (iii)Stimulated emission may also increase probe intensity.

- **Positive Signal — Photoinduced or Excited-State Absorption (PIA/ESA)**

Photoinduced or Excited-State Absorption (PIA/ESA) appears when ΔA>0, i.e. $I(\lambda, \Delta t) < I(\lambda)$ i.e., the probe is more absorbed due to excited-state transitions created by the pump.

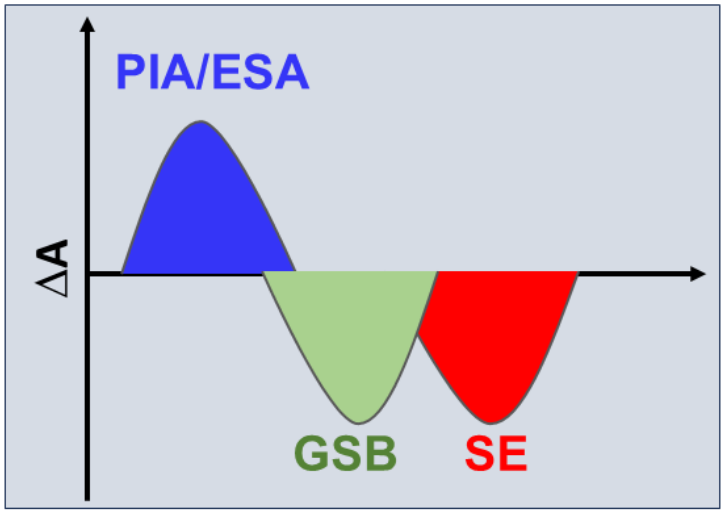

Scheme 2.4. Schematic of different types of signals produced in TAS

2.4.3.2.4. Data Analysis in Our Setup

The collected TA data were analysed using Surface Explorer (SX) software. The SX software can display transient spectra and kinetics, generate 3D contour plots, correct artifacts (background, scattering, chirp, time zero, etc.), and also perform SVD and global analysis. For kinetic fitting, SX uses a sum of Gauss-convoluted exponential decay functions[8-11]

$$S(t) = e^{-((t-t_0)/t_p)^2} \sum_i A_i e^{-(t-t_0)/\tau_i} \qquad (2.15)$$

where, t_p = IRF / (2 \ln 2). IRF (50–100 fs) is the instrument response and sets the time resolution and t_0 is the pump–probe overlap point (time zero). A_i and τ_i are the amplitudes and lifetimes of different decay components. By optimizing these parameters, the best fit for the decay curve is obtained.

2.4.3.3. Time-Resolved Confocal Fluorescence Microscopy

Optical microscopes are essential tools for visualizing microscopic objects, and the clarity of the observed images strongly depends on the instrument's resolution. This resolution is governed by factors such as the excitation wavelength and the numerical aperture of the objective lens. By modifying the excitation source or altering the microscope configuration, one can optimize the resolution for specific requirements.

Confocal Fluorescence Microscopy (CFM) offers distinct advantages, particularly its high temporal resolution, which can reach the nanosecond scale. The use of multiple pinholes in the detection pathway enables the collection of only in-focus light, thereby defining a precise confocal volume. Scheme 2.5 illustrates the layout of a typical time-resolved confocal microscope. In this thesis, all confocal fluorescence measurements were conducted using the PicoQuant MicroTime 200 system. The excitation source was a picosecond pulsed diode laser operating at 403 nm with an adjustable repetition rate between 1 and 80 MHz. The laser output was delivered to the main optical unit through a polarization-maintaining single-mode fiber and directed into an inverted microscope (Olympus IX71) via a dichroic mirror. A 60× water-immersion objective (UPlanSApo, NA 1.2) was used for focusing.

Samples were mounted on coverslips, and their precise positioning was controlled with a piezo scanning stage integrated into the microscope body. Manual coarse adjustments were accomplished using micrometer screws, while software-controlled piezo movements enabled accurate and repeatable XY scanning and Z-axis focusing. A CCD camera monitored the focal point on the sample during alignment. The emitted fluorescence was collected by the same objective, passed through the dichroic mirror, and focused onto a 50 μm pinhole to remove out-of-focus light. The transmitted signal was then re-collimated and directed to single-photon avalanche photodiodes (SPADs). Depending on the experiment, either single or multiple SPAD detectors were employed. Data were processed using the PicoHarp 300 Time-Correlated Single Photon Counting (TCSPC) module in time-tagged time-resolved (TTTR) mode through the SymPhoTime software package.

This setup enabled time-resolved confocal fluorescence measurements, including Fluorescence Correlation Spectroscopy (FCS) and Fluorescence Lifetime Imaging (FLIM), which are described below.

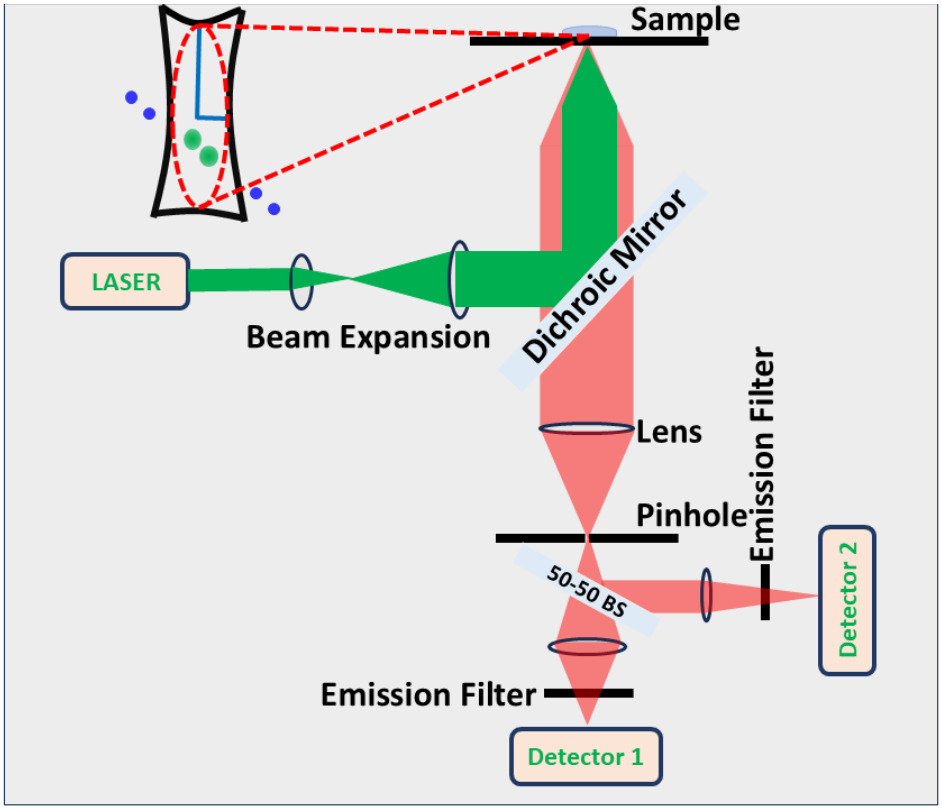

Scheme 2.5. Schematic of Time-resolved confocal fluorescence microscope setup.

2.4.3.3.1. Fluorescence Correlation Spectroscopy (FCS)

Fluorescence Correlation Spectroscopy is a non-invasive method that analyzes fluctuations in fluorescence intensity to gain insight into dynamic processes occurring at the molecular level. In a confocal setup, fluorophores diffusing through the confined excitation volume produce time-dependent intensity variations. These fluctuations may result from events such as molecular binding, translational or rotational diffusion, or other excited-state processes.

To detect these fluctuations effectively, the number of fluorescent species within the confocal volume must be small; hence, measurements are typically performed at nanomolar concentrations to achieve single-molecule sensitivity. The collected intensity traces are mathematically correlated to generate autocorrelation curves. Because FCS relies on stochastic diffusion events, the detected signals follow Poisson statistics.

Scheme 2.6 illustrates the diffusion of a fluorophore through the ellipsoidal confocal volume.

Cross-correlation of signals recorded from two detectors further improves temporal resolution and enhances the signal-to-noise ratio in FCS experiments.

The autocorrelation function $G(\tau)$ is defined as the time-averaged product of the fluorescence intensity fluctuations $\delta F(t)$and $\delta F(t+\tau)$, as shown in Equation[6]

$$G(\tau) = \frac{\langle \delta F(t)\, \delta F(t+\tau) \rangle}{\langle F(t) \rangle^2} \tag{2.16}$$

where $\delta F(t)$and $\delta F(t+\tau)$are given by:

$$\delta F(t) = F(t) - \langle F(t) \rangle \tag{2.17}$$

$$\delta F(t+\tau) = F(t+\tau) - \langle F(t) \rangle \tag{2.18}$$

For purely diffusive motion in three dimensions, the autocorrelation function takes the form shown in Equation:

$$G(\tau) = \frac{1}{N}\left(1 + \frac{\tau}{\tau_D}\right)^{-1}\left(1 + \frac{\tau}{\kappa^2 \tau_D}\right)^{-1/2} \tag{2.19}$$

Here,

- ✓ N= average number of fluorophores in the confocal volume
- ✓ τ_D= diffusion time
- ✓ $\kappa = \frac{\omega_z}{\omega_{xy}}$= structural parameter of the confocal volume

The diffusion coefficient D is obtained from:

$$D = \frac{\omega_{xy}^2}{4\tau_D} \tag{2.20}$$

The hydrodynamic radius R_h of the fluorophore is then calculated using the Stokes–Einstein relation[6]

$$R_h = \frac{k_B T}{6\pi\eta D} \tag{2.21}$$

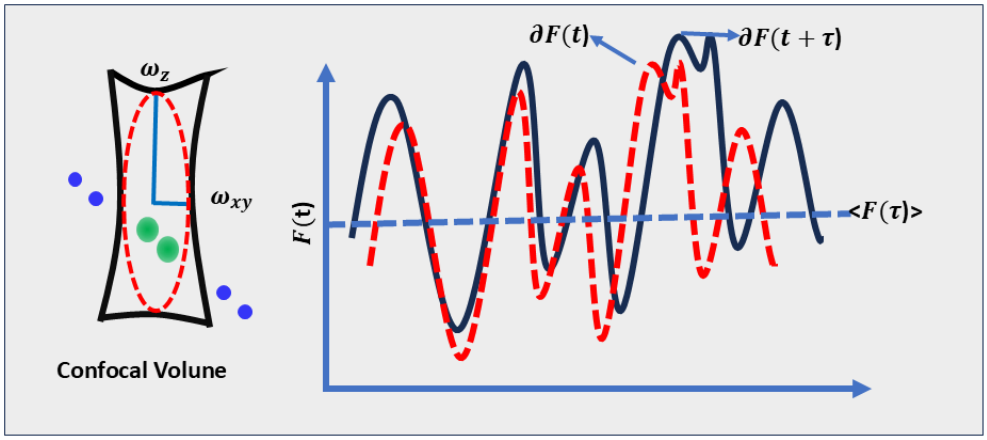

Scheme2.6. Scheme illustrates the diffusion of a fluorophore through the ellipsoidal confocal volume.

2.4.3.3.2. Fluorescence Lifetime Imaging (FLIM)

Using the TTTR mode of the confocal setup, fluorescence lifetime imaging can also be performed without altering the optical configuration. By scanning the sample in two dimensions with the piezo stage, spatially resolved photon arrival data are acquired alongside TCSPC information. The fluorescence lifetime at each pixel is determined from the detected photon distribution, enabling construction of a lifetime map.

FLIM provides valuable insight into spatial variations in the photophysical environment of fluorophores. It directly connects structural or morphological features with fluorescence intensity and lifetime, making it particularly useful for studying heterogeneous nanomaterial systems.

2.4.4. Nuclear Magnetic Resonance (NMR) spectroscopy

All the NMR measurements were carried out on a 9.4 T Bruker Avance NMR spectrometer with400.1 MHz Larmor frequencies for H^1

The self-diffusion coefficient of imidazolium base cation has been determined using a pulse field gradient (PFG) NMR technique. A stimulated echo bipolar pulse-gradient pulse (stebpgp) sequence has been applied with a maximum gradient pulse strength of 50 G/cm. The echo heights have been attained by varying the gradient pulse strength from 2 to 95% at 16 equal

intervals. The echo heights have been fitted using Stejskal−Tanner equation, which is given below[12]

$$S(g) = S(0)exp^{[-D\gamma^2\delta^2g^2\left(\Delta-\delta/3\right)]} \quad (2.22)$$

Where S(g) and S(0) are the echo height at the gradient strength g and 0, respectively. γ and δ are the gyromagnetic ratio of the proton and gradient pulse length, respectively, while Δ is the duration between the two gradient pulses.

2.4.5. Dynamic Light Scattering

Dynamic Light Scattering (DLS) is an analytical technique widely used to determine the size distribution and zeta potential of nanomaterials. It provides important information about the colloidal behavior of nanoparticles, which is essential for optimizing their use in areas such as drug delivery, nanomedicine, and materials synthesis. By monitoring the time-dependent fluctuations in scattered light, DLS helps characterize the dynamic properties of nanoparticles and assess how they interact with different analytes. This understanding is critical for the rational design and development of nanomaterial-based systems.

In this thesis, a Malvern Zetasizer instrument has been employed to measure the zeta potential of nanomaterials both in the absence and presence of the analytes under investigation.

2.4.5. X-ray Diffraction (XRD)

X-rays are electromagnetic waves with wavelengths around 1 Å, comparable to the spacing between crystal lattice planes, making them suitable for studying crystal structures. When a monochromatic X-ray beam strikes a crystal, it undergoes elastic scattering (shown in Scheme 2.7). Because electrons are unevenly distributed within the lattice, the scattered waves interfere with one another.

W. L. Bragg provided a simple description of this diffraction process by assuming elastic scattering from parallel lattice planes. Constructive interference, and thus observable diffraction peaks, occurs when the Bragg condition is satisfied[13-14]

$$2d\sin\,\theta = n\lambda \qquad (2.23)$$

Here, d is the interplanar spacing, λ is the X-ray wavelength, and θ is the incident angle. Typically, only the first-order diffraction ($n = 1$) is considered.

The peak position in an XRD pattern gives structural information, while its width, measured by the full width at half maximum (FWHM) reflects crystallite size and structural disorder. For cubic crystals, the interplanar spacing d_{hkl} relates to lattice parameter $a$through[13-14]

$$d_{hkl} = \frac{a}{\sqrt{h^2+k^2+l^2}} \qquad (2.24)$$

Nanocrystals generally produce broader diffraction peaks due to their small size. The crystallite size can be estimated using the Scherrer equation[13-14]

$$x = \frac{K\lambda}{\beta\cos\,\theta} \qquad (2.25)$$

where x is the particle size, $K$is the shape factor, and β is the FWHM. Final structural identification is achieved by comparing the experimental pattern with reference data from the Joint Committee on Powder Diffraction Standards (JCPDS).

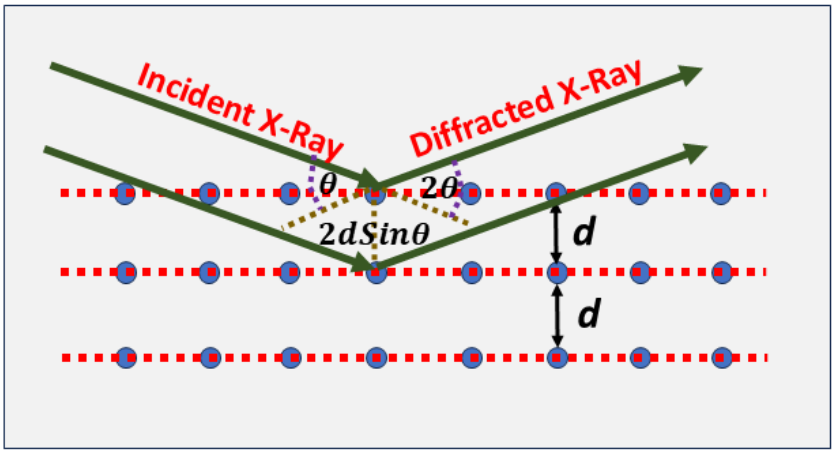

Scheme 2.7. Schematic depiction of the Bragg condition. The incident X-ray beam strikes the lattice plane at an angle θ, and the reflected beam emerges at the same angle, producing constructive interference when the Bragg equation is satisfied.

2.5. Standard Error Limit

Table 2.1. Standard error limits involved in the experimental results are

Experimental Parameter	Error
λ_{max} (abs./flu.)	±1-2 nm
QY	±2
τ_f (> 1ns)	±5%
The energy transfer rate	±5%
Diffusion coefficient (through FCS)	±5-10%

2.6. References

1. Protesescu, L.; Yakunin, S.; Bodnarchuk, M. I.; Krieg, F.; Caputo, R.; Hendon, C. H.; Yang, R. X.; Walsh, A.; Kovalenko, M. V. Nanocrystals of Cesium Lead Halide Perovskites ($CsPbX_3$, X = Cl, Br,and I): Novel Optoelectronic Materials Showing Bright Emission with Wide Color Gamut. *Nano Lett.* **2015**, *15*, 3692−3696.
2. Seth, S.; Samanta, A. Photoluminescence of Zero-Dimensional Perovskites and Perovskite-Related Materials. *J. Phys. Chem. Lett.* **2018**, *9*, 176−183.
3. Sahu, P. K.; Das, S. K.; Sarkar, M. Fluorescence response of a dipolar organic solute in a dicationic ionic liquid (IL): is the behavior of di-cationic IL different from that of usual monocationic IL? *Phys. Chem. Chem. Phys.* **2014**, *16*, 12918-12928.
4. Vaishanav, S. K.; Korram, J.; Nagwanshi, R.; Karbhal, I.; Dewangan, L.; Ghosh K. K.; Satnami, M. L. Interaction of Folic Acid with Mn2+ Doped CdTe/ZnS Quantum Dots: In Situ Detection of Folic Acid. *J Fluoresc* **2021**, *31*, 951-960.
5. Rohatgi-Mukherjee, K. Fundamentals of Photochemistry. *New Age International*, **1978**.
6. Lakowicz, J. R., Principles of Fluorescence Spectroscopy. *Springer*, **2006**.
7. Berberan-Santos, B. V. a. M. N., Molecular Fluorescence: Principles and Applications. John *Wiley & Sons*, **2012**.

8. Diels, J.C.; Rudolph, W. Ultrashort Laser Pulse Phenomena. Fundamentals, Techniques, and Applications on a Femtosecond Time Scale. Academic Press, London, **1996**.

1. Kafka, J.D.; Watts, M.L.; Pieterse J.W.J. Picosecond and Femtosecond Pulse Generation in a Generatively Mode-Locked Ti: Sapphire Laser, IEEE J. Quant. Electron. **1992**, 28, 2151.

2. Abramczyk, H. Introduction to Laser Spectroscopy. Elsevier, **2005**.

3. Berera, R.; van Grondelle, R.; Kennis, J. T. M. Ultrafast Transient Absorption Spectroscopy: Principles and Application to Photosynthetic Systems. Photosynth. Res. **2009**, 101, 105–118.

4. Stejskal, E. O.; Tanner, J. E. Spin Diffusion Measurements: Spin Echoes in the Presence of a Time-Dependent Field Gradient. *J. Chem. Phys.***1965** *42*, 288–292.

5. Bragg, WL. The Specular Reflexion of X-rays. Nature, **1912**, 90 2250, 410.

6. Scherrer, P. Determination of the internal structure and size of colloidal particles by means of X-rays. In: Colloid Chemistry A Textbook. Chemical technology in single representations. Springer, Berlin, Heidelberg, **1912**.

CHAPTER 3

Surface Modification of $CsPbX_3$ (X = Cl and Br) Nanocrystals by Treatment with Imidazolium-Based Ionic Liquids in Enhancing the Stability and Photoluminescence Quantum Yield

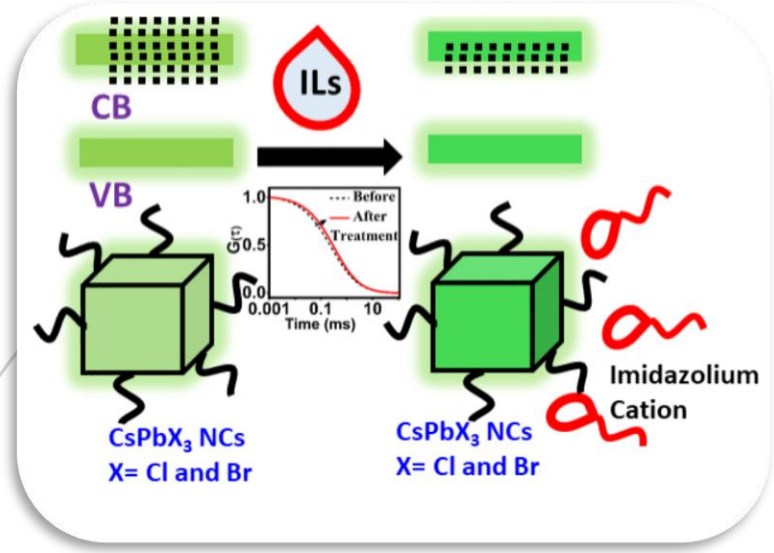

Abstract

Even though perovskite nanocrystals (PNCs) are quite attractive for optoelectronic applications, issues such as low photoluminescence quantum yield (PLQY) and poor chemical stability of PNCs still remain a formidable challenge that needs to be tackled. Since ionic liquids (ILs) possess some interesting physicochemical properties, the present study is undertaken to find out the suitability of ILs in obtaining stable and defect-free PNCs. To explore this possibility, the interaction of ILs with PNCs has been investigated by both spectroscopy and microscopy. Studies have demonstrated that a significant enhancement in the PLQY of PNCs can be obtained after post-synthetic treatment of PNCs with chosen ILs. Analysis of time-resolved fluorescence studies, XPS, and IR data has suggested that ILs help in removing excess lead from the surface of PNCs. Interestingly, it has also been observed that the chemical stability of PNCs can be increased considerably in the presence of ILs. More interestingly, the investigations have further shown that IL-treated PNCs are stable even at the single particle level. The outcomes essentially show that ILs can effectively be used in obtaining the chemical and photo-stable PNCs having improved Photophysical properties.

3.1. Introduction

In recent times, all-inorganic lead halide perovskite ($CsPbX_3$; X = Cl, Br, or I) nanocrystals (PNCs) have attracted considerable attention from both academia and industry owing to their striking optoelectronic properties like broad absorption, high photoluminescence quantum yield (PLQY) with narrow band width.[1-6] Along with these interesting properties, they also possess high defect tolerance capability and band gap tunability, which have opened up applications for $CsPbX_3$ NCs as bright emitters in the visible spectral region and as an efficient photovoltaic system having high power conversion efficiency (PCE).[7-14] However, in case of

PNCs, it is also known that the optical properties of these systems are highly sensitive towards the synthetic condition and its composition, which causes low photoluminescence quantum yield (PLQY) in case of PNCs.[15-19] Very often defects are created during the synthetic procedure and there by act as trap states for charge carriers (electrons and holes) and lower the radiative decay of PNCs.[20-22] The multiexponential photoluminescence decay kinetics of these materials are also a clear indication of defects,[23-30] which might be due to their intrinsic nature[31-33] or surface modifications.[34] Due to the high surface-to-volume ratio of PNCs, the major contribution of the defects in PNCs comes from the surface.[35,36] This issue lowers the PLQY of PNCs, which causes a significant barrier in terms of their application in optoelectronic and photovoltaic domains.

Previously, several attempts have been made to improve the PLQY of PNCs through surface treatment by employing various methods that are based on chemical treatments.[25,37-42] These surface modifications have been done basically in two ways, one through pre-synthetic treatment[37,38] and the other through post-synthetic treatment.[25,39-42] It has been observed that the emission of $CsPbCl_3$ NCs, which usually exhibit low PLQY, can be improved when the halide precursor is changed during the hot-injection synthetic method.[43] Moreover, Several groups have also shown an enhancement in PLQY of $CsPbBr_3$ NCs by simply treating Na/NH_4 thiocyanate salts,[25] lead bromide,[41] tetrafluoroborate salts,[29] didodecyldimethylammonium bromide,[39] metal halides,[37,41,] and didodecyldimethylammonium sulfide.[40] Hence, it is very important to obtain defect-free PNCs through surface treatment using appropriate reagents. In this context, ionic liquids (ILs), being a designer solvent, are expected to be an attractive candidate to obtain PNCs having improved PLQYs and chemical stability.

ILs possess unique physicochemical properties such as low vapour pressure, high viscosity, high thermal stability, good ionic conductivity, high electrochemical stability etc.[44-46] which serves in different chemical, biological and industrial applications like photovoltaics,

catalysis, batteries, telescopes, separation of chemicals etc.[46,47] Since ILs have been known as a combination of cations and anions, and these combinations can be done by changing either the cations or anions or both. Therefore, an IL with desired properties can be designed for a particular application by employing proper cation-anion combinations.[47] It has been found that efficiency and stability of the perovskite solar cell device can be improved by tuning the crystallization kinetics of the perovskite active layer and providing high hydrophobicity through ILs treatment.[48-50] Along with this, thermal and electrochemical stability and high ionic conductivity of ILs have shown a tremendous effect on the photovoltaic performance of the perovskite devices.[49,51] Moreover, recently, some ILs have been found to be suitable for surface passivation on perovskite materials.[51-53] These ILs have been incorporated in the perovskite precursor, and this has helped to improve the PCE by reducing charge recombination.[54] This discussion have pointed out that even though ILs are found to be effective in PCE and SCE (solar conversion efficiency) but such studies are very limited. Moreover, studies that are carried out by focusing on improving PLQYs of PNCs by using ILs are elusive. More importantly mechanism of interaction between PNCs and ILs is also not properly known. Therefore, it will be interesting to look at the outcomes of the interaction of PNCs with ILs, which eventually can be helpful in developing defect-free and stable perovskite NCs for photonic devices and energy-related applications.

Keeping all the above facts in mind, the present work has been carried out to understand the mechanism of interaction of PNCs that are stable and free from defects using post-synthetic treatment of selected ILs. The current set of ILs (1-ethyl-3-methylimidazolium tetrafluoroborate ($EMIMBF_4$), 1-ethyl-3-methylimidazolium acetate (EMIMOAc), 1-ethyl-3-methylimidazolium methanesulfonate (EMS), 1-butyl-3-methylimidazolium tetrafluoroborate ($BMIMBF_4$), and 1-hexyl-3-methylimidazolium tetrafluoroborate ($HMIMBF_4$)) are purposefully chosen keeping in mind the fact that these ILs can participate in interaction with

Pb adatoms (due to the presence of BF_4^-,$CH_3COO^-$and $CH_3SO_3^-$ anions) and thereby, can help in removing the defects, which is caused by the presence of Pb (0) nanoparticles and Pb adatoms on the surface of PNCs.[29] Moreover, these sets of ILs are also known to form a protective layer on PNCs.[51] Here, both steady state and time-resolved fluorescence measurements of PNCs have been performed in the presence and absence of ILs. The molecular structures of the above-mentioned ILs have been represented in Chart 3.1. Mechanism of interaction between PNCs and ILs has been further investigated by IR, XPS and NMR techniques. The outcomes of these studies show that the chemical and photostability of PNCs in the presence of ILs can be improved both at the ensemble average and single molecular level studies.

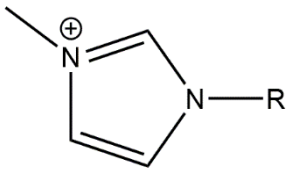

Imidazolium based cation.
R = Ethyl, Butyl, Hexyl

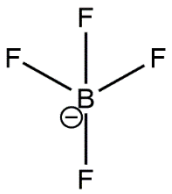

Tetrafluoroborate anion

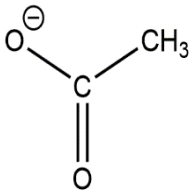

Acetate anion

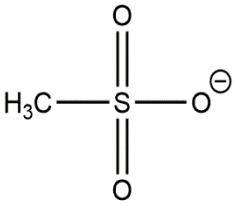

Methanesulphonate anion

Chart 3.1. Molecular structures of ILs

3.2. Results and Discussion

In the present work, we have synthesized colloidal PNCs through hot injection synthetic method following a reported procedure with minor modifications[43] (see experimental section). The synthesized $CsPbX_3$ NCs have been characterized using microscopic techniques (transmission electron microscopy-TEM), and their surface morphology has been shown in Figure APX3.1. The TEM image in Figure APX3.1 shows that $CsPbCl_3$ NCs have a regular cubic morphology, with an average edge length of ~9.1 nm (size distribution of this monodisperse solution has been shown in the inset of Figure APX3.1. The high-resolution

TEM (HR-TEM) images in Figure APX3.1 show a lattice spacing of 0.57 nm for the (100) plane for $CsPbCl_3$, and from selected area electron diffraction (SAED) (Figure APX3.1) it has been found that there exist different types of lattice planes in $CsPbCl_3$ NCs. Similarly, in the case of $CsPbBr_3$, the TEM image also shows a cubic morphology with an edge length of ~9.5 nm (Figure APX3.1) and lattice spacing of 0.58 nm for the (100) plane. However, upon magnification, we have observed the poly-crystalline planes (Figure APX3.1), which indicated the crystallinity of the NCs, and this has been further substantiated by the SAED image (Figure APX3.1). The crystal structures of these materials have also been analysed with powder XRD measurement, as shown in Figure APX3.2. Typically the diffraction planes of (100), (110), (200), (211), (220) for $CsPbCl_3$ NCs, (100), (110), (111), (200), (211) for $CsPbBr_3$ NCs and (012), (021), (120), (022), (200) etc. for $CsPbI_3$ NCs can be clearly observed, indicating that $CsPbCl_3$ and $CsPbBr_3$ NCs are in cubic phase and $CsPbI_3$ NCs in orthorhombic phase.

In order to analyze the basic optoelectronic properties of synthesized NCs, steady-state optical measurements have been performed. The UV-visible absorption and fluorescence spectra of PNCs are shown in Figure APX3.3. It is to be noted that the band gap of this material can be tuned by changing the halide anion.[43,55] In the absorption spectral profiles for the NCs, the peaks at 394 nm, 476 nm, and 660 nm correspond to the excitonic peak of $CsPbCl_3$, $CsPbBr_3$, and $CsPbI_3$ NCs, respectively.[4,43,55] In case of PL measurements (Figure APX3.3), the peaks for $CsPbCl_3$, $CsPbBr_3$, and $CsPbI_3$ NCs are observed at 406 nm, 503 nm, and 687 nm, respectively. The significant red shift in the emission maxima on going from $CsPbCl_3$ to $CsPbI_3$ can be attributed to the lowering of the band gap due to a change in the halide ions of the concerned materials. It implies that as the size of the halide ion increases, the energy band gap decreases and thus the wavelength increases. We also note here that the full-width at half maxima (FWHM) for the PNCs are estimated to be 14 nm, 20 nm, and 30 nm for $CsPbCl_3$, $CsPbBr_3$, and $CsPbI_3$, respectively. The calculated PLQYs of as-synthesized $CsPbCl_3$, $CsPbBr_3$,

and $CsPbI_3$ NCs are found to be low and measured to be ~11%, ~22% and 40% respectively. This low PLQY of PNC indicates the presence of defect states in these perovskite NCs.[15-19] As discussed earlier, ILs are expected to be helpful in enhancing the stability and PLQY of PNCs, we have carried out post-synthetic treatment of PNCs with several ILs. During the investigations, ILs have been chosen with various anions, keeping the cation (imidazolium) fixed so that the effect of anions on the photophysics of the PNCs can be understood clearly. In order to know the role of cation, if any, on the photophysics and stability of PNCs the alkyl chain length of the imidazolium moieties are also varied. During the experiments, the solution of ILs in chloroform has been directly added into various PNC solution. The mixtures are stirred at 25^0C and are analysed further through microscopy and spectroscopy.

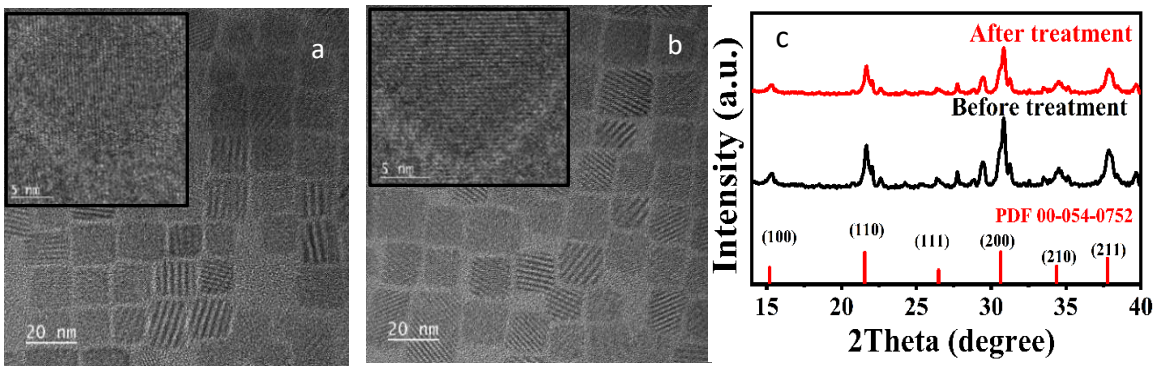

Figure 3.1. TEM image of $CsPbBr_3$ PNCs (a) before and (b) after treatment of ILs. (c) Powder X- ray diffraction patterns of $CsPbBr_3$ PNCs before and after treatment of ILs (Inset of (a) and (b) shows the HRTEM image of their respective samples).

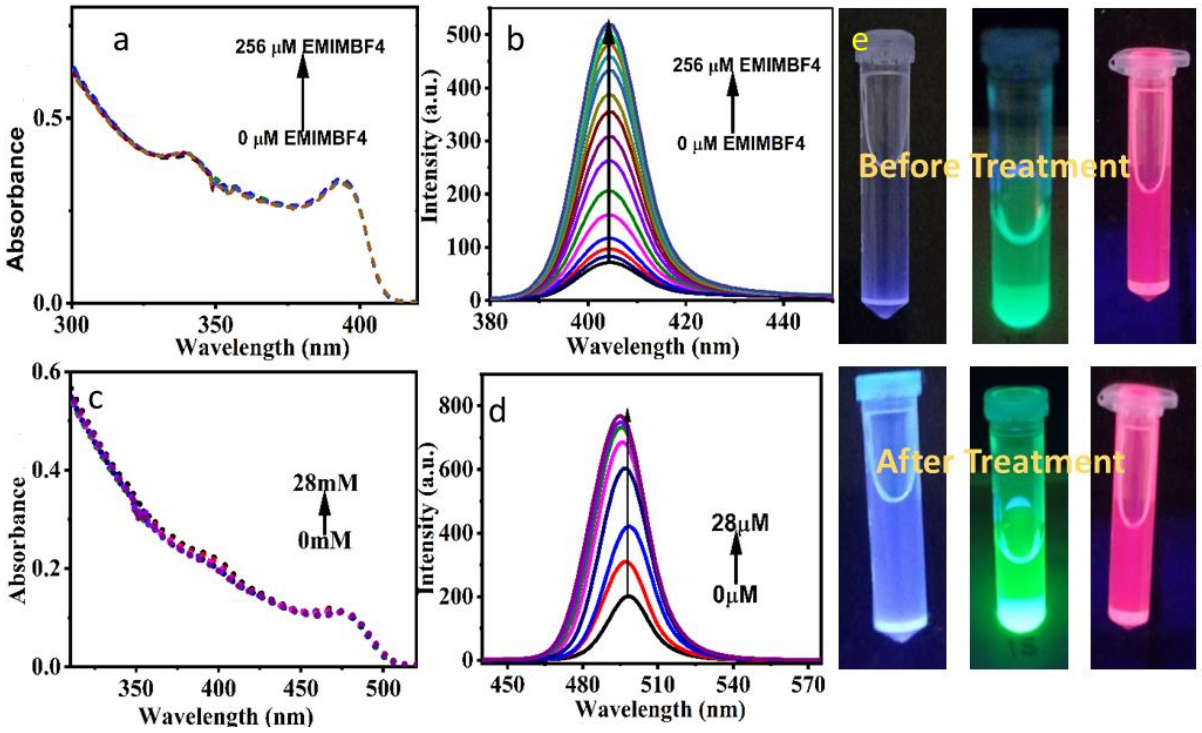

Figure 3.2. (a) Absorption and (b) emission spectra of $CsPbCl_3$ PNCs with gradual addition of $EMIMBF_4$ (c) Absorption and (d) emission spectra of $CsPbBr_3$ PNCs with gradual addition of $EMIMBF_4$ (e) Photographs of colloidal solutions of PNCs (blue-$CsPbCl_3$, green-$CsPbBr_3$, and red-$CsPbI_3$ NCs solution) before and after treatment with ILs.

TEM micrograph of various PNCs are shown in Figure 3.1 and Figure APX3.1. As can be seen from the figures, the size of the $CsPbBr_3$ NCs remains unchanged (Figure 3.1) before and after the treatment of PNCs with ILs. Moreover, the HR-TEM image (inset of Figure 3.1) has revealed no change in the lattice spacing (0.58 nm) for (100) plane of $CsPbBr_3$ NCs before and after the treatment with ILs. The PXRD peak positions of $CsPbBr_3$ are also found to be the same in the absence and presence of ILs. All these results have indicated that the microscopic structure of the PNCs remains intact before and after the treatment with ILs. During optical studies, upon gradual treatment of $CsPbBr_3$ NCs with $EMIMBF_4$ IL, no appreciable change can be observed in the absorption spectrum (Figure 3.2), whereas, in the PL spectrum (Figure 3.2), a ~4-fold enhancement in the PL intensity of the PNC in the presence of IL can be observed. When similar IL treatment is carried out with $CsPbCl_3$ NCs, no change in the absorption but ~8 times increase in the PL intensity of the said PNC after the treatment with $EMIMBF_4$ is

observed (Figure 3.2). However, no significant improvement in the PL intensity of $CsPbI_3$ NCs after treating it with the IL can be observed. These studies have demonstrated that when the PNCs are treated with IL, no change in the shape, size, and crystal structure of PNCs takes place, but the treatment helps in the considerable improvement in the PLQY for $CsPbCl_3$ and $CsPbBr_3$ NCs. For example, the calculation reveals that after treating NCs with $IMIMBF_4$ IL, an increment of PLQY from 20% to 90% for $CsPbBr_3$ and from 11% to 88% for $CsPbCl_3$ has been achieved (Table 3.1). The enhancement of PLQY indicates that the treatment of the $CsPbCl_3$ and $CsPbBr_3$ NCs with IL possibly facilitates in removal of the shallow emissive energy levels (associated with the surface of NCs) from the said PNCs. [23,25,29,30,37,40] The observation also indicates that the lowering of PLQY for $CsPbI_3$ NCs may not be related to the surface defects and thus IL has a negligible effect on its photophysics. The investigations have been carried out further by employing several commonly used ILs having different anions so as to find out whether other types of IL play any role in modulating the PLQY of PNCs (Table 3.1).

Table 3.1. PL peak and QY of the perovskite NCs before and after treatment

Materials	**λ_{max}**	**PLQY(%)**	**Error**
$CsPbCl_3$	406	11	±2
$CsPbCl_3$+$EMIMBF_4$	406	88	±5
$CsPbCl_3$+$BMIMBF_4$	406	80	±1
$CsPbCl_3$+$HMIMBF_4$	406	77	±2
$CsPbCl_3$+EMIMOAc	406	78	±6
$CsPbCl_3$+EMIMMS	406	80	±6
$CsPbBr_3$	503	22	±5

$CsPbBr_3$+$EMIMBF_4$	499	90	±5
$CsPbBr_3$+$BMIMBF_4$	499	82	±5
$CsPbBr_3$+$HMIMBF_4$	499	75	±3
$CsPbBr_3$+EMIMOAc	499	78	±3
$CsPbBr_3$+EMIMMS	499	80	±2
$CsPbI_3$	687	40	±5

In order to know more about the photophysical response of synthesized PNCs, time resolved fluorescence measurements have been performed in the absence and presence of different ILs. Figure 3.3 shows the PL decay curves of $CsPbBr_3$ NCs in the absence and presence of $EMIMBF_4$. The corresponding decay parameters have been collected in Table 3.2. For other systems, the PL decay curves have been represented in Figure APX3.4. It has been observed that the PNCs generally possess multiexponential PL decay components, indicating the presence of multiple radiative de-excitation pathways for the system.[23-30] We note that multiexponential decay behaviour also indicates the involvement of defect/trap states during the overall decay process.[25,29,30] In the absence of ILs, $CsPbCl_3$ and $CsPbBr_3$ NCs individually possess a shorter (0.1 ns and 0.4 ns), intermediate (2.4 ns and 3.6 ns), and longer lifetime component (17.6 ns and 9.9 ns), respectively.[23-25,29] The shorter component has been attributed to the emission from surface trap state, the intermediate one has been attributed to the band edge emission, and the longer decay component has been attributed to shallow trap states.[29] However, when we carefully look at the relative contribution of the individual lifetime components (Table APX3.1) of concern PNCs in absence of ILs, one can find that the relative contribution of the shorter PL decay component is more as compared to the other components, which suggests that most of the charge carrier populates in their respective trap state and the excitonic recombination predominantly happens from this energy state. When the synthesized

PNCs are treated with various ILs, the average lifetime of PNCs increases (Table APX3.1). However, along with this, it is important to consider their individual PL decay components in the absence and presence of ILs that are used in these studies so as to know the mechanistic aspects of PNC-IL interaction. For example, in case of $EMIMBF_4$, when added to the $CsPbBr_3$ NCs solution, shows an increase in the average lifetime from 0.96 ns to 3.69 ns (Table APX3.1) It can be clearly observed from Table APX3.1 that the shorter component which increased from 0.4 ns to 1.0 ns shows a decrease in the relative contribution from 0.85 to 0.34 is mainly caused due to the surface state radiative recombination process. However, in case of the longer component, the lifetime decreases from 17.5 ns to 12.9 ns with no change in the relative contribution. This concomitantly arises due to the shallow trap mediated recombination process. The increase and decrease of the shorter and the longer component of $CsPbBr_3$ NCs in the presence of $EMIMBF_4$ indicate that there is a gradual removal of surface states due to the ground state interactions of the PNCs surface with $EMIMBF_4$ (Table 3.2). Similar observation has been found in case of acetate (CH_3COO^-) and methansulfonate ($CH_3SO_3^-$) anion, the shorter component corresponding to the surface trap state is found to increase with decrease in their relative contribution (Table APX3.1). However, the longer component corresponding to the shallow trap states show a decrease with not much change in the relative contribution in presence of ILs (Table APX3.1). A similar trend has been found in case of $CsPbCl_3$ NCs when it is treated with various ILs (Table APX3.1). When we change alkyl chain length (ethyl, butyl, and hexyl) of cation we have observed not much change in lifetime. It shows that alkyl chain length does not have much effect in PLQY of PNCs. Additionally, it has also been observed that average lifetime as well as lifetime component of $CsPbI_3$ NCs remain unchanged before and after the treatment with ILs, which may be due to the presence of low surface defect and high intrinsic defect states in $CsPbI_3$ NCs.

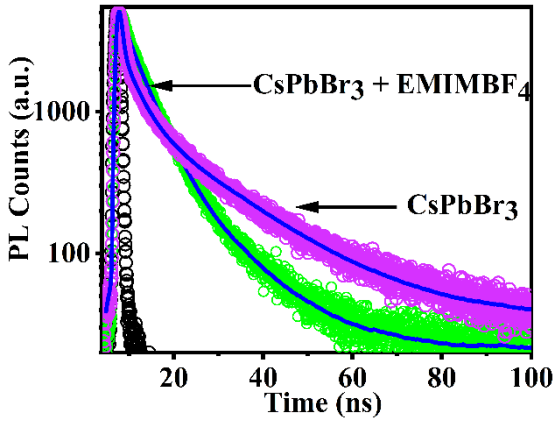

Figure 3.3. PL decay curve of $CsPbBr_3$ NCs before and after treatment with $EMIMBF_4$.

Table 3.2. PL Decay Parameters of $CsPbBr_3$ With addition of $EMIMBF_4$

$EMIMBF_4$	τ_1 (α_1) ns	τ_2 (α_2) ns	τ_3 (α_3) ns	τ_{av} ns	χ^2
0μM	0.39 (0.85)	3.55 (0.14)	17.46 (0.01)	0.96	1.05
28 μM	1.07 (0.34)	4.95 (0.65)	12.86 (0.01)	3.69	1.02

In order to understand the interaction mechanism between PNCs and ILs, we have thoroughly analysed the data and eventually found an enhancement in the PLQY and stability (*vide infra*) of the PNCs. As stated earlier, similar PXRD peak position, same lattice spacing, and similar absorption spectra of the $CsPbBr_3$ NCs in the absence and presence of ILs have revealed that the crystallinity and size of the system are not affected in the presence of ILs. Therefore, the enhancement of PLQY may be due to the surface modification.

In order to realize the surface chemistry of PNCs in the absence and presence of ILs and to comprehend the reason behind the enhancement of PL, X-ray photoelectron spectroscopy (XPS), infrared spectroscopy (IR), and energy dispersive X-ray (EDX) measurements have also been performed. Before the IL treatment, analysis of the XPS data (Figure 3.4a) for $CsPbBr_3$ NCs has revealed that the ratio of Br:Pb in the said NC is 3.1. We

note here that this observed Br:Pb ratio for PNC is relatively higher than the expected ratio (Br:Pb = 3.0), This can be attributed to the presence of excess Br on the surface of the NCs. Interestingly, after treatment of $CsPbBr_3$ with [EMIM][BF_4], the Br: Pb ratio is found to be higher (3.3) than that for untreated $CsPbBr_3$ which indicates that some amount of Pb has been removed from the NCs surface after IL treatment.[29,56,57] Again when we deconvolute the XPS spectra of Pb 4f of the untreated $CsPbBr_3$ NCs, 4 peaks has been found as shown in Figure 3.4a. Peaks at 138.8 eV ($4f_{7/2}$) and 144.0 eV ($4f_{5/2}$) with spin-orbit splitting 5.2 eV corresponding to the Pb in +2 oxidation state. Along with Pb^{+2} peaks, two peaks at 136.6 eV and 142.2 eV has been found, which correspond to $4f_{7/2}$ and $4f_{5/2}$ of Pb (0).[29,58] Oron and coworkers[59] and Samanta and coworkers[29] have shown independently that during the synthesis of PNCs by the hot injection method, formation of Pb-nanoparticle (Pb-NPs) and Pb (0)-adatoms is unavoidable. They have also demonstrated that labile Pb-NPs and Pb (0)-adatoms are responsible for the creation of trap states. Essentially, it implies that defects are caused primarily from Pb-rich surface and their removal by certain ILs facilitates the improvement of PLQY of PNCs. The removal of Pb is further confirmed by the EDX spectrum (Figure APX3.5). It is to be noted that no signature of fluorine (i.e. ~685 eV) can be observed in XPS spectra (Figure APX3.6). FTIR spectra of $CsPbBr_3$ in the absence and presence of [EMIM][BF_4] are shown in Figure 3.4b. It can be observed that the $CsPbBr_3$ NCs (black color) shows no prominent peak and [EMIM][BF_4] (blue color) shows a small peak at 1080 $cm^{-1,}$ respectively. However, in case of ($CsPbBr_3$+ [EMIM][BF_4]) (red color), the 1080 cm^{-1} peak is broadened which is attributed to the broadening B-F stretching frequency due to the interaction between BF_4^- and Pb.[29,60] A peak appears at 1560 cm^{-1} (for $CsPbBr_3$ + [EMIM][BF_4]) corresponding to C=O stretching frequency of the oleate moiety that dislodged due to the BF_4^--Pb interaction.[25] However, considering the overall stability of the PNCs, packing of the PNCs through TEM micrograph (images) and peak position of PL spectra of PNCs, before and after treatment with ILs, we may infer that

BF_4^- can access only specific regions of PNCs surface from where the dislodging of some amount of ligand takes place. Due to this, the NCs remain stable in the presence of the ILs[29,25]. Therefore, we may now conjecture that the removal of Pb (0)-adatoms and Pb-NPs (which creates trap states) from the $CsPbBr_3$ surface eventually improves the PLQY of the $CsPbBr_3$ NCs. Similar observations have been obtained (Figure APX3.7) in case of EMIMOAc and EMS, where the broadening of 1646 cm-1 and 1054 cm-1 bands appears due to the C-O and S-O stretching frequency of the acetate and methane sulfonate ion. From the above discussion one can realize that there is ~ 8-fold enhancement of PLQY of $CsPbCl_3$ NCs by treating with [EMIM][BF_4] is due to the removal of surface defects after the treatment with ILs. The facts that there is no improvement of PLQY for $CsPbI_3$ even after the treatment with several ILs shows that the intrinsic defects (due to structural distortion arising from larger iodine) are prominent in these NCs which are also responsible for their low PLQY.[21,29] We would also like to mention here that weak passivation by the ligand can't be also complete ruled out for the observed behavior.[61]

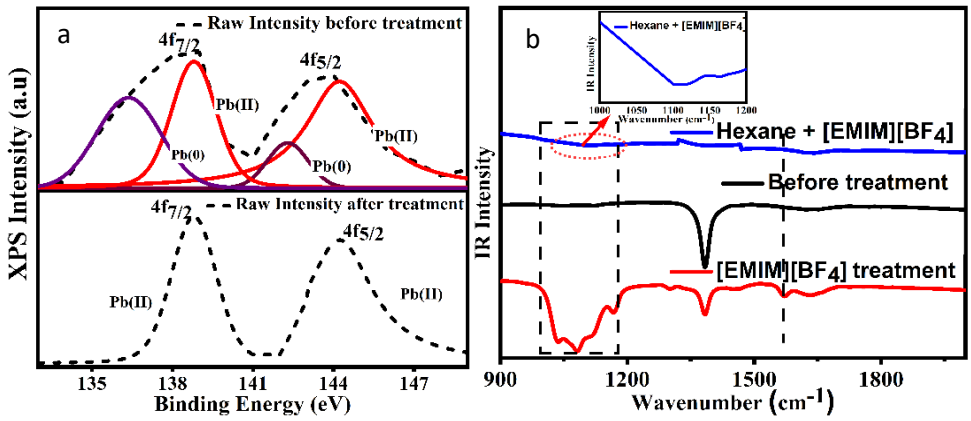

Figure 3.4. (a) XPS spectra of Pb $4f_{7/2}$ and $4f_{7/2}$ of $CsPbBr_3$ before and after the treatment with [EMIM][BF_4].(b) Fourier transformed infrared spectroscopy (FTIR) transmission spectra of [EMIM][BF_4] in hexane, $CsPbBr_3$ NCs before and after treatment with [EMIM][BF_4].Region of interest is (900 – 2000) cm^{-1}. After treatment a broad peak around 1080 cm^{-1} corresponds to B-F stretching of BF_4^- bound to lead[60] and another peak arises at around 1560 cm^{-1} corresponds to the C=O bond stretching of oleate.[25]

Stability of PNCs in common solvents is an important issue for their long-term use, and even though inorganic salts have been used to improve the PLQY of the PNCs,[29,25] it would be interesting to check how ILs qualify for the same. For this purpose, the stability of the $CsPbBr_3$ NCs, in the presence of inorganic salts ($NaBF_4$, NaSCN) and ILs, has been examined separately using fluorescence intensity values with respect to time. The relative fluorescence intensity (F/F^0, where F^0 and F are the PL intensity of PNCs at 0 time and successive time interval, respectively) of $CsPbBr_3$ NCs in the presence of $NaBF_4$ and [EMIM][BF_4] have been graphically represented in Figure 3.5a. It has been found that the F/F^0 of $CsPbBr_3$ NCs decreased in both $NaBF_4$ and [EMIM][BF_4], however, the decrease in presence of [EMIM][BF_4] (1 to 0.78) is found to be less than that in presence of $NaBF_4$ (1 to 0.28) in 15 days. This suggests that in presence of [EMIM][BF_4], the degradation process of $CsPbBr_3$ NCs is delayed. Similar results have been observed where NaSCN behaves as $NaBF_4$ and $BMIMBF_4$ and $HMIMBF_4$ behaves as $EMIMBF_4$. This conclusion is further supported by the outcome of pulse field gradient (PFG) NMR study. The experimental details for the PFG NMR study have been provided in the electronic supplementary information. Through this technique, we measure the translation diffusion coefficient (D) of the imidazolium moiety of [EMIM][BF_4] and ([EMIM][BF_4] + $CsPbBr_3$ NCs) systems, which in turn gives an idea about the hydrodynamic radius of the diffusive species.[46] The diffusion coefficient have been found to be 3.41×10^{-10} and 2.90×10^{-10} m^2/s (Table APX3.2) for the former and the latter system, respectively. The lowering of D value of [EMIM][BF_4] in the presence of $CsPbBr_3$ NCs indicates a relatively slower motion for the latter than the former. This observation can be rationalized by considering the interaction between the imidazolium moiety of the IL and $CsPbBr_3$ NCs. Additionally, we have also observed a decrease in the surface charges (from —11.0 mV to —2.6 mV) of $CsPbBr_3$ NCs in the presence of [EMIM][BF_4] IL through zeta potential measurements. The decrease in surface charges of PNCs in the presence of ILs also

suggests the interaction between the negatively charged $CsPbBr_3$ NCs and the positively charged of imidazolium moiety.

Along with chemical stability, we have also investigated the photostability of the $CsPbBr_3$ NCs before and after the treatment with $EMIMBF_4$, by exposing the sample under continuous irradiation of light. Figure 3.5b and Figure 3.5c show the plot of relative PL intensity (F/F^0) and relative PL lifetime (τ/τ^0) with respect to time, respectively. Interestingly, it has been found that F/F^0 of $CsPbBr_3$ NCs with time (20 hours) remain unchanged after treatment with $EMIMBF_4$, whereas the untreated sample has shown some decrease. This suggests that in the presence of $EMIMBF_4$, the photostability of $CsPbBr_3$ NCs is enhanced. Moreover, τ/τ^0 of $CsPbBr_3$ NCs in the presence of $EMIMBF_4$ with time (20 hours) remain unaltered; on the other hand, the untreated NCs have shown some decrease, which further establishes the photostability of the materials. Furthermore, keeping in mind the applications of PNCs in LED, fluorescence measurements of the CsPbBr3 NCs have also been carried out by preparing films of CsPbBr3 NCs. The experiment is basically done to monitor the chemical and photo stability of the said PNCs as a function of time. Figure APX3.8 (plot of F/F0 vs time), depicts that EMIMBF4-treated $CsPbBr_3$ NCs films are both chemically and photo-stable under normal atmospheric conditions as well as under continuous irradiation of light.

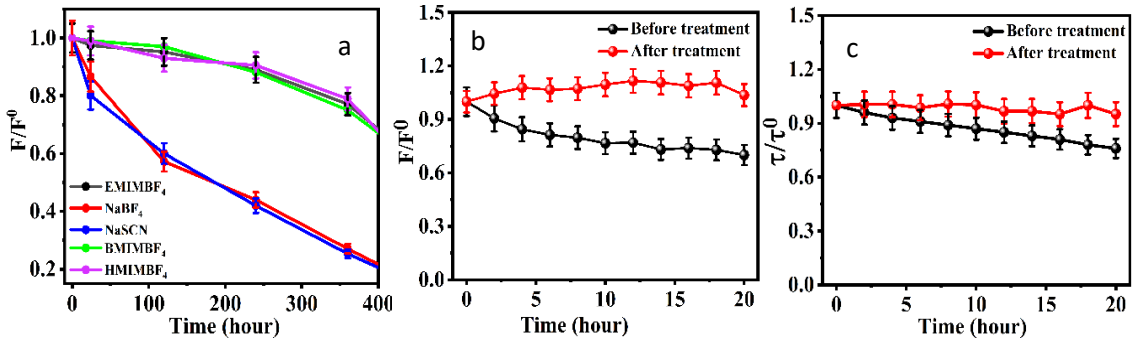

Figure 3.5. (a) Plot of relative fluorescence intensity (F/F_0) versus time showing the stability of $CsPbBr_3$ PNCs in presence of $EMIMBF_4$, $BMIMBF_4$, $HMIMBF_4$, $NaBF_4$, and NaSCN. (b) Relative fluorescence intensity, (c) relative PL lifetime of $CsPbBr_3$ NCs before and after the treatment with $EMIMBF_4$, with time under the continuous irradiation of light of $CsPbBr_3$ NCs.

Apart from ensemble average measurements, we have also performed FCS study (at the single-particle level) for an in-depth understanding of the mechanism of interaction between $CsPbBr_3$ NCs and $EMIMBF_4$. It is to be noted that FCS is a sensitive tool to monitor the fluorescence fluctuations of the fluorophores at low concentration regime. In this technique, we have performed translational diffusion studies of $CsPbBr_3$ NCs, by evaluating the diffusion coefficient of $CsPbBr_3$ NCs before and after the treatment with $EMIMBF_4$. In the present work, we have monitored the translation diffusion time (τ_D) of $CsPbBr_3$ NCs before and after the treatment with $EMIMBF_4$. The detail procedure has been provided in Appendix and data has been analysed using eqn 3.1.

$$G(\tau) = \left[\frac{1}{N\times\left[1+\left(\tau/\tau_D\right)^{\beta}\right]\times\left[\sqrt{1+\left(\tau/\tau_D\right)^{\beta}\left(\frac{1}{k^2}\right)}\right]}\right] \qquad (3.1)$$

The fluorescence diffusion curves of $CsPbBr_3$ NCs before and after the treatment with $EMIMBF_4$ has been shown in Figure 3.6. It has been observed that there is an increase in diffusion time of $CsPbBr_3$ NCs after treatment with $EMIMBF_4$. Additionally, we have also found that the diffusion time of $CsPbBr_3$ NCs remains unchanged with time (after 10 hours) as shown in Table APX3.3. All this indicates that $CsPbBr_3$ NCs with $EMIMBF_4$ is quite stable even at the single particle level in terms of both chemical stability and photostability. Thus, we might conclude that [EMIM][BF_4] can act as a protective layer onto the PNCs to suppress the corrosion, aggregation, and subsequent precipitation as well as the removed Pb-adatoms from the surface of PNCs (shown in Scheme 3.1).[37] Hence, ILs can be useful as a solvent for long-term use of PNCs in various applications.

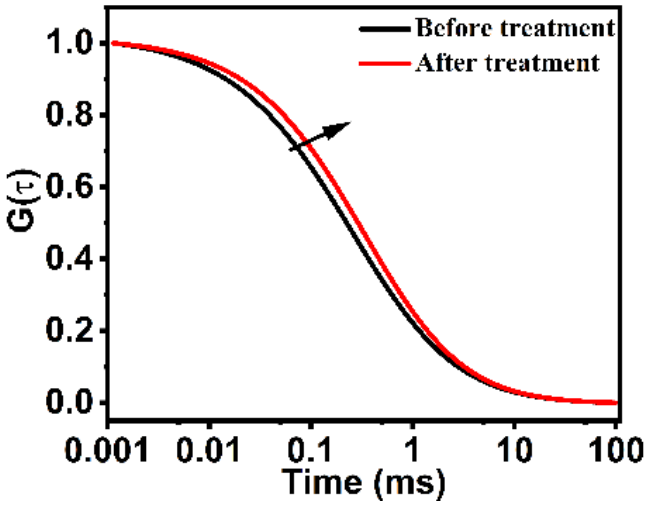

Figure 3.6. Normalized fitted Fluorescence correlation curves of the $CsPbBr_3$ NCs before and after the treatment with $EMIMBF_4$.

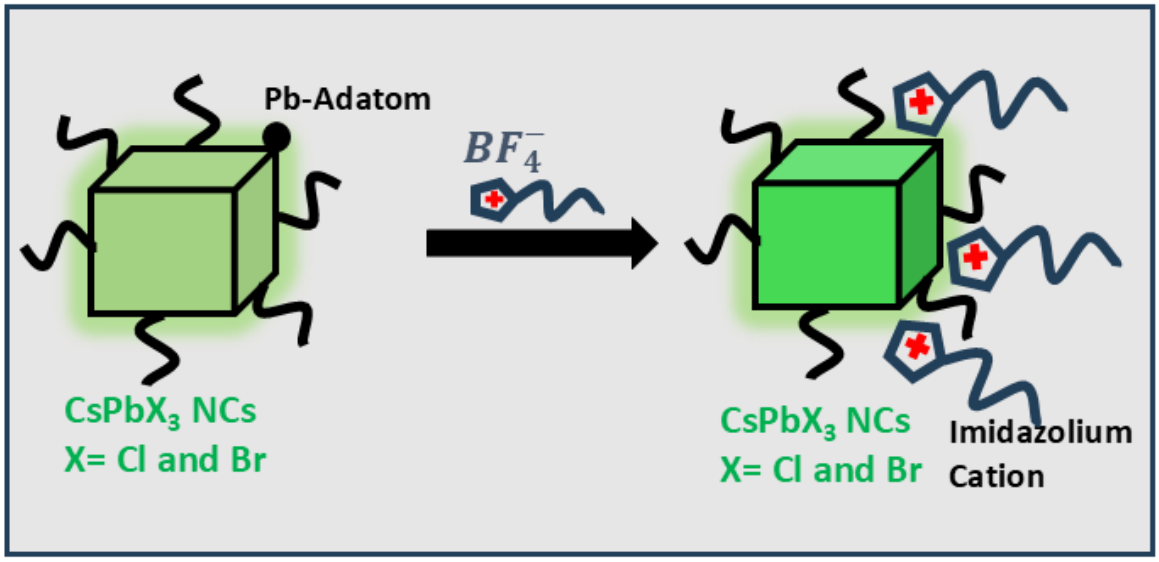

Scheme 3.1. Schematic representation of surface passivation of ILs on the perovskite surface.

3.3. Conclusion

In summary, significant improvement in PLQY of $CsPbX_3$ NCs in the solution phase are achieved when PNCs are treated with some selected ILs. After the treatment of PNCs with ILs the enhancement in the PLQY for $CsPbCl_3$ and $CsPbBr_3$ are estimated to be 8- and 4-fold, respectively. The above studies have concluded that the fluorescence enhancement of PNCs is not due to the structural changes (as evident from XRD and TEM) rather due to the surface

modification of PNCs in a sense that the anionic part of ILs causes the removal of trap states by removing excess of Pb from the surface of the PNCs. The interaction between the imidazolium cation and PNCs is found to play an important role in providing higher stability to PNCs. Photoirradiation on the sample $CsPbBr_3$ NCs for a significant time have demonstrated that NCs upon treatment with $EMIMBF_4$ are photostable both in terms of intensity and decay time. In case of $CsPbI_3$ not much change in its PLQY after treatment with ILs could be observed which is not due to surface defects, rather the intrinsic defects are more prominent in these NCs that causes their low PLQY. Interestingly, material stability of PNCs in solution phase is found to be relatively higher when the treatment is done with ILs as compared to situation where treatment is done with $NaBF_4$ and NaSCN. Essentially, the outcome of this study indicates that $EMIMBF_4$ can be employed for the fabrication of defect-free, chemically and photostable $CsPbX_3$ PNCs. Studies on FCS have shown that IL-treated PNCs can also be used for various single-particle level studies.

3.4 Appendix

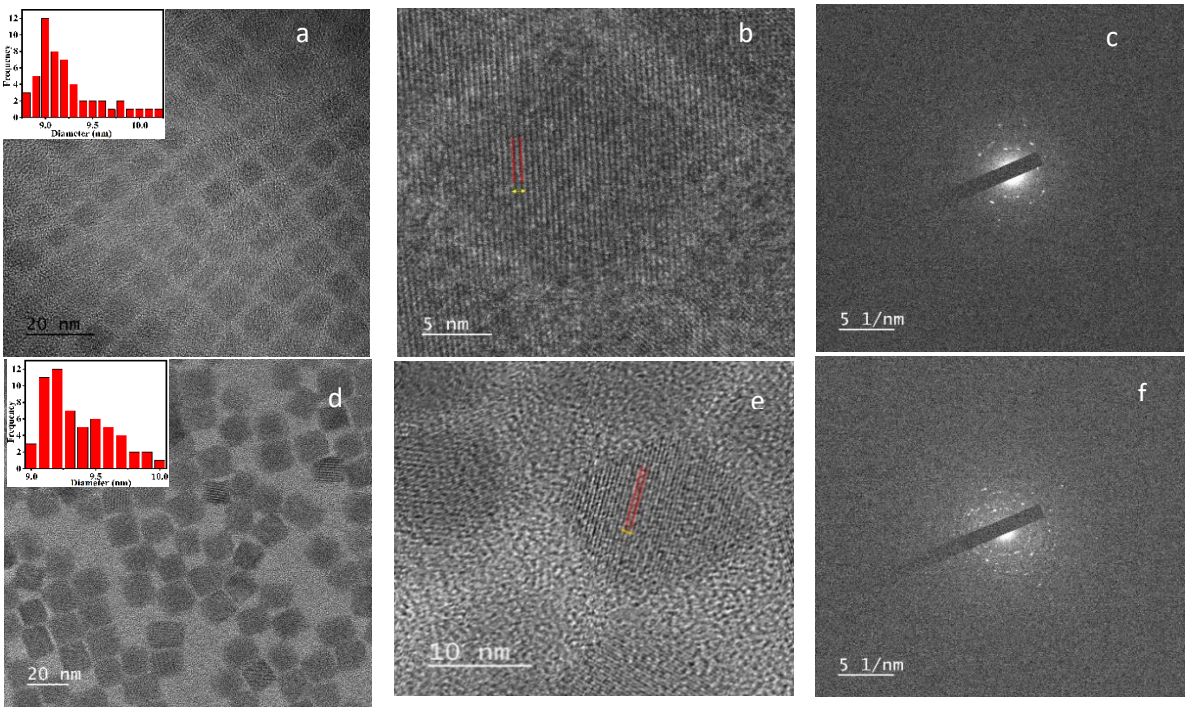

Figure APX3.1. (a) TEM, (b) HRTEM and (c) SAED images of $CsPbCl_3$ PNCs (d) TEM, (e) HRTEM and (f) SAED images of $CsPbBr_3$ NCs.

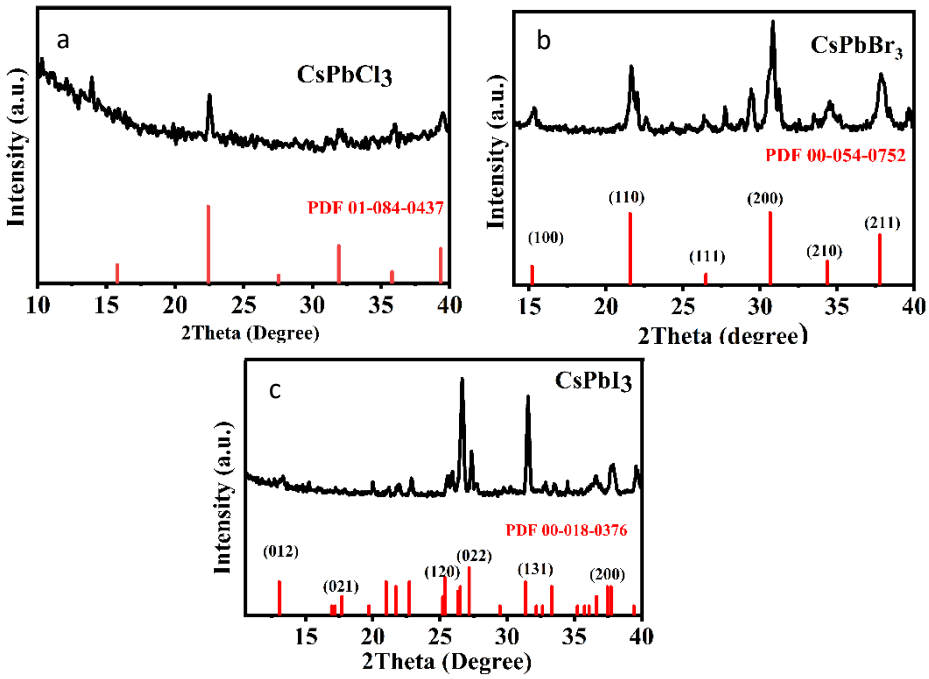

Figure APX3.2. Powder X-ray diffraction patterns of (a) $CsPbCl_3$ (b) $CsPbBr_3$ and (c) $CsPbI_3$ NCs.

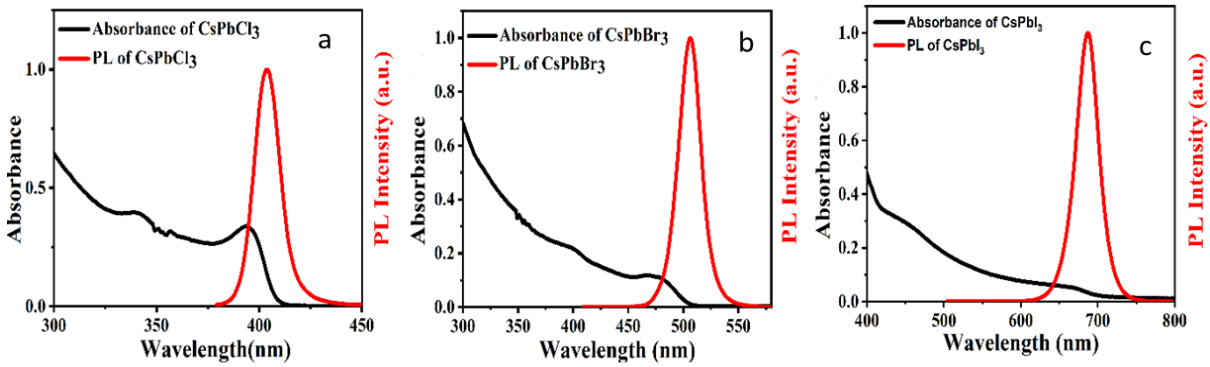

Figure APX3.3. UV−vis absorption (black line) and PL (red line) spectra of (a) the $CsPbCl_3$, (b) $CsPbBr_3$ and (c) $CsPbI_3$ Perovskite NCs.

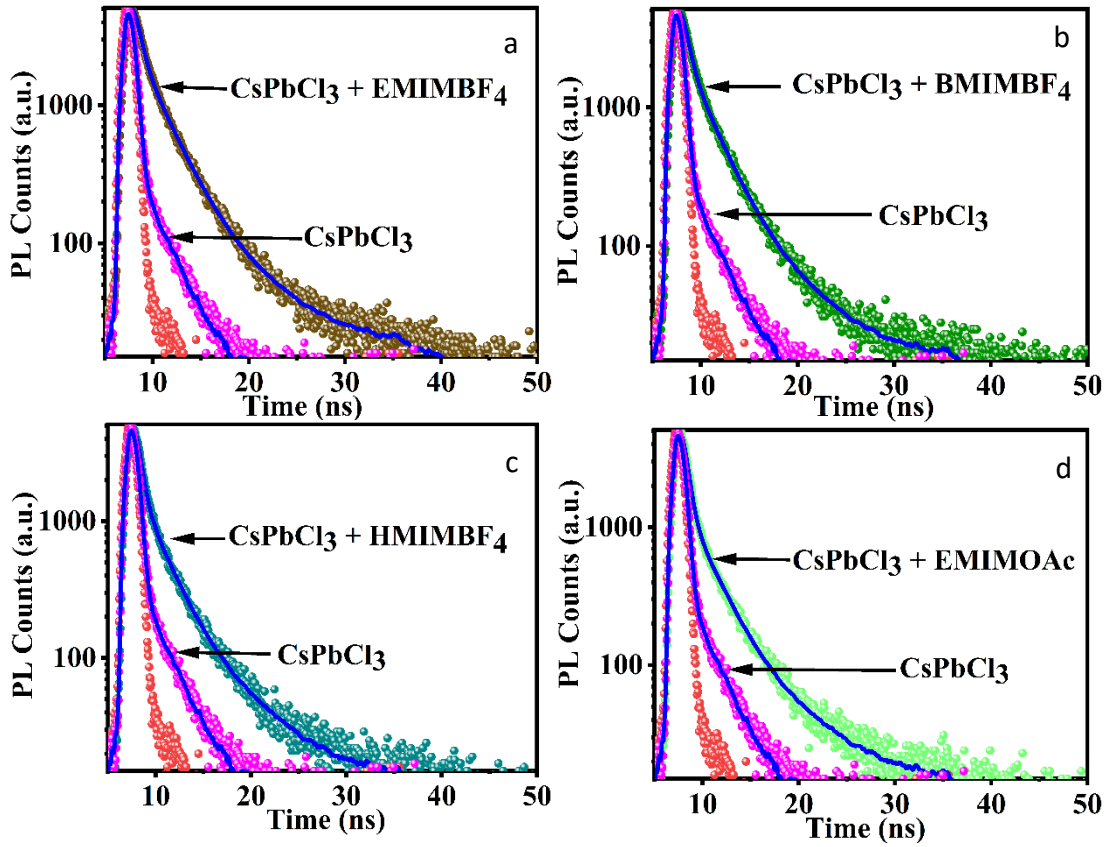

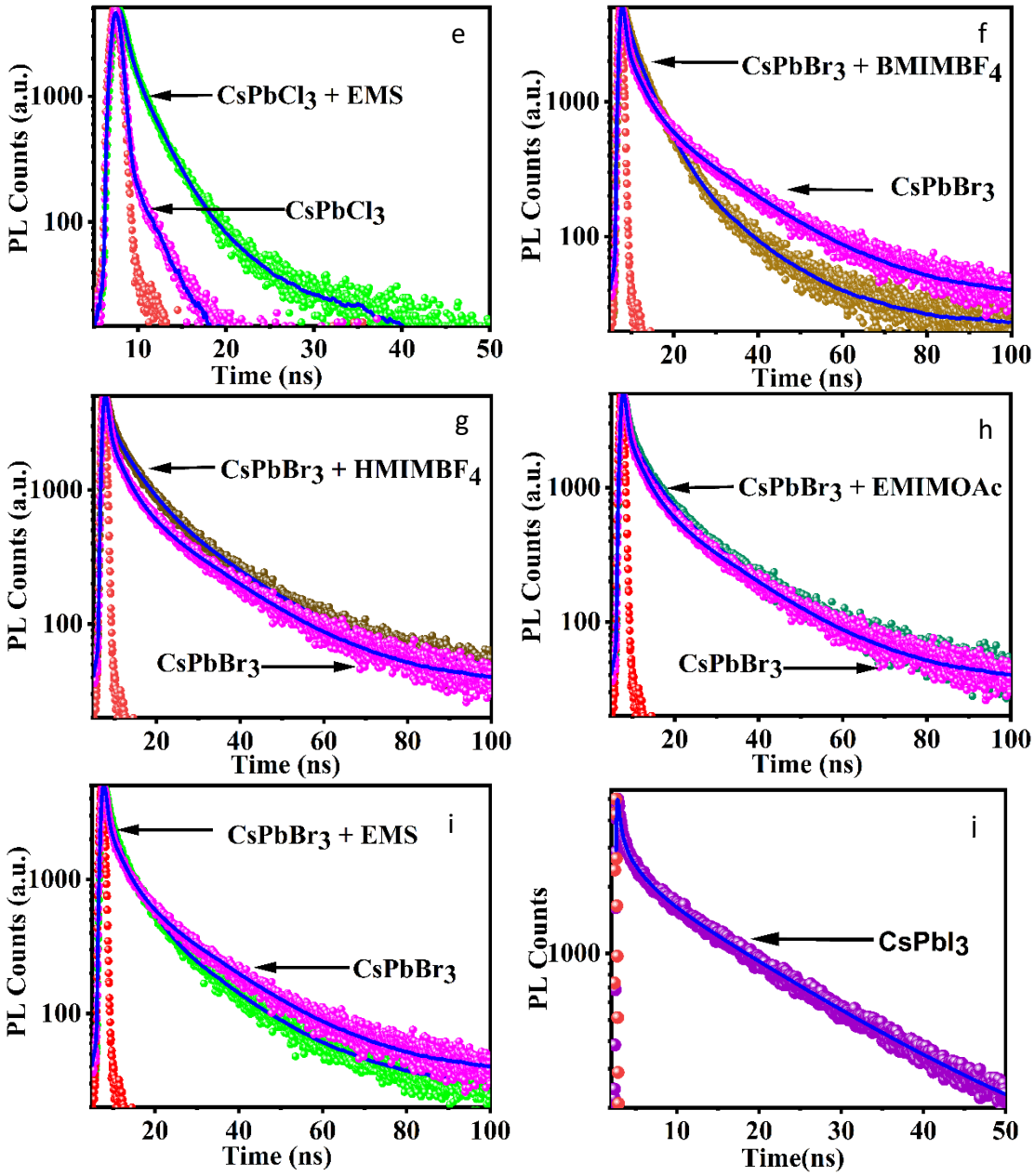

Figure APX3.4. PL Decay curves of a-e) CsPbCl3 f-i) CsPbBr3 j) CsPbI3 in absence and presence of selected ILs.

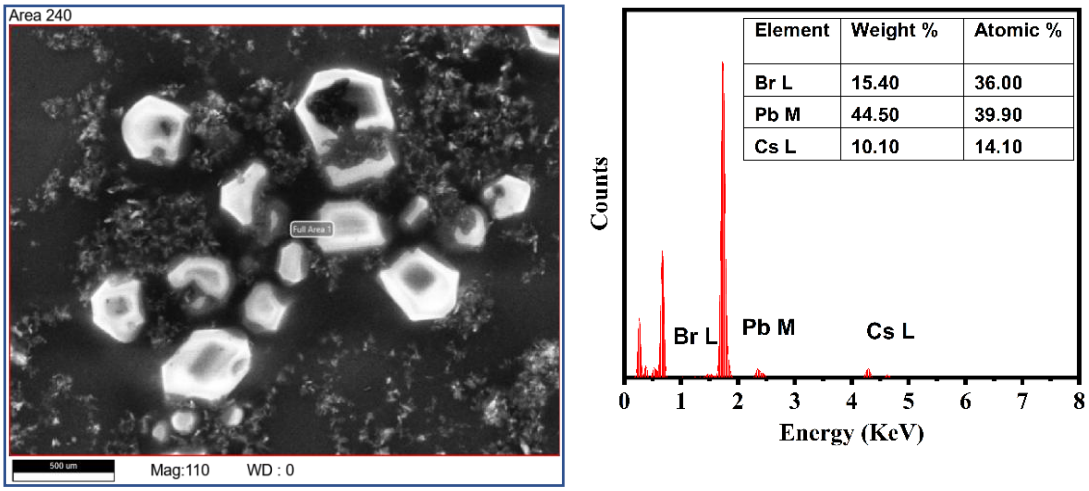

Figure APX3.5. SEM image, EDX, and elemental composition of precipitated (of Pb(0)-BF_4 mixture) solid after several washes and centrifugation of $CsPbBr_3$ NC solution after treatment with $EMIMBF_4$. Presence of excess lead is observed as Br:Pb=12:13

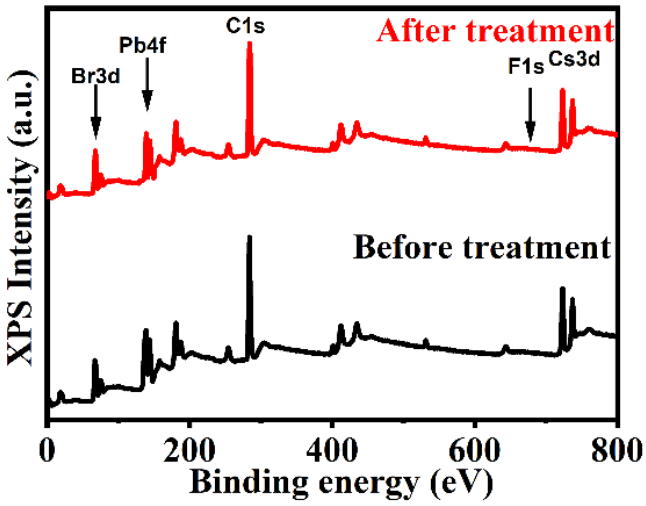

Figure APX3.6. XPS survey spectra of $CsPbBr_3$ NCs before and after treatment. No peak for F could be seen at around 685 eV after treatment.

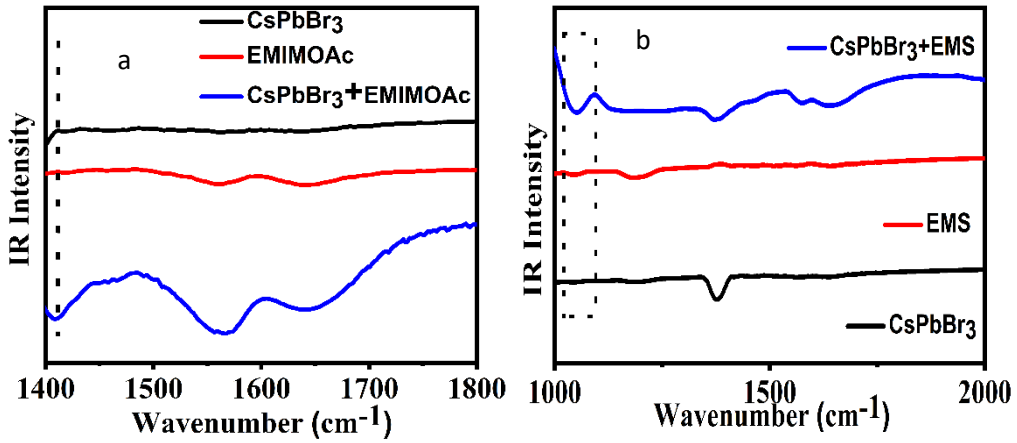

Figure APX3.7. Fourier-transform infrared spectroscopy (FTIR) transmission spectra of (a) [EMIM][OAc] in hexane, $CsPbBr_3$ NCs before and after treatment with [EMIM][OAc], (b) EMS in hexane, $CsPbBr_3$ NCs before and after treatment with EMS.

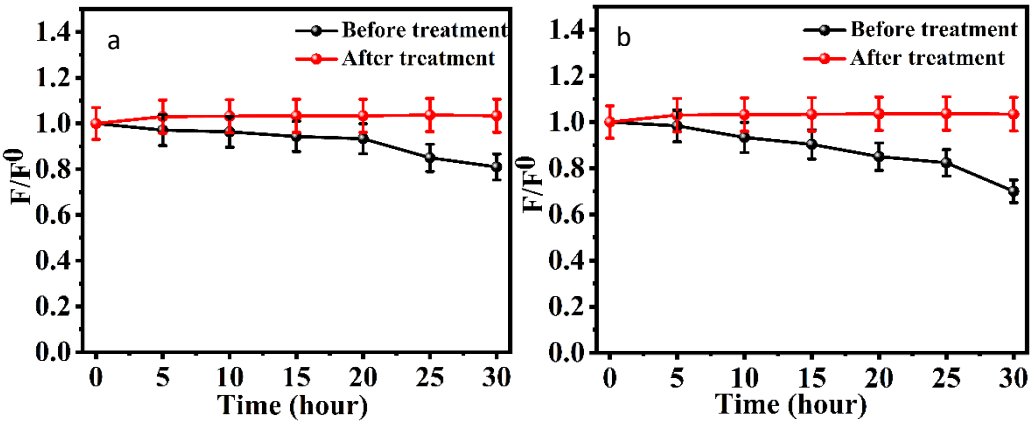

Figure APX3.8. Relative fluorescence intensity of $CsPbBr_3$ NCs film before and after the treatment with $EMIMBF_4$ with time (a) under normal atmospheric conditions and (b) under the continuous irradiation of light.

Table APX3.1. PL Decay Parameters of the PNCs in the presence and absence of various ILs

Materials	**τ_1 (α_1) ns**	**τ_2 (α_2) ns**	**τ_3 (α_3) ns**	**τ_{av} ns**
$CsPbCl_3$	0.10 (0.94)	2.40 (0.06)	9.97 (0.01)	0.27
$CsPbCl_3$+$EMIMBF_4$	0.56 (0.72)	2.47 (0.26)	8.04 (0.02)	1.20
$CsPbCl_3$+$BMIMBF_4$	0.50 (0.74)	2.50 (0.24)	8.01 (0.02)	1.11
$CsPbCl_3$+$HMIMBF_4$	0.49 (0.75)	2.33 (0.23)	6.89 (0.02)	1.04
$CsPbCl_3$+EMIMOAc	0.37 (0.86)	2.16 (0.12)	6.58 (0.02)	0.69
$CsPbCl_3$+EMIMMS	0.38 (0.89)	2.44 (0.10)	8.11 (0.01)	0.65

$CsPbBr_3$	0.39 (0.85)	3.55 (0.14)	17.64 (0.01)	0.96
$CsPbBr_3$+$EMIMBF_4$	1.07 (0.34)	4.95 (0.65)	12.86 (0.01)	3.69
$CsPbBr_3$+$BMIMBF_4$	1.02 (0.44)	5.00 (0.49)	15.81 (0.06)	3.88
$CsPbBr_3$+$HMIMBF_4$	0.98 (0.60)	5.02 (0.31)	17.93 (0.06)	3.59
$CsPbBr_3$+EMIMOAc	0.85 (0.67)	5.11 (0.29)	18.19 (0.09)	3.59
$CsPbBr_3$+EMIMMS	0.99 (0.61)	4.61 (0.30)	16.68 (0.08)	3.41
$CsPbI_3$	0.36 (0.5)	2.38 (0.17)	17.76 (0.33)	6.35

Table APX3.2. Estimated Translational Diffusion Coefficient of [EMIM][BF_4] in presence and absence of $CsPbBr_3$ NCs.

System	Translation Diffusion Coefficient (D) m^2/s
[EMIM][BF_4]	3.41×10^{-10}
[EMIM][BF_4] + $CsPbBr_3$ NCs	2.90×10^{-10}

Table APX3.3. Translational diffusion time of $CsPbBr_3$ NCs in absent and the presence (recorded after 0 hour, 5 hour, 10 hour) of $EMIMBF_4$.

System	Time (hour)	Diffusion time (τ_D) µs
$CsPbBr_3$ NCs	0	450
$CsPbBr_3$ NCs	5	445
$CsPbBr_3$ NCs	10	453
$CsPbBr_3$ NCs +$EMIMBF_4$	0	588
$CsPbBr_3$ NCs +$EMIMBF_4$	5	581
$CsPbBr_3$ NCs +$EMIMBF_4$	10	583

3.5 References

1. Aldakov, D.; Reiss, P. Safer-by-Design Fluorescent Nanocrystals: Metal Halide Perovskites Vs Semiconductor Quantum Dots. *J. Phys. Chem. C* **2019**, *123*, 12527−12541.
2. Roo, J. D.; Ibanez, M.; Geiregat, P.; Nedelcu, G.; Walravens, W.; Maes, J.; Martins, J. C.; Van Driessche, I.; Kovalenko, M. V.; Hens, Z. Highly Dynamic Ligand Binding and Light Absorption Coefficient of Cesium Lead Bromide Perovskite Nanocrystals. *ACS Nano* **2016**, *10*, 2071−2081.
3. Dutta, A.; Behera, R. K.; Pal, P.; Baitalik, S.; Pradhan, N. Near- Unity Photoluminescence Quantum Efficiency for All $CsPbX_3$ (X = Cl, Br, and I) Perovskite Nanocrystals: A Generic Synthesis Approach. *Angew., Chem. Int. Ed.* **2019**, *58*, 5552−5556.
4. Swarnkar, A.; Chulliyil, R.; Ravi, V. K.; Irfanullah, M.; Chowdhury, A.; Nag, A. Colloidal $CsPbBr_3$ Perovskite Nanocrystals: Luminescence beyond Traditional Quantum Dots. *Angew. Chem., Int. Ed.* **2015**, *54*, 15424−15428.
5. Ghosh, S.; Mandal, S.; Mukherjee, S.; De, C. K.; Samanta, T.; Mandal, M.; Roy, D.; Mandal, P. K. Near-Unity Photoluminescence Quantum Yield and Highly Suppressed Blinking in a Toxic-Metal-Free Quantum Dot. *J. Phys. Chem. Lett.* **2021**, *12*, 1426-1431.
6. Tian, Y.; Scheblykin, I. G. Artifacts in Absorption Measurements of Organometal Halide Perovskite Materials: What Are the Real Spectra*? J. Phys. Chem. Lett.* **2015**, *6*, 17, 3466–3470.
7. Begum, R.; Parida, M. R.; Abdelhady, A. L.; Murali, B.; Alyami, N. M.; Ahmed, G. H.; Hedhili, M. N.; Bakr, O. M.; Mohammed, O. F. Engineering Interfacial Charge Transfer in $CsPbBr_3$ Perovskite Nanocrystals by Heterovalent Doping. *J. Am. Chem. Soc.* **2017**, *139*, 731−737.

8. Wang, Y.; Li, X.; Song, J.; Xiao, L.; Zeng, H.; Sun, H. All-Inorganic Colloidal Perovskite Quantum Dots: A New Class of Lasing Materials with Favorable Characteristics. *Adv. Mater.* **2015**, *27*, 7101−7108.

9. Jeon, N. J.; Noh, J. H.; Yang, W. S.; Kim, Y. C.; Ryu, S.; Seo, J.; Seok, S. Compositional engineering of perovskite materials for high-performance solar cells. *Nature* **2015**, *517*, 476-480.

10. Ramasamy, P.; Lim, D.H.; Kim, B.; Lee, S.-H.; Lee, M.-S.; Lee, J. S. All-inorganic cesium lead halide perovskite nanocrystals for photodetector applications. *Chem. Commun.* **2016**, *52*, 2067−2070.

11. Wang, J.; Wang, N.; Jin, Y.; Si, J.; Tan, Z.; Du, H.; Cheng, L.; Dai, X.; Bai, S.; He, H.; Ye, Z.; Lai, M. L.; Friend, R. H.; Huang, W. Interfacial Control Toward Efficient and Low-Voltage Perovskite Light-Emitting Diodes. *Adv. Mater.* **2015**, *27*, 2311-2316.

12. Jaramillo-Quintero, O. A.; Sanchez, R. S.; Rincon, M.; Mora-Sero, I. Bright Visible-Infrared Light Emitting Diodes Based on Hybrid Halide Perovskite with Spiro-OMeTAD as a Hole-Injecting Layer. *J. Phys. Chem. Lett.* **2015**, *6*, 1883-1890.

13. Zhang, X.; Lin, H.; Huang, H.; Reckmeier, C.; Zhang, Y.; Choy, W. C. H.; Rogach, A. L. Enhancing the Brightness of Cesium Lead Halide Perovskite Nanocrystal Based Green Light-Emitting Devices through the Interface Engineering with Perfluorinated Ionomer. *Nano Lett.* **2016**, *16*, 1415−1420.

14. Swarnkar, A.; Marshall, A. R.; Sanehira, E. M.; Chernomordik, B. D.; Moore, D. T.; Christians, J. A.; Chakrabarti, T.; Luther, J. M. Quantum dot−induced phase stabilization of α-$CsPbI_3$ perovskite for high-efficiency photovoltaics. *Science* **2016**, *354*, 92−95.

15. Yang, D.; Li, X.; Zeng, H. Surface Chemistry of All Inorganic Halide Perovskite Nanocrystals: Passivation Mechanism and Stability. *Adv. Mater. Interfaces* **2018**, *5*, 1701662.

16. Grisorio, R.; Di Clemente, M. E.; Fanizza, E.; Allegretta, I.; Altamura, D.; Striccoli, M.; Terzano, R.; Giannini, C.; Irimia-Vladu, M.; Suranna, G. P. Exploring the surface chemistry of cesium lead halide perovskite nanocrystals. *Nanoscale* **2019**, *11*, 986– 999.
17. Kovalenko, V. M.; Protesescu, L.; Bodnarchuk, M. I. Properties and Potential Optoelectronic Applications of Lead Halide Perovskite Nanocrystals. *Science* **2017**, *358*, 745−750.
18. Swarnkar, A.; Ravi, V. K.; Nag, A. Beyond Colloidal Cesium Lead Halide Perovskite Nanocrystals: Analogous Metal Halides and Doping. *ACS Energy Lett.* **2017**, *2*, 1089−1098.
19. Giansante, C.; Infante, I. Surface Traps in Colloidal Quantum Dots: A Combined Experimental and Theoretical Perspective. *J. Phys. Chem. Lett.* **2017**, *8*, 5209−5215.
20. Buin, A.; Pietsch, P.; Xu, J.; Voznyy, O.; Ip, A. H.; Comin, R.; Sargent, E. H. Materials Processing Routes to Trap-Free Halide Perovskites. *Nano Lett.* **2014**, *14*, 6281−6286.
21. Huang, H.; Bodnarchuk, M. I.; Kershaw, S. V.; Kovalenko, M. V.; Rogach, A. L. Lead Halide Perovskite Nanocrystals in the Research Spotlight: Stability and Defect Tolerance. *ACS Energy Lett.* **2017**, *2*, 2071−2083.
22. Kang, J.; Wang, L. W. High Defect Tolerance in Lead Halide Perovskite CsPbBr3**.** *J. Phys. Chem. Lett.* **2017**, *8*, 489−493.
23. Mondal, N.; Samanta, A. Complete ultrafast charge carrier dynamics in photo-excited all-inorganic perovskite nanocrystals ($CsPbX_3$). *Nanoscale* **2017**, *9*, 1878−1885.
24. Jin, H.; Debroye, E.; Keshavarz, M.; Scheblykin, I. G.; Roeffaers, M. B. J.; Hofkens, J.; Steele, J. A. It's a trap! On the nature of localised states and charge trapping in lead halide perovskites. *Mater. Horiz.* **2020**, *7*, 397-410.

25. Koscher, B. A.; Swabeck, J. K.; Bronstein, N. D.; Alivisatos, A. P. Essentially trap-free $CsPbBr_3$ colloidal nanocrystals by post-synthetic thiocyanate surface treatment. *J. Am. Chem. Soc.* **2017**, *139*, 6566− 6569.

26. Raino, G.; Nedelcu, G.; Protesescu, L.; Bodnarchuk, M. I.; Kovalenko, M. V.; Mahrt, R. F.; Stöferle, T. Single Cesium Lead Halide Perovskite Nanocrystals at Low Temperature: Fast SinglePhoton Emission, Reduced Blinking, and Exciton Fine Structure. *ACS Nano* **2016**, *10*, 2485−2490.

27. Li, X.; Wu, Y.; Zhang, S.; Cai, B.; Gu, Y.; Song, J.; Zeng, H. $CsPbX_3$ Quantum Dots for Lighting and Displays: Room-Temperature Synthesis, Photoluminescence Superiorities, Underlying Origins and White Light-Emitting Diodes. *Adv. Funct. Mater*. **2016**, *26*, 2435−2445.

28. Hu, F.; Zhang, H.; Sun, C.; Yin, C.; Lv, B.; Zhang, C.; Yu, W. W.; Wang, X.; Zhang, Y.; Xiao, M. Superior Optical Properties of Perovskite Nanocrystals as Single Photon Emitters. *ACS Nano* **2015**, *9*, 12410−12416.

29. Ahmed, T.; Seth, S.; Samanta, A. Boosting the Photoluminescence of CsPbX3 (X = Cl, Br, I) Perovskite Nanocrystals Covering a Wide Wavelength Range by Postsynthetic Treatment with Tetrafluoroborate Salts. *Chem. Mater*. **2018**, *30*, 3633−3637.

30. Mandal, S.; Mukherjee, S.; De, C. K.; Roy, D.; Ghosh, S.; Mandal, P. K. Extent of Shallow/Deep Trap States beyond the Conduction Band Minimum in Defect-Tolerant CsPbBr3 Perovskite Quantum Dot: Control over the Degree of Charge Carrier Recombination. *J. Phys. Chem. Lett.* **2020**, *11*, 1702−1707.

31. Kim, J.; Lee, S. H.; Lee, J. H.; Hong, K. H. The Role of Intrinsic Defects in Methylammonium Lead Iodide Perovskite. *J. Phys. Chem. Lett.* **2014**, *5*, 1312−1317.

32. Smyth, D. M. Defects and Order in Perovskite-Related Oxides. *Annu. Rev. Mater. Sci.* **1985**, *15*, 329−357.

33. Xiao, Z.; Zhou, Y.; Hosono, H.; Kamiya, T. Intrinsic defects in a photovoltaic perovskite variant Cs_2SnI_6. *Phys. Chem. Chem. Phys.* **2015**, *17*, 18900−18903.

34. Tachikawa, T.; Karimata, I.; Kobori, Y. Surface Charge Trapping in Organolead Halide Perovskites Explored by Single-Particle Photoluminescence Imaging. *J. Phys. Chem. Lett.* **2015**, *6*, 3195−3201.

35. Mududli, S.; Pandey, P.; Devatha, G.; Babar, R.; Kothari, T. M. D. C.; Kabir, M.; Pillai, P. P.; Ogale, S. B. Photoluminescence Quenching in Self-assembled $CsPbBr_3$ Qunatum Dots on Few Layer Black Phosphorous Sheets. *Angew. Chem. Int. Ed.* **2018**, *57*, 7682-7686.

36. Chakraborty, I. N.; Roy, P.; Rao, A.; Devatha, G.; Roy, S.; Pillai, P. P. The unconventional role of surface ligands in dictating the light harvesting properties of quantum dots. *J. Mater. Chem. A* **2021**, *9*, 7422−7457.

37. Woo, J. Y.; Kim, Y.; Bae, J.; Kim, T. G.; Kim, J. W.; Lee, D. C.; Jeong, S. Highly Stable Cesium Lead Halide Perovskite Nanocrystals through in Situ Lead Halide Inorganic Passivation. *Chem. Mater.* **2017**, *29*, 7088−7092.

38. Liu, F.; Zhang, Y.; Ding, C.; Kobayashi, S.; Izuishi, T.; Nakazawa, N.; Toyoda, T.; Ohta, T.; Hayase, S.; Minemoto, T.; Yoshino, K.; Dai, S.; Shen, Q. Highly Luminescent Phase-Stable $CsPbI_3$ Perovskite Quantum Dots Achieving Near 100% Absolute Photoluminescence Quantum Yield. *ACS Nano* **2017**, *11*, 10373−10383.

39. Pan, J.; Quan, L. N.; Zhao, Y.; Peng, W.; Murali, B.; Sarmah, S. P.; Yuan, M.; Sinatra, L.; Alyami, N. M.; Liu, J.; Yassitepe, E.; Yang, Z.; Voznyy, O.; Comin, R.; Hedhili, M. N.; Mohammed, O. F.; Lu, Z. H.; Kim, D. H.; Sargent, E. H.; Bakr, O. M. Highly Efficient Perovskite-Quantum-Dot Light-Emitting Diodes by Surface Engineering. *Adv. Mater.* **2016**, *28*, 8718−8725.

40. Pan, J.; Sarmah, S. P.; Murali, B.; Dursun, I.; Peng, W.; Parida, M. R.; Liu, J.; Sinatra, L.; Alyami, N.; Zhao, C.; Alarousu, E.; Ng, T. K.; Ooi, B. S.; Bakr, O. M.; Mohammed, O. F.

Air-Stable Surface-Passivated Perovskite Quantum Dots for Ultra-Robust, Single- and Two-Photon-Induced Amplified Spontaneous Emission. *J. Phys. Chem. Lett.* **2015**, *6*, 5027−5033.

41. Stasio, F. D.; Christodoulou, S.; Huo, N.; Konstantatos, G. Near-Unity Photoluminescence Quantum Yield in $CsPbBr_3$ Nanocrystal Solid-State Films via Postsynthesis Treatment with Lead Bromide. *Chem. Mater.* **2017**, *29*, 7663−7667.
42. Pan, J.; Shang, Y.; Yin, J.; Bastiani, M. D.; Peng, W.; Dursun, I.; Sinatra, L.; El-Zohry, A. M.; Hedhili, M. N.; Emwas, A. H.; Mohammed, O. F.; Ning, Z.; Bakr, O. M. Bidentate Ligand-Passivated $CsPbI_3$ Perovskite Nanocrystals for Stable Near-Unity Photoluminescence Quantum Yield and Efficient Red Light-Emitting Diodes. *J. Am. Chem. Soc.* **2018**, *140*, 562−565.
43. Protesescu, L.; Yakunin, S.; Bodnarchuk, M. I.; Krieg, F.; Caputo, R.; Hendon, C. H.; Yang, R. X.; Walsh, A.; Kovalenko, M. V. Nanocrystals of Cesium Lead Halide Perovskites ($CsPbX_3$, X = Cl, Br,and I): Novel Optoelectronic Materials Showing Bright Emission with Wide Color Gamut. *Nano Lett.* **2015**, *15*, 3692−3696.
44. MacFarlane, D. R.; Meakin, P.; Sun, J.; Amini, N.; Forsyth, M. Pyrrolidinium Imides: A New Family of Molten Salts and Conductive Plastic Crystal Phases. *J. Phys. Chem. B* **1999**, *103*, 4164− 4170.
45. Hallett, J. P.; Welton, T. Room-Temperature Ionic Liquids: Solvents for Synthesis and Catalysis. *Chem. Rev.* **2011**, *111*, 3508− 3576.
46. Welton, T. Room-Temperature Ionic Liquids. Solvents for Synthesis and Catalysis. *Chem. Rev.* **1999**, *99*, 2071−2084.
47. Rogers, R. D.; Seddon, K. R. Perspective Article: Ionic Liquids Solvents of the Future. *Science* **2003**, *302*, 792−793.

48. Wang, S.; Li, Z.; Zhang, Y.; Liu, X.; Han, J.; Li, X.; Liu, Z.; Frank Liu, S.; Choy, W. C. H. Water-Soluble Triazolium Ionic-LiquidInduced Surface Self-Assembly to Enhance the Stability and Efficiency of Perovskite Solar Cells. *Adv. Funct. Mater.* **2019**, *29*, 1900417.

49. Salado, M.; Ramos, F. J.; Manzanares, V. M.; Gao, P.; Nazeeruddin, K.; Dyson, P. J.; Ahmad, S. Extending the Lifetime of Perovskite Solar Cells using a Perfluorinated Dopant. *Chem. Sus. Chem.* **2016**, *9*, 2708−2714.

50. Dong, W.; Sun, C.; Sun, M.; Ge, H.; Asiri, A. M.; Marwani, H. M.; Ni, R.; Wang, S. Interface Engineering of Imidazolium Ionic Liquids toward Efficient and Stable $CsPbBr_3$ Perovskite Solar Cells. *ACS Appl. Mater. Interfaces* **2020**, *12*, 4540−4548.

51. Shahiduzzaman, Md.; Muslih, E. Y.; Hasan, A. K. M.; Wang, L.; Fukaya, S.; Nakano, M.; Karakawa, M.; Takahashi, K.; Akhtaruzzaman, M.; Nunzi, J. M.; Taima, T. The benefits of ionic liquids for the fabrication of efficient and stable perovskite photovoltaics. *Chem. Eng. J.* **2021**, *411*, 128461.

52. Shahiduzzaman, M.; Yamamoto, K.; Furumoto, Y.; Kuwabara, T.; Takahashi, K.; Taima, T. Ionic Liquid-Assisted Growth of Methylammonium Lead Iodide Spherical Nanoparticles by a Simple Spin-coating Method and Photovoltaic Properties of Perovskite Solar Cells. *RSC Adv.* **2015**, *5*, 77495−77500.

53. Wan, Y.; Dong, S.; Wang, Y.; Yang, L.; Qin, W.; Cao, H.; Yao, C.; Ge, Z.; Yin, S. Ionic Liquid-assisted Perovskite Crystal Film Growth for High Performance Planar Heterojunction Perovskite Solar Cells. *RSC Adv.* **2016**, *6*, 97848−97852.

54. Li, M.; Zhao, C.; Wang, Z. K.; Zhang, C. C.; Lee, H. K. H.; Pockett, A.; Barb´e, J.; Tsoi, W. C.; Yang, Y. G.; Carnie, M.J.; Gao, X. Y.; Yang, W. X.; Durrant, J. R.; Liao, L. S.; Jain, S. M. Interface modification by ionic liquid: a promising candidate for indoor light harvesting and stability improvement of planar perovskite solar cells. *Adv. Energy Mater.* **2018**, *8*, 1801509.

55. Akkerman, Q. A.; D'Innocenzo, V.; Accornero, S.; Scarpellini, A.; Petrozza, A.; Prato, M.; Manna, L. Tuning the Optical Properties of Cesium Lead Halide Perovskite Nanocrystals by Anion Exchange Reactions. *J. Am. Chem. Soc.* **2015**, *137*, 10276−10281.

56. Rosen, E. L.; Buonsanti, R.; Llordes, A.; Sawvel, A. M.; Milliron, D. J.; Helms, B. A. Exceptionally Mild Reactive Stripping of Native Ligands from Nanocrystal Surfaces by Using Meerweins Salt. *Angew. Chem., Int. Ed.* **2012**, *51*, 684−689.

57. Dai, Q.; Zhang, Y.; Wang, Y.; Wang, Y.; Zou, B.; Yu, W. W.; Hu, M. Z. Ligand Effects on Synthesis and Post-Synthetic Stability of PbSe Nanocrystals. *J. Phys. Chem. C* **2010**, *114*, 16160−16167.

58. Ravi, V. K.; Santra, P. K.; Joshi, N.; Chugh, J.; Singh, S. K.; Rensmo, H.; Ghosh, P.; Nag, A. Origin of the Substitution Mechanism for the Binding of Organic Ligands on the Surface of $CsPbBr_3$ Perovskite Nanocubes. *J. Phys. Chem. Lett.* **2017**, *8*, 4988−4994.

59. Udayabhaskararao, T.; Kazes, M.; Houben, L.; Lin, H.; Oron, D. Nucleation, Growth, and Structural Transformations of Perovskite Nanocrystals. *Chem. Mater.* **2017**, *29*, 1302−1308.

60. Nagane, S.; Bansode, U.; Game, O.; Chhatre, S.; Ogale, S. $CH_3NH_3PbI_{(3-x)}(BF_4)_x$: molecular ion substituted hybrid perovskite. *Chem. Commun*. **2014**, *50*, 9741−9744.

61. Li, C.-H. A.; Zhou, Z.; Vashishtha, P.; Halpert, J. E. The Future Is Blue (LEDs): Why Chemistry Is the Key to Perovskite Displays. *Chem. Mater.* **2019**, *31*, 6003−6032.

CHAPTER 4

Ionic Liquid Engineered Defect-Driven Green Emitting Zero Dimensional Cs_4PbBr_6 Microdisks

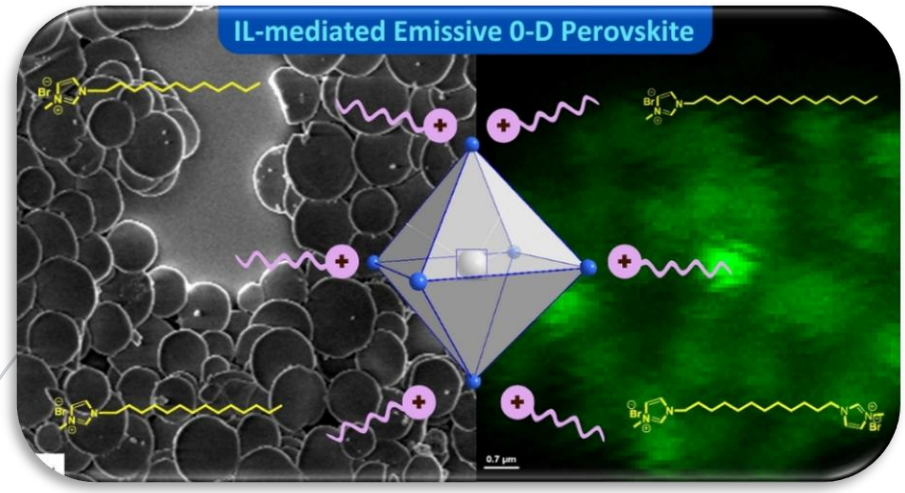

Abstract

Quantum-confined perovskites represent an emerging class of materials with great potential for optoelectronic applications. Specifically, zero-dimensional (0D) perovskites have garnered significant attention for their unique excitonic properties. However, achieving phase-pure, size-tunable 0D perovskite materials and gaining a clear understanding of their photophysical behavior remains challenging. Herein, we report a simple, room-temperature synthesis of phase-pure Cs_4PbBr_6 microdisks (MDs) via ionic liquid (IL)-mediated antisolvent precipitation method. By varying the alkyl-chain length, type, and concentration of mono-/di- cationic ILs, we have successfully modulated the morphology and optical characteristics of the resulting MDs. Structural characterization through TEM, SAED, PXRD, and EDX confirms the formation of highly crystalline, compositionally pure Cs_4PbBr_6 MDs. Photoluminescence (PL) and fluorescence lifetime imaging microscopy (FLIM) have revealed strong, intrinsic green emission from the MDs, with no detectable contribution from $CsPbBr_3$ impurities. Moreover, FLIM studies indicate heterogeneity in PL intensity and lifetime, attributed to variations in trap-state distributions across the MDs. Temperature-dependent PL measurements have further substantiated an excitonic PL mechanism, exhibiting a high exciton-binding energy (~222 meV) and pronounced exciton–phonon coupling. These findings affirm that the green emission originates from defect-mediated mid-gap recombination within Cs_4PbBr_6, highlighting the utility of ILs as effective ligands in tuning the morphology and optical response of 0D-perovskites.

4.1. Introduction

Low-dimensional perovskite materials have gained increasing attention in the fields of optoelectronics, photovoltaics, and photodetection due to their superior structural stability and unique optical and electronic characteristics.[1-7] Unlike their higher-dimensional counterparts, these materials often exhibit enhanced photoluminescence (PL) in the solid state, making them highly suitable for next-generation optoelectronic devices.[1-6] Structurally, these perovskites are generally represented by the formula Cs_nPbX_{2+n} (n = 1-4), where variations in *n* correspond to dimensional transitions from three-dimensional nanocubes (n = 1) to two-dimensional nanoplatelets (n = 2), one-dimensional nanowires (n = 3), and ultimately to zero-dimensional quantum dots (n = 4).[8-13] Among these, zero-dimensional (0D) perovskite-type materials are particularly fascinating, as they exhibit quantum confinement effects within isolated $[PbX_6]^{4-}$ octahedra, despite their relatively larger particle sizes.[14-16]

However, synthesizing these 0D perovskites in a phase-pure form remains a non-trivial challenge.[17] In this context, ionic liquids (ILs), which are highly customizable in terms of ionic structure and physicochemical properties, offer significant potential as growth-directing ligands for 0D perovskite synthesis.[18-20] Due to their modular ionic components, ILs allow precise tuning of parameters such as polarity, solvation capacity, and viscosity.[21-22] Furthermore, the self-assembly behavior and nanoscale organization of ILs vary widely depending on their molecular architecture, which enhances their suitability for use in functional material design.[18-20,23-24] Particularly, dicationic ionic liquids (DILs), comprising two cationic centers connected via a molecular spacer, offer improved thermal stability and stronger ionic interactions, which can assist in guiding nanocrystal growth, stabilizing intermediates, and directing crystallization pathways.[25-29]

All-inorganic cesium lead halide perovskites have shown tremendous promise for optoelectronic technologies, owing to their favorable characteristics like broad absorption spectra, sharp PL lines, tunable band gaps, high PL quantum yields, low trap-state densities, and excellent charge transport.[30-35] Among them, $CsPbX_3$ (X = Cl, Br, I) is a leading candidate, offering highly tunable photophysical characteristics.[30] In $CsPbX_3$, the electronic band edges are primarily governed by the Pb^{2+} and halide ions, while the spatial arrangement of $[PbX_6]^{4-}$ octahedra significantly influences the band gap.[30,36] When these octahedra are completely isolated from one another, the resulting structure is referred to as 0D perovskite, where excitons are confined within individual octahedral units.[14-16] A well-known example is Cs_4PbBr_6, a rhombohedral 0D perovskite in which each $[PbBr_6]^{4-}$ unit is separated by CsBr linkages.[14] This spatial confinement leads to significantly higher exciton binding energies (≥170 meV) compared to 3D $CsPbX_3$ nanocrystals (~40 meV).[13,16,30] Despite increasing interest in 3D and layered perovskites, 0D systems remain underexplored due to limited synthetic control and the frequent formation of $CsPbX_3$ as an impurity, which complicates phase identification and characterization.[14-16,37-39]

The luminescence behavior of Cs_4PbBr_6 is still debated. Some studies report strong green emission in the range of 515–520 nm,[14-16] while others find these nanocrystals to be non-emissive in the visible region due to a large band gap (>3.2 eV).[40] Ligand-mediated transformation from green-emitting $CsPbBr_3$ to non-fluorescent Cs_4PbBr_6 has also been demonstrated.[17,39] Moreover, PL in Cs_4PbBr_6 single crystals has been attributed to mid-gap states induced by halide vacancies.[41] The successful synthesis of highly luminescent Cs_4PbBr_6 microdisks (MDs) using surfactant ligands by Samanta and coworkers[42] underscores the critical role of surface chemistry in tuning optical properties. In this light, ionic liquids, particularly those with long alkyl chains, offer exciting potential as designer surface ligands for achieving precise control over phase purity, PL efficiency, and stability in 0D perovskite systems.

Nevertheless, the full potential of ILs in this context remains largely untapped and calls for further investigation.

In this work, we present a straightforward, room-temperature approach for synthesizing phase-pure Cs_4PbBr_6 MDs using an ionic liquid (IL)-mediated antisolvent precipitation method. This strategy allows for control over MDs morphology and size by tuning the alkyl chain length of mono-cationic ILs (MILs), adjusting their concentration, or incorporating dicationic ILs (DILs).[22,24] Recent reports suggest that the molecular organization of ILs is strongly dependent on both alkyl chain length and the specific nature of the ionic components.[25-29] Accordingly, both MILs and DILs function as growth-directing agents, guiding the morphology and optical features of the resulting 0D perovskites. Our findings show that ILs can effectively act as ligands to obtain phase-pure, highly stable 0D Cs_4PbBr_6 materials. Single-particle PL intensity and lifetime imaging confirm that the observed green emission is originated intrinsically from the MDs and not due to any fluorescent impurities. The green PL is attributed to defect-mediated recombination within the MDs, supported by temperature-dependent PL studies, which further reinforce an excitonic PL mechanism in these 0D structures.

4.2. Results and Discussion

Cs_4PbBr_6 MDs are synthesized via a ligand-assisted reprecipitation (LARP) method, where toluene is added as an anti-solvent to a vigorously stirred DMF solution containing CsBr and $PbBr_2$ in a 1:1 molar ratio, along with ionic liquids (ILs) serving as surface ligands. It is to be noted that the ILs serve as both surface-capping agents and directional growth templates (refer to Experimental Section for details).[18-20,42-43] Introducing toluene triggers the self-assembly of ILs into micelle-like structured domains, thereby establishing a spatially confined environment conducive to crystal nucleation and growth of the MDs through supersaturation.[42-

[43] It has also been established that the volume of anti-solvent added significantly influences the nucleation rate, particle size distribution, and optical features of the resulting MDs.[42] In the present investigation, a series of ionic liquids (ILs), namely [C_{12}mim]Br, [C_{14}mim]Br, [C_{16}mim]Br, and [C_{12}(mim)$_2$]Br_2, are employed as surface ligands during the synthesis of cesium lead bromide (Cs_4PbBr_6) MDs. The chemical structures of these ILs are illustrated in Chart APX4.1. These ILs are deliberately selected due to the presence of alkyl side chains, which are known to significantly influence the microscopic self-organization and phase behavior of IL assemblies. The length of the alkyl chain directly affects the molecular packing, steric hindrance, and interfacial interaction with the growing perovskite crystals. By exploiting ILs with different alkyl chain lengths, the study seeks to understand their influence on guiding the morphological development of the resulting microstructures.[25,42] In addition to the chain-length variation, the concentration of each IL is systematically adjusted throughout the synthesis. It is observed that each IL exhibits a specific optimal concentration window where the formation of well-faceted, monodisperse, and structurally consistent disk-shaped microcrystals is maximized. These findings highlight the critical role of both alkyl chain architecture and IL dosage in tailoring perovskite MDs formation.

To analyze the structural and morphological features of the synthesized Cs_4PbBr_6 MDs, a combination of advanced characterization techniques is employed. Field emission scanning electron microscopy (FESEM) and transmission electron microscopy (TEM) reveal that the MDs possess an average lateral size of ~1 μm, as shown in Figure 4.1a and Figure APX4.1. The corresponding thickness is estimated to be approximately 300 nm (Figure APX4.1). Elemental mapping (Figure 4.1b) demonstrates a homogeneous distribution of Cs, Pb, and Br throughout the MDs and also confirms the presence of surface-bound ionic liquids (ILs), indicating effective capping. To further investigate this interaction, we have performed FTIR measurements to establish the presence and binding mode of the ionic liquid as a surface

capping ligand. As shown in Figures APX4.2a and APX4.2b, the characteristic C–N stretching vibration of the imidazolium ring appears at ~1170 cm^{-1} for the free MILs and DILs. However, upon passivation with surface Pb^{2+} sites of Cs_4PbBr_6 MDs, this band is found to shift to a lower wavenumber by ~12 cm^{-1} for MIL and ~20 cm^{-1} for DIL (Figures APX4.2a and APX4.2b), clearly indicating electron density withdrawal from the C–N bond and confirming the binding interaction between the ionic liquid and the perovskite surface.

High-resolution TEM (HRTEM) imaging (Figure 4.1c) reveals distinct lattice fringes that correspond to the (110) and (300) crystallographic planes, which dominate the in-plane and side facets of the MDs, respectively. These observations are further established by the selected area electron diffraction (SAED) pattern (Figure 4.1d), which displays well-defined diffraction spots associated with the same planes, confirming the single-crystalline nature of the structures. Energy-dispersive X-ray spectroscopy (EDX) analysis (Figure 4.1e) provides an elemental composition close to Cs:Pb:Br = 4.4:1:6.9, which aligns well with the expected stoichiometry of Cs_4PbBr_6. Additionally, powder X-ray diffraction (PXRD) measurements (Figure 4.1f) verify that the MDs are composed solely of phase-pure rhombohedral Cs_4PbBr_6, with no detectable traces of secondary phases like $CsPbBr_3$. This observation is crucial, as the presence of $CsPbBr_3$ within the rhombohedral Cs_4PbBr_6 structure is often associated with the PL exhibited by the material.[15-38] The agreement between the SAED and PXRD results further confirms the high crystallinity and purity of the synthesized MDs.

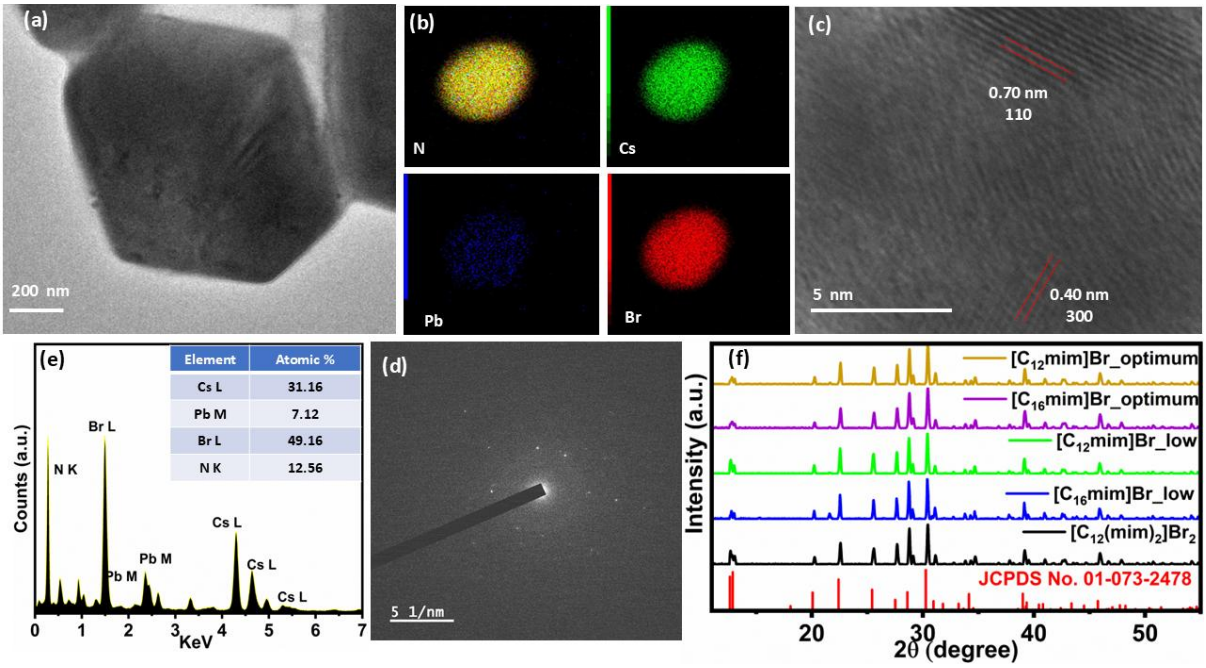

Figure 4.1. (a) TEM image of the Cs_4PbBr_6 MDs. (b) Elemental mapping confirms the uniform distribution of N, Cs, Pb, and Br elements across the MDs (c) HRTEM image showing lattice fringes of the (110) and (300) planes. (d) SAED pattern of a single MD indicating multiple crystallographic planes. (e) EDX spectrum and elemental composition of Cs_4PbBr_6. (f) Powder X-ray diffraction patterns of Cs_4PbBr_6 perovskite microstructure with different ILs and its different concentrations.

The morphology of Cs_4PbBr_6 MDs is found to be highly tunable by varying both the concentration and the structural nature of the ionic liquids (ILs) used in the precursor solution. FLIM images (Figure 4.2 and APX4.3) reveals that changes in IL concentration and chain length lead to significant differences in shape and size of the resulting microstructures. At lower IL concentrations (~0.05 mM), the ligands preferentially adsorb onto the (110) crystallographic plane, effectively restricting growth along this direction while facilitating accelerated extension perpendicular to it. This anisotropic growth results in the formation of large, spherical MDs with average diameters around 3 μm and comparatively thinner profiles, as shown in Figure APX4.4. In contrast, increasing the IL concentration to approximately 0.1 mM modifies the ligand-crystal interactions, promoting more uniform adsorption across multiple planes. This shift favors the development of well-defined polyhedral structures with sharp edges (Figure

4.2b). Interestingly, despite the isolated nature of $PbBr_6^{4-}$ octahedra within Cs_4PbBr_6, the Cs^+ ions help establish connectivity among them, which supports the emergence of polyhedral morphologies. This facet-controlled growth is further supported by high-resolution TEM analysis (Figure 4.1c), which shows that the MDs are enclosed by (110) and (300) planes along their in-plane and side-plane facets, respectively, consistent with their distinctive disk-like shape. The observation suggests a strong binding affinity of ILs for the (110) plane, thereby influencing growth direction and final morphology. At even higher IL concentrations (approaching saturation), a mixed morphology is observed, where both polyhedral MDs and micrometer-sized wires are simultaneously formed (Figure 4.2d). These wire-like structures likely correspond to a secondary phase, $CsPb_2Br_5$, as supported by SEM image (Figure APX4.5). Notably, similar microwire formation has previously been observed in related systems by Samanta and coworkers.[42] The role of IL structure is equally significant. FESEM images (Figure APX4.1, APX4.3 and APX4.4a) demonstrate that increasing the alkyl chain length in monocationic ILs leads to thicker nanoplatelets. Furthermore, the use of dicationic ionic liquids (DILs), even at lower concentrations (0.05 mM), results in the growth of well-defined polyhedral Cs_4PbBr_6 structures (Figure APX4.3), highlighting the templating ability of these ligands. Crucially, all these morphological variations maintain the same chemical composition, as confirmed by energy-dispersive X-ray (EDX) spectroscopy and elemental mapping (Figures APX4.4b,c), which show a consistent Cs:Pb:Br ratio matching Cs_4PbBr_6. The PXRD patterns (Figure 4.1f) of the spherical disks closely resemble those of the polyhedral structures, indicating similar crystalline characteristics and confirming their single-phase purity. Importantly, unlike many higher-dimensional perovskite structures, the IL-mediated Cs_4PbBr_6 MDs display remarkable ambient stability. They retain their shape and structure over several months under normal environmental conditions, underscoring their potential for practical applications.

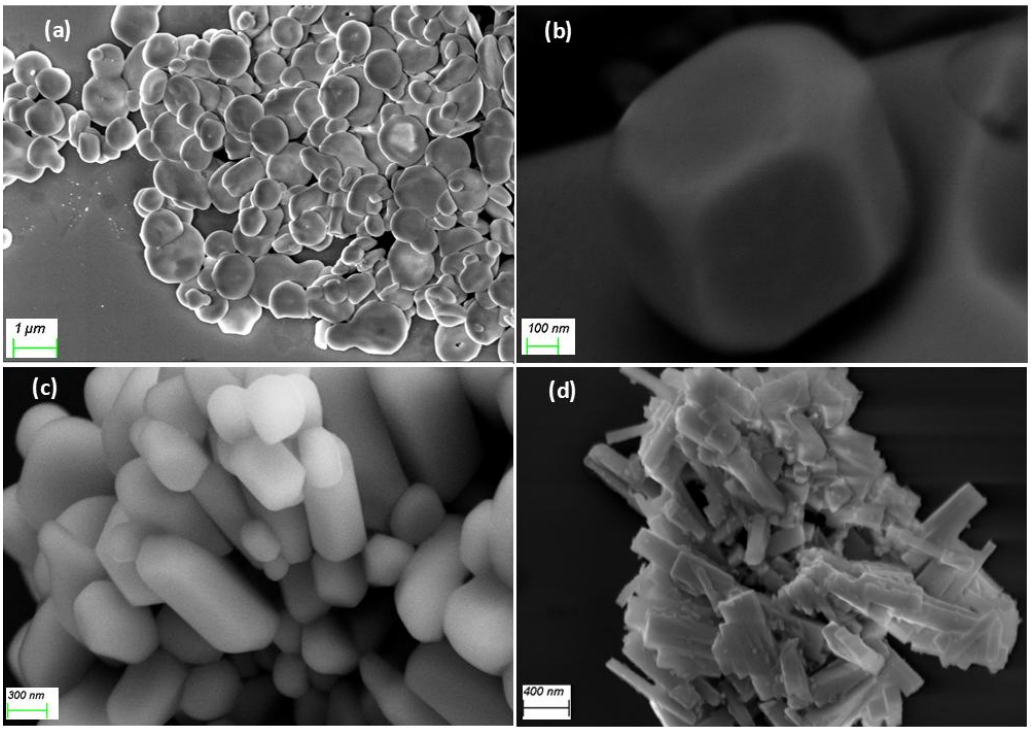

Figure 4.2. FESEM images showing the concentration-dependent morphological evolution of Cs_4PbBr_6 MDs synthesized using varying concentrations of $[C_{16}mim]Br$ ionic liquid: (a) 0.05 mM, (b) 0.1 mM, (c) 0.15 mM, and (d) 0.20 mM.

The well characterized Cs_4PbBr_6 microcrystals (MDs), as synthesized, exhibit striking green PL, making them highly promising for optoelectronic applications. Their optical behavior is comprehensively analyzed through steady-state ultraviolet-visible (UV-vis) absorption, PL, and excitation spectroscopy, as presented in Figure 4.3a. The PL spectrum reveals a sharp and intense PL peak centered at 515 nm (equivalent to 2.41 eV), with a narrow full width at half maximum (FWHM) of only 22 nm, indicative of high color purity and minimal defect-related broadening. The UV-vis absorption profile shows a distinct shoulder around 512 nm (2.42 eV), which is attributed to band-edge or excitonic transitions, along with a strong absorption band at 318 nm arising from higher-energy electronic transitions. Moreover, the extended absorbance tail also possibly indicates the existence of trap states or mid-gap energy levels within the material. Furthermore, the PL excitation spectrum demonstrates a well-defined peak at 508 nm (2.44 eV), which closely aligns with the absorption shoulder, suggesting that the

green emission originates from band-edge excitation processes. This spectral agreement underscores the high optical quality and well-defined electronic structure of the Cs_4PbBr_6 MDs.

The optical spectra of the as-synthesized Cs_4PbBr_6 microcrystals (MDs) closely resemble previous findings reported for Cs_4PbBr_6 powders and nanocrystals (NCs), with only minor deviations appearing in the short-wavelength region.[15-16] These subtle variations are commonly observed and are typically attributed to sample-dependent factors such as crystal size distribution or morphology. Based on the UV-visible absorption spectra and PL excitation data, the estimated optical band gap is approximately 2.43 eV. This value aligns well with the observed PL peak at 515 nm, which is consistent with semiconductor materials possessing a band gap near 2.4 eV.[17-42] The PL quantum yield (Table APX4.1) of the MDs reaches up to ~50% under optimized conditions. However, the PL efficiency proves to be highly sensitive to the synthetic environment, particularly the amount of antisolvent and the type of ionic liquid (IL) employed. When excessive antisolvent is used, the precursor solution becomes destabilized, resulting in uncontrolled formation of micelles and a broader size distribution of MDs.[44] These factors contribute to a noticeable reduction in PLQY, emphasizing the importance of finely tuned synthesis parameters. The PL characteristics of the MDs are also influenced by the alkyl chain length of the ILs. As the chain length increases, the PL progressively blue-shifts, from 525 nm to 515 nm (Figure 4.3b), accompanied by a corresponding increase in PLQY. This trend suggests that longer alkyl chains provide enhanced surface passivation or modify the local dielectric environment around the emissive centers. Additionally, MDs capped with dialkylimidazolium (DIL) ILs exhibit a more pronounced blue shift compared to those stabilized by monoalkylimidazolium (MIL), indicating stronger ligand-crystal interactions in the DIL systems. A concentration-dependent effect of $[C_{16}mim]Br$ ILs on PLQY is also evident. As shown in Figure 4.3c, the quantum yield increases with $[C_{16}mim]Br$ ILs concentration up to an optimal point, beyond which further increases lead to a

decline in PLQY. This behavior likely arises from oversaturation effects or the introduction of non-radiative recombination pathways due to excess surface-bound ILs. Moreover, the precursor-to-antisolvent volume ratio significantly impacts the crystal quality; a 4:1 ratio yields MDs with the most favorable structural and optical properties. The impact of morphology on optical response is further evaluated by comparing spherical and polyhedral MDs. While both forms exhibit comparable spectral profiles, the spherical MDs show a slight red shift (~3 nm) in their absorption, excitation, and PL spectra (Figure APX4.6). Their PLQY also drops slightly to ~30%, which can be attributed to their relatively larger particle size that may enhance non-radiative decay. Nonetheless, these values remain notably high, especially in contrast to the substantially reduced PLQY typically observed in thin-film forms of otherwise highly emissive perovskite nanocrystals.[45]

The PL behavior of 0D Cs_4PbBr_6 has been a topic of considerable debate in the literature. While many studies report strong green emission from Cs_4PbBr_6, there remains uncertainty regarding its true origin.[14-16,37-41] Several researchers have proposed that the observed PL may arise not from the Cs_4PbBr_6 phase itself but from trace quantities of $CsPbBr_3$ nanocrystals (NCs), which are often difficult to detect via conventional powder X-ray diffraction (PXRD) techniques.[46–47] Furthermore, the majority of prior investigations have relied on ensemble-level measurements, complicating the identification of the actual emitting species.

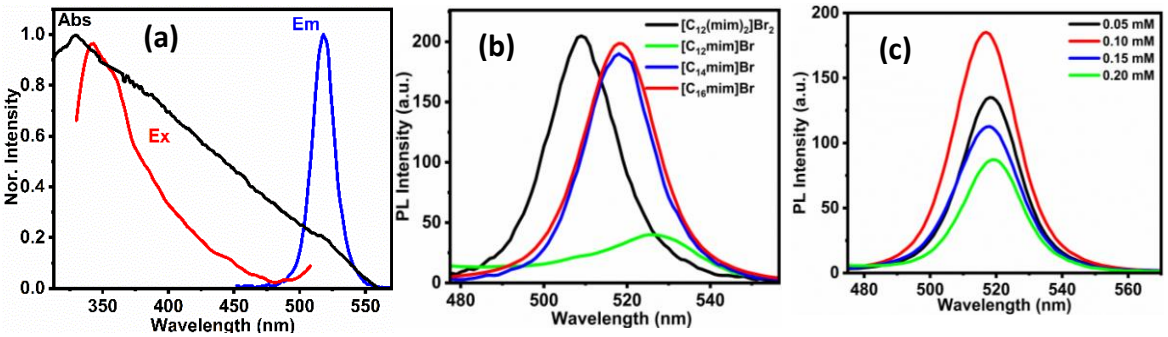

Figure 4.3. (a) Absorption, excitation (λ_{em}=515 nm), and PL spectra (λ_{ex}=405 nm) of Polyhedron Cs_4PbBr_6 MDs (b) PL spectra of $[C_{12}mim]Br$, $[C_{14}mim]Br$, $[C_{16}mim]Br$, and

$[C_{12}(mim)_2]Br_2$ ILs mediated Cs_4PbBr_6 MDs (C) PL spectra of Cs_4PbBr_6 MDs for various concentration of $[C_{16}mim]Br$ ILs as ligand during synthesis

To address this ambiguity and inspired by observation reported by Samanta and coworkers,[42] we have employed both steady-state and time-resolved confocal fluorescence microscopy at the single-particle level, focusing specifically on individual Cs_4PbBr_6 MDs (MDs). Fluorescence lifetime imaging microscopy (FLIM), along with corresponding intensity maps (Figure 4.4a-d, and APX4.7), reveals uniform PL across the surfaces of individual MDs. Such homogeneity strongly suggests that the luminescence originates intrinsically from the MDs rather than from localized defects or impurity phases. Had the PL stemmed from substantial amounts of $CsPbBr_3$ impurities, their presence would likely have been identifiable through PXRD or selected area electron diffraction (SAED). However, both techniques consistently confirm the exclusive formation of phase-pure Cs_4PbBr_6,[42] further supporting the conclusion that the observed PL is intrinsic to this phase. To reinforce this claim, we have performed halide exchange experiments using PbI_2 in DMF, a method well-known to induce rapid halide exchange in $CsPbBr_3$, but not in Cs_4PbBr_6.[16,43,48] Upon addition of the iodide source, the green PL of a $CsPbBr_3$ sample immediately redshifts, indicating the formation of iodide-substituted perovskites. In contrast, no spectral change is observed in the PL of the Cs_4PbBr_6dispersion, even after iodide exposure (Figure APX4.8a). This stark contrast confirms the absence of $CsPbBr_3$ contamination in our Cs_4PbBr_6 MD samples, as any such impurity would have undergone halide exchange, resulting in a visible PL shift.

Further support for the intrinsic nature of the PL is provided by fluorescence imaging of samples containing a known mixture of Cs_4PbBr_6 MDs and non-emissive $CsPb_2Br_5$ microwires, produced under specific IL concentrations (Figure APX4.5). In these mixed systems, only the MDs are visible in the FLIM images (Figure APX4.8b), whereas $CsPb_2Br_5$ microwires remain non-luminescent. If the PL had originated from dispersed $CsPbBr_3$ NCs,

both components would have been fluorescent due to equal distribution of the emissive impurity, an outcome that is clearly not observed.

To assess phase stability and the possibility of phase transformation under halide-rich conditions, we introduce a DMF solution of $PbBr_2$ to the MD dispersion. Field-emission scanning electron microscopy (FESEM) and energy-dispersive X-ray spectroscopy (EDX) (Figure APX4.9a-c) reveal that the MDs retain their original shape and dimensions, with elemental analysis confirming their Cs_4PbBr_6 stoichiometry. The bulk phase observed in the background is identified as excess $PbBr_2$. Notably, no signs of transformation into $CsPbBr_3$, upon addition of $PbBr_2$ with Cs_4PbBr_6 MDs, are detected, either morphologically or compositionally.

Moreover, PL measurements over time reveal only a slow and marginal decline in intensity (Figure APX4.9d), which we attribute to polar solvent–induced defect formation, consistent with previous reports.[42] Importantly, no abrupt change in PL intensity or profile is observed, which further argues against the presence of latent $CsPbBr_3$ undergoing conversion or degradation. Taken together, the uniform PL pattern, absence of phase impurities in structural analyses, stability against halide exchange, and selective fluorescence in mixed-phase systems unambiguously demonstrate that the green PL of these Cs_4PbBr_6 MDs is intrinsic. Unlike their nanocrystal counterparts, which often suffer from low or absent PL, these MDs represent a structurally stable and inherently luminescent form of Cs_4PbBr_6.

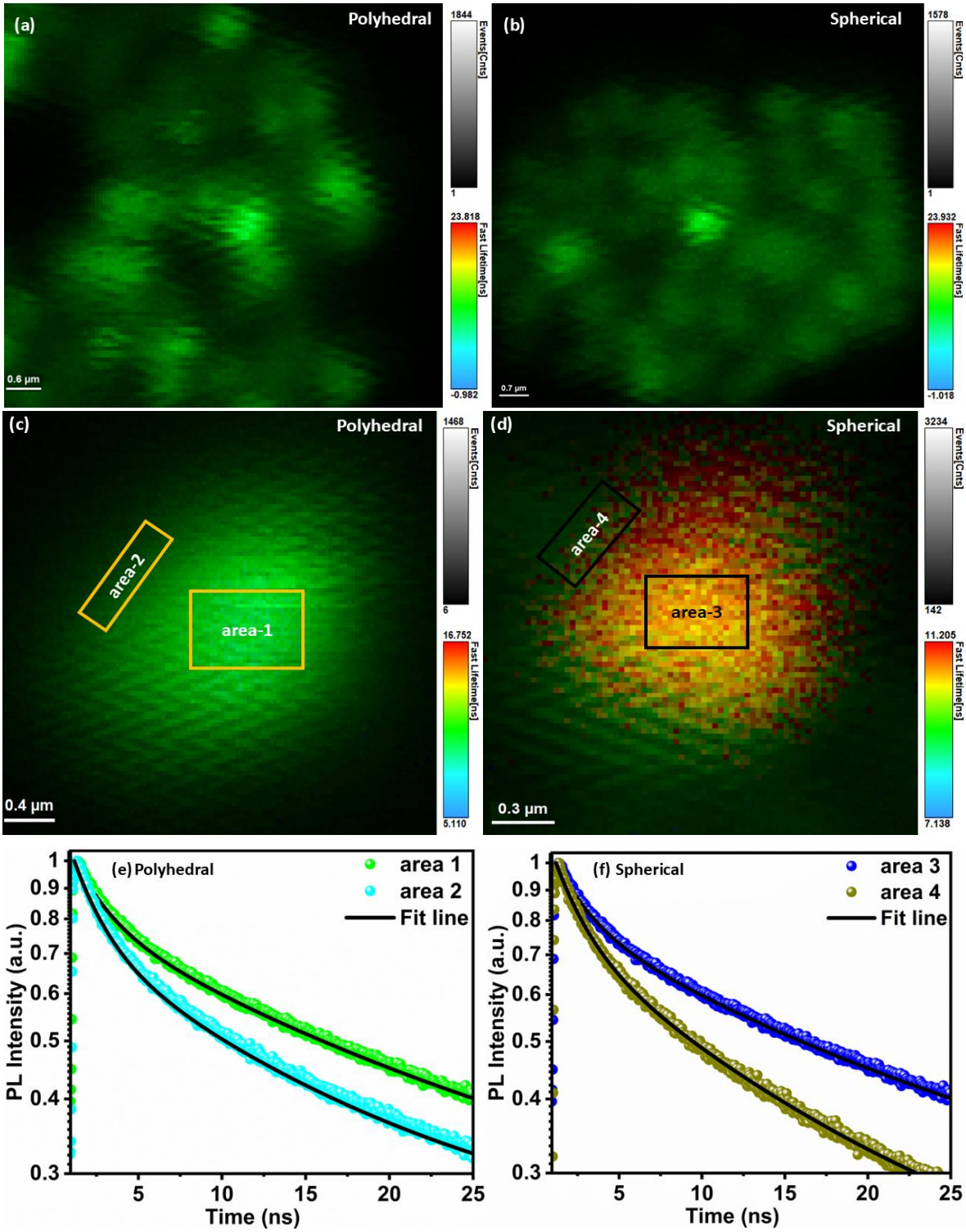

Figure 4.4. Fluorescence intensity and lifetime images (FLIM) of Cs_4PbBr_6 MDs highlighting spatial variation: (a) polyhedral particle, (b) spherical particles; (c, d) corresponding fluorescence intensity and lifetime images of single polyhedral and spherical MDs respectively. (e, f) PL decay curves from selected regions of the polyhedral (e) and spherical (f) MDs.

Fluorescence lifetime imaging microscopy (FLIM), combined with confocal fluorescence imaging, offers critical insights into the spatial dynamics of PL within individual Cs_4PbBr_6 MDs. As shown in Figure 4.4, the PL across the MDs is spatially non-uniform; central regions exhibit notably stronger PL intensity and longer lifetimes compared to the outer edges. This contrast implies a variation in local nonradiative recombination rates, which is likely driven by an increased density of surface defects near the periphery.[42] To quantitatively assess this heterogeneity, we extract localized PL decay profiles from specific regions of the polyhedral and spherical MDs (highlighted in Figure 4.4c, d, respectively). The decay curves conform well to a biexponential model, and the fitted parameters are presented in Table 4.1. In both polyhedral and spherical MDs, the inner regions (area-1, area-3) consistently show longer average PL lifetimes than the corresponding edge regions (area-2, area-4). This trend remains consistent across more than 10 individual MDs, with additional statistical details provided in Table APX4.2 (Appendix). Interestingly, while the short-lived lifetime component (τ_2) remains relatively constant across all sampled regions, the long-lived component (τ_3) exhibits significant spatial variability. The amplitude coefficients (α_2, α_3) further indicate a gradual enhancement in nonradiative decay pathways associated with deep trap states as one moves from the center toward the edges of the MDs. This suggests that nonradiative recombination becomes increasingly dominant at the particle boundaries, likely due to a higher concentration of surface-associated defects. These spatially resolved lifetime dynamics offer important clues about the nature of the green emission observed in Cs_4PbBr_6 MDs. Conventionally, the Cs_4PbBr_6 crystal structure, with its fully isolated $PbBr_6^{4-}$ octahedra, is associated with a wide band gap ($\geq$3.8 eV), which should preclude visible PL through direct band-to-band transitions.[40-41] However, the presence of green PL in our samples, alongside the absence of any detectable $CsPbBr_3$ impurities, points toward a defect-mediated recombination mechanism.[42,49-53]

This hypothesis is further supported by the dual-lifetime behavior observed in our FLIM data. The shorter lifetime component likely corresponds to the rapid recombination of excitons confined within the bulk of the microcrystals, an assignment consistent with the strong exciton binding energies reported for these materials.[17-18,41] The longer component, on the other hand, varies significantly across regions and is thus attributed to slower recombination via surface- or interface-related trap states. The central regions of the MDs, where the PL is brightest and the average lifetime longest, appear to be dominated by interior, shallower trap states. In contrast, the edges exhibit shorter average lifetimes and reduced PL, pointing to a prevalence of deep surface traps that facilitate faster nonradiative decay. These observations align well with earlier studies on similar systems[42] and reinforce the view that surface quality and defect passivation mediated by ionic liquid ligands critically influence the PL characteristics of Cs_4PbBr_6 microstructures. It is to be noted that the present observation indicates that sub-band-gap excitation leads to strong green emission via defect-assisted radiative recombination, which is consistent with the literature reports[41-42] attributing emissive mid-gap states to halogen vacancies or similar structural defects in 0-D perovskites. In this context, we also note that recent DFT studies on tin-based perovskites have also shown that iodine vacancies, which generate shallow traps in $CsSnI_3$, become deeper when the structure transforms to the zero-dimensional Cs_2SnI_6 phase[54]. By the same analogy, a similar mechanism is expected to occur in the present Cs_4PbBr_6, where the 0-D structural motif could stabilize deeper mid-gap states.

Table 4.1. Photoluminescence decay parameters of various regions of different MDs.

Sample	Region	τ_2 (α_2) ns	τ_3 (α_3) ns	τ_{av} ns[a]
Polyhedran MDs	area-1	2.45(0.25)	20.00(0.75)	15.61

Polyhedran MDs	area-2	2.04(0.35)	18.07(0.65)	12.45
Spherical MDs	area-3	2.70 (0.20)	19.00 (0.80)	15.74
Spherical MDs	area-4	2.50 (0.35)	16.00 (0.65)	11.28

[a]Experimental error = ±5%

In summary, our spatially resolved lifetime analysis clearly demonstrates that the green emission in Cs_4PbBr_6 MDs originates from intrinsic defect-related processes rather than band-edge transitions or extrinsic phases. The biexponential decay behavior, coupled with spatial variation in amplitude and lifetime, provides a coherent model in which both bulk and surface trap states govern the recombination pathway, with surface traps playing a larger role in nonradiative losses at the periphery of the MDs.

To gain deeper insight into the origin of PL in Cs_4PbBr_6 MDs, temperature-dependent PL spectra are recorded across the 90–300 K range (Figure 4.5a). The PL intensity demonstrates clear thermal sensitivity: from 90 K to 200 K, the PL intensity gradually decreases, followed by a more pronounced and monotonic decline between 200 K and 300 K. This evolution is more evident in the integrated PL intensity plot (Figure 4.5b).

Such temperature-induced quenching allows for the estimation of the exciton binding energy (E_a), a fundamental parameter dictating radiative recombination in semiconductors. The behavior is modeled using the Arrhenius equation:[55-56]

$$I(T) = \frac{I_0}{1+Ae^{-Ea/(k_BT)}} \quad (4.1)$$

where $I(T)$ is the PL intensity at temperature T, I_0 is the extrapolated intensity at 0 K, k_B is the Boltzmann constant, and A is a fitting constant. Using this model, the binding energy for

Cs_4PbBr_6 MDs is determined to be approximately 222 meV (Figure 4.5b), which significantly exceeds that of $CsPbBr_3$ quantum dots (~40 meV), yet is comparable to values reported for $CH_3NH_3PbBr_3$ quantum dots (~375 meV).[55-56] This high binding energy underscores that PL in Cs_4PbBr_6 arises predominantly through excitonic recombination rather than free-carrier transitions.

In parallel with PL quenching, a temperature-induced broadening of the PL band is observed (Figure 4.5c). The full-width at half-maximum (FWHM) increases from 9 nm at 90 K to 22 nm at 300 K. This trend is attributed to exciton–phonon interactions, which become more pronounced at elevated temperatures.[56-57] The temperature dependence of the FWHM is modeled using the Bose–Einstein equation:[56-57]

$$\Gamma(T) = \Gamma_0 + \sigma T + \frac{\Gamma_{op}}{e^{-\hbar\omega_{0p}/(k_B T)} - 1} \qquad (4.2)$$

where $\Gamma(T)$ is the linewidth at temperature T, Γ_0 accounts for inhomogeneous broadening, σ represents exciton–acoustic phonon coupling, and Γ_{op} and $\hbar\omega_{0p}$ characterize exciton–optical phonon interactions. The fitted parameters (Figure 4.5d) indicate that optical phonon coupling dominates in Cs_4PbBr_6 MDs. The extracted phonon energy (~42 meV) is consistent with the vibrational mode observed in Raman spectra (~314 cm^{-1}; Figure 4.5e), supporting strong exciton–optical phonon coupling.[57] Interestingly, the PL also exhibits a blue-shift with rising temperature (Figure 4.5a), which has also been reported in other perovskite and semiconductor systems such as $CH_3NH_3PbX_3$ and PbS.[58] This shift is likely a result of thermal redistribution of excitons: at lower temperatures, excitons occupy lower-energy trap states; as the temperature increases, phonon-mediated activation populates higher-energy states, resulting in a blue shift of the PL.[59-60] These findings collectively highlight the strong exciton localization and phonon interactions governing the optical behavior of Cs_4PbBr_6 MDs. The large exciton binding

energy, PL broadening, and thermally induced spectral shift all indicate that excitonic recombination plays a pivotal role in their photophysical properties.

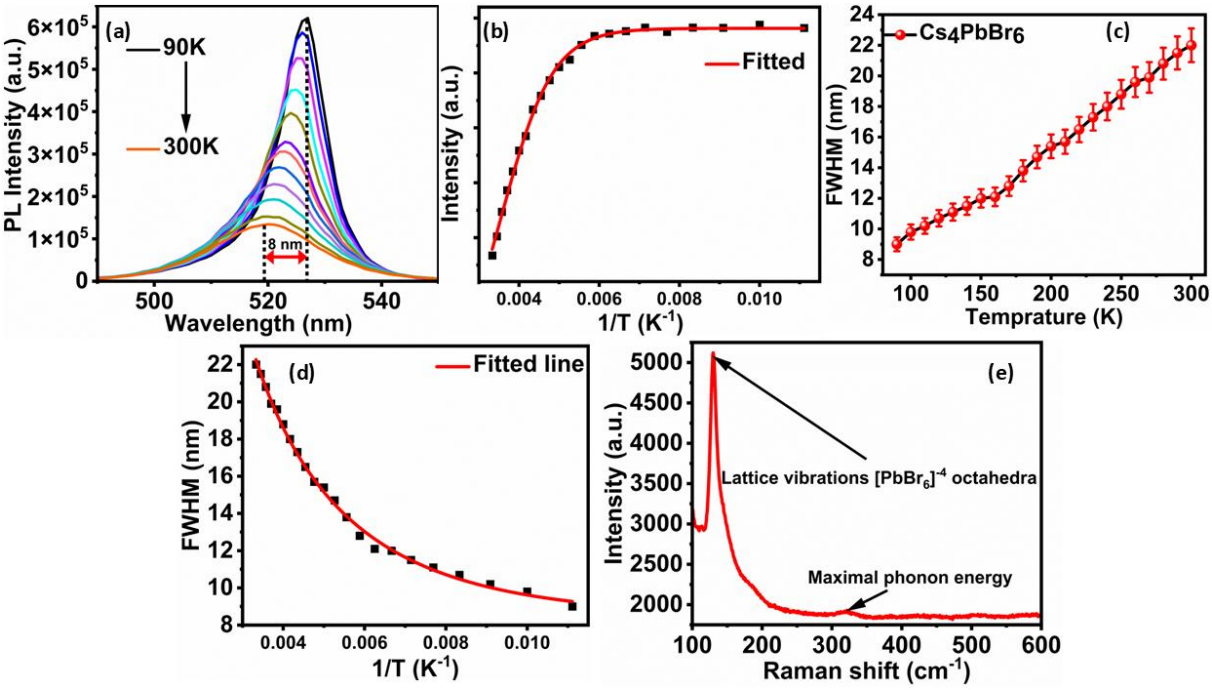

Figure 4.5. (a) Temperature-dependent PL spectra of Cs_4PbBr_6 MDs. (b) Integrated PL intensity, (c) plot of FWHM with temperature of Cs_4PbBr_6 MDs, and (d) plot of FWHM with 1/T of Cs_4PbBr_6 MDs (e) Raman spectrum of Cs_4PbBr_6 MDs sample.

4.3. Conclusion

In summary, we have developed a simple, room-temperature ionic liquid (IL)-mediated antisolvent precipitation method for synthesizing phase-pure Cs_4PbBr_6 MDs with tunable morphology. By adjusting the concentration and alkyl chain length of mono- and di-cationic ILs, we have successfully directed the shape evolution of the MDs from spherical to well-defined polyhedral structures. Comprehensive structural and elemental analyses, including PXRD, TEM, SAED, and EDX, confirm the high phase purity and single-crystalline nature of the synthesized MDs. Moreover, detailed photophysical investigations, including steady-state and time-resolved confocal fluorescence microscopic study, have clearly demonstrated that the green PL is originated intrinsically to the Cs_4PbBr_6 MDs and not due to $CsPbBr_3$ impurities.

FLIM imaging studies at the single-particle level have revealed significant spatial heterogeneity in PL intensity and lifetime, suggesting a crucial role of surface and interior defect states in the recombination dynamics. The coexistence of short and long PL decay components have supported two distinct recombination pathways, (i) exciton trapping in the bulk and (ii) surface trap-mediated recombination. Moreover, temperature-dependent PL studies have verified the excitonic origin of the PL, indicating a high exciton binding energy (~222 meV) and strong exciton–phonon coupling, both characteristic features of 0D perovskite systems. Additionally, the observed blue shift in the PL of 0D perovskite MDs with rising temperature is attributed to phonon-assisted thermal activation of higher-energy excitonic states. Interestingly, our findings have not only established the phase purity and intrinsic green emission of Cs_4PbBr_6 MDs but also provided deep insight into their excitonic recombination dynamics. These results underscore the potential of IL-mediated synthetic design strategies in tailoring the optical properties of low-dimensional perovskites for advanced optoelectronic applications.

4.4. Appendix

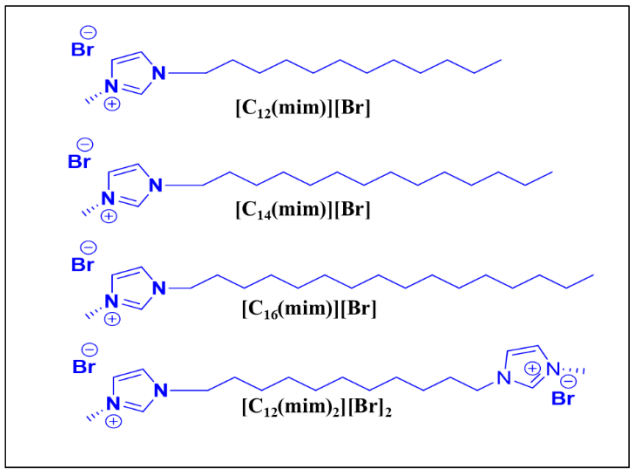

Chart APX4.1: Structure of MILs and DILs

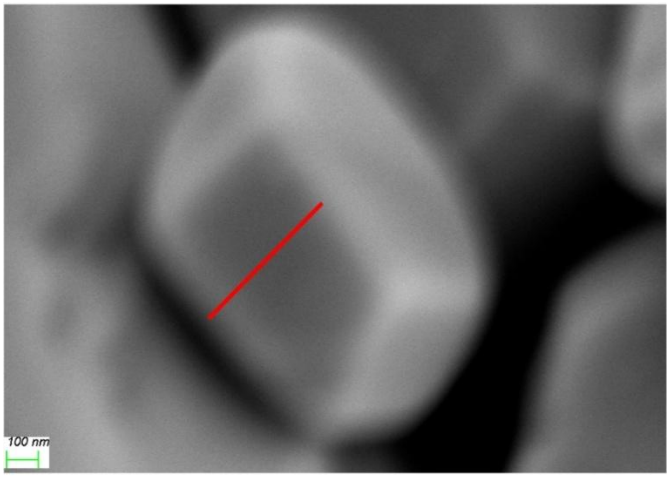

Figure APX4.1. FESEM image of polyhedron MDs showing thickness.

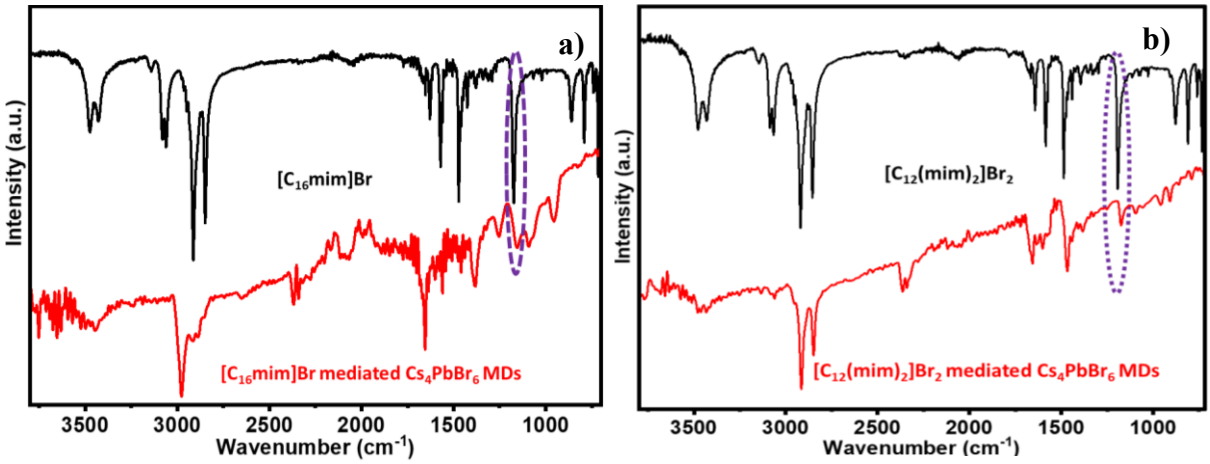

Figure APX4.2. FTIR spectra of a) $[C_{16}mim]Br$ and $[C_{16}mim]Br$ IL mediated Cs_4PbBr_6 MDs, b) $[C_{12}(mim)_2]Br_2$ and $[C_{12}(mim)_2]Br_2$ mediated Cs_4PbBr_6 MDs.

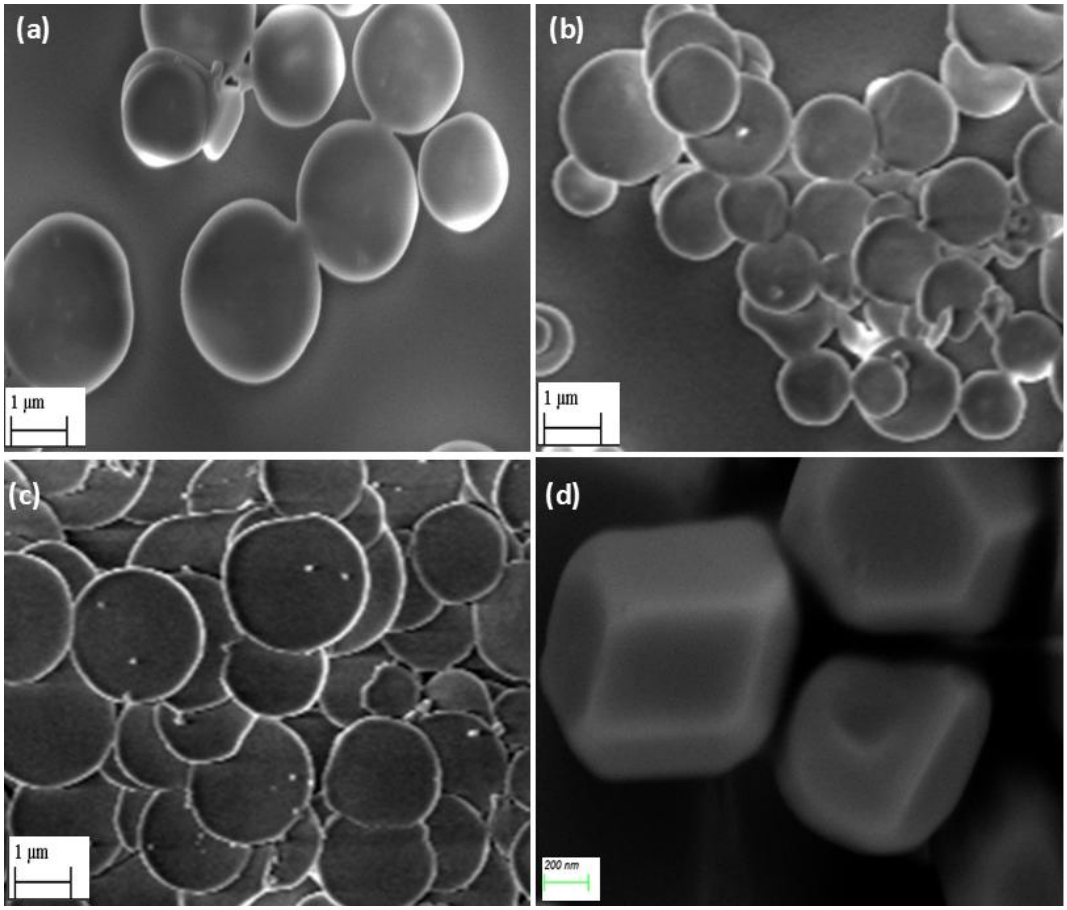

Figure APX4.3. FESEM image of (a) $[C_{12}mim]Br$, (b) $[C_{14}mim]Br$, (c) $[C_{16}mim]Br$ and (d) $[C_{12}(mim)_2]Br_2$ ILs mediated of Cs_4PbBr_6 perovskite MDs

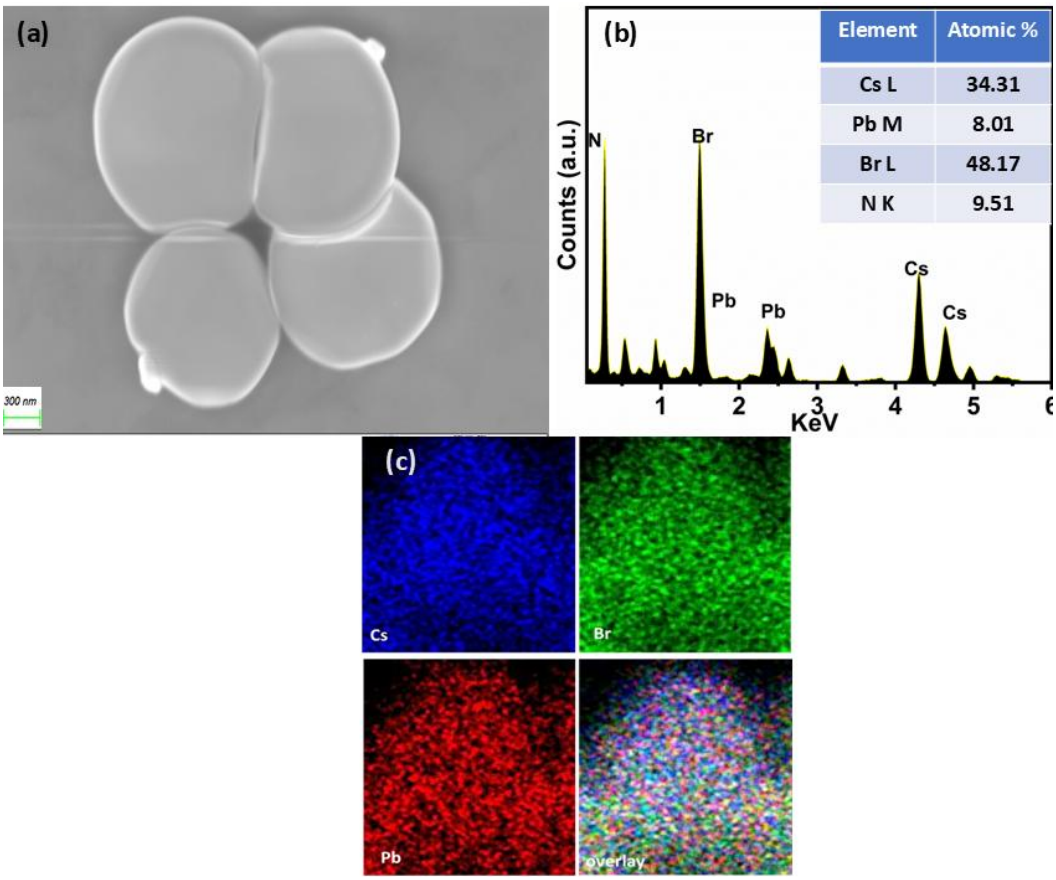

Figure APX4.4. (a) FESEM image of Spherical microdisks. (b) EDX spectrum confirms Cs_4PbBr_6 composition. (c) Elemental mapping of constituent elements shows their even distribution in the MDs.

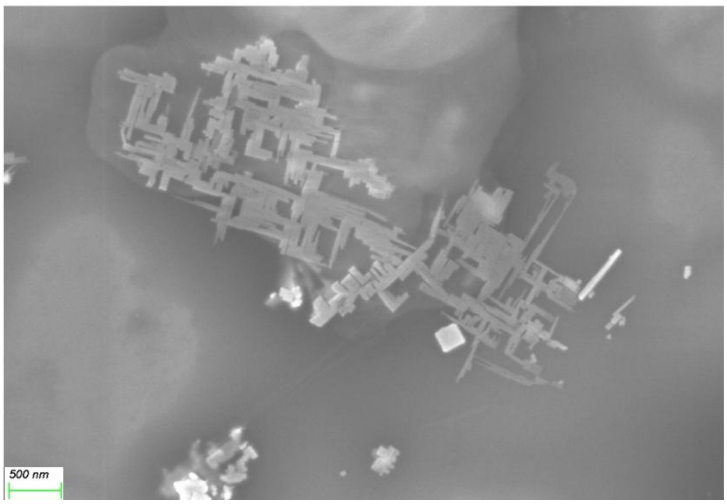

Figure APX4.5. FESEM image of the microwires particles.

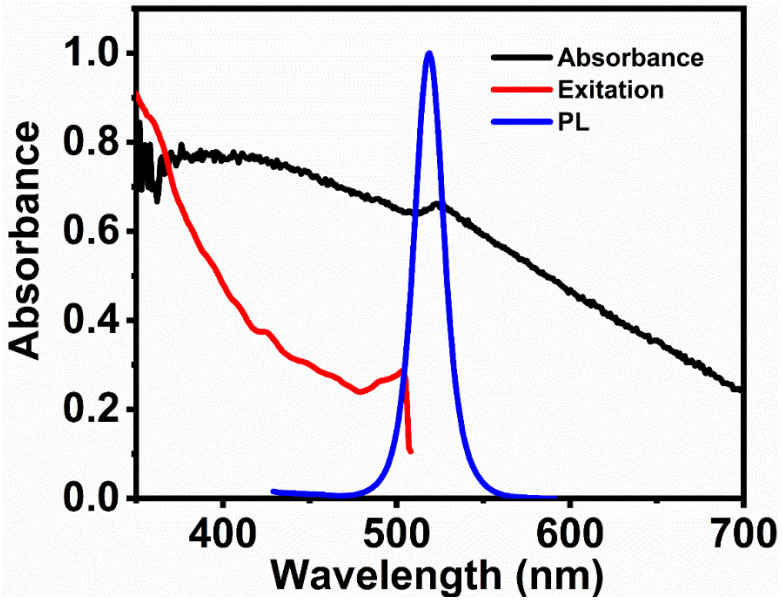

Figure APX4.6. Absorption, excitation and emission spectra of spherical Cs_4PbBr_6 MDs.

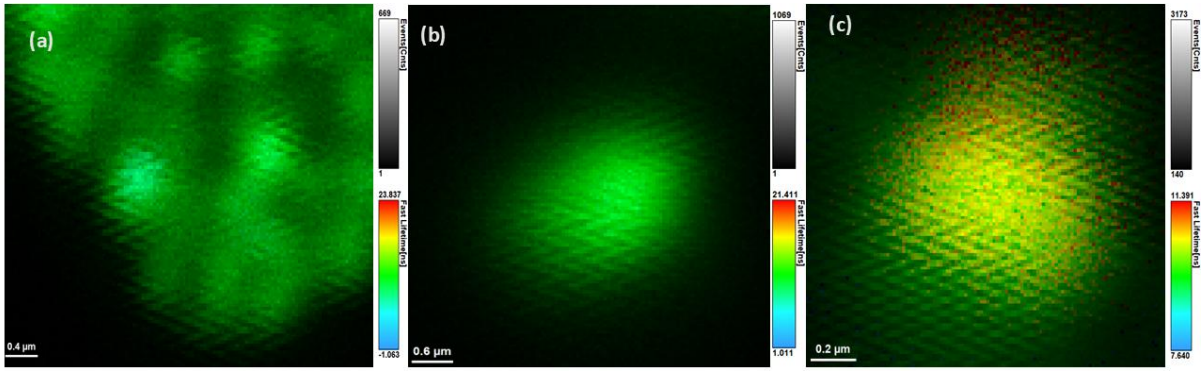

Figure APX4.7. FLIM images of (a) collective and (b, c) single Cs_4PbBr_6 MDs.

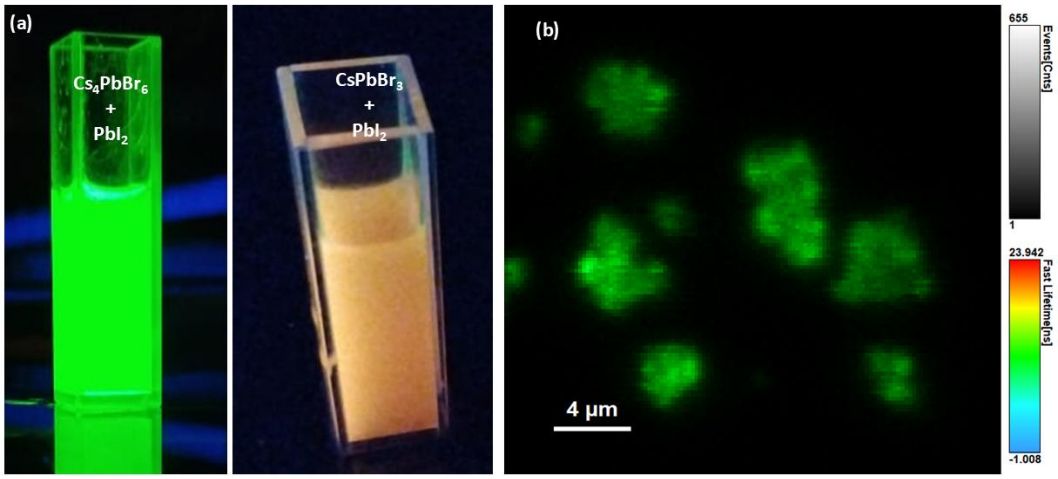

Figure APX4.8. (a) Digital image of PL (under UV light) of Cs_4PbBr_6 and $CsPbBr_3$ perovskite sample after adding PbI_2. (b) FLIM image of a mixture of microwire and MDs sample.

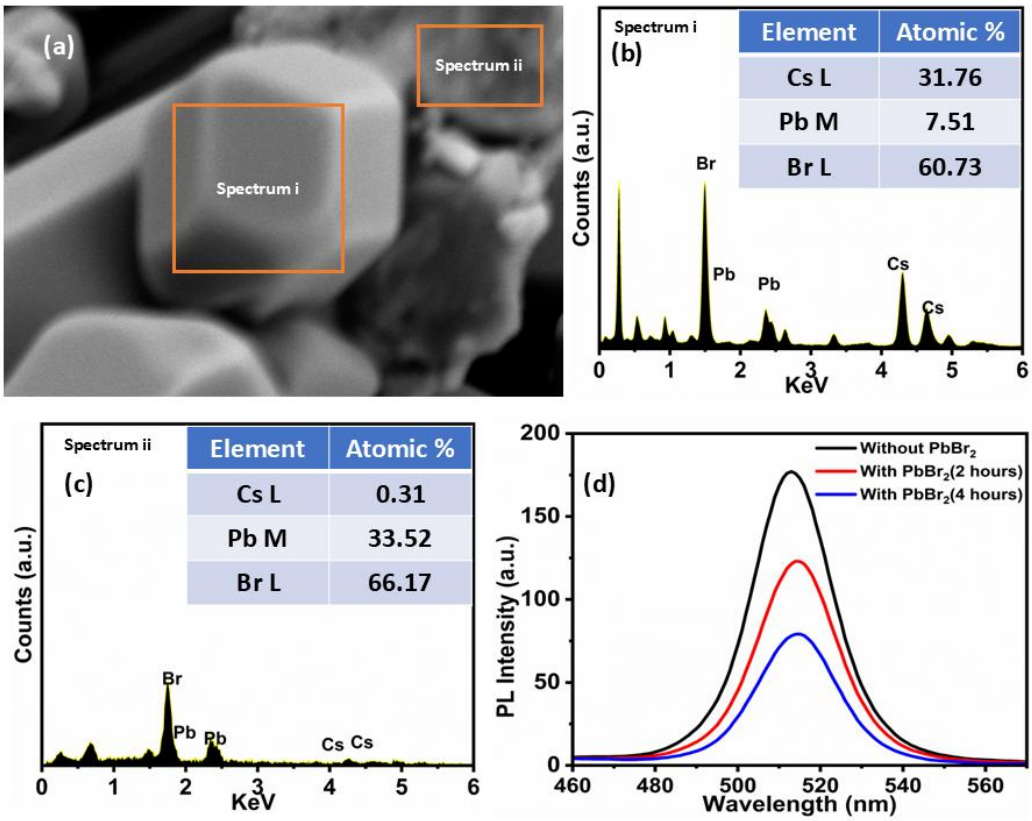

Figure APX4.9. (a) FESEM image of $PbBr_2$ solution added sample of Cs_4PbBr_6. (b) and (c) EDX spectra of different region as marked in panel a. (d) Change in emission spectrum (λ_{exc} = 405 nm) with time of adding DMF solution of $PbBr_2$ to a toluene dispersion of Cs_4PbBr_6 MDs

Table APX4.1. PLQY of different IL mediated Cs_4PbBr_6 MDs

Materials	**$\lambda_{Excitation}$**	**PLQY(%)**	**Error**
$[C_{12}mim]Br$ mediated Cs_4PbBr_6	405	30	±3
$[C_{14}mim]Br$ mediated Cs_4PbBr_6	405	40	±4
$[C_{16}mim]Br$ mediated Cs_4PbBr_6	405	45	±4
$[C_{12}(mim)_2]Br_2$ mediated Cs_4PbBr_6	405	50	±4

Table APX4.2. Average lifetime components along with their mean deviations of centre and edge areas on 10 individual MDs.

Sample	Region	τ_2 (α_2) ns	τ_3 (α_3) ns
MDs	Centre area	2.56±0.20(0.27±0.02)	20.72±0.93(0.73±0.03)
MDs	Edge area	2.16±0.09(0.37±0.02)	17.27±0.87(0.63±0.02)

4.5. References

1. Zhu, P.; Zhu, J. Low-dimensional metal halide perovskites and related optoelectronic applications. *InfoMat.* **2020**, *2*, 341–378.
2. Zhang, Y.; Liu, J.; Wang, Z.; Xue, Y.; Ou, Q.; Polavarapu, L.; Zheng, J.; Qiae, X.; Bao, Q. Synthesis, properties, and optical applications of low-dimensional perovskites. *Chem. Commun.*, **2016**, *52*, 13637-13655.
3. Chu, Z.; Chu, X.; Zhao, Y.; Ye, Q.; Jiang, J.; Zhang, X.; You, J. Emerging Low-Dimensional Crystal Structure of Metal Halide Perovskite Optoelectronic Materials and Devices. *Small Struct.* **2021**, 2, 2000133.
4. Wang, H.-P.; Li, S.; Liu, X.; Shi, Z.; Fang, X.; He, J.-H. Low-Dimensional Metal Halide Perovskite Photodetectors. *Adv. Mater.* **2021**, *33*, 2003309.
5. Yusoff, A. R. M.; Nazeeruddin, M. K. Low-Dimensional Perovskites: From Synthesis to Stability in Perovskite Solar Cells. *Adv. Energy Mater.* **2018**, *8*, 1702073.
6. Hoye, R. L. Z.; Hidalgo, J.; Jagt, R. A.; Correa-Baena, J.-P.; Fix, T.; MacManus-Driscol, J. L. The Role of Dimensionality on the Optoelectronic Properties of Oxide and Halide Perovskites, and their Halide Derivatives. *Adv. Energy Mater.* **2022**, 12, 2100499.
7. Manser, J. S.; Christians, J. A.; Kamat, P. V. Intriguing Optoelectronic Properties of Metal Halide Perovskites. *Chem. Rev.* **2016**, *116* (21), 12956–13008.15.

8. Akkerman, Q. A.; Motti, S. G.; Srimath Kandada, A. R.; Mosconi, E.; D'Innocenzo, V.; Bertoni, G.; Marras, S.; Kamino, B. A.; Miranda, L.; De Angelis, F. Solution synthesis approach to colloidal cesium lead halide perovskite nanoplatelets with monolayer-level thickness control. *J. Am. Chem. Soc.* **2016**, *138* (3), 1010-1016.
9. Amgar, D.; Stern, A.; Rotem, D.; Porath, D.; Etgar, L. Tunable length and optical properties of CsPbX3 (X= Cl, Br, I) nanowires with a few unit cells. *Nano Lett.* **2017**, 17 (2), 1007-1013.
10. Bekenstein, Y.; Koscher, B. A.; Eaton, S. W.; Yang, P.; Alivisatos, A. P. Highly luminescent colloidal nanoplates of perovskite cesium lead halide and their oriented assemblies. *J. Am. Chem. Soc.* **2015**, *137* (51), 16008-16011.
11. Imran, M.; Di Stasio, F.; Dang, Z.; Canale, C.; Khan, A. H.; Shamsi, J.; Brescia, R.; Prato, M.; Manna, L. Colloidal synthesis of strongly fluorescent CsPbBr3 nanowires with width tunable down to the quantum confinement regime. *Chem. Mater.* **2016**, *28* (18), 6450-6454.
12. Seth, S.; Samanta, A. A facile methodology for engineering the morphology of CsPbX3 perovskite nanocrystals under ambient condition. *Scientific Reports* **2016**, 6 (1), 37693.
13. Sun, S.; Yuan, D.; Xu, Y.; Wang, A.; Deng, Z. Ligand-mediated synthesis of shape-controlled cesium lead halide perovskite nanocrystals via reprecipitation process at room temperature. *ACS Nano* **2016**, *10* (3), 3648-3657.
14. Cha, J.-H.; Han, J. H.; Yin, W.; Park, C.; Park, Y.; Ahn, T. K.; Cho, J. H.; Jung, D.-Y. Photoresponse of CsPbBr3 and Cs4PbBr6 perovskite single crystals. *J. Phys. Chem. Lett.* **2017**, *8* (3), 565-570.
15. Saidaminov, M. I.; Almutlaq, J.; Sarmah, S.; Dursun, I.; Zhumekenov, A. A.; Begum, R.; Pan, J.; Cho, N.; Mohammed, O. F.; Bakr, O. M. Pure Cs4PbBr6: highly luminescent zero-dimensional perovskite solids. *ACS Energy Lett.* **2016**, *1* (4), 840-845.

16. Zhang, Y.; Saidaminov, M. I.; Dursun, I.; Yang, H.; Murali, B.; Alarousu, E.; Yengel, E.; Alshankiti, B. A.; Bakr, O. M.; Mohammed, O. F. Zero-dimensional Cs4PbBr6 perovskite nanocrystals. *J. Phys. Chem. Lett.* **2017**, *8* (5), 961-965.
17. Seth, S.; Samanta, A. Photoluminescence of Zero-Dimensional Perovskites and Perovskite-Related Materials. *J. Phys. Chem. Lett.* **2018**, *9*, 176−183.
18. Shahiduzzaman, M.; Yamamoto, K.; Furumoto, Y.; Kuwabara, T.; Takahashi, K.; Taima, T. Ionic Liquid-Assisted Growth of Methylammonium Lead Iodide Spherical Nanoparticles by a Simple Spin-coating Method and Photovoltaic Properties of Perovskite Solar Cells. *RSC Adv.* **2015**, *5*, 77495.
19. Shahiduzzaman, M.; Muslih, E. Y.; Hasan, A. K. M.; Wang, L.; Fukaya, S.; Nakano, M.; Karakawa, M.; Takahashi, K.; Akhtaruzzaman, M.; Nunzi, J. M.; Taima, T. The benefits of ionic liquids for the fabrication of efficient and stable perovskite photovoltaics. *Chem. Eng. J.* **2021**, *411*, 128461.
20. Wang, S.; Li, Z.; Zhang, Y.; Liu, X.; Han, J.; Li, X.; Liu, Z.; Liu, S. F.; Choy, W. C. H. Water-Soluble Triazolium Ionic-Liquid Induced Surface Self-Assembly to Enhance the Stability and Efficiency of Perovskite Solar Cells. *Adv. Funct. Mater.* **2019**, *29*, 1900417.
21. Welton, T. Room-Temperature Ionic Liquids. Solvents for Synthesis and Catalysis. *Chem. Rev.* **1999**, *99,* 2071.
22. Geng, F.; Liu, J.; Zheng, L.; Yu, L.; Li, Z.; Li, G.; Tung, C. Micelle Formation of Long-Chain Imidazolium Ionic Liquids in Aqueous Solution Measured by Isothermal Titration Microcalorimetry. *J. Chem. Eng. Data* **2010**, *55*(1), 147–151.
23. Zhang, W.; Liu, X.; He, B.; Gong, Z.; Zhu, J.;Ding, Y.; Chen, H.; Tang, Q. Interface Engineering of Imidazolium Ionic Liquids toward Efficient and Stable CsPbBr3 Perovskite Solar Cells. *ACS Appl. Mater. Interfaces* **2020**, *12*, 4540.

24. Wang, T.; Kaper, H. Antonietti, M. Smarsly, B. Templating Behavior of a Long-Chain Ionic Liquid in the Hydrothermal Synthesis of Mesoporous Silica. *Langmuir* **2007**, *23*(3) 1489–1495.

25. Das, S. K.; Majhi, D.; Sahu, P. K.; Sarkar, M. Investigation of the influence of alkyl side chain length on the fluorescence response of C153 in a series of room temperature ionic liquids. *RSC Adv.*, **2015**, *5*, 41585.

26. Daschakraborty, S.; Biswas, R. Stokes Shift Dynamics in (Ionic Liquid + Polar Solvent) Binary Mixtures: Composition Dependence. *J. Phys. Chem. B* **2011**, *115*, 14, 4011–4024.

27. Sahu, P. K.; Das, S. K.; Sarkar, M. Fluorescence response of a dipolar organic solute in a dicationic ionic liquid (IL): is the behavior of di-cationic IL different from that of usual monocationic IL? *Phys. Chem. Chem. Phys.* **2014**, *16*, 12918-12928.

28. Majhi, D.; Seth, S.; Sarkar, M. Differences in the behavior of dicationic and monocationic ionic liquids as revealed by time resolved-fluorescence, NMR and fluorescence correlation spectroscopy. *Phys. Chem. Chem. Phys.*, **2018**, *20*, 7844-7856.

29. Sahu, P. K.; Das, S. K.; Sarkar, M. Toward Understanding Solute−Solvent Interaction in Room-Temperature Mono- and Dicationic Ionic Liquids: A Combined Fluorescence Spectroscopy and Mass Spectrometry Analysis. *J. Phys. Chem. B* **2014**, *118*, 1907−1915.

30. Protesescu, L.; Yakunin, S.; Bodnarchuk, M. I.; Krieg, F.; Caputo, R.; Hendon, C. H.; Yang, R. X.; Walsh, A.; Kovalenko, M. V. Nanocrystals of cesium lead halide perovskites (CsPbX3, X= Cl, Br, and I): novel optoelectronic materials showing bright emission with wide color gamut. *Nano Lett.* **2015**, *15* (6), 3692-3696.

31. Ramasamy, P.; Lim, D.-H.; Kim, B.; Lee, S.-H.; Lee, M.-S.; Lee, J.-S. All-inorganic cesium lead halide perovskite nanocrystals for photodetector applications. *Chem. Commun.* **2016**, *52* (10), 2067-2070.
32. Song, J.; Li, J.; Li, X.; Xu, L.; Dong, Y.; Zeng, H. Quantum dot light-emitting diodes based on inorganic perovskite cesium lead halides (CsPbX3). *Advanced materials* **2015**, *27* (44), 7162-7167.
33. Swarnkar, A.; Marshall, A. R.; Sanehira, E. M.; Chernomordik, B. D.; Moore, D. T.; Christians, J. A.; Chakrabarti, T.; Luther, J. M. Quantum dot-induced phase stabilization of alpha-CsPbI3 perovskite for high-efficiency photovoltaics. *Science* **2016**, *354* (6308), 92-95.
34. Yakunin, S.; Protesescu, L.; Krieg, F.; Bodnarchuk, M. I.; Nedelcu, G.; Humer, M.; De Luca, G.; Fiebig, M.; Heiss, W.; Kovalenko, M. V. Low-threshold amplified spontaneous emission and lasing from colloidal nanocrystals of caesium lead halide perovskites. *Nature Commun.* **2015**, *6* (1), 8056.
35. Zhang, Q.; Su, R.; Liu, X.; Xing, J.; Sum, T. C.; Xiong, Q. High-quality whispering-gallery-mode lasing from cesium lead halide perovskite nanoplatelets. *Adv. Funct. Mater.* **2016**, *26* (34), 6238-6245.
36. Saparov, B.; Mitzi, D. B. Organic–inorganic perovskites: structural versatility for functional materials design. *Chem. Rev.* **2016**, *116* (7), 4558-4596.
37. Chen, D.; Wan, Z.; Chen, X.; Yuan, Y.; Zhong, J. Large-scale room-temperature synthesis and optical properties of perovskite-related Cs4PbBr6 fluorophores. *J. Mater. Chem. C* **2016**, *4* (45), 10646-10653.
38. Huang, K.; Li, D.; Yang, L.; Liu, S.; Yang, F. Solution-processed approach to highly luminescent trigonal Cs4PbBr6 nanodisks and their underlying shape evolution. *J. Alloys Compd.* **2017**, *710*, 244-252.

39. Liu, Z.; Bekenstein, Y.; Ye, X.; Nguyen, S. C.; Swabeck, J.; Zhang, D.; Lee, S.-T.; Yang, P.; Ma, W.; Alivisatos, A. P. Ligand mediated transformation of cesium lead bromide perovskite nanocrystals to lead depleted Cs4PbBr6 nanocrystals. *J. Am. Chem. Soc.* **2017**, *139* (15), 5309-5312.

40. Akkerman, Q. A.; Park, S.; Radicchi, E.; Nunzi, F.; Mosconi, E.; De Angelis, F.; Brescia, R.; Rastogi, P.; Prato, M.; Manna, L. Nearly monodisperse insulator Cs4PbX6 (X= Cl, Br, I) nanocrystals, their mixed halide compositions, and their transformation into CsPbX3 nanocrystals. *Nano Lett.* **2017**, *17* (3), 1924-1930.

41. De Bastiani, M.; Dursun, I.; Zhang, Y.; Alshankiti, B. A.; Miao, X.-H.; Yin, J.; Yengel, E.; Alarousu, E.; Turedi, B.; Almutlaq, J. M.; Saidaminov, M. I.; Mitra, S.; Gereige, I.; AlSaggaf, A.; Zhu, Y.; Han, Y.; Roqan, I. S.; Bredas, J.-L.; Mohammed, O. F.; Bakr, O. M. Inside Perovskites: Quantum Luminescence from Bulk Cs4PbBr6 Single Crystals. *Chem. Mater.* **2017**, *29* (17), 7108-7113.

42. Seth, S.; Samanta, A. Fluorescent Phase-Pure Zero-Dimensional Perovskite-Related Cs4PbBr6 Microdisks: Synthesis and Single-Particle Imaging Study. *J. Phys. Chem. Lett.* **2017**, *8* (18), 4461-4467.

43. Seth, S.; Samanta, A. A Facile Methodology for Engineering the Morphology of CsPbX3 Perovskite Nanocrystals under Ambient Condition. *Sci. Rep.* **2016**, *6*, 37693.

44. Frank, K.; Henke, N. A.; Lampe, C.; Lorenzen, T.; März, B.; Sun, X.; Haas, S.; Gutowski, O.; Dippel, A. C.; Mayer, V.; Müller-Caspary, K.; Urban, A. S.; Nickel, B. Antisolvent controls the shape and size of anisotropic lead halide perovskite nanocrystals. *Nat Commun.* **2024,** *17*,15, 8952.

45. Kim, Y.; Yassitepe, E.; Voznyy, O.; Comin, R.; Walters, G.; Gong, X.; Kanjanaboos, P.; Nogueira, A. F.; Sargent, E. H. Efficient Luminescence from Perovskite Quantum Dot Solids. *ACS Appl. Mater. Interfaces* **2015**, *7*, 25007−25013.

46. Akkerman, Q. A.; Park, S.; Radicchi, E.; Nunzi, F.; Mosconi, E.; De Angelis, F.; Brescia, R.; Rastogi, P.; Prato, M.; Manna, L. Nearly Monodisperse Insulator Cs4PbX6 (X = Cl, Br, I) Nanocrystals, Their Mixed Halide Compositions, and Their Transformation into CsPbX3 Nanocrystals. *Nano Lett.* **2017**, *17*, 1924−1930.

47. Li, X.; Cao, F.; Yu, D.; Chen, J.; Sun, Z.; Shen, Y.; Zhu, Y.; Wang, L.; Wei, Y.; Wu, Y.; et al. All Inorganic Halide Perovskites Nanosystem: Synthesis, Structural Features, Optical Properties and Optoelectronic Applications. *Small* **2017**, *13*, 1603996.

48. Nedelcu, G.; Protesescu, L.; Yakunin, S.; Bodnarchuk, M. I.; Grotevent, M. J.; Kovalenko, M. V. Fast Anion-Exchange in Highly Luminescent Nanocrystals of Cesium Lead Halide Perovskites (CsPbX3, X = Cl, Br, I). *Nano Lett.* **2015**, *15*, 5635−5640.

49. Seth, S.; Mondal, N.; Patra, S.; Samanta, A. Fluorescence Blinking and Photoactivation of All-Inorganic Perovskite Nanocrystals CsPbBr3 and CsPbBr2I. *J. Phys. Chem. Lett.* **2016**, *7*, 266−271.

50. Ball, J. M.; Petrozza, A. Defects in Perovskite-Halides and their Effects in Solar Cells. *Nat. Energy* **2016**, *1*, 16149.

51. Kang, J.; Wang, L.-W. High Defect Tolerance in Lead Halide Perovskite CsPbBr3. *J. Phys. Chem. Lett.* **2017**, *8*, 489−493.

52. Krishnan, E.; Elizabeth, V.; Thomas, M.; Prasad, L.; Thomas, K. G. Trap States in Semiconductor Quantum Dots: Friends or Foes. *J. Phys. Chem. C* **2024**, *128*, 4373−4382.

53. Mandal, S.; Mukherjee, S.; De, C. K.; Roy, D.; Ghosh, S.; and Mandal, P. K. Extent of Shallow/Deep Trap States Beyond Conduction Band Minimum in Defect Tolerant CsPbBr3 Perovskite Quantum Dot: Control Over the Degree of Charge Carrier Recombination. *J. Phys. Chem. Lett.* **2020**, *11*, 1702-1707.

54. Xiao, Z.; Zhou, Y.; Hosono, H.; Kamiya, T. Intrinsic defects in aphotovoltaic perovskite variant Cs2SnI6. *Phys. Chem. Chem. Phys.* **2015**, *17*, 18900−18903.

55. Zhang, F.; Zhong, H. Chen, C.; Wu, X.; Hu, X.; Huang, H.; Han, J.; Zou, B.; Dong, Y. Brightly Luminescent and Color-Tunable Colloidal $CH_3NH_3PbX_3$(X = Br, I, Cl) Quantum Dots: Potential Alternatives for Display Technology. *ACS Nano* **2015**, *9*, 4533–4542.

56. Li, X.; Wu, Y.; Zhang, S.; Cai, B.; Gu, Y.; Song, J.; Zeng, H. $CsPbX_3$ Quantum Dots for Lighting and Displays: Room-Temperature Synthesis, Photoluminescence Superiorities, Underlying Origins and White Light-Emitting Diodes. *Adv. Funct. Mater.* **2016**, *26*, 2435–2445.

57. Diroll, B. T.; Murray, C. B. High-Temperature Photoluminescence of CdSe/CdS Core/Shell Nanoheterostructures, *ACS Nano* **2014**, *8,* 6466–6474.

58. Deya, P.; Paula, J.; Bylsmaa, J.; Karaiskaja, D.; Lutherb, J. M.; Beardb, M. C.; Romero, A. H. Origin of the temperature dependence of the band gap of PbS and PbSe quantum dots. *Solid State Commun.* **2013**, *165*, 49–54.

59. Ozel, T.; Hernandez-Martinez, P. L.; Mutlugun, E.; Akin, O.; Nizamoglu, S.; Ozel, I.; Zhang, Q.; Xiong, Q.; Demir, H. V. Observation of Selective Plasmon-Exciton Coupling in Nonradiative Energy Transfer: Donor-Selective versus Acceptor-Selective Plexcitons. *Nano Lett.* **2013**, *13*(7), 3065–3072.

60. Kulakovskii, V. D.; Bacher, G.; Weigand, R.; Kummell T.; Forchel, A. Fine Structure of Biexciton Emission in Symmetric and Asymmetric CdSeZnSe Single Quantum Dots. *Phys. Rev. Lett.* **1999**, *82*, 1780.

CHAPTER 5

Energy Transfer Induced Enhanced Valley Splitting of Emission of Inorganic CdTe@ZnS QDs in Presence of Organic J-Aggregates

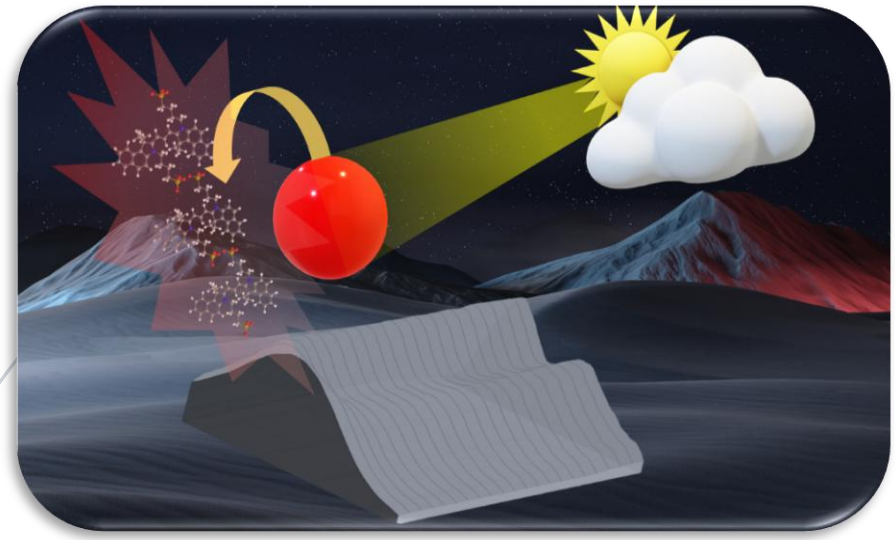

Abstract

An inorganic-organic nanohybrid material comprising an inorganic exciton (CdTe@ZnS Quantum Dots) and an organic exciton (J-aggregates) has been synthesized, and subsequently investigations on exciton-exciton coupling between two components of the materials are carried out by employing various spectroscopic techniques. Analysis of the data has revealed very high Förster-type resonance energy transfer (FRET) from the donor QDs to acceptor J-aggregates. Interestingly, a clear splitting of the QD emission band is observed during the FRET event, indicating efficient coupling between inorganic and organic excitons. The observation of valley splitting of QD emission by organic J-aggregates, even in the absence of an external field is new and exciting. More interestingly, the investigations have also shown that the valley splitting of the QD emission can be controlled by regulating the FRET process. In fact, a linear relationship between the energy separation value of the valley splitting and FRET efficiency between QD and J-aggregate is obtained. Moreover, in the present hybrid system, the presence of organic moiety becomes advantageous in a sense that the valley splitting can also be controlled easily through chemical modification of the organic moiety. The outcome of the present investigation essentially demonstrated that the present nanohybrid system can be considered as a potential candidate for the fabrication of valleytronic materials.

5.1. Introduction

Materials combining semiconductor quantum dots (QDs) and J-aggregates are expected to have tremendous potential in terms of producing a new excitonic material where the coupled excitations can be found to be very different than those of the optical excitations of the individual components.[1-12] Interestingly, these hybrid associates can also open up possibilities of fabricating new photon processing materials at the nanometer length scale whose optical and

electronic properties would require the long-range transport of electrons and holes.[11-14] Efficient coupling between the excitonic components can give rise to exciting processes such as photoluminance (PL) valley splitting, Rabi splitting, etc., which can have significant implications in the field of valleytronics.[15-21] While it is known that molecular aggregates can be coupled coherently with inorganic photonics/excitonic materials, a very limited amount of information is available on how they talk to each other in a nanohybrid assembly, and more importantly, how to control the coupling that happens between the interacting components of the concerned materials.

Strong coupling usually happens involving two systems, where one needs to be strongly confined and another needs to possess a strong transition dipole moment.[22-26] The strength of such coupling can be given as $g = \mu_e|E_{vac}| \propto \mu_e/\sqrt{V}$, where g is the coupling strength, E_{vac} is the vacuum field, and V is the mode volume.[22-23] In recent times, strongly coupled nanoscale assembly in which coupling between local surface plasmon resonance (LSPR) with excitons, excitons with photons, etc.[22,23,27,28] have attracted considerable attention from academia and industry owing to their potential applications in the field of artificial light harvesting, threshold-less lasing, sensing, quantum information processing, optical computing, etc.[29-32] In fact, it has been recently proposed that strong coupling between two suitable interacting systems, such as exciton-exciton, exciton-plasmon, exciton–photon and photon-plasmon, can produce future-generation materials for various optoelectronic applications.[29-33] Strong coupling has also been demonstrated in the hybrid nanosystems comprising of plasmonic nanoparticles and cyanine dye J-aggregates.[18] Interestingly, it has been demonstrated that strong coupling can also lead to an interesting process known as valley splitting, where the observed emission band gets split into two distinct emission bands due to the lifting of the degeneracy of the existing two excitonic states of the emitting species (QDs).[15,34] The valley splitting phenomenon has been observed in the plasmonic absorption band of nanomaterials in presence of inorganic exciton

(QDs)[35-36], organic exciton (aggregates)[6,37], and also in presence of 2D transition metal dichalcogenide.[38-39] Very recently, Omata and co-worker have shown that strong exciton-exciton coupling between PbSe QDs can lead to valley splitting of QD emission and they have also shown that interdot distance can control the extent of valley splitting.[40] From the above discussions, one can realize that the information available on strong coupling phenomena is not large rather very limited. More importantly, no information is available in the literature where the organic exciton (Frankel) is shown to participate in the valley splitting of the inorganic excitonic (Wannier-Mott) emission band. Hence, it would be a worthwhile objective to develop these inorganic-organic nanohybrid materials, parallelly understanding the fundamentals behind their mechanism of interaction, and possibly control the coupling process by acquiring knowledge about their interaction mechanism.

Keeping the above facts in mind, a nanohybrid material by comprising colloidal CdTe@ZnS QD as inorganic part and J-aggregate of S2165 cyanine dye molecules (molecular structure shown in Chart APX5.1) as organic part has been developed. It is expected that these inorganic-organic nanohybrid materials can show strong coupling due to the presence of strong confinement of QDs and the strong dipole moment provided by organic J-aggregates.[4,7,10,12,41-42]Moreover, CdTe@ZnS QD is chosen as inorganic exciton[43-46] and organic cyanine dye-based J-aggregate as organic exciton due to their favourable optical properties. [4,7,10,12,42] Analysis of spectroscopic data has revealed efficient electronic energy transfer (EET) from QD to J-aggregate. More interestingly, the splitting of emission spectra of the QD with the gradual addition of J-aggregate, indicating the presence of efficient exciton-exciton interaction between inorganic (Wannier-Mott) exciton and organic (Frenkel) exciton, has been observed. It has also been observed that with an increase in EET efficiency, valley splitting also gets enhanced without applying any apparent external field. To the best of our knowledge, this work provides the first evidence of valley splitting of inorganic QD by organic J-aggregates.

5.2. Results and Discussion

Prior to the photophysical investigation on the inorganic-organic hybrid system, the individual components of the nanohybrid material, QDs and J-aggregate, have been studied. The CdTe@ZnS QD has been characterized through EDAX (Figure APX5.1), and its size is found to be 4.7 nm from the HRTEM image, and the interplanar distance is found to be 0.356 nm (shown in Figure APX5.2a and APX5.2b), which matches with the literature value of 111 crystal lattice plane of CdTe@ZnS QDs[48]. From the PXRD data (shown in Figure APX5.2c), it is also found that CdTe@ZnS QDs have with zinc blende crystalline-like structure. The steady-state absorption and emission spectra of the synthesized QD are shown in Figure 5.1a. It can be observed that the absorption spectra of QD show a broad band with a characteristic absorbance peak at ~560 nm, whereas the emission spectra of QD show a relatively narrower band having a peak centered at 585 nm. It has been shown earlier that for this QD, the number of surface defect states are reduced during the formation of ZnS shell around the CdTe core, and because of this, the PL intensity of QD gets increased.[46-47]

In the present study, S2165 dye is purposefully chosen as an organic precursor for J-aggregate formation as it easily forms aggregates in the presence of salt. S2165 dye in its molecular form exhibits broad absorption with peaks at 546 nm and 583 nm (Figure 5.1b).[4,7,12,42] It is to be noted that upon addition of KCl, cyanine dye molecules spontaneously form aggregates with the characteristic narrow and red-shifted absorption band (Figure 5.1b).[41-42] As per molecular exciton theory, aggregates of cyanine dye molecules are well-known to form charge-neutral molecular excitations or Frenkel excitons.[4,7,10,12,42] According to Frenkel's excitons theory the electronic excitation in the self-assembled aggregates is not confined to the monomeric unit rather it is coherently delocalized over several monomers through excitation wave.[49-50] Figure 5.1b demonstrates the absorption spectra of the QD, dye, J-aggregate, and

QD–J aggregate. The number of dye molecules across which the exciton is delocalized can be estimated by eq (5.1),[4,49-51]

$$N_c = 1.5 \times \left(\frac{\Delta M}{\Delta J}\right)^2 \quad (5.1)$$

where, ΔM and ΔJ are the hwhh (half-width at half height) of the absorption peak of the monomer and J-aggregate, respectively, as calculated from the deconvolution spectra shown in Figure APX5.3. The lower bound of average number of dye molecules (N_c) that form J-aggregate is estimated to be ~19, and the exciton domain length of the J-aggregate of S2165 is calculated to be 28.5 nm.[51] In the current study, the spectral shift (ΔE) between monomer and aggregate is found to be 198.7 meV. The extent of exciton coupling energy (J_{ex}) of the aggregate is found to be 97.06 meV by using the following eq (5.2),

$$J_{ex} = \frac{(\Delta E)^2}{4E_m} + \frac{\Delta E}{2} \quad (5.2)$$

where, ΔE = spectral shift between the monomer and aggregated dye, and E_m = energy of main monomer transition = 2.1325 eV. Please note that the estimated J_{ex} value is 3.8 times higher than room temperature thermal energy (25.7 meV), which suggests that the interaction between molecular electronic transitions is very strong even at room temperature.

With the addition of dye solution into QD, the appearance of a new narrow red-shifted absorption band (λ_{abs}^{max}=639 nm), indicating the formation of J-aggregate, can be seen (Figure 5.1b). We also note here that when a similar concentration of dye is prepared alone (without QDs), no J-band formation can be seen, indicating the role of QD-surface on the J-aggregate formation. The fact that both J-aggregate and QD are in interaction is evident with the blue shift of the J-band of the hybrid (solid green line in Figure 5.1b) as compared to the J-band of only dye aggregate (blue dotted line in Figure 5.1b). From ζ-potential measurements, the lowering of negative zeta potential value from -32.4 mV to -12.5 mV for QDs and nanohybrid respectively, indicates electrostatic interaction between anionic QD surface and cationic dye

aggregate (see Appendix for detailed discussion, Figure APX5.4, Table APX5.1). Furthermore, association free energy change (ΔG) of the nanohybrid systems as estimated from van't Hoff equation (eq APX5.4, APX5.5), is also found to be negative, which further supports the fact that the association of J-aggregate over QD is thermodynamically feasible[52] (see Appendix for detailed discussion, Figure APX5.5, Table APX5.2). Moreover, from the TEM micrograph, it can be seen that the J-aggregated molecules are surrounded by the QD surface, and the estimated size of the J-aggregate is found to be ~20nm. (shown in Figure APX5.6). From Figure APX5.7, one can observe that the emission spectrum of S2165 dye J-aggregate (λ_{em}^{max}=650 nm) is narrow and red-shifted as compared to that of dye monomer. On the other hand, QD alone exhibits a broad absorbance and a relatively narrower emission band (λ_{em}^{max}=585 nm) (Figure 5.1a). Further, we have also found a significant overlap between the emission spectrum of QD and absorption spectrum of J-aggregate (Figure 5.1c), which implies the electronic states of QD (donor) and J-aggregate (acceptor) components in the nanohybrid associates are electronically coupled, and thus allow them to act as an efficient FRET pair (shown in Scheme 5.1). The overlap integral (J(λ)) value between donor emission and acceptor absorbance, and Förster distance (R_0) of the corresponding FRET pair system are estimated to be 1.23 $\times 10^{15}$ $M^{-1}cm^{-1}nm^4$ and ~47 Å, respectively (Shown in Table APX5.3).

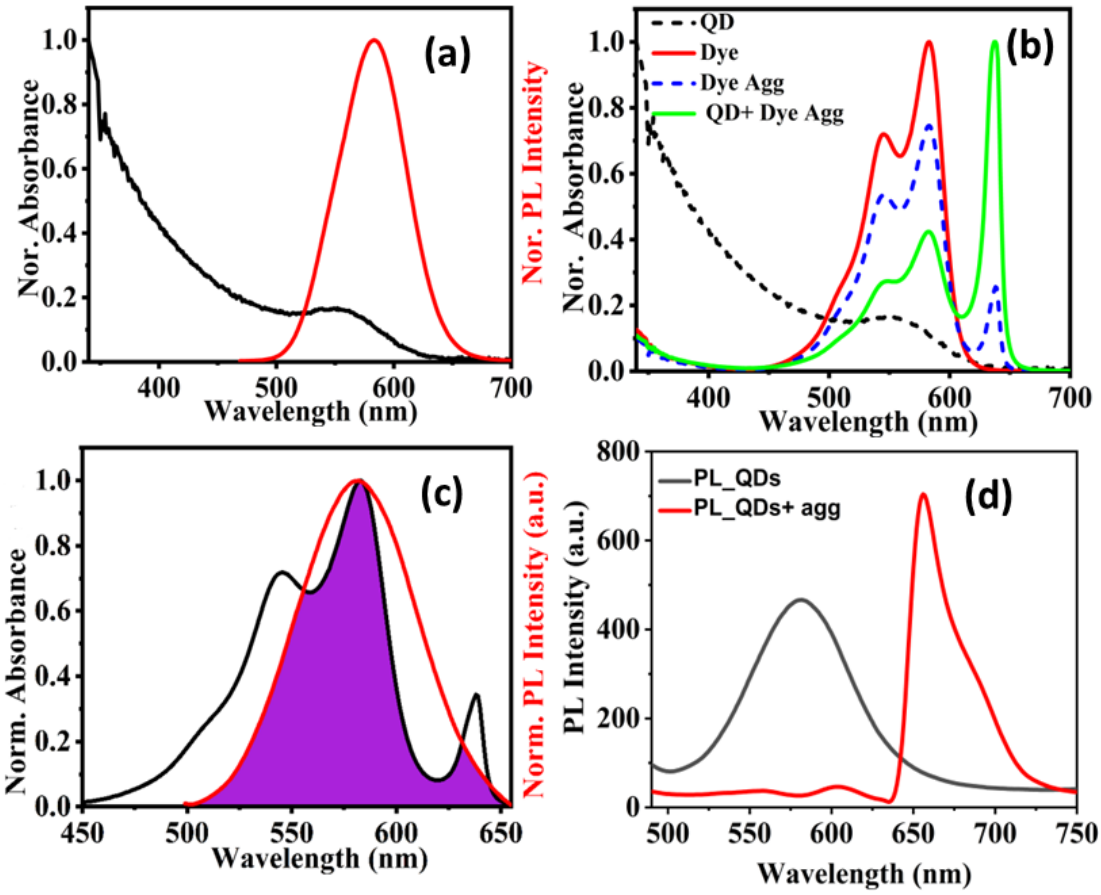

Figure 5.1. (a) Normalized absorption (black) and emission (red) spectra of QD. (b) Absorption spectra of QD (black), dye molecule (red), dye J-aggregate (blue dash), and QD/dye aggregate hybrid system (green). (c) Spectral overlap between the emission spectrum of QD (red) and absorption spectrum of S2165 dye aggregate (black). (d) Steady-state PL spectra of QD and QD J-aggregate nanohybrid (red) at 405 nm excitation.

The study of the interaction between QD and J-aggregate of S2165 dye has been carried out by monitoring the change in donor's emission in the absence and presence of acceptor.[42,52] The PL spectra of QD and QD_J-aggregate (Figure 5.1d) show emission maxima (λ_{em}^{max}) at 585 nm and 650 nm, respectively. Interestingly, in the presence of acceptor (J-aggregate), the PL intensity of the donor (QD) is observed to be quenched with simultaneous enhancement in the PL intensity of the acceptor. This observation clearly suggested ET from QD to J-aggregate for the present nanohybrid system.[4,7] We note here that similar observations have also been reported by other researchers [4,7] to explain the ET process from QD to J-aggregate.

Additionally, we have performed a controlled experiment to confirm that the PL quenching of the donor with concomitant increase in the PL intensity of acceptor is due to ET and not due to any other reason (see Appendix for detailed discussions). Studies have also demonstrated that ET from QD to J-aggregate is due to dipole-dipole interaction (Förster type).[4,12,42] Emission spectra of QD with gradual addition of dye and its corresponding change in PL intensity has been shown in Figure 5.2. From Figure 5.2, the ET efficiency of the donor in the presence of the acceptor is estimated to be as high as 90% (see Appendix for calculation). Further, we have also estimated the ET efficiency of QD in the presence of S2165 dye aggregate at inter valley splitting emission maxima wavelength i.e., 560 nm and 605 nm. The corresponding ET efficiency is found to be 81% and 78%, which is in good agreement with the overlap integral values (7×10^{14} $M^{-1}cm^{-1}nm^4$ and 5×10^{14} $M^{-1}cm^{-1}nm^4$) shown in Figure APX5.8 and Table APX5.3 in the Appendix.

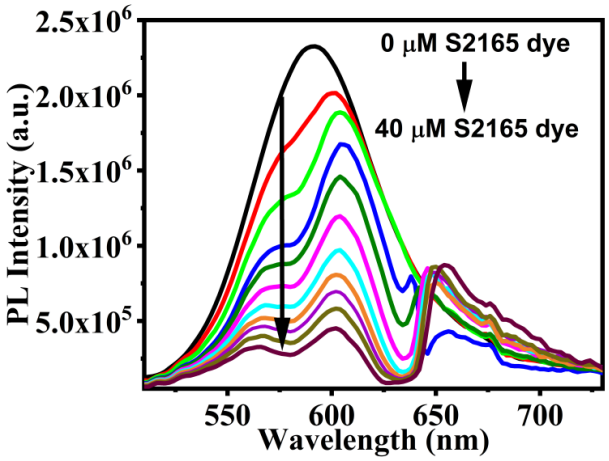

Figure 5.2. PL spectra of CdTe@ZnS QD with increasing concentration of S2165 dye (λ_{ex} = 405 nm).

Such a high ET efficiency value indicates the efficient coupling of the energy levels of donor and acceptor systems. We would also like to mention here that the ET from QD to monomer dye is ignored due to the presence of an insignificant amount of monomer dye at higher concentrations.[10,12] Interestingly, when the emission spectra of QDs with progressive addition

of dye are examined, a distinct and prominent splitting of the QD emission band have been observed. This is an exciting observation in a sense that the emission band of QDs usually decreases during the ET process with no change in the shape in terms of splitting. This is referred as valley splitting. This observation is noteworthy since there is no evidence in literature that J-aggregate participates in the valley splitting of QD emission band.

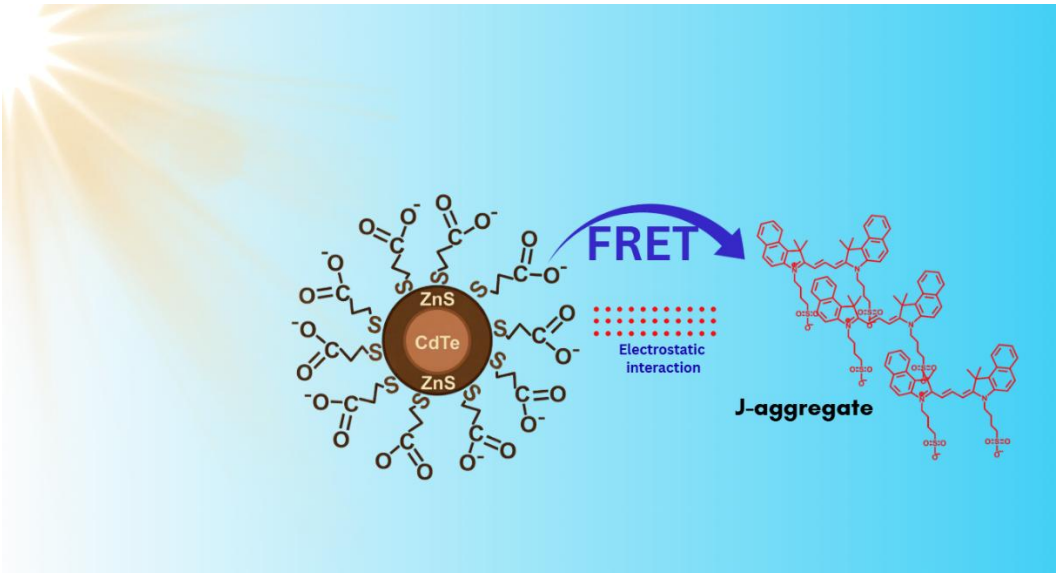

Scheme 5.1. Schematic representation of the interaction of CdTe@ZnS QDs with J-aggregate.

To obtain a deeper insight into the emission valley splitting of the QD in the presence of J-aggregate, we have separately plotted the emission spectra of QDs with increasing concentrations of dye (Figure 5.3a). Interestingly, it can be seen from Figure 5.3a that the emission spectra of CdTe@ZnS QD get split with the gradual addition of dye. One can also find from the said plot that the PL valley splitting of the QDs is gradually increased with the increasing concentration of dye aggregate (0μM to 40 μM). For example, the magnitude of the valley splitting (i.e., energy separation between the two bands) is increased from 55 meV to 150 meV with the gradual addition of dye. To understand the mechanism of splitting of the emission band of the QD in the nanocomposite, which might undergo through homo-FRET or hetero-FRET, we have performed a concentration-dependent experiment with CdTe@ZnS QD (shown in Figure APX5.9). With the increase in the concentration of QD in the absence of J-

aggregate, we observed no splitting of the emission band of the QDs. So we can rule out the possibility of valley splitting due to homo-FRET and conclude that hetero-FRET is responsible for the valley splitting of QD's emission band. It is to be noted that we have also observed the increase in FRET efficiency from QD to J-aggregate as the concentration of J-aggregate is increased (Figure 5.3b). Therefore, to find out the correlation between the FRET efficiency and valley splitting, we have plotted the energy separation value of the valley splitting against FRET efficiency (Figure 5.3c). From Figure 5.3c, a linear relation has been found between FRET efficiency and the energy separation value of the valley splitting. This observation is a clear indication of the fact that the electronic coupling that leads to FRET is also closely related to the enhanced valley splitting of QDs emission band. It is relevant to mention here that recently, Omata and co-worker[40] have shown that the electronic coupling leading to FRET may enhance the valley splitting. This observation is very interesting in a sense that the valley splitting can be tuned by simply controlling the FRET process from QD to J-aggregate without applying any external field. In order to understand the variation of the emission bands of the QD in detail, the PL spectra of QDs are deconvoluted satisfactorily by fitting with two Gaussian bands (Figures 5.4a,b, c, and d), which indicate the existence of multiple emitting states. Since the present QD has a unimodal distribution in size (Figure APX5.2a and APX5.2b), the two emission bands are certainly not caused due to the presence of two coexisting groups of QDs with different diameters.[40]

It is known that Cd-chalcogenides crystallize in the zinc blende structure.[53] The valence band maxima and conduction band minima of Cd-chalcogenides are both situated at the Γ-point in the Brillouin zone.[54] Since there are four Γ -points per face-centered cubic Brillouin zone,[15] the fundamental bandgap becomes eight-fold degenerate (considering spin degeneracy).[15,54] This eight-fold fundamental bandgap, in turn, yields a 64-fold degenerate lowest exciton state ($1S_h$ –$1S_e$).[15,40] This degeneracy can partially be lifted by a number of effects, such as intra-band

coupling, inter-valley couplings, and electron-hole exchange, etc. [15,54] These effects are primarily responsible for creating a fine exciton structure.[15] The electron-hole exchange may also lead to an intricate exciton fine structure consisting of several bright and dark states.[15] In case of CdTe@ZnS QD's emission in the presence of J-aggregate, the two emission peaks can be ascribed to two bright exciton fine structure states in the 64-manifold $1S_h$ –$1S_e$ state of the QDs.[15] Though the coexistence of emission from two different states without thermalization in organic molecules is a common (viz., singlet and triplet states) thing[55-56,] but is unusual for semiconductor NCs at low exciton densities. Nevertheless, Donega and co-workers have shown that the two coexisting emission transitions of PbSe/CdSe NCs are attributed to the existence of two exciton emitting states with different degrees of spatial localization.[15] Therefore, two emitting states of CdTe@ZnS QDs should be ascribed to the fine–structure excitonic states originating from a partial lifting of the 64-fold degeneracy of the 1Sh–1Se exciton by exciton-exciton efficient coupling.

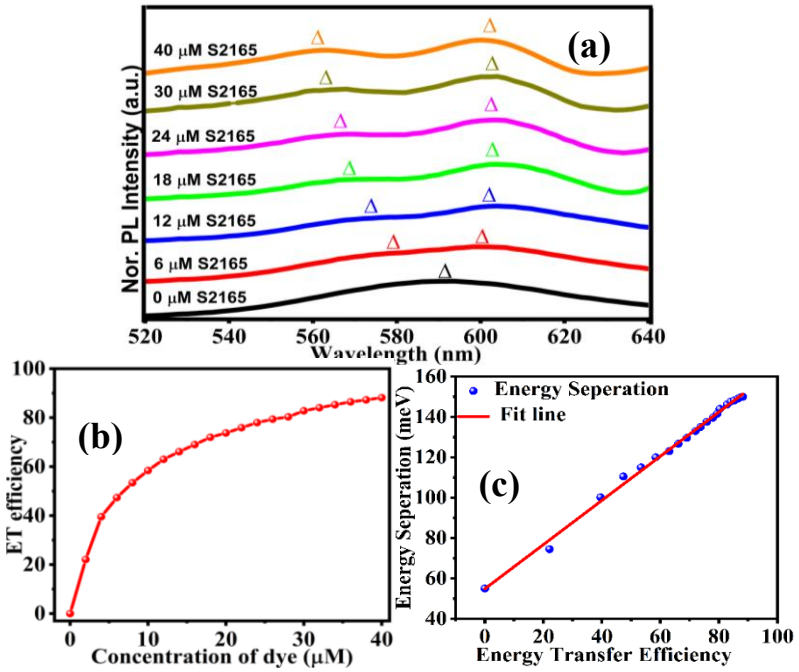

Figure 5.3. (a) CdTe ZnS QDs PL spectra with gradual addition of j-aggregated dye (b) change in ET efficiency as a function of dye (acceptor) concentration and (c) plot of energy separation between two emission peaks versus ET efficiency.

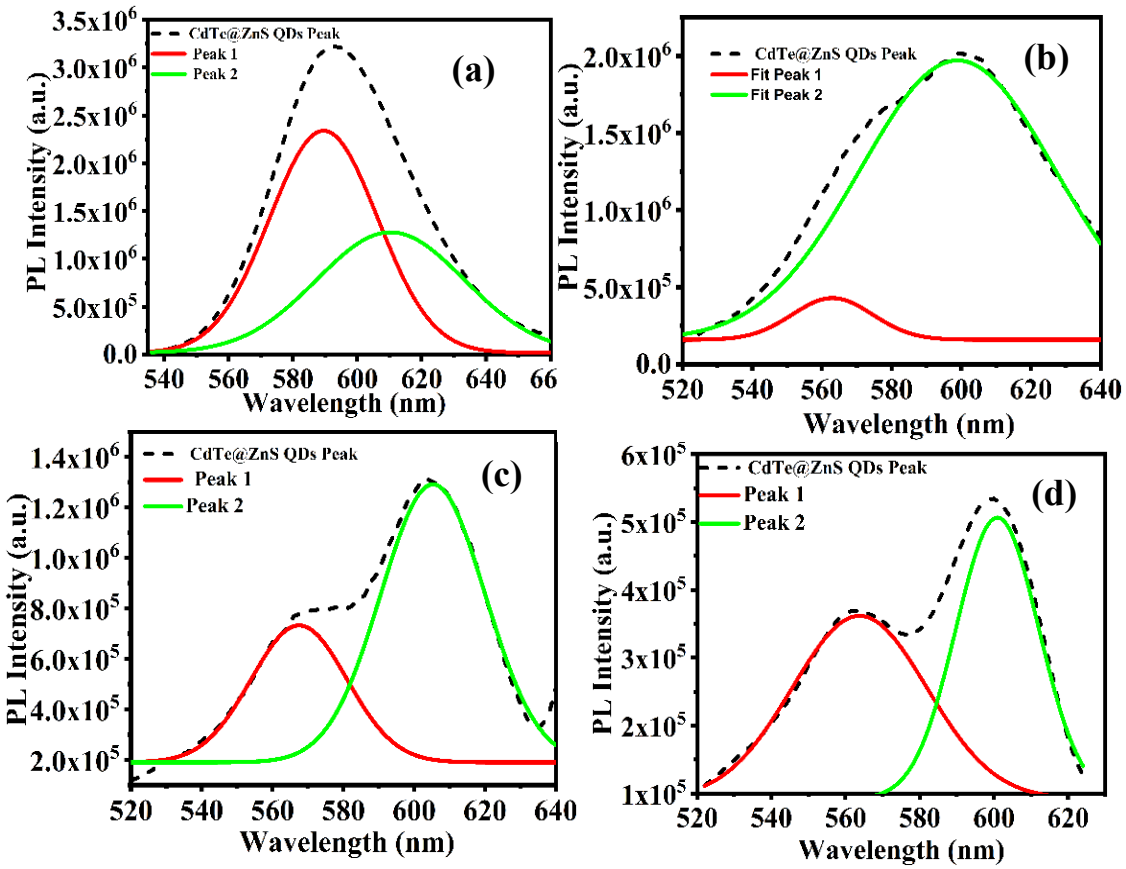

Figure 5.4. Deconvoluation of PL spectra of CdTe@ZnS QDs (a) without addition of dye aggregate, (b) at low concentration of dye aggregate, (c) at moderate concentration and (d) at high concentration of dye aggregate.

To realize the PL quenching mechanism overtly, time-resolved PL measurements have also been performed. The PL decay curves for QD in the absence and presence of acceptor (S2165 aggregate) are shown in Figure 5.5, and the corresponding decay parameters are provided in Table APX5.4. In the presence of dye aggregate, the average PL lifetime of CdTe@ZnS QD has been remarkably quenched from 18.2 ns to 0.6 ns, which again indicates the RET process from QD (donor) to J-aggregate (acceptor) in the nanohybrid associate.[51,57] Moreover, the ultrafast PL decay plot (inset of Figure 5.5) and its corresponding decay parameters (Table APX5.5) clearly indicate RET from QD to J-aggregate system. From the time-resolved PL measurement, the ET efficiency is found to be 97% which is in good agreement with the result obtained from steady-state measurements (see Appendix for detailed

discussion). However, when we monitored inter-valley splitting of emission maxima wavelength, the observation is different. At 560 nm, the fluorescence lifetime of QD in the absence and presence of acceptor is found to be 18.23 ns and 5.3 ns, while at 605 nm it is found to be 19.94 ns and 7.44 ns, respectively. (Figure APX5.10) The ET efficiency (from lifetime measurement) at 560 nm and 605 nm is found to be 71% and 63% respectively. (Table APX5.6) Although the ET efficiency from steady-state and time-resolved fluorescence measurements are similar, but when monitored at different wavelengths (560 nm and 605 nm), there is a difference. This difference might be due to the heterogeneity of the system. At both wavelengths, a linear relationship between ET efficiency and valley splitting energy separation is maintained (Figure APX5.11).

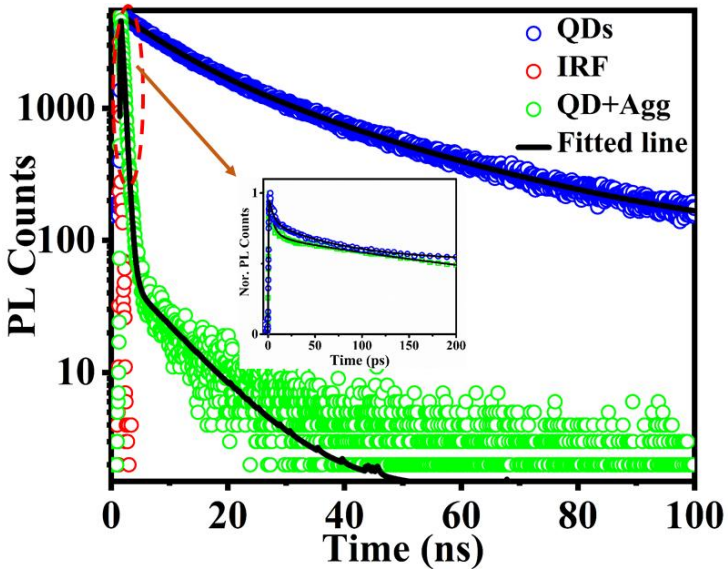

Figure 5.5. Time-resolved PL decay curves of CdTe@ZnS QD alone and in the presence of J-aggregate (monitored at 585 nm) at λ_{exc}= 405 nm (inset shows ultra-fast PL decay).

In addition, the fluorescence correlation spectroscopy (FCS) technique has also been employed for a better understanding of the mechanism of CdTe@ZnS QD:::S2165 dye interaction at the single molecular level.[58] Figure 5.6 shows the normalized FCS curves for QD in the absence and presence of J-aggregates. Their corresponding diffusion time is estimated to be 150 µs and 950 µs, respectively. The increased diffusion time of QD in the presence of J-aggregate clearly

indicates the binding interaction between QD and the J-aggregate system. We have also estimated the hydrodynamic radius of the QD as well as the nanohybrid system, which is found to be ~4 nm and ~22 nm, respectively. Moreover, a 90% FRET efficiency is also observed during FRET-FLIM measurement (Figure APX5.12a and Figure APX5.12b), indicating the utility of these nanoscale materials in real-time applications.

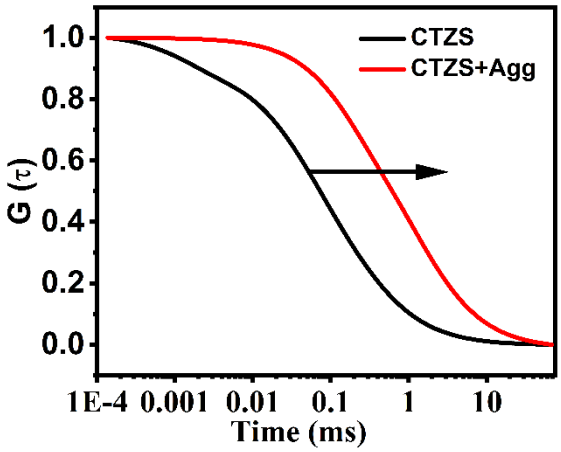

Figure 5.6. Normalized FCS curve of QD alone (black) and in presence of dye aggregate (red).

Interestingly, all the above studies have indicated that efficient exciton (inorganic)-exciton (organic) coupling between QD and J-aggregate is responsible for valley splitting. More interestingly, the electronic coupling between QD and J-aggregate, which leads to FRET, can also lead to increase in the intervalley coupling, implying that FRET can be an effective tool for controlling the valley splitting. It is to be noted that there is no evidence in literatures where J-aggregate is found to participate in the valley splitting of QD emission band. Involvement of the J-aggregate in the aforementioned process is highly fascinating since it will enable further tailoring of the FRET process and, consequently, valley splitting by performing chemical modification of cyanine dye. Such FRET induced valley splitting, in absence of any external field, also suggests that this inorganic-organic nanohybrid system can serve as a potential candidate for valleytronic material.[19-21]

5.3. Conclusion

In conclusion, the CdTe@ZnS_J-aggregate nanohybrid associate has been fabricated to investigate strong exciton-exciton interaction between both components. These nanohybrids are formed by the electrostatically driven and thermodynamically favorable process. The initial investigation reveals an efficient FRET between QD (donor) and J-aggregate (acceptor). However, a more careful analysis of the data reveals that apart from usual quenching of donor emission, prominent valley splitting of QD's emission can also be seen. This observation indicates efficient electronic coupling between QD and J-aggregate. Interestingly, further investigation reveals that the energy separation value of the valley splitting of QD's emission is linearly related to the FRET efficiency between QD and J-aggregate. Therefore, the study has also categorically demonstrated that the FRET process can effectively be used in controlling the extent of valley splitting process. The observation of valley splitting of QD emission in presence of J-aggregate without the application of external field is new and exciting. Essentially, the outcome of the current study has suggested that the present nanohybrid system has the potential to be used as a suitable nanoscale system for the fabrication of valleytronic materials.

5.4 Appendix

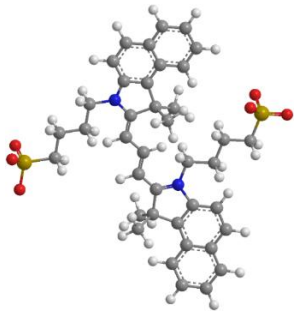

Chart APX5.1. Molecular structure of S2165 dye.

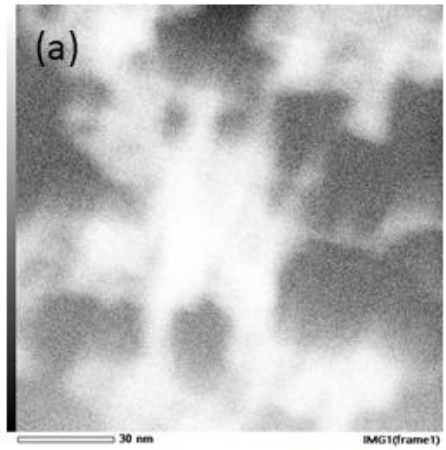

Element	Atom %
Cd	38
Te	36
Zn	12
S	14

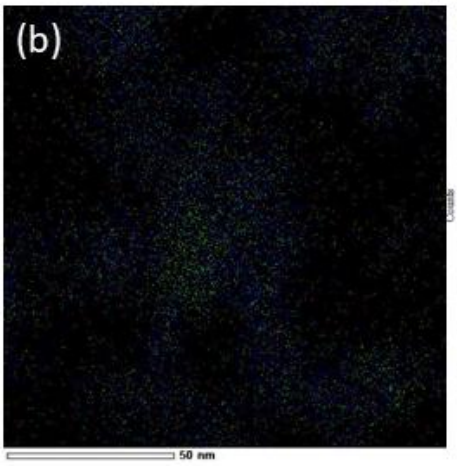

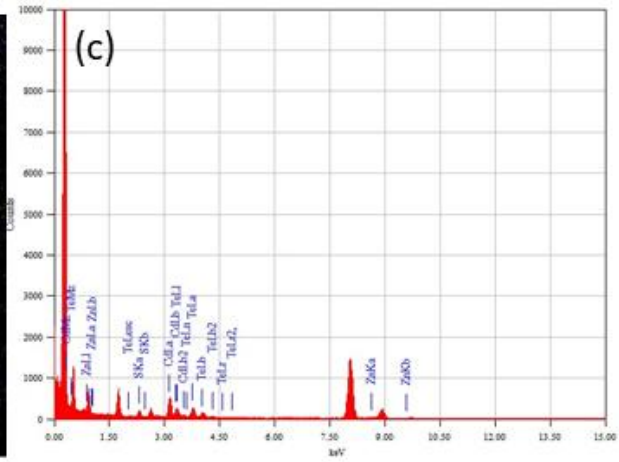

Figure APX5.1. EDS elemental mapping of CdTe@ZnS QD (a) image and (b) overlay elemental mapping of Cd, Te, Zn, and S elements and right corner atom% of elements. (c) area EDS spectrum of CdTe@ZnS QD.

The presence of Cadmium, Telerium, Zinc, and Sulphur in CdTe@ZnS QD is confirmed through FESEM-EDS elemental mapping (shown in Figure APX5.1) and area EDAX spectrum of (shown in Figure APX5.1). From PXRD data, we have found crystal plane (111), (220), and (311) (Shown in Figure APX5.2c) well matched with literature report.[47]

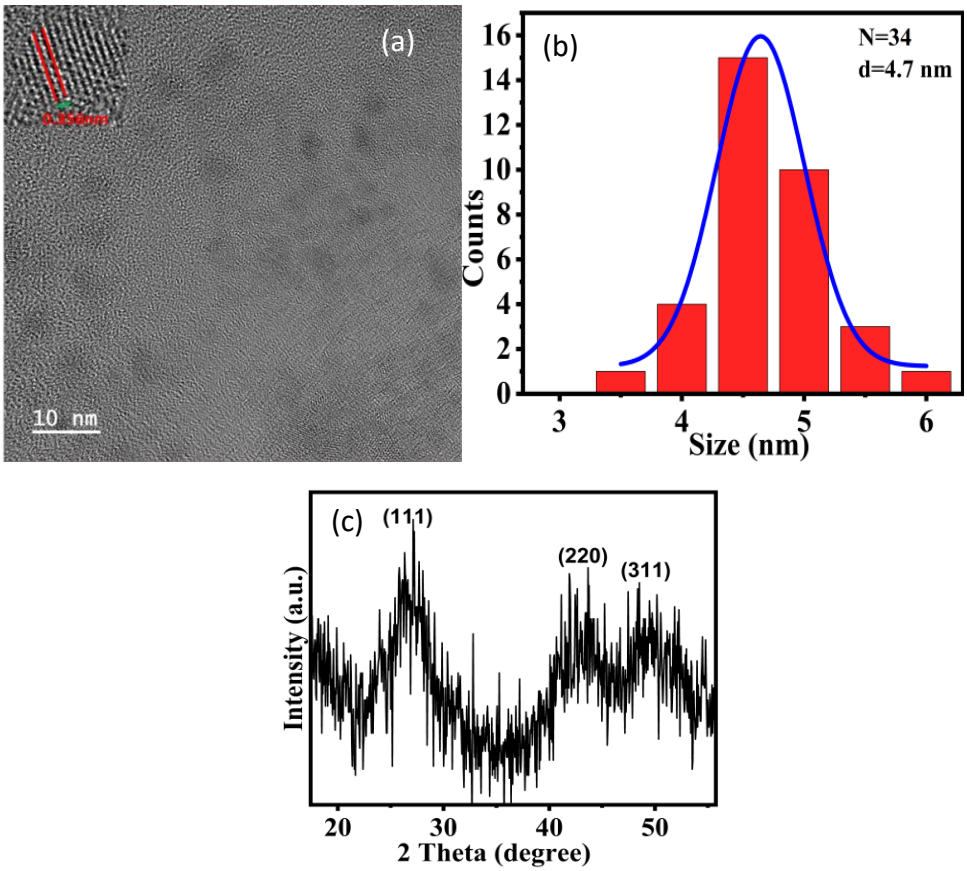

Figure APX5.2. a) TEM image and Inset HRTEM image b) size distribution of TEM of CdTe@ZnS QDs and c) XRD of CdTe@ZnS QDs.

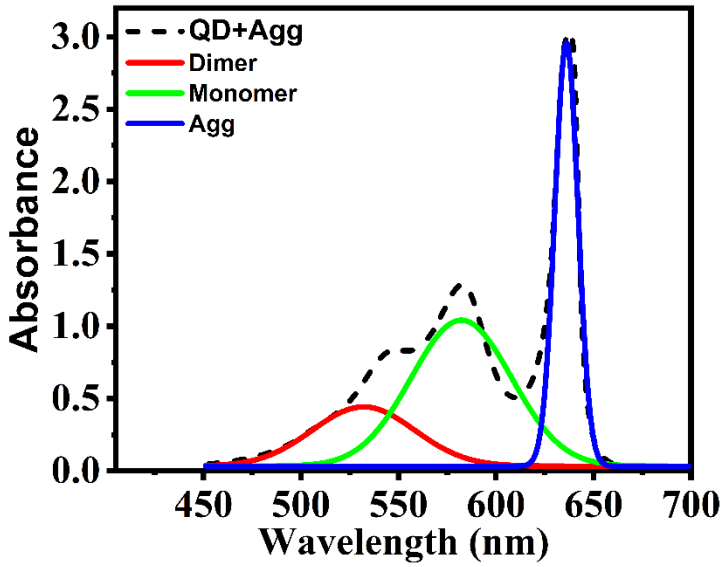

Figure APX5.3. Absorption spectra of QD-J aggregate which is deconvoluted by multiple fit analysis.

The FWHM values corresponding to the absorption spectra of monomer dye and J-aggregate are estimated to be 36 nm and 10 nm respectively. The FWHM of the J-band is obtained by deconvoluting the absorbance spectrum of J-aggregate (shown in Figure APX5.3).[49,50]

5.4.1. ζ-Potential Measurements

For the synthesis of CdTe@ZnS QD we have used 3-mercapto propionic acid and sodium sulphide as capping agents.[47] Owing to the presence of negatively charged group in the capping agents, it is expected that the surface charge of the QD should be negative. The surface charge of QD, dye aggregate, and the QD/dye aggregate hybrid system have been determined with the help of ζ-potential measurements. The relevant plots are provided in Figure APX5.4, and the ζ-potential values are tabulated in Table APX5.1. ζ-potential value confirms that the CdTe@ZnS QD are negatively charged with of -32.4 mV. Moreover, the negative charge on CdTe@ZnS QD decreases from -32.4 mV to -12.5 mV in presence of (positive) dye aggregate. This decrease in the negative ζ-potential value in presence S2165 dye aggregate surely provides evidence in favor of electrostatic interactions between the oppositely charged moieties QD and J-aggregate, which is consistent with some previously mentioned literature reports.[52] This investigation have suggested that the hybrid structure is formed mainly due of strong electrostatic attraction between QD and dye aggregate which also facilitate efficient FRET process between them.[52]

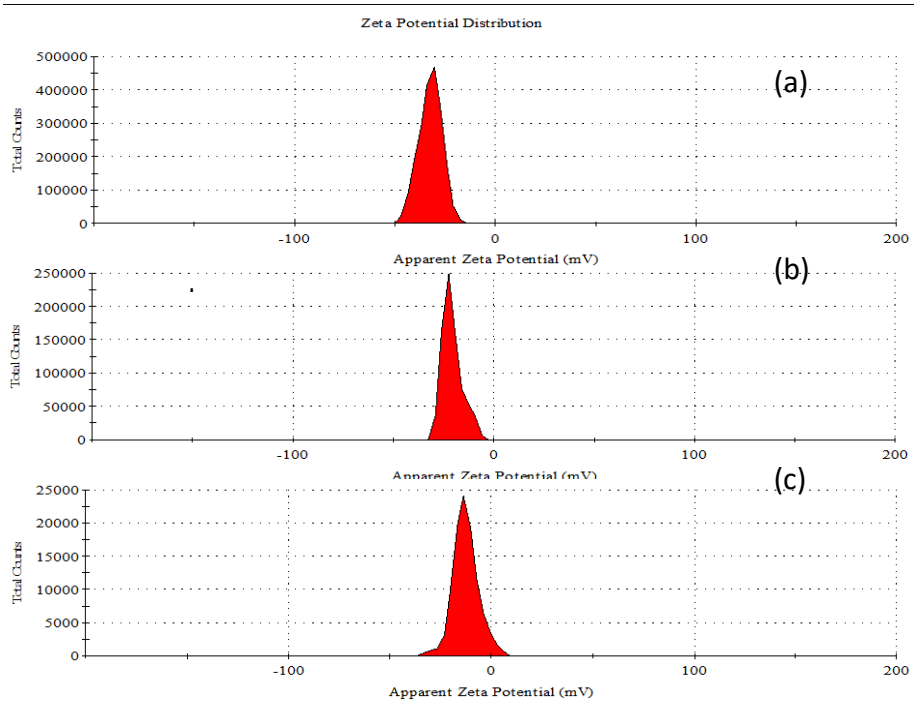

Figure APX5.4. Zeta potential graphs for the (a) CdTe@ZnS QDs, (b) CdTe@ZnS QDs+ S2165 dye, and (c) hybrid system of CdTe@ZnS QDs+ S2165 dye aggregate.

Table APX5.1. Zeta potential of CdTe@ZnS QD with and without dye and dye aggregate.

Sample	**Zeta Potential (mV)**
CdTe@ZnS QDs	-32.4
CdTe@ZnS QDs + Dye	-20.8
CdTe@ZnS QDs + Dye Aggregate	-12.5

From the SV equation is given by,[58]

$$\frac{F_0}{F} = 1 + K_{sv}[Q] \qquad \text{(APX5.1)}$$

where F_0 and F are the PL intensities of CdTe@ZnS QD (donor) alone and in the presence of dye (quencher) respectively. K_{SV} and [Q] are the SV constant and quencher concentration

respectively. K_{SV} is estimated to be 1.29 x 105 M-1. The linearity of Stern-Volmer plot in the Figure APX5.5 suggests the possibility of pure static or dynamic quenching. However, the decrease in slope of versus [Q] plot with increase in temperature F_0 /F indicates that static quenching prevails during the quenching event.

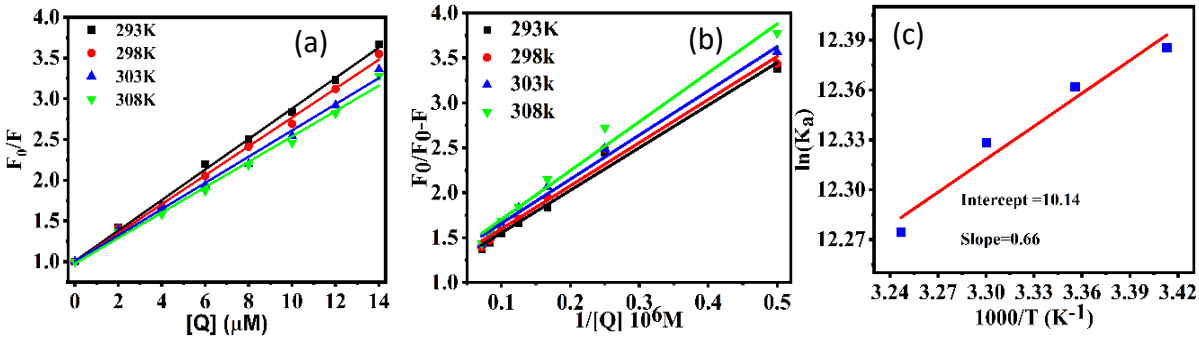

Figure APX5.5. (a) The Stern–Volmer plot of relative fluorescence intensity vs. quencher concentration. (b) Plot of F0/(F0 – F) versus 1/[Q] at various temperatures. (c) van't Hoff plot (ln Ka vs. 1000//T) corresponding to the quenching event.

Table APX5.2. Stern-Volmer quenching constant and thermodynamic parameters for the interaction between CdTe@ZnS QD and S2165 dye at various temperatures

T (K)	K_a (10^5 L mol^{-1})	R^2	ΔH (kJ mol^{-1})	ΔS (J mol^{-1} K^{-1})	ΔG (kJ mol^{-1})
293	2.393	0.998			-30.19
298	2.337	0.997	-5.49	+84.30	-30.61
303	2.260	0.999			-31.03
308	2.141	0.998			-31.45

Experimental error = ±5%

5.4.2. Thermodynamic parameter calculation In order to find the thermodynamic parameters, we need the association constant (K_a) for which a modified Stern– Volmer equation (APX5.2)

$$\frac{F_0}{F_0-F} = \frac{1}{f_a K_a [Q]} + \frac{1}{f_a} \qquad \text{(APX5.2)}$$

where f_a is the fraction of accessible fluorescence, K_a is the association constant, and F_0 and F

are the fluorescence intensity in the absence and presence of a quencher. Therefore, the association constant (Ka) is utilized in determining the relevant thermodynamic parameters with the help of van't Hoff equations APX5.3 and APX5.4.

$$\ln(K_a) = -\frac{\Delta H}{RT} + \frac{\Delta S}{R} \quad \text{(APX5.3)}$$

$$\Delta G = \Delta H - T\Delta S \quad \text{(APX5.4)}$$

Where, $\Delta H, R$, T, ΔS and ΔG are the enthalpy change, molar gas constant, temperature in Kelvin, the entropy change, and the free energy change ,respectively for the association process of S2165 dye on the QD surface. The van't Hoff plot is provided in Figure APX5.5. From the slope and intercept of the plot, the values of ΔH and ΔS can be calculated respectively. The negative value of ΔH (from Table APX5.2) suggests that CdTe@ZnS QD:::S2165 dye interaction is exothermic process,. In contrast, positive value of ΔS indicates that during this process there occurs increase in the value of entropy of the system. It can be seen that negative enthalpy along with positive entropy change for similar association processes occurs due to electrostatic interaction between the components.[49] Moreover, the negative free energy change for the present association process (Table APX5.2) is conclusive evidence that the present nanohybrid associate formation is spontaneous (thermodynamically favorable).

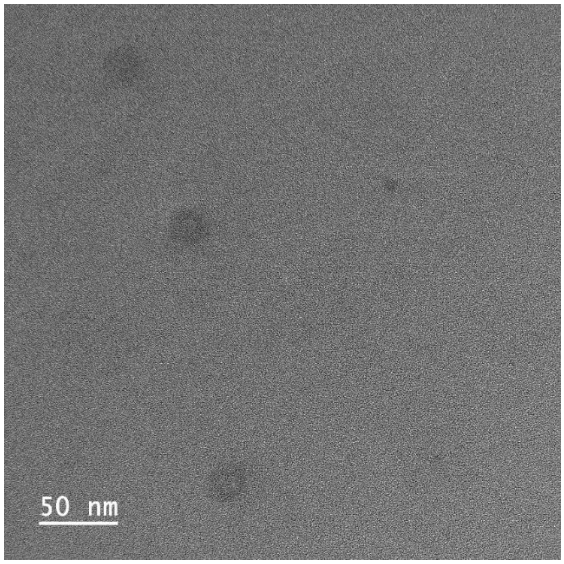

Figure APX5.6. TEM image of CdTe@ZnS QD-J-aggregate nanocomposite.

5.4.3. Secondary inner filter correction To take accounts for reabsorption we have performed secondary inner filter correction with the help of equation APX5.5.[59]

$$\frac{F_0}{F} = \alpha = \frac{10^{-Ds \times ls}\,(10^{Ds \times \Delta ls/2} - 10^{-Ds \times \Delta ls/2})}{2.303 \times Ds \times \Delta ls} \qquad \text{(APX5.5)}$$

Where F and F_0 are the observed and corrected fluorescence intensity of donor, D_S, Δl_S, and l_S are the optical density of the acceptor at the donor's emission maxima, emitted light beam width and distances from the point inside the cell at which luminescence is observed to the exit cell wall respectively. The efficiency of ET process after reabsorption is estimated to be ~90%. We also note that, all the dye molecule may not form J-aggregate, hence there is also a possibility of ET from QD to dye monomer but the ET efficiency has been found to be low and can be ignored.

5.4.4. Controlled Experiment

For that, emission spectrum of aqueous solution of QD (donor) is recorded with gradual addition of dye (acceptor) with increasing concentration of dye aggregate. Again in another parallel experiment same amount of dye is added gradually to salt solution without the donor

and emission of the aggregate is recorded. Upon comparing the emission spectra of acceptor in both cases, a clear increase of emission for J-aggregate in presence of QD can be seen confirming the FRET process between the inorganic and the organic components. Next we have subtracted the later from the former to get the corrected PL intensity of the solution containing nanohybrid associate. From this corrected PL intensity we have calculated PL quenching of donor along with increase in efficiency of ET associated with this process as a function of increasing acceptor concentration.

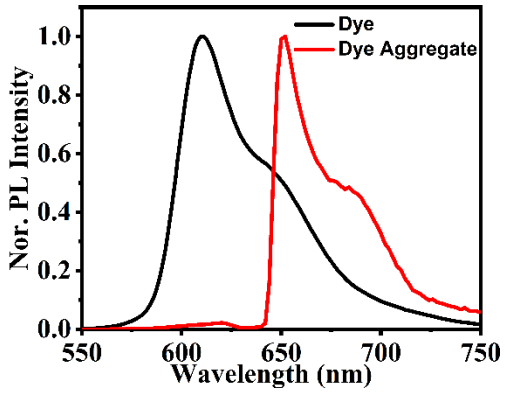

Figure APX5.7. Emission spectra of S2165 dye and it's J-aggregate.

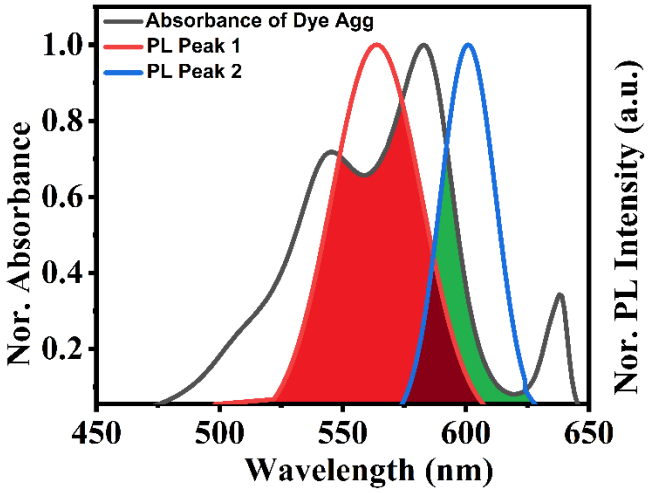

Figure APX5.8. Spectral overlap between the emission spectrum of QD (red for 560nm peak and blue for 605nm peak) and absorption spectrum of S2165 dye aggregate (black).

Table APX5.3. FRET parameters of CdTe@ZnS QD_S2165 J-aggregate nanohybrid associate.

Sample	J(λ) ($M^{-1}cm^{-1}nm^4$)	R_0 (Å)	E (%)	R_{DA} (Å)	k_{ET} (s^{-1})
QD+S0041 aggregate (overall)	1.23×10^{15}	47.0	90	33.4	4.19×10^8
QD+S0041 aggregate (by mitoring left side peak	7×10^{14}	43.0	82	33.3	2.68×10^8
QD+S0041 aggregate (by mitoring right side peak	5×10^{14}	40.8	78	33	1.60×10^8

Table APX5.4. PL decay parameters of CdTe@ZnS QD alone and in presence of S2165 dye aggregate

Sample	τ_1(ns)	α_1	τ_2 (ns)	α_2	τ_{av} (ns)[a]
CdTe@ZnS QD (at 585 nm)	9.4	0.54	28.6	0.46	18.2
CdTe@ZnS QD+S0041 aggregate (at 585 nm)	0.5	0.97	2.8	0.03	0.6

[a] Experimental error = ±5

Table APX5.5. Ultra-fast PL decay parameters of CdTe@ZnS QD alone and in presence of S2165 dye aggregate.

Sample	τ_1(ps)	α_1	τ_2 (ps)	α_2	τ_3 (ps)	α_3	τ_{av} (ps)[a]
CdTe@ZnS QD (at 585 nm)	5.4	0.20	85.2	0.27	18200	0.53	9670
CdTe@ZnS QD+S0041 aggregate (at 585 nm)	2.5	0.20	12.0	0.20	1084	0.60	653.3

[a]Experimental error = ±8%

5.4.5. ET efficiency calculation by PL lifetime

Using eqation APX5.6, $E = 1 - \frac{\tau_{DA}}{\tau_D}$, where τ_D and τ_{DA} are the lifetime of donor alone and in presence of acceptor respectively ET efficiency has been calculated. ET efficiency is found to be as high as 97%.

5.4.6. Controlled experiment to rule out the possibility of valley splitting due to homo-FRET: In order to rule out the possibility of valley splitting due to homo-FRET in CdTe@ZnS and J-aggregate, we have performed a concentration-dependent experiment with CdTe@ZnS QD.

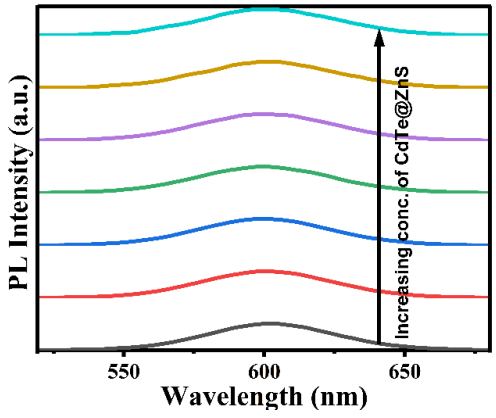

Figure APX5.9. PL Spectra of CdTe@ZnS QDs with increasing concentration of the same QD.

With the increase in the concentration of QD in the absence of J-aggregate, we observed no splitting of the emission band of the QDs (Figure APX5.9). So we can safely conclude that valley splitting due to homo-FRET is not possible in our system.

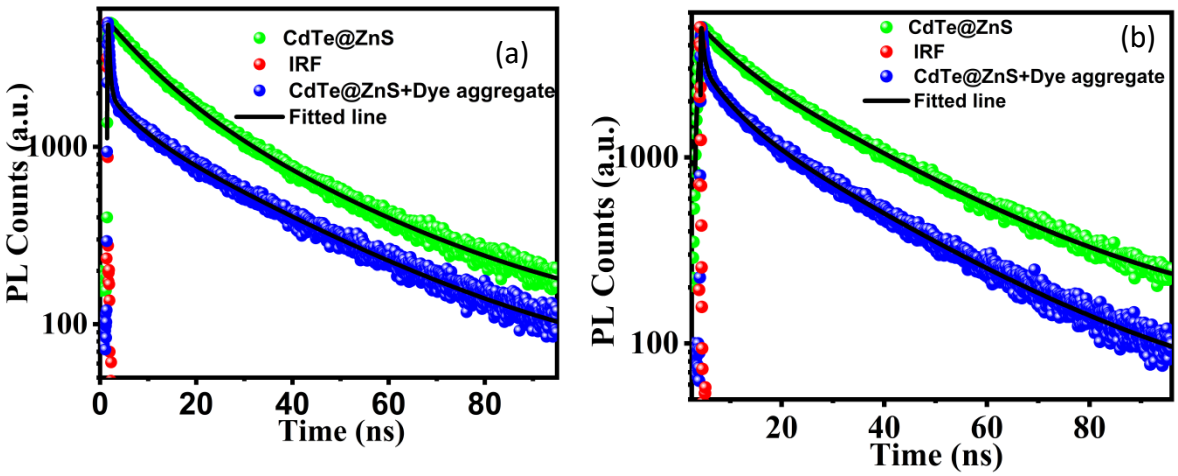

Figure APX5.10. Time-resolved PL decay curves of CdTe@ZnS QD alone and in the presence of J-aggregate monitored at (a) λ_{em} = 560nm and (b) λ_{em} = 605nm with λ_{exc}= 405 nm.

Table APX5.6. PL decay parameters of CdTe@ZnS QD alone and in the presence of S2165 dye aggregate at λ_{em} = 560 nm and λ_{em} = 605 nm with λ_{exc}= 405 nm and their ET efficiency.

Sample	τ_1(ns)	β_1	τ_2(ns)	β_2	τ_3(ns)	β_3	τ_{av}(ns)	ET efficiency
CdTe@ZnS at λ_{em}=560nm	--	--	9.38	0.54	28.64	0.46	18.23	--
CdTe@ZnS +J-agg at λ_{em}=560nm	0.28	0.76	5.8	0.08	29.00	0.16	5.30	71
CdTe@ZnS at λ_{em}=605nm	--	--	5.93	0.32	26.6	0.68	19.94	--
CdTe@ZnS+J-agg at λ_{em}=605nm	0.42	0.57	5.48	0.18	25.8	0.24	7.44	63

Experimental error= $\pm$5%

We have calculated the ET efficiency at both the emission wavelengths (560nm and 605nm). Using eq $E = 1 - \frac{F_{DA}}{F_D}$ (where, F_D and $F\tau_{DA}$ PL intensity donor alone and in the presence of acceptor), we have estimated the ET efficiency at 560 nm and 605 nm to be 81% and 78% respectively (shown in Figure APX5.11a and APX5.11c). We have also performed ET

efficiency versus valley splitting energy separation plot emission at 560nm peak and 605nm peak, both show a linear relation between ET efficiency and valley splitting energy separation (shown in Figure APX5.11b and APX5.11d).

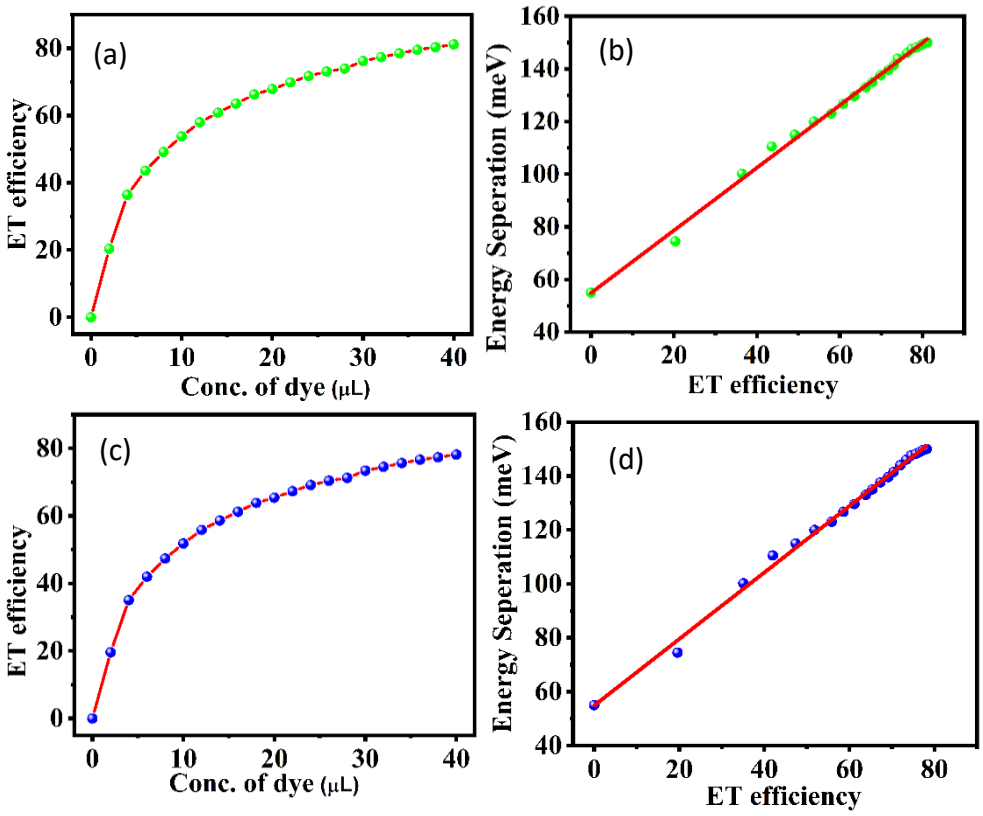

Figure APX5.11. Change in ET efficiency as a function of dye (acceptor) concentration (a) and (c) for 560nm peak and 605nm peak respectively. Plot of energy separation between two emission peaks versus ET efficiency (b), (d) for 560nm peak and 605nm peak respectively.

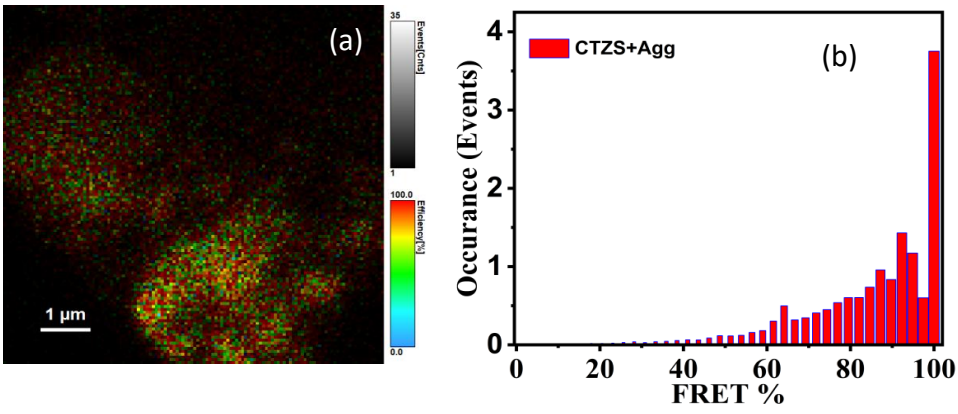

Figure APX5.12. (a) FRET-FLIM image of QD in presence of J-aggregate (b) plot of occurrence of events against FRET.

5.5 References

1. Kundu, S.; Patra, A. Nanoscale Strategies for Light Harvesting. *Chem. Rev.* **2017**, *117*, 712–757.
2. Thomas, A.; Sandeep, K.; Somasundaran, S. M.; Thomas, K. G. How Trap States Affect Charge Carrier Dynamics of CdSe and InP Quantum Dots: Visualization through Complexation with Viologen. *ACS Energy Lett*. **2018**, *3*, 2368−2375.
3. Zhang, Q.; Atay, T.; Tischler, J. R.; Bradley, M. S.; Bulović, V.; Nurmikko, A. V. Highly Efficient Resonant Coupling of Optical Excitations in Hybrid Organic/Inorganic Semiconductor Nanostructures. *Nat. Nanotechnol*. **2007**, *2*, 555−559.
4. Savateeva, D.; Melnikau, D.; Lesnyak, V.; Gaponik, N.; Rakovich, Y. P. Hybrid Organic/Inorganic Semiconductor Nanostructures with Highly Efficient Energy Transfer. *J. Mater. Chem.* **2012**, *22*, 10816−10820.
5. Bhandari, S.; Pramanik, S.; Khandelia, R.; Chattopadhyay, A. Gold Nanocluster and Quantum Dot Complex in Protein for Biofriendly White-Light-Emitting Material. *ACS Appl. Mater. Interfaces* **2016**, *8*, 1600−1605.
6. Zengin, G.; Wersäll, M.; Nilsson, S.; Antosiewicz, T. J.; Käll, M.; Shegai, T. Realizing Strong Light-Matter Interactions between Single-Nanoparticle Plasmons and Molecular Excitons at Ambient Conditions. *Phys. Rev. Lett.* **2015**, *114*, 157401
7. Smirnov, M. S.; Ovchinnikov, O. V.; Dedikova, A. O.; Shapiro, B. I.; Vitukhnovsky, A. G.; Shatskikh, T. S. Luminescence Properties of Hybrid Associates of Colloidal CdS Quantum Dots with J-Aggregates of Thiatrimethine Cyanine Dye. *J. Lumin*. **2016**, *176*, 77−85.
8. Hoffman, J. B.; Choi, H.; Kamat, P. V. Size-Dependent Energy Transfer Pathways in CdSe Quantum Dot−Squaraine Light-Harvesting Assemblies: Förster versus Dexter. *J. Phys. Chem. C* **2014**, *118*, 18453–18461.

9. Qiao, Y.; Polzer, F.; Kirmse, H.; Steeg, E.; Kuhn, S.; Friede, S.; Kirstein, S.; Rabe, J. P. Nanotubular J-Aggregates and Quantum Dots Coupled for Efficient Resonance Excitation Energy Transfer. *ACS Nano* **2015**, *9*, 1552–1560.
10. Freyria, F. S.; Cordero, J. M.; Caram, J. R.; Doria, S.; Dodin, A.; Chen, Y.; Willard, A. P.; Bawendi, M. G. Near-Infrared Quantum Dot Emission Enhanced by Stabilized Self-Assembled J-Aggregate Antennas. *Nano Lett.* **2017**, *17*, 7665−7674.
11. Shahar, C.; Tidhar, Y.; Jung, Y.; Weissman, H.; Cohen, S. R.; Bitton, R.; Pinkas, I.; Haran, G.; Rybtchinski, B. Control over size, shape, and photonics of self-assembled organic nanocrystals. *J. Org. Chem.* **2021**, *17,* 42–51.
12. Halpert, J. E.; Tischler, J. R.; Nair, G.; Walker, B. J.; Liu, W.; Bulović, V.; Bawendi, M. G. Electrostatic Formation of Quantum Dot/J-aggregate FRET Pairs in Solution. *J. Phys. Chem. C.* **2009**, *113*, 9986−9992.
13. Sadhu, S.; Haldar, K. K.; Patra, A. Size Dependent Resonance Energy Transfer between Semiconductor Quantum Dots and Dye Using FRET and Kinetic Model. *J. Phys. Chem. C* **2010**, *114*, 3891−3897.
14. Wang, C.; Weiss, E. A. Sub-Nanosecond Resonance Energy Transfer in the Near-Infrared within Self-Assembled Conjugates of PbS Quantum Dots and Cyanine Dye J-aggregates. *J. Am. Chem. Soc.* **2016**, *138*, 9557−9564.
15. Grodzinska, D.; Evers, W. H.; Dorland, R.; Van Rijssel, J.; Van´ Huis, M. A.; Meijerink, A.; De Mello Donegá, C.; Vanmaekelbergh, D. Two-Fold Emission from the S-Shell of PbSe/CdSe Core/Shell Quantum Dots. Small **2011**, *7*, 3493−3501.
16. Overgaag, K.; Vanmaekelbergh, D.; Liljeroth, P.; Mahieu, G.; Grandidier, B.; Delerue, C.; Allan, G. Electron-Phonon Coupling and Intervalley Splitting Determine the Linewidth of Single-Electron Transport through PbSe Nanocrystals. J. Chem. Phys. **2009**, *131*, 224510.

17. Fofang, N. T.; Grady, N. K.; Fan, Z.; Govorov, A. O.; Halas, N. J. Plexciton Dynamics: ExcitonPlasmon Coupling in a J-Aggregate Au Nanoshell Complex Provides a Mechanism for Nonlinearity. *Nano Lett.* **2011**, *11*, 1556–1560.
18. Wersall, M.; Cuadra, J.; Antosiewicz, T. J.; Balci, S.; Shegai, T. Observation of Mode Splitting in Photoluminescence of Individual Plasmonic Nanoparticles Strongly Coupled to Molecular Excitons. *Nano Lett.* **2017**, *17*, 551−558.
19. Vitale, S. A.; Nezich, D.; Varghese, J. O.; Kim, P.; Gedik, N.; Jarillo-Herrero, P.; Xiao, D.; Rothschild, M. Valleytronics: Opportunities, Challenges, and Paths Forward. *Small* **2018**, *14,* 1801483.
20. Huang, B.; McGuire, M. A.; May, A. F.; Xiao, D.; JarilloHerrero, P.; Xu, X. Emergent Phenomena and Proximity Effects in Two-Dimensional Magnets and Heterostructures. *Nat. Mater.* **2020**, *19*, 1276−1289.
21. Schaibley, J. R.; Yu, H.; Clark, G.; Rivera, P.; Ross, J. S.; Seyler, K. L.; Yao, W.; Xu, X. Valleytronics in 2D Materials. *Nat. Rev. Mater*. **2016**, *1*, 16055.
22. Törma, P.; Barnes, W. L. Strong coupling between surface plasmon polaritons and emitters: a review. *Rep. Prog. Phys.* **2015**, 78, 013901.
23. Khitrova, G.; Gibbs, H. M.; Kira, M.; Koch, S. W.; Scherer, A. Vacuum Rabi splitting in semiconductors *Nat. Phys.* **2006**, 2, 81−90.
24. Thomas, R.; Thomas, A.; Pullanchery, S.; Joseph, L.; Somasundaran, S. M.; Swathi, R. S.; Gray, S. K.; Thomas K. G. Plexcitons: The Role of Oscillator Strengths and Spectral Widths in Determining Strong Coupling. *ACS Nano.* **2018**, *12*, 402−415.
25. Thomas, E. M.; Cortes, C. L.; Paul, L.; Gray, S. K.; Thomas, K. G. Combined effects of emitter–emitter and emitter–plasmonic surface separations dictate photoluminescence enhancement in a plasmonic field. *Phys. Chem. Chem. Phys.* **2022**, *24*, 17250-17262.

26. Bitton, O.; Haran, G. Plasmonic Cavities and Individual Quantum Emitters in the Strong Coupling Limit. *Acc. Chem. Res.* **2022**, *55*, 1659−1668.

27. Das, K.; Dey, J.; Verma, M. S.; Kumar M.; Chandra M. Probing the role of oscillator strength and charge of exciton forming molecular J-aggregates in controlling nanoscale plasmon–exciton interactions. *Phys. Chem. Chem. Phys.* **2020**, *22*, 20499—20506.

28. Go´mez, D. E.; Vernon, K. C.; Mulvaney, P.; Davis, T. J. Surface Plasmon Mediated Strong Exciton-Photon Coupling in Semiconductor Nanocrystals. *Nano Lett.* **2010**, *10*, 274-278.

29. Manuel, A. P.; Kirkey, A.; Mahdi, N.; Shankar, K. Plexcitonics – fundamental principles and optoelectronic applications. *J. Mater. Chem. C* **2019**, *7*, 1821–1853.

30. Cao, E.; Lin, W.; Sun, M.; Liang, W.; Song, Y. Exciton-plasmon coupling interactions: from principle to applications. *Nanophotonics* **2018**, *7,* 145–167.

31. Gonzalez-Ballestero, C.; Feist, J.; Moreno, E.; GarciaVidal, F. J. Harvesting excitons through plasmonic strong coupling. *Phys. Rev. B: Condens. Matter Mater. Phys.* **2015**, *92*, 121402.

32. Krivenkov, V.; Goncharov, S.; Nabiev, I.; Rakovich, Y. P. Induced Transparency in Plasmon–Exciton Nanostructures for Sensing Applications. *Laser Photonics Rev*. **2019**, *13*, 1800176.

33. Flatten, L. C.; Christodoulou, S.; Patel, R. K.; Buccheri, A.; Coles, D. M.; Reid, B. P. L.; Taylor, R. A.; Moreels, I.; Smith, J. M. Strong Exciton–Photon Coupling with Colloidal Nanoplatelets in an Open Microcavity. *Nano Lett.* **2016**, *11*, 7137-7141.

34. Donegá, C. de M. Formation of nanoscale spatially indirect excitons: Evolution of the type-II optical character of CdTe/CdSe heteronanocrystals. *Phys. Rev. B* **2010**, *81* , 165303 .

35. Yoshie, T.; Scherer, A.; Hendrickson, J.; Khitrova, G.; Gibbs, H. M.; Rupper, G.; Ell, C.; Shchekin, O. B.; Deppe, D. G. Vacuum Rabi splitting with a single quantum dot in a photonic crystal nanocavity. *Nature* **2004**, *432*, 200–203.

36. Park, K.-D.; May, M. A.; Leng, H.; Wang, J.; Kropp, J. A.; Gougousi, T.; Pelton, M.; Raschke, M. B. Tip-enhanced strong coupling spectroscopy, imaging, and control of a single quantum emitter. *Sci. Adv.* **2019**, *5*, eaav5931.

37. Zengin, G.; Johansson, G.; Johansson, P.; Antosiewicz, T. J.; Käll, M.; Shegai, T. Approaching the strong coupling limit in single plasmonic nanorods interacting with J-aggregates**.** *Sci. Rep.* **2013**, *3*, 3074.

38. Wang, S.; Li, S.; Chervy, T.; Shalabney, A.; Azzini, S.; Orgiu, E.; Hutchison, J. A.; Genet, C.; Samorì, P.; Ebbesen, T. W. Coherent Coupling of WS_2 Monolayers with Metallic Photonic Nanostructures at Room Temperature. *Nano Lett.* **2016**, *16*, 4368–4374.

39. Zheng, D.; Zhang, S.; Deng, Q.; Kang, M.; Nordlander, P.; Xu, H. Manipulating Coherent Plasmon–Exciton Interaction in a Single Silver Nanorod on Monolayer WSe_2. *Nano Lett.* **2017**, *17*, 3809–3814.

40. Omata, T.; Asano, H.; Sakai, M.; Terai, Y.; Kita M. Enhanced Valley Splitting of Exciton Emission in Colloidal PbSe Quantum Dots When the Interdot Distance Coincides with Onset of Förster Resonance Energy Transfer. *J. Phys. Chem. Lett.* **2021**, *12*, 3120−3126.

41. Saikin, S. K.; Eisfeld, A.; Valleau, S.; Aspuru-Guzik, A. Photonics Meets Excitonics: Natural and Artificial Molecular Aggregates. *Nanophotonics* **2013**, *2*, 21−38.

42. Doria, S.; Sinclair, T. S.; Klein, N. D.; Bennett, D. I. G.; Chuang, C.; Freyria, F. S.; Steiner, C. P.; Foggi, P.; Nelson, K. A.; Cao, J.; Aspuru-Guzik, A.; Lloyd, S.; Caram, J. R.; Bawendi, M. G. Photochemical Control of Exciton Superradiance in Light-Harvesting Nanotubes. *ACS Nano* **2018**, *12*, 4556–4564.

43. Asano, H.; Tsukuda, S.; Kita, M.; Fujimoto, S.; Omata, T. Colloidal Zn(Te,Se)/ZnS Core/Shell Quantum Dots Exhibiting Narrow-Band and Green Photoluminescence. *ACS Omega* **2018**, *3*, 6703–6709.

44. Asano, H.; Arai, K.; Kita, M.; Omata, T. Synthesis of colloidal Zn(Te,Se) alloy quantum dots. *Mater. Res. Express* **2017**, *4*, 106501.

45. Roy, D.; Das, A.; De, C. K.; Mandal, S.; Bangal, P. R.; Mandal, P. K. Highly Photoluminescent InP Based Core Alloy Shell QDs from Air-Stable Precursors: Excitation Wavelength Dependent Photoluminescence Quantum Yield, Photoluminescence Decay Dynamics, and Single Particle Blinking Dynamics. *J. Phys. Chem. C* **2019**, *123*, 6922–6933.

46. Sattler, K. D. Handbook of nanophysics: Nanoparticles and Quantum Dots; CRC Press, USA, 2011.

47. Wang, Y.; Si, B.; Lu, S.; Ma, X.; Liu, E.; Fan, J.; Li, X.; Hu, X. Effective improvement in optical properties of colloidal CdTe@ZnS quantum dots synthesized from aqueous solution. *Nanotechnology* **2016**, *27*, 365707.

48. Vaishanav, S. K.; Korram, J.; Nagwanshi, R.; Karbhal, I.; Dewangan, L.; Ghosh K. K.; Satnami, M. L. Interaction of Folic Acid with Mn2+ Doped CdTe/ZnS Quantum Dots: In Situ Detection of Folic Acid. *J Fluoresc* **2021**, *31*, 951-960.

49. Knapp, E. W. Lineshapes of molecular aggregates, exchange narrowing and intersite correlation. *Chem. Phys.* **1984**, *85*, 73–82.

50. Kasha, M. Relation between Exciton Bands and Conduction Bands in Molecular Lamellar Systems. *Rev. Mod. Phys.* **1959**, *31*, 162–169.

51. Horng, M. L.; Quitevis, E. L. Visible Absorption Spectroscopy and Structure of Cyanine Dimers in Aqueous Solution: An Experiment for Physical Chemistry**.** J. Chem. Educ. **2000**, *5*, 637–639.

52. Preeyanka, N.; Dey, H.; Seth, S.; Rahaman, A.; Sarkar, M. Highly efficient energy transfer from a water soluble zinc silver indium sulphide quantum dot to organic J-aggregates. *Phys. Chem. Chem. Phys.* **2020**, *22*, 12772.

53. Kale, S.; Kale, A.; Gholap, H.; Rana, A.; Desai, R.; Banpurkar, A.; Ogale, S.; Shastry, P.; Quantum dot bio-conjugate: as a western blot probe for highly sensitive detection of cellular proteins. *J Nanopart Res*. **2012**, *14*,732.

54. Sharma, S.; Verma, A. S.; Sarkar, B. K.; Bhandari, R.; Jindal, V. K. In *AIP Conference Proceedings,* International conference on advances in condensed and nanomaterials, Chandigarh, India, Feb 23–26, 2011, Tripathi, S. K., Dharamvir, K., Kumar, R., Saini, G. S. S., Eds.; AIP Publishing Center, USA, 2011.

55. Oomen, E. W. J. L.; Smit, W. M. A.; Blasse, G. Jahn-Teller effect in the Sb^{3+} emission in zircon-structured phosphates. *Chem. Phys. Lett.* **1984**, *112*, 547.

56. Jacobs, P. W. M. Alkali halide crystals containing impurity ions with the ns^2 ground-state electronic configuration. *J. Phys. Chem. Solids* **1991**, *52*, 35.

57. Roy, P.; Devatha, G.; Roy, S.; Rao, A.; Pillai, P. P. Electrostatically Driven Resonance Energy Transfer in an All-Quantum Dot Based Donor–Acceptor System. *J. Phys. Chem. Lett*. **2020**, *11*, 5354−5360.

58. Lakowicz, J. R. Principles of Fluorescence Spectroscopy; Springer: New York, 2006.

59. Kubista, M.; Sjoback, R.; Eriksson, S.; Albinsson, B. Experimental correction for the inner-filter effect in fluorescence spectra. *Analyst* **1994**, *119*, 417–419.

CHAPTER 6

Charge-Transfer Dynamics between CdTe@ZnS Quantum Dots and Pyridinium-Based Ionic Liquids

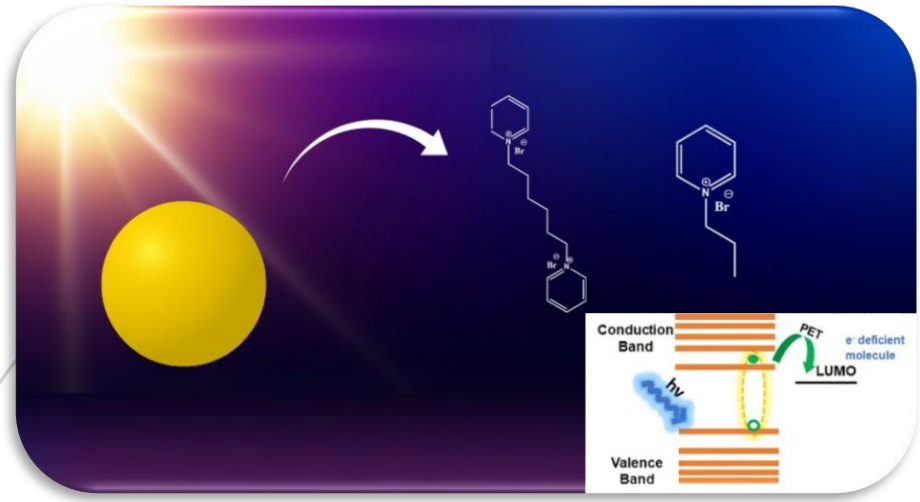

Abstract

This study investigates the photoinduced charge-transfer dynamics between CdTe@ZnS quantum dots (QDs) and a series of pyridinium-based ionic liquids (ILs)-C_3PyBr, C_6PyBr, and $[C_6Py_2]Br_2$, which are chosen for their strong electron-accepting characteristics. Steady-state photoluminescence measurements reveal pronounced quenching of QD emission upon interaction with the ILs, while the absence of spectral overlap between QD emission and IL absorption bands excludes energy-transfer processes. Stern-Volmer analysis demonstrates contributions from both static and dynamic quenching pathways, with the dicationic IL ($[C_6Py_2]Br_2$) exhibiting the highest quenching efficiency. Time-resolved PL measurements further confirm substantial reductions in QD lifetimes, indicating efficient electron transfer from QDs to the IL acceptors. Ultrafast transient absorption spectroscopy provides direct evidence of accelerated carrier extraction and faster bleach recovery in the QD–IL hybrid systems, validating the proposed photo-induced charge-transfer mechanism. Collectively, these findings establish pyridinium-based ILs as effective electron acceptors capable of modulating exciton dynamics in CdTe@ZnS QDs. The insights gained from this work offer a fundamental understanding of interfacial electron transfer in QD–IL hybrids and provide valuable guidance for designing advanced optoelectronic and energy-conversion materials combining both QDs and ILs.

6.1. Introduction

In recent years, quantum dots (QDs) and room-temperature ionic liquids (ILs) have come up as two standout families of advanced functional materials, each with distinct characteristics yet highly complementary in many research and application domains.[1-15] Though QDs and ILs

differ fundamentally, QDs being tiny semiconductor nanocrystals (usually under ~10 nm) whose optical and electronic traits depend on their size and ILs being primarily organic salts that remain liquid near ambient temperature have found growing use across fields like optoelectronics, energy systems, nanotechnology, and sustainable chemistry.[16-20]

Quantum dots (QDs) are nanoscale semiconductor crystals whose properties are dictated by quantum confinement, when their dimensions shrink to below the material's exciton Bohr radius, discrete energy levels emerge and the optical bandgap increases as size decreases.[1-10] This results in size-tunable absorption and emission, enabling fine control over their optical response. Upon photoexcitation, QDs emit light whose wavelength depends on particle size.[1-10] In comparison to traditional organic fluorophores, quantum dots provide broad spectral absorption, sharp and bright emission bands, high molar extinction coefficients, strong photostability and thermal resilience, and extended fluorescence lifetimes.[1-5] These characteristics make QDs particularly suitable for applications in bioimaging, light-emitting devices, and photodetectors.[21-23] Many QDs also exhibit multiple exciton generation (MEG), a process in which absorption of a single high-energy photon yields more than one electron-hole pair.[24-25] This effect has been shown to have the potential to exceed the Shockley–Queisser limit in photovoltaic cells by generating additional photocurrent from high-energy photons.[25-27] Finally, ongoing improvements in synthesis, such as scalable colloidal routes, surface passivation strategies, and core-shell architectures, have significantly improved QD colloidal stability and manufacturability. These advancements have helped reduce costs and broaden the practical deployment of QDs in solar energy conversion, high-performance displays, and chemical sensors.[28-29] It is important to note that excited quantum dots (QDs) readily donate electrons in photoinduced electron transfer (PET) processes, causing fluorescence quenching in the presence of effective electron acceptors.[30]

In parallel, room-temperature ionic liquids (ILs), typically salts made from bulky, asymmetric organic cations (e.g., imidazolium, pyridinium, ammonium) paired with diverse organic or inorganic anions, have transformed solvent chemistry due to their exceptional physicochemical characteristics.[11-15] These include almost zero vapor pressure, excellent thermal and chemical robustness, wide electrochemical windows, high ionic conductivity, and easily tunable polarity.[11-13] Their favorable properties make ILs high-performance electrolytes in energy conversion and storage systems, such as lithium-ion batteries, supercapacitors, fuel cells, and actuators, providing low volatility, electrochemical inertness, and enhanced ionic mobility.[16-20] Moreover, by rationally designing their cationic and anionic constituents, ILs can be tailored to function as electron acceptors, enabling controlled interfacial charge-transfer processes that are advantageous for electrochemical sensors, electrocatalysis, and electrodeposition.[11-12] In organic synthesis, electron-accepting ILs act as efficient catalytic media, stabilizing reactive intermediates and improving selectivity within recyclable and environmentally benign solvent systems.[31-32] In energy storage devices, they facilitate stable solid–electrolyte interphase formation and enhance energy density, while in photovoltaic systems, particularly dye-sensitized and perovskite solar cells, ILs promote efficient charge transport, defect passivation, and improved film morphology.[33] Moreover, their strong affinity toward CO_2 enables ILs to capture and activate CO_2 molecules, making them promising candidates for electrochemical CO_2 reduction and carbon recycling.[34-35] The present study is motivated by the need to understand how such unique solvation and interfacial dynamics of ionic liquids influence electron-transfer behavior, which is essential for optimizing their functionality as electrolytes and active media in next-generation energy technologies.

The integration of quantum dots (QDs) with room-temperature ionic liquids (ILs) is continuously attracting considerable attention, particularly in quantum dot-sensitized solar cells (QDSCs).[36-39] Conventional electrolytes used in these devices such as sulfide/polysulfide

or ferri/ferrocyanide in aqueous media suffer from volatility and leakage issues that compromise long-term stability.[40] Replacing them with IL-based electrolytes can address such drawbacks and boost device durability. ILs have the ability to stabilize charged species and facilitate electron transfer reactions, positioning them as promising acceptors in PET processes.[11-12] For instance, customized imidazolium ILs have been shown to stabilize CdTe nanocrystals in both polar and nonpolar environments, forming well-dispersed QD–IL composites ideal for hybrid functional systems.[11] Understanding the quenching mechanisms within these hybrids is pivotal for optimizing optoelectronic devices and fluorescence sensors. Key factors include the IL's cation–anion pair, its viscosity, and the nature of interactions at the QD–IL interface, all of which govern electron-transfer efficiency and the degree of fluorescence suppression. Moreover, the specific IL composition and its microstructural environment affect charge separation and recombination dynamics. While Pyridinium-based ILs have been identified as promising electron-accepting species, especially when paired with organic dye donors,[12] Yet systematic electron transfer studies involving QDs as electron donors and ILs as acceptors are rare. Likewise, the comparative influence of mono- versus dicationic ILs structures on charge-transfer kinetics in QD–IL hybrids is elusive.

Keeping the above facts in mind, in this study, we have examined fluorescence quenching mediated by electron transfer in QD–IL hybrid systems. For this purpose, we have employed CdTe@ZnS quantum dots as electron donors and task-specific pyridinium-based ionic liquids, namely, C_3PyBr, C_6PyBr, and $[C_6Py_2]Br_2$ (molecular structure shown in Chart 6.1), as electron acceptors. These hybrid materials have been systematically characterized, and by conducting time-resolved measurements and Stern–Volmer analysis, we aim to dissect how interfacial charge transfer pathways influence emission behavior. Moreover, transient absorption Spectroscopic (TAS) analyses have confirmed that charge transfer from the CdTe@ZnS QDs to the IL acceptors, revealing interfacial electron-transfer dynamics. Our findings have

elucidated how molecular design and interface engineering influence quenching behavior and have provided practical insights for the design of next-generation optoelectronic hybrid materials.

6.2. Result and discussion

The CdTe@ZnS quantum dots (QDs) were thoroughly characterized to gain a comprehensive understanding of their structural and optical features. Elemental composition analysis have been performed using energy-dispersive X-ray analysis (EDAX) (Figure APX6.1), which confirmed the presence of cadmium (Cd), tellurium (Te), zinc (Zn), and sulfur (S) elements in the expected stoichiometric ratio. This result verified the successful formation of the core–shell CdTe@ZnS heterostructure. High-resolution transmission electron microscopy (HRTEM) images have revealed that the QDs are nearly spherical and uniformly dispersed, with an average particle size of approximately 4.4 nm (Figure APX6.2). The lattice-resolved image has also displayed distinct lattice fringes with an interplanar spacing of about 0.356 nm, which can be assigned to the (111) crystallographic plane of CdTe@ZnS. This observation is consistent with previously reported values for CdTe-based QDs, confirming the crystalline quality of the synthesized nanoparticles.[41] Furthermore, Powder X-ray diffraction (PXRD) analysis (Figure APX6.2) provided additional evidence of the crystalline phase of the material. From PXRD data, we have found crystal plane (111), (220), and (311) (Shown in Figure APX6.2c) well matched with literature report.[41] The diffraction peaks correspond well with those of the zinc blende (cubic) crystal structure, suggesting that the CdTe@ZnS QDs maintain a well-defined crystalline framework. The optical properties of the CdTe@ZnS QDs have been investigated using steady-state absorption and photoluminescence (PL) spectroscopy (Figure 6.1). The absorption spectrum has demonstrated a broad band with a distinct excitonic feature around 515 nm, characteristic of the quantum confinement effect in nanocrystalline semiconductors

(Figure 6.1). The photoluminescence spectrum has exhibited a relatively narrow and symmetric emission band centered at approximately 560 nm (Figure 6.1). The observed redshift between the absorption edge and the emission maximum is attributed to the Stokes shift, which is typical of quantum-confined systems and arises from exciton relaxation to lower-energy states before radiative recombination. The ZnS overlayer can be attributed to efficient surface passivation, which improves the PLQY.[42-43] Additionally, the ZnS shell provides chemical and photostability, effectively protecting the CdTe core from environmental degradation.[42-43]

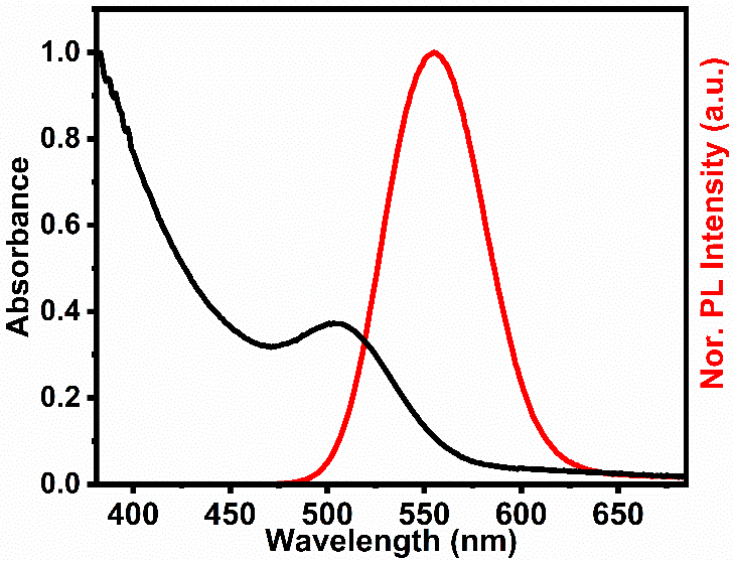

Figure 6.1. Normalized absorption (black) and emission (red) spectra of CdTe@ ZnS QD.

In the present study, the pyridinium-based ionic liquids C_3PyBr, C_6PyBr, and $[C_6Py_2]Br_2$ have been deliberately chosen as electron acceptors, as this class of ionic liquids has been recognized as an efficient family of electron-accepting species.[12] It is important to note that no spectral overlap has been observed between the QD emission and the absorption bands of these ILs, which has ruled out the possibility of an electronic energy-transfer (EET) pathway in the current system. To probe the interaction between the QDs and the pyridinium-based ILs, the fluorescence response of the QDs has been measured independently both in the absence of ILs and in the presence of each IL—C_3PyBr, C_6PyBr, and $[C_6Py_2]Br_2$. The interaction has been

further examined by monitoring the changes in the donor (QD) emission upon addition of the acceptor (ILs). The PL spectra of the QDs in the presence and absence of the ILs are shown in Figure 6.2(a-c). Interestingly, upon introducing the ILs, the PL intensity of the QDs has been quenched, indicating the occurrence of charge transfer can happen from the QDs to the ILs. Similar charge-transfer-mediated quenching involving pyridinium-based ILs has been reported previously.[12] Moreover, the quenching efficiency of the dicationic IL, $[C_6Py_2]Br_2$, is found to be considerably higher than that of the monocationic ILs, C_3PyBr and C_6PyBr. The emission spectra collected with sequential additions of each IL and the corresponding decrease in QD fluorescence intensity have been presented in Figure 6.2a-c. Interestingly, upon introducing the ILs, the PL intensity of the QDs has been quenched, indicating the occurrence of energy/charge transfer can happen from the QDs to the ILs. It is important to note that no spectral overlap (shown in Figure APX6.3) has been observed between the QD emission and the absorption bands of these ILs, which has ruled out the possibility of an electronic energy-transfer (EET) pathway in the current system. Therefore, the charge transfer is the only possibility in this case. Similar charge-transfer-mediated quenching involving pyridinium-based ILs has been reported previously.[12] It is be noted that upon addition of the acceptor, the donor emission undergoes a slight red shift. TEM micrographs (Figure APX6.4) reveal no discernible change in the size of the QDs before and after the addition of all three ILs, indicating that the observed red shift does not originate from structural modifications. Instead, this spectral shift is most likely attributed to the charge-transfer interactions between the nanocrystals (NCs) and the acceptor moiety.[44-46] Based on the data shown in Figure 6.2d-f, the charge-transfer efficiencies for C_3PyBr, C_6PyBr, and $[C_6Py_2]Br_2$ have been estimated to be approximately 66%, 64%, and 84%, respectively. Furthermore, the steady-state PL quenching data have been analysed using Stern–Volmer (SV) plots (F_0/F vs. [Q]) for the QDs in the presence of each of the three ionic liquids, as shown in Figure 6.2. Interestingly, the upward curvature observed in the Stern–Volmer (SV)

plots (F_0/F vs. [Q]) (Shown in Figure 6.2d-f) for all IL systems has suggested that both static and dynamic quenching pathways can contribute to the overall quenching mechanism in the present system. The static quenching constants (K_S) values are estimated to be ~1.11 × 10^4, ~1.00 × 10^4, and ~4.14 × 10^4 M^{-1} for QD-C_3PyBr, QD-C_6PyBr, and QD-[C_6Py_2]Br_2 respectively, at 298 K, whereas the corresponding dynamic quenching constants (K_D) values are found to be ~2.67 × 10^3, ~2.60 × 10^3, and ~7.14 × 10^3 M^{-1}, respectively. Moreover, the negative ζ-potential of the CdTe@ZnS QDs (Figure APX6.5 and Table APX6.1) indicates the presence of negatively charged mercaptopropionic acid (MPA) ligands on the QD surface. This negative surface potential is expected to promote electrostatic interactions with the cationic pyridinium moieties of the ILs, facilitating their association with the QDs and leading to electrostatically driven photoluminescence (PL) quenching. Upon the addition of ILs, the magnitude of the negative ζ-potential decreases, with a more pronounced reduction observed in the presence of the dicationic ILs, as shown in Figure APX6.5 and Table APX6.1. This observation further supports that the interaction between the QDs and ILs is predominantly electrostatically driven. The fact that photo-induced electron transfer (PET) process can be driven by electrostatic interaction the donor and the acceptor moieties has also been reported by Pillai and co-workers earleir.[47] A schematic representation of the said event is depicted in Scheme 6.1. Furthermore, fluorescence correlation spectroscopy (FCS) has been employed to investigate the QD–C_3PyBr, QD–C_6PyBr, and QD–[C_6Py_2]Br_2 interactions at the single-molecule level. As shown in Figure APX6.6, the normalized FCS curves exhibit an increase in diffusion time from ~170 μs for pristine QDs to ~650, 620, and 870 μs for the respective QD–pyridinium-based IL systems, confirming binding interactions between the QDs and ionic liquids.

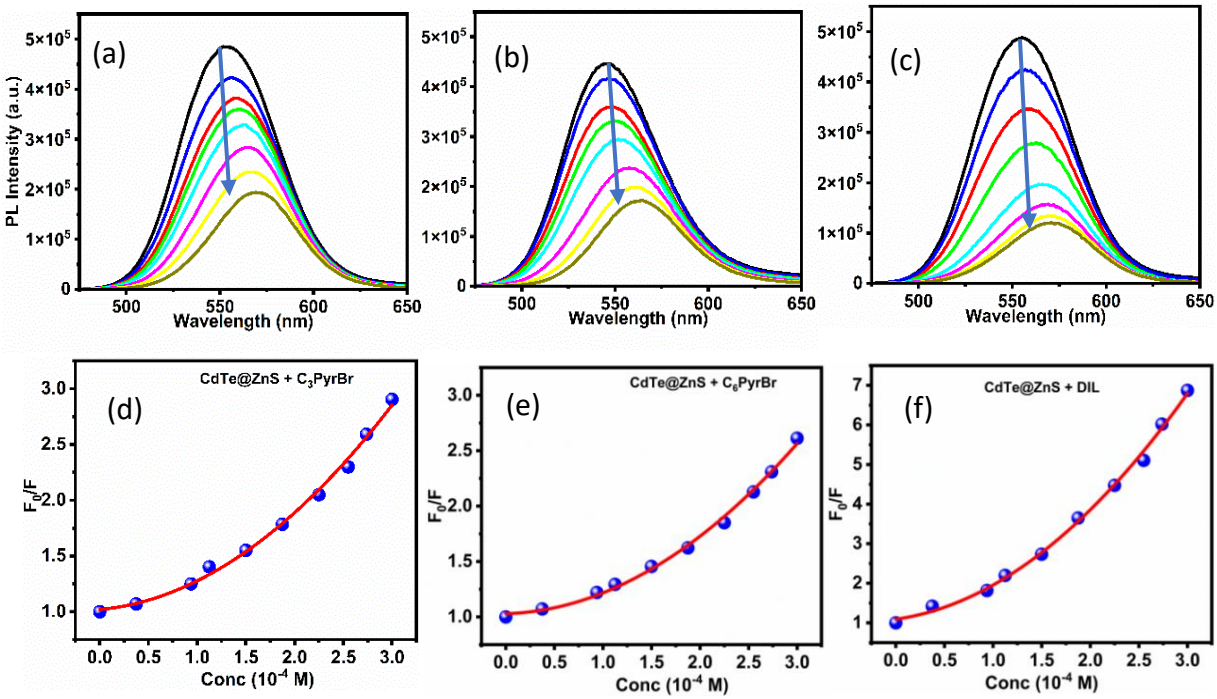

Figure 6.2. (a–c) Emission spectra of the CdTe@ZnS QDs recorded with successive additions of C_3PyBr, C_6PyBr, and $C_6(Py)_2Br_2$. (d–f) Corresponding Stern–Volmer plots illustrating the fluorescence quenching behaviour of the CdTe@ZnS QDs in the presence of increasing concentrations of C_3PyBr, C_6PyBr, and $C_6(Py)_2Br_2$ ILs.

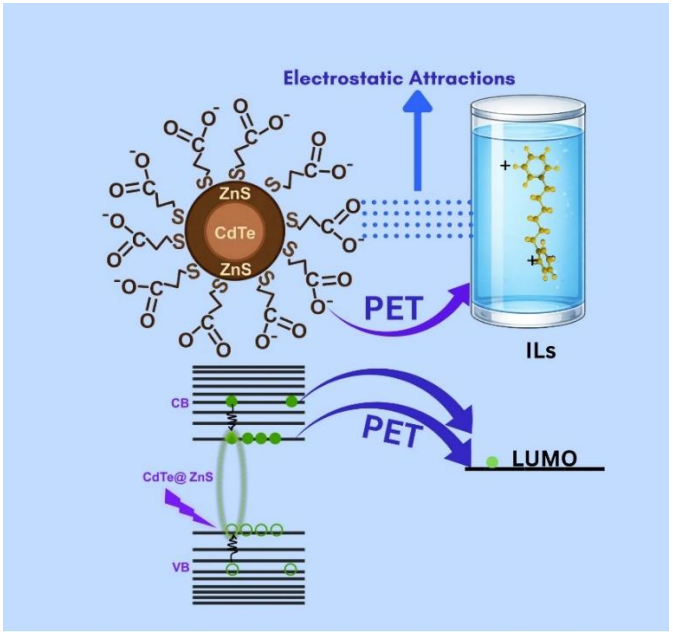

Scheme 6.1. The schematic representation of photoinduced charge transfer dynamics from CdTe@ZnS QDs to Pyridinium-based ILs.

To gain deeper insight into the PL quenching mechanism, time-resolved PL (TRPL) measurements have been carried out. The PL decay profiles of the QDs in the absence and presence of the ILs are presented in Figure 6.3, and the corresponding decay parameters are summarized in Table APX6.2. In the presence of C_3PyBr, C_6PyBr, and $C_6(Py)_2Br_2$, the average PL lifetime of the CdTe@ZnS QDs has been significantly reduced. For example, the average PL lifetime for the pristine QDs decreases from 10.63 ns to 6.31 ns, 6.50 ns, and 3.34 ns for QDs in the presence of C_3PyBr, C_6PyBr, and $C_6(Py)_2Br$, respectively, as depicted in Table APX6.2.This substantial decrease in the PL lifetime further supports the occurrence of charge transfer from the QDs (donor) to the ILs within the nanohybrid assemblies.[12] Moreover, from the TRPL data, the charge-transfer efficiencies for the QD–IL systems have been estimated to be 43%, 42%, and 70% in the presence of C_3PyBr, C_6PyBr, and $C_6(Py)_2Br_2$, respectively. These values are in good agreement with those obtained from the steady-state fluorescence measurements, where contributions from both static and dynamic quenching processes have been identified in the QD-ILs nanohybrid systems.

Additionally, the linear Stern–Volmer plots (τ_0/τ vs. [Q]) with positive slopes (Figure 6.3) for all three QD-ILs systems have confirmed the involvement of dynamic quenching pathways in the overall quenching process. Furthermore, the dicationic ILs ($C_6(Py)_2Br_2$) has exhibited a considerably higher quenching efficiency compared to the monocationic ILs, C_3PyBr and C_6PyBr, consistent with its stronger electron-accepting capability. The dynamic bimolecular quenching rate constants (k_q) for the QD-C3PyBr, QD-C6PyBr, and QD-$[C_6Py_2]Br_2$ systems are estimated to be 2.5×10^{11}, 2.4×10^{11}, and 6.7×10^{11} M^{-1} s^{-1}, respectively. Furthermore, the dicationic ILs C6(Py)2Br2 have exhibited a considerably higher quenching efficiency compared to the monocationic ILs, of C_3PyBr and C_6PyBr, consistent with their stronger electron-accepting capability. The above results further reveal that the PET process between QD and ILs is largely insensitive to the alkyl chain length of the ionic liquids,

while being predominantly governed by the pyridinium moiety, highlighting the crucial role of ionic liquid molecular architecture in the PET process. It is pertinent to mention that the simultaneous occurrence of static and dynamic photoluminescence (PL) quenching in core–shell quantum dot systems has also been reported for quantum dot–organic dye assemblies, where the photoinduced electron transfer (PET) process is driven by electrostatic interactions between the donor and acceptor moieties.[47] Therefore, the present interpretation of the quenching mechanism is consistent with previously reported observations.

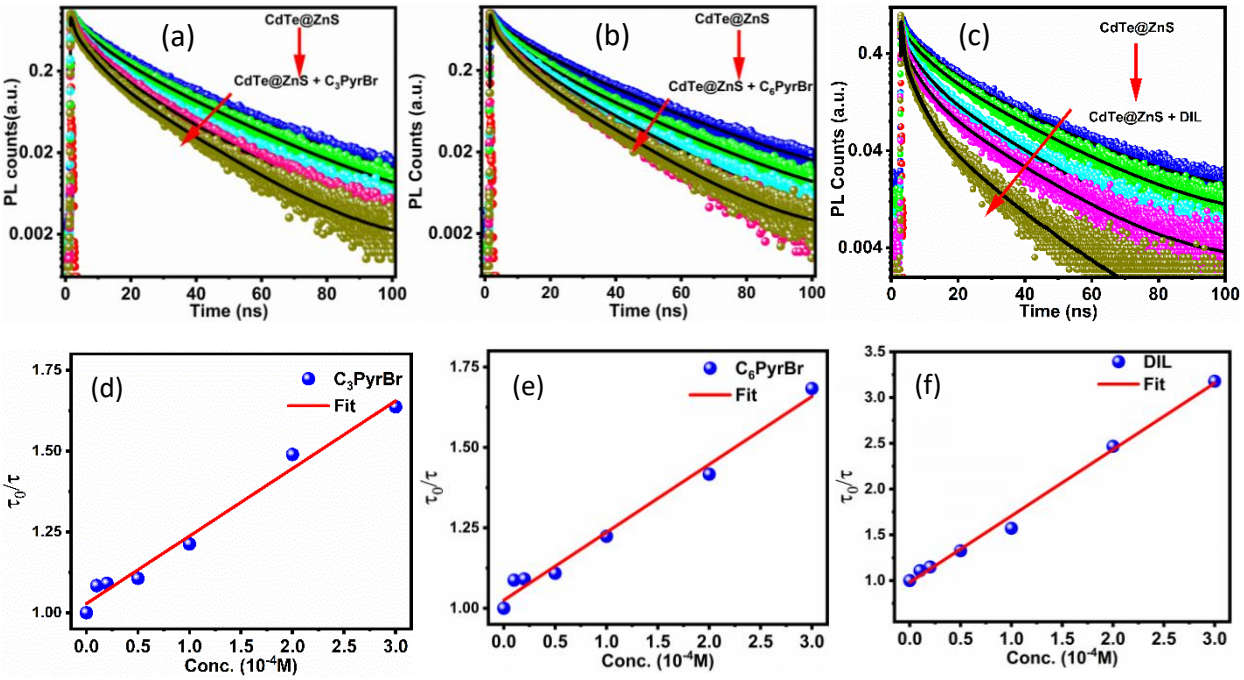

Figure 6.3. (a–c) Fluorescence decay profiles of the CdTe@ZnS QDs recorded with successive additions of C_3PyBr, C_6PyBr, and $C_6(Py)_2Br_2$. (d–f) Corresponds plots of τ_0/τ versus of concentrations of C_3PyBr, C_6PyBr, and $C_6(Py)_2Br_2$ ILs.

Results from both steady-state and time-resolved measurements have indicated that electron transfer from the QDs to the pyridinium-based ILs has played a key role in the quenching of QD emission. Under normal conditions, the photoluminescence decay of isolated QDs, primarily governed by exciton recombination, has typically occurred on the nanosecond timescale. However, in the presence of these ionic liquids, the decay has shifted to the

femtosecond regime, revealing an ultrafast quenching channel that has become active due to the QD–IL interaction.

To interpret this behaviour, the energetic alignment of the conduction and valence bands of the QDs with the LUMO and HOMO levels of the pyridinium-based ILs has been considered. Moreover, the observation of negative free-energy changes, obtained by using Rehm-Weller equation[48]1.11, have clearly suggested that the light-induced electron transfer from the QDs to all three systems is energetically accessible and thermodynamically favourable.

To obtain direct mechanistic insight into the ultrafast charge-carrier dynamics governing the interaction between CdTe@ZnS quantum dots (QDs) and ionic liquids, ultrafast transient absorption (TA) spectroscopy has been employed as a decisive probe. This technique has enabled real-time tracking of carrier relaxation and interfacial electron-transfer processes on femtosecond to nanosecond time scales.[49-50] TA measurements have been performed for pristine CdTe@ZnS QDs and for QDs in the presence of pyridinium-based ionic liquids under identical experimental conditions. Following excitation at 2.95 eV (420 nm), transient absorption spectra of pristine CdTe@ZnS QDs were recorded across the 440-700 nm spectral window at various pump-probe delay times, as shown in Figure 6.4a. The TA spectra of pristine CdTe@ZnS QDs exhibit a pronounced ground-state bleach centered at 516 nm, corresponding to the band-edge excitonic transition and in excellent agreement with the steady-state absorption maximum (Figure 6.1).[51] Upon introduction of the ionic liquids, the overall spectral signatures remain qualitatively similar, confirming preservation of the QD electronic structure; however, a marked reduction in bleach intensity has been observed for all QD-IL hybrids (Figure 6.4c-d). Notably, the bleach amplitude decreases (Figure 6.4d) most significantly in the presence of the dicationic ionic liquid $[C_6Py_2]Br_2$, reaching approximately half of that observed for pristine QDs, while the monocationic ILs induce comparatively smaller reductions. Because

both pump fluence and optical density have been carefully maintained constant, the diminished bleach intensity unambiguously indicates efficient photoinduced hot electron transfer from the QDs to the ionic liquids rather than changes in excitation density or absorption. [52-53]

Further compelling evidence for this interfacial electron-transfer process has been obtained from the TA kinetic traces monitored at the bleach maximum (Figure 6.5). It is to be noted here that carrier dynamics of the pristine CdTe@ZnS QDs have been previously studied by several researchers using TAS.[53-54] The kinetics of pristine have been characterized by an initial sub-picosecond rise associated with hot-carrier relaxation to the band-edge states, followed by multicomponent bleach recovery reflecting carrier trapping, detrapping, and recombination processes (Table 6.1). For example, in pristine QD, the rise time τ_g = 250 fs (Table 6.1) corresponds to hot-carrier relaxation from higher excitonic states to the band edge.[50-54] The subsequent bleach recovery is fitted in time constants of τ_1 =1.10 ps (−38.8%), and τ_2 =18.5 ps (-31.7%) and τ_3 =>1 ns (−29.5%) (Table 6.1). The shortest decay component (τ_1) is attributed to the shallow trapping of band-edge charge carriers at defect states,[50–54] whereas the intermediate decay component (τ_2) corresponds to deep trap states. The longest decay component (τ_3) is associated with charge recombination processes.[50-54] Similar multicomponent relaxation dynamics have been reported in related quantum dot systems by Samanta and co-workers and Ghosh and co-workers.[53-54] A similar mechanistic interpretation has been used to rationalize the PET kinetics of quantum dots in the presence of organic and inorganic analytes. As can be seen from Figure 6.5a, the presence of ionic liquids dramatically modifies these dynamics. It is to be noted that the excitation at 420 nm initially promotes carriers to high-energy states well above the conduction band minimum. The subsequent relaxation of these non-thermalized electrons toward the band edge, leading to the formation of cold carriers, is predominantly observed as the growth of the bleach signal. Consequently, the ~250 fs rise time represents the intraband relaxation (thermalization) of hot electrons. The

photoinduced bleach is inherently majorly contributed by electrons rather than by holes due to the substantially lower electron effective mass ($m_h/m_e \approx 4$) and the higher degeneracy of the valence band in CdTe.[53] In the presence of all three ILs, the growth time is found to be significantly reduced, even lower than the temporal resolution of our femtosecond setup (<0.1ps), which confirms the ultrafast hot electron transfer from the QDs to ILs. Notably, the band edge bleach intensity (Figure 6.5b) of the QDs is reduced to half and three-fourth in the presence of DILs and both MILs, respectively, which indicates ~50% of the hot electrons are transferred from the QDs to DILs, whereas ~25% transfer is observed for MILs. Under these conditions, bleach formation is no longer dominated by electron cooling but is instead governed by the relaxation dynamics of hot holes, providing compelling evidence for efficient hot-electron extraction by the ionic liquids before complete band-edge thermalization.[53] Concomitantly, the bleach recovery accelerates substantially in the presence of ILs, providing direct spectroscopic evidence for rapid band edge electron transfer from the QDs to the ionic liquids. In this regime, the temporal evolution of the bleach primarily reflects the dynamics of hole trapping and the subsequent recombination. Because the presence of an electron acceptor rapidly removes electrons from the QDs, exciton dissociation is enhanced, and the recovery of the bleach is no longer governed by electron dynamics. It is pertinent to mention here that efficient light-induced electron-transfer processes from core-shell quantum dots to organic and inorganic acceptor are well documented in the literature.[47,53-55]

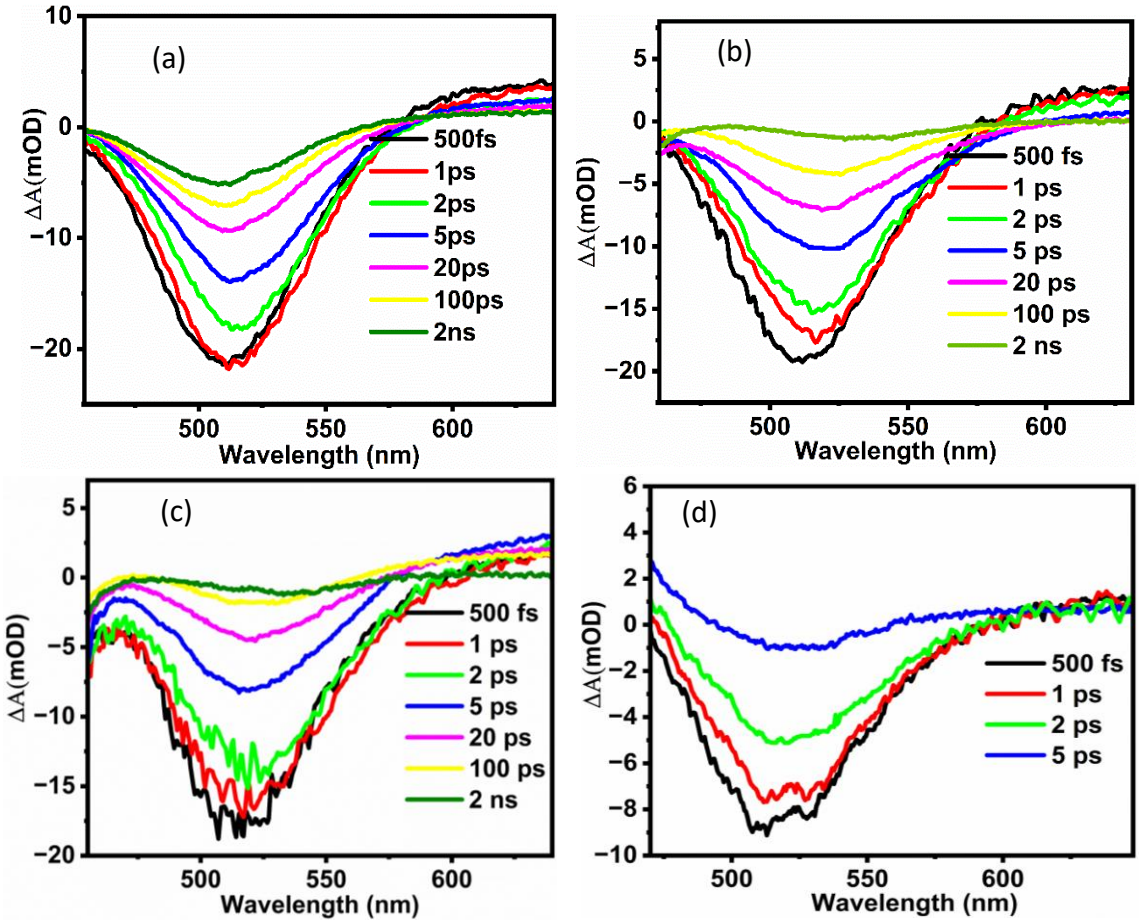

Figure 6.4. Transient absorption spectra of CdTe@ZnS QDs in (a) absence ILs and in presence of (b) C_3PyBr, (c) C_6PyBr, and (d)$[C_6Py_2]Br_2$ ILs plotted at different pump-probe delay times after the photoexcitation of 420 nm.

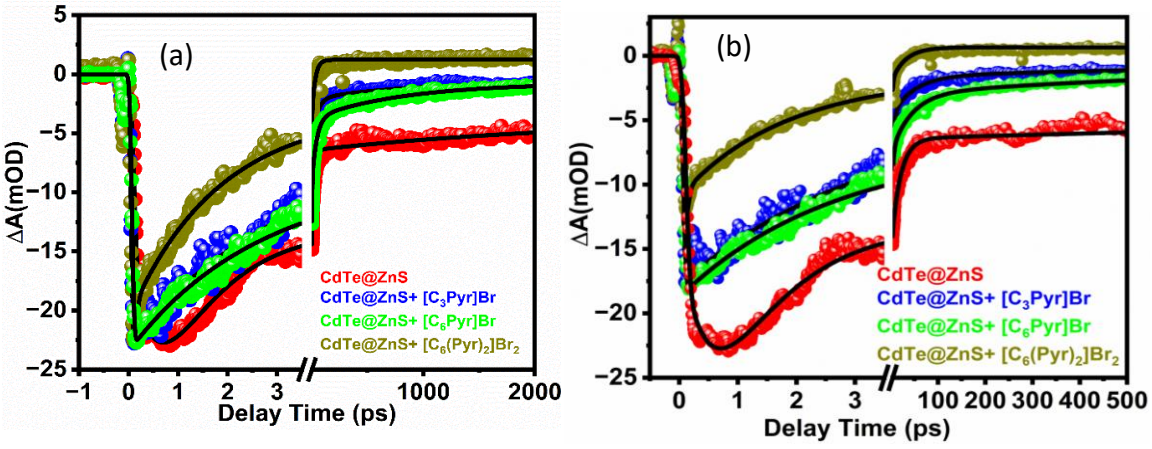

Figure 6.5. (a) Normalized TA kinetics of CdTe@ZnS QDs in the absence and presence of various pyridinium-based ILs probed at 516 nm after the photoexcitation of 420 nm. (b) Comparative kinetics for CdTe@ZnS QDs in the absence and presence of C_3PyBr, C_6PyBr, and $[C_6Py_2]Br_2$ at their bleach maxima (516 nm).

Table 6.1. Kinetic Fitting Parameters for the Probe Monitored at the Bleach Position (516 nm).

System	τg(ps) α1	τ1(ps) α1	τ2(ps) α2	τ3 α3
QDs	0.25 (100%)	1.07 (-39%)	18.50 (-31%)	>1 ns (-30%)
QDs-C_3PyBr	<0.1 (100%)	1.40 (-53.4%)	23.00 (-37.6%)	>1 ns (-19%)
QDs-C_6PyBr	<0.1 (100%)	1.73 (-54.5%)	25.00 (-27.1%)	>1 ns (-18.4%)
QDs-[C_6Py_2]Br_2	<0.1 (100%)	0.10 (-26%)	1.10 (-55%)	19.3 ps (-19%)

Among the studied systems, the fastest bleach recovery has been observed for the [C_6Py_2]Br_2-treated QDs, clearly demonstrating that the dicationic ionic liquid possesses the highest electron-accepting capability. This trend correlates strongly with the molecular architecture and enhanced electron affinity of the dicationic IL and is fully consistent with the results obtained from steady-state and time-resolved photoluminescence measurements. The more favorable thermodynamic driving force for electron transfer in the dicationic system further rationalizes the observed acceleration in carrier extraction dynamics. Based on these observations, a coherent picture of the photoinduced charge-transfer mechanism has emerged. Upon photoexcitation, electrons in CdTe@ZnS QDs are promoted to high-energy conduction-band states. In the absence of ionic liquids, these carriers relax to the band edge and recombine radiatively, giving rise to photoluminescence. In the presence of pyridinium-based ionic liquids, however, an energetically favorable interfacial pathway becomes operative, enabling ultrafast transfer of conduction-band electrons from the QDs to the LUMO levels of the ionic liquids. This efficient electron extraction suppresses radiative recombination, leading to pronounced quenching of both photoluminescence intensity and lifetime. The efficiency of this process is dictated by the electron-accepting strength of the ionic liquids, with the dicationic

$[C_6Py_2]Br_2$ enabling the most efficient charge extraction. A schematic illustration of the photoinduced charge-transfer mechanism is presented in Scheme 6.1. Hence, these ultrafast spectroscopic results constitute the most direct and compelling evidence for the role of pyridinium-based ionic liquids as efficient photoinduced electron acceptors from CdTe@ZnS QDs. The TA measurements firmly establish interfacial electron transfer as the dominant quenching mechanism and highlight molecular design of ionic liquids as a powerful strategy for controlling carrier dynamics at QD interfaces.

6.3. Conclusion

In this study, we have systematically investigated the charge-transfer dynamics between CdTe@ZnS quantum dots and a series of pyridinium-based ionic liquids—C_3PyBr, C_6PyBr, and $[C_6Py_2]Br_2$, which are chosen for their strong electron-accepting capabilities. Steady-state photoluminescence measurements have revealed pronounced quenching of QD emission upon the addition of these ILs, while the absence of spectral overlap between the donor emission and IL absorption bands has confirmed that the quenching event does not proceed through an energy-transfer mechanism. Instead, the observed decrease in emission intensity, along with Stern–Volmer behavior, has indicated that both static and dynamic quenching processes contribute to the interaction, with the dicationic IL consistently demonstrating the highest quenching efficiency. Time-resolved PL studies have further substantiated these observations by showing a significant shortening of the QD lifetimes in the presence of the ILs, consistent with effective electron transfer from the QDs to the ionic acceptors. The trend in charge-transfer efficiencies (highest for $[C_6Py_2]Br_2$) correlates well with the molecular structure and electron-accepting strength of the ILs. Complementary ultrafast transient absorption measurements have provided direct evidence of accelerated carrier extraction and faster bleach recovery dynamics in the IL-treated QDs, further confirming the significant role of the interfacial electron transfer

process in governing the quenching mechanism. Overall, the combined steady-state, time-resolved, and ultrafast spectroscopic analyses have established that pyridinium-based ILs efficiently modulate exciton recombination in CdTe@ZnS QDs through rapid electron-transfer pathways. The enhanced charge-accepting ability of the dicationic IL underscores the importance of molecular design in tuning interfacial interactions. These insights not only deepen our understanding of QD–IL electronic coupling but also provide valuable guidelines for designing next-generation hybrid materials for optoelectronic and energy-conversion applications.

5.4 Appendix

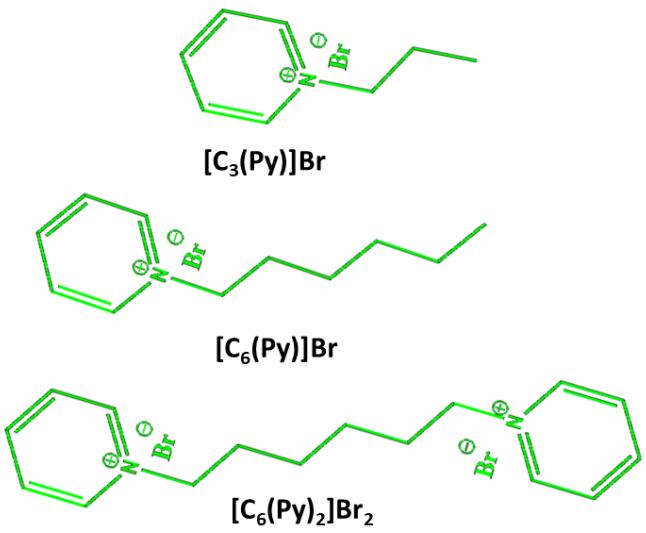

Chart APX6.1. Molecular structure of $[C_3(Py)]Br$, $[C_6(Py)]Br$, and $[C_6(Py)_2]Br_2$ ILs.

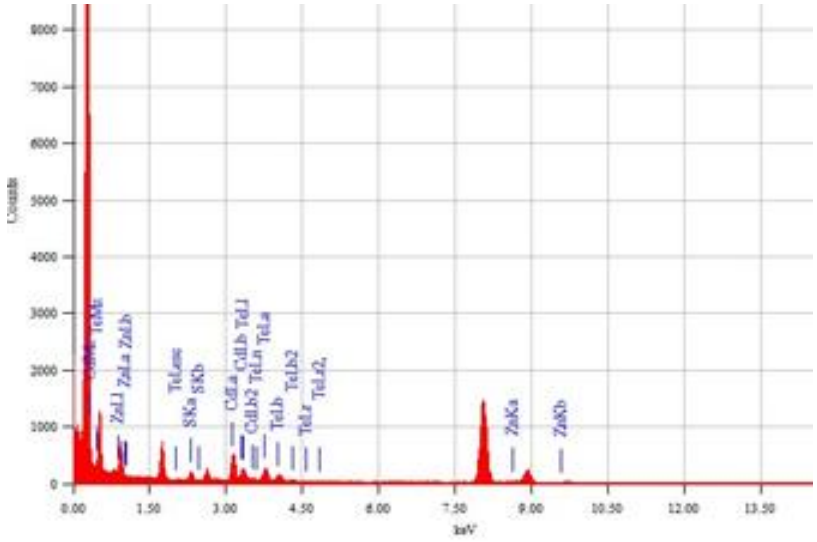

Figure APX6.1. EDS spectrum of CdTe@ZnS QD.

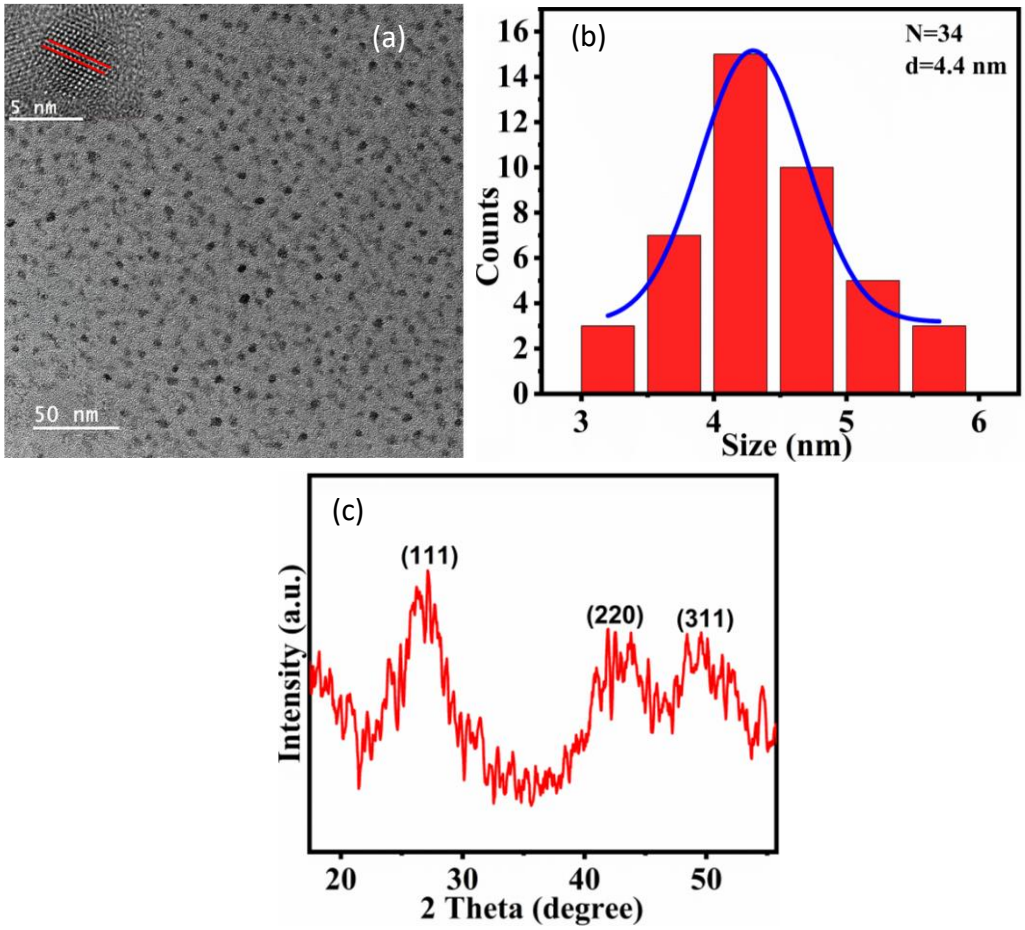

Figure APX6.2. a) TEM image and Inset HRTEM image b) size distribution of TEM of CdTe@ZnS QDs and c) XRD of CdTe@ZnS QDs.

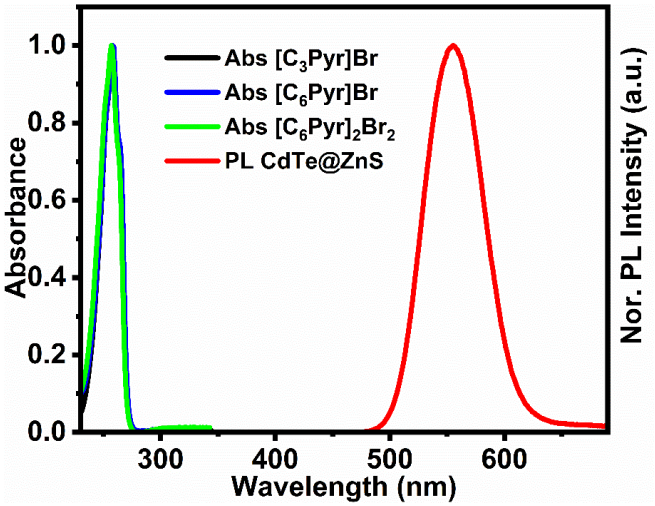

Figure APD6.3. Spectral overlap between absorbance of ILs and PL of CdTe@ZnS QDs

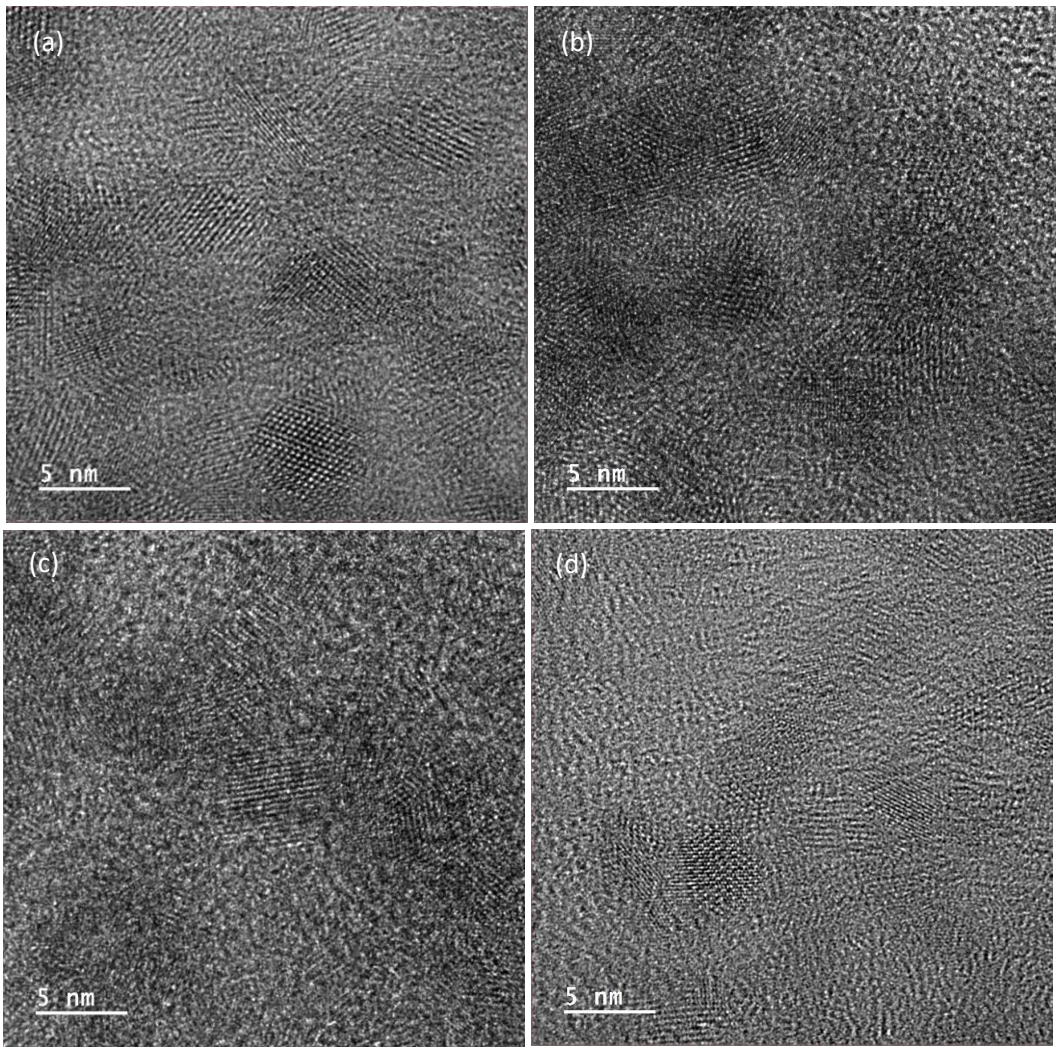

Figure APV6.4. TEM image of CdTe@ZnS QDs in (a) absence and presence of (b)C_3(Py)]Br, (c)[C_6(Py)]Br, and (d)[C_6(Py)$_2$]Br$_2$ ILs.

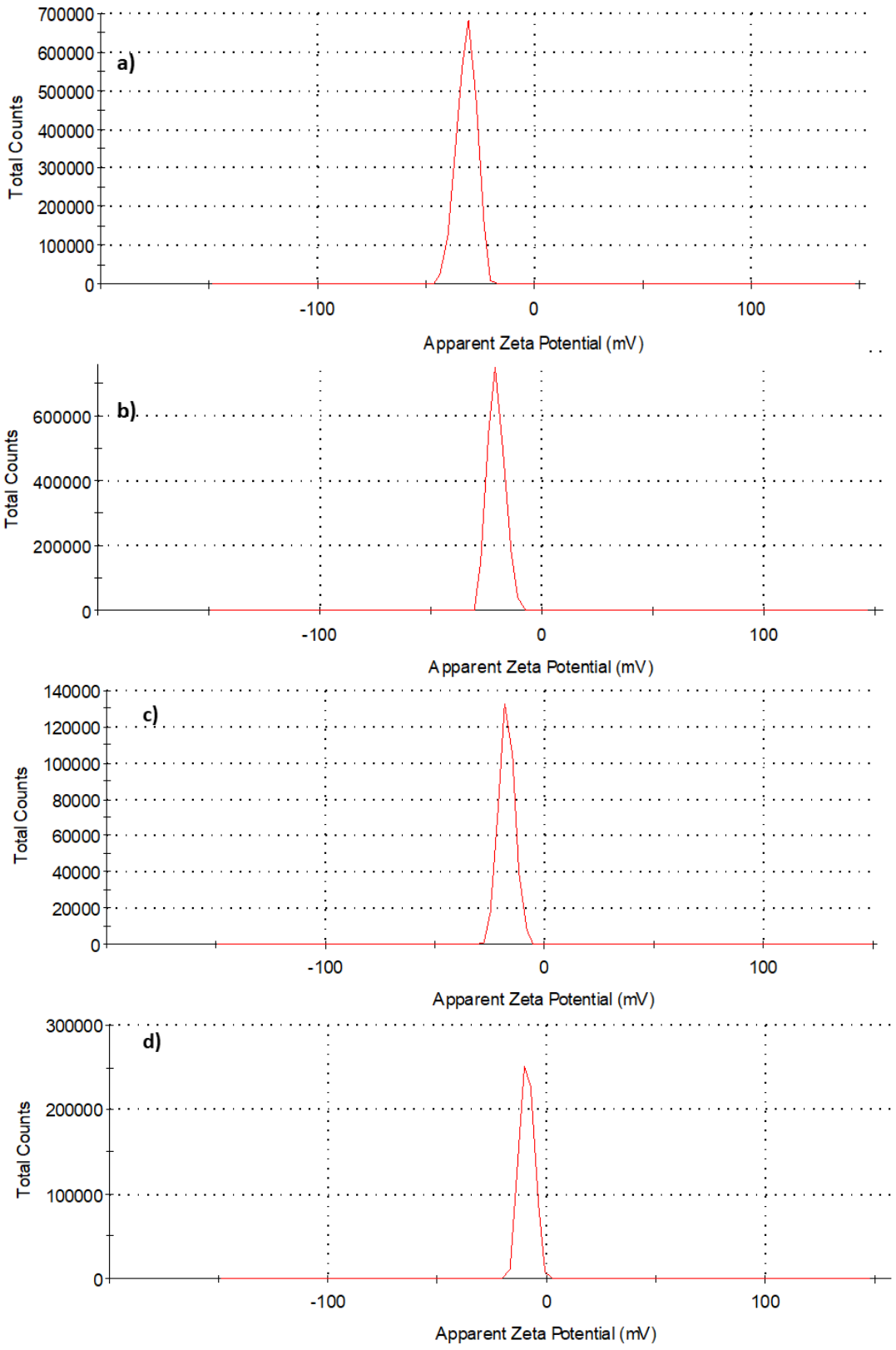

Figure APX6.5. Zeta potential graphs for the CdTe@ZnS QDs in (a) absence of ILs and in the presence of (b)C_3PyBr, (c) C_6PyBr, and (d)[C_6Py_2]Br_2 ILs.

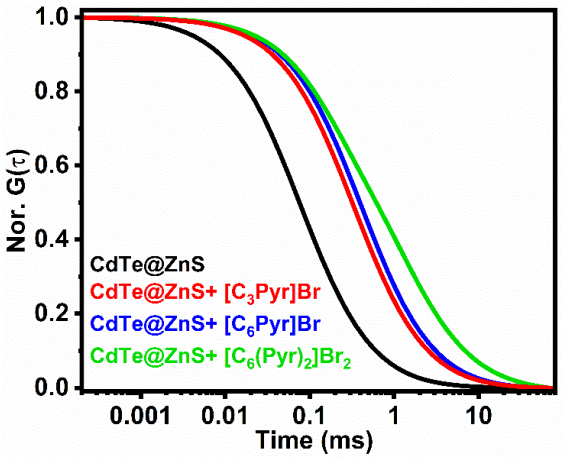

Figure APX6.6. FCS spectra of CdTe@ZnS QDs in the absence and presence of ILs.

Table APX6.1. Zeta potential of CdTe@ZnS QDs in absence of ILs and in the presence of C_3PyBr, C_6PyBr, and $[C_6Py_2]Br_2$ ILs.

Sample	**Zeta Potential (mV)**
CdTe@ZnS QDs	-31.3
CdTe@ZnS QDs in the presence of C_3PyBr	-19.3
CdTe@ZnS QDs in the presence of C_6PyBr	-17.1
CdTe@ZnS QDs in the presence of $[C_6Py_2]Br_2$	-9.0

Table APX6.2. PL decay parameters of CdTe@ZnS QD alone and in presence of ILs.

Sample	τ_1(ns)	α_1	τ_2 (ns)	α_2	τ_3 (ns)	α_3	τ_{av} (ns)[a]
CdTe@ZnS QD	0.63	0.33	6.70	0.32	23.85	0.35	10.63
QDs+C_3PyBr	0.65	0.39	5.26	0.37	17.23	0.24	6.31

QDs+C_6PyBr	0.56	0.42	5.27	0.32	17.63	0.26	6.50
QDs+$[C_6Py_2]Br_2$	0.47	0.62	4.13	0.27	17.27	0.11	3.34

Experimental error = ±8%

6.5. References

1. Kamat, P. V. Quantum Dot Solar Cells. Semiconductor Nanocrystals as Light Harvesters. *J. Phys. Chem. C* **2008**, *112*, 48, 18737–18753.
2. Nozik, A. J.; Beard, M. C.; Luther, J. M.; Law, M.; Ellingson, R. J.; Johnson, J. C. Semiconductor Quantum Dots and Quantum Dot Arrays and Applications of Multiple Exciton Generation to Third Generation Photovoltaic Solar Cells. *Chem. Rev.* **2010**, *110,* 11, 6873–6890.
3. Klimov, V. I. Semiconductor and Metal Nanocrystals: Synthesis and Electronic and Optical Properties; CRC Press: *Boca Raton*, **2003**.
4. Duan, L.; Hu, L.; Guan, X.; Lin, C.-H.; Chu, D.; Huang, S.; Liu, X.; Yuan, J.; Wu, T. Quantum Dots for Photovoltaics: A Tale of Two Materials. *Adv. Energy Mater*. **2021,** *11*, 2100354 (1-23).
5. Takagahara, T.; Takeda, K. Theory of the quantum confinement effect on excitons in quantum dots of indirect-gap materials. *Phys. Rev. B* **1992,** *46*, 15578-15581.
6. Nirmal, M.; Brus, L. Luminescence Photophysics in Semiconductor Nanocrystals. *Acc. Chem. Res.* **1999,** *32*, 407-414.
7. Bawendi, M. G.; Steigerwald, M. L.; Brus, L. E. The Quantum Mechanics of Larger Semiconductor Clusters ("Quantum Dots"). *Annu. Rev. Phys. Chem.* **1990,** *41*, 477-496.

8. Yu, W. W.; Qu, L.; Guo, W.; Peng, X. Experimental Determination of the Extinction Coefficient of CdTe, CdSe, and CdS Nanocrystals. *Chem. Mater.* **2003,** *15*, 2854-2860.
9. Brus, L. E. A simple model for the ionization potential, electron affinity, and aqueous redox potentials of small semiconductor crystallites. *J. Chem. Phys.* **1983,** *79*, 5566-5571.
10. Wang, Y.; Herron, N. Nanometer-sized semiconductor clusters: materials synthesis, quantum size effects, and photophysical properties. *J. Phys. Chem.* **1991,** *95*, 525-532.
11. Santhosh, K.; Samanta, A. Exploring the CdTe Quantum Dots in Ionic Liquids by Employing a Luminescent Hybrid of the Two. *J. Phys. Chem. C* **2012**, *116*, 20643−20650.
12. Saladin, M.; Maroncelli, M. Electron Transfer Kinetics between an Electron-Accepting Ionic Liquid and Coumarin Dyes. *J. Phys. Chem. B* **2020**, 124, 50, 11431–11445.
13. Sahu, P. K.; Das, S. K.; Sarkar, M. Fluorescence response of a dipolar organic solute in a dicationic ionic liquid (IL): is the behavior of di-cationic IL different from that of usual monocationic IL? *Phys. Chem. Chem. Phys.* **2014**, *16*, 12918-12928.
14. Majhi, D.; Seth, S.; Sarkar, M. Differences in the behavior of dicationic and monocationic ionic liquids as revealed by time resolved-fluorescence, NMR and fluorescence correlation spectroscopy. *Phys. Chem. Chem. Phys.*, **2018**, *20*, 7844-7856.
15. Sahu, P. K.; Das, S. K.; Sarkar, M. Toward Understanding Solute−Solvent Interaction in Room-Temperature Mono- and Dicationic Ionic Liquids: A Combined Fluorescence Spectroscopy and Mass Spectrometry Analysis. *J. Phys. Chem. B* **2014**, *118*, 1907−1915.
16. Wang, S.; Li, Z.; Zhang, Y.; Liu, X.; Han, J.; Li, X.; Liu, Z.; Frank Liu, S.; Choy, W. C. H. Water-Soluble Triazolium Ionic-Liquid-Induced Surface Self-Assembly to Enhance the Stability and Efficiency of Perovskite Solar Cells. *Adv. Funct. Mater.* **2019**, *29*, 1900417.
17. Salado, M.; Ramos, F. J.; Manzanares, V. M.; Gao, P.; Nazeeruddin, K.; Dyson, P. J.; Ahmad, S. Extending the Lifetime of Perovskite Solar Cells using a Perfluorinated Dopant. *Chem. Sus. Chem.* **2016**, *9*, 2708−2714.

18. Dong, W.; Sun, C.; Sun, M.; Ge, H.; Asiri, A. M.; Marwani, H. M.; Ni, R.; Wang, S. Interface Engineering of Imidazolium Ionic Liquids toward Efficient and Stable $CsPbBr_3$ Perovskite Solar Cells. *ACS Appl. Mater. Interfaces* **2020**, *12*, 4540−4548.

19. Shahiduzzaman, Md.; Muslih, E. Y.; Hasan, A. K. M.; Wang, L.; Fukaya, S.; Nakano, M.; Karakawa, M.; Takahashi, K.; Akhtaruzzaman, M.; Nunzi, J. M.; Taima, T. The benefits of ionic liquids for the fabrication of efficient and stable perovskite photovoltaics. *Chem. Eng. J.* **2021**, *411*, 128461.

20. Shahiduzzaman, M.; Yamamoto, K.; Furumoto, Y.; Kuwabara, T.; Takahashi, K.; Taima, T. Ionic Liquid-Assisted Growth of Methylammonium Lead Iodide Spherical Nanoparticles by a Simple Spin-coating Method and Photovoltaic Properties of Perovskite Solar Cells. *RSC Adv.* **2015**, *5*, 77495−77500.

21. Gao, X.; Nie, S. Molecular profiling of single cells and tissue specimens with quantum dots. *Trends in Biotechnology* **2003,** *21*, 371-373.

22. Hodes, G. Comparison of Dye- and Semiconductor-Sensitized Porous Nanocrystalline Liquid Junction Solar Cells. *J. Phys. Chem. C* **2008,** *112*, 17778-17787.

23. Duan, L.; Hu, L.; Guan, X.; Lin, C.-H.; Chu, D.; Huang, S.; Liu, X.; Yuan, J.; Wu, T. Quantum Dots for Photovoltaics: A Tale of Two Materials. *Adv. Energy Mater*. **2021,** *11*, 2100354 (1-23).

24. Nozik, A. J.; Beard, M. C.; Luther, J. M.; Law, M.; Ellingson, R. J.; Johnson, J. C. Semiconductor Quantum Dots and Quantum Dot Arrays and Applications of Multiple Exciton Generation to Third Generation Photovoltaic Solar Cells. *Chem. Rev.* **2010**, *110,* 11, 6873–6890.

25. Zhu, X. Exceeding the Limit in Solar Energy Conversion with Multiple Excitons. *Acc. Chem. Res.* **2013**, *46*, 6, 1239–1241.

26. Lee, Y. H. Beyond the Shockley-Queisser limit: Exploring new frontiers in solar energy harvest. *Science* **2024**, *383*,e4308.

27. Wang, Y.; Ye, S.; Lim, J. W. M.; Giovanni, D.; Feng, M.; Fu, J.; Krishnamoorthy, H. N. S.; Zhang, Q.; Xu, Q.; Cai, R.; *et.al.* Carrier multiplication in perovskite solar cells with internal quantum efficiency exceeding 100%. *Nature Communications* **2023**, *14*, 6293.

28. Jean, J.; Xiao, J.; Nick, R.; Moody, N.; Nasilowski, M.; Bawendi, M.; Bulović a V. Synthesis cost dictates the commercial viability of lead sulfide and perovskite quantum dot photovoltaics. *Energy Environ. Sci.* **2018**, *11*, 2295-2305.

29. Niu, H.; Liu, J.; O'Connor, H. M.; Gunnlaugsson, T.; James, T. D.; Zhang, H. Photoinduced electron transfer (PeT) based fluorescent probes for cellular imaging and disease therapy. *Chem. Soc. Rev.* **2023**, *52*, 2322-2357.

30. Amiri, Z.; Taromi, P.; Alavi, K.; Ghahramani, P.; Cho, W. C.; Farani, M. R.; Huh, Y. S. Quantum dot-infused nanocomposites: revolutionizing diagnostic sensitivity. *Nanoscale*, **2025**, *17*, 18477-18504.

31. Mohurle, S.; Maiti, B. Recent trends in ionic liquid-mediated synthesis of thiazoles: toward greener methodologies. *RSC Adv.* **2025**, *15*, 40912-40966.

32. Alreshidi, M. A.; *et. al.* A review on the evolution of ionic liquids: Sustainable synthesis, applications, and future prospects. *Materials Today Sustainability* **2025**, *31*, 101160.

33. Bousrez, G.; Renier, O.; Adranno, B.; Smetana, V.; Mudring, A.-V. Ionic Liquid-Based Dye-Sensitized Solar Cells—Insights into Electrolyte and Redox Mediator Design. *ACS Sustainable Chem. Eng.* **2021**, 9, 24, 8107–8114.

34. Yousefe, M.; Glińska, K.; Sweeney, M.; Moura, L.; Swadźba-Kwaśny, M.; Puga A. CO2 capture by carboxylate ionic liquids: fine-tuning the performance by altering hydrogen bonding motifs. *RSC Sustainability*, **2025**, *3*, 2952-296.

35. Dongare, S.; *et. al.* Reactive capture and electrochemical conversion of CO2 with ionic liquids and deep eutectic solvents. *Chem. Soc. Rev.* **2024**, *53*, 8563-863.

36. Kamat, P. V.; Tvrdy, K.; Baker, D. R.; Radich, J. G. Beyond photovoltaics: semiconductor nanoarchitectures for liquid-junction solar cells. *Chem. Rev.* **2010**, *110*, 6664−6688.

37. Etgar, L.; Zhang, W.; Gabriel, S.; Hickey, S. G.; Nazeeruddin, M. K.; Eychmüller, A.; Liu, B.; Grätzel, M. High Efficiency Quantum Dot Heterojunction Solar Cell Using Anatase (001) TiO2 Nanosheets. *Adv. Mater.* **2012**, *24*, 2202−2206.

38. Yang, Z.; Chen, C.-Y.; Roy, P.; Chang, H.-T. Facile In Situ Growth of Copper Sulfide Nanostructured Films Directly on FTO Coated Glass Substrates as Efficient Counter Electrodes for Quantum Dot-Sensitized Solar Cells. *Chem. Commun.* **2011**, *47*, 9561−9571.

39. Schaller, R. D.; Klimov, V. I. High Efficiency Carrier Multiplication in PbSe Nanocrystals: Implications for Solar Energy Conversion. *Phys. Rev. Lett.* **2004**, *92*, 186601.

40. Zakeeruddin, S. M.; Grätzel, M. Solvent-Free Ionic Liquid Electrolytes for Mesoscopic Dye-Sensitized Solar Cells. *Adv. Funct. Mater.* **2009**, 19, 2187−2202.

41. Vaishanav, S. K.; Korram, J.; Nagwanshi, R.; Karbhal, I.; Dewangan, L.; Ghosh K. K.; Satnami, M. L. Interaction of Folic Acid with Mn2+ Doped CdTe/ZnS Quantum Dots: In Situ Detection of Folic Acid. *J Fluoresc* **2021**, *31*, 951-960

42. Sattler, K. D. Handbook of nanophysics: Nanoparticles and Quantum Dots; CRC Press, USA, 2011.

43. Wang, Y.; Si, B.; Lu, S.; Ma, X.; Liu, E.; Fan, J.; Li, X.; Hu, X. Effective improvement in optical properties of colloidal CdTe@ZnS quantum dots synthesized from aqueous solution. *Nanotechnology* **2016**, *27*, 365707.

44. Hao, L.; Chen, X.; Liu, D.; Bian, Y.; Zhao, W.; Tang, K.; Zhang, R.; Zheng, Y.; Gu, S. Charge transfer dynamics of the CdTe quantum dots fluorescence quenching induced by

ferrous (II) ionsCharge transfer dynamics of the CdTe quantum dots fluorescence quenching induced by ferrous (II) ions. *Appl. Phys. Lett.* **2020***, 116*, 012105.

45. Gan, T. T.; Zhang, Y. J.; Zhao, N. J.; Xiao, X.; Yin, G. F.; Yu, S. H.; Wang, H. B.; Duan, J. B.; Shi, C. Y.; Liu, W. Q. Hydrothermal synthetic mercaptopropionic acid stabled CdTe quantum dots as fluorescent probes for detection of Ag^{+}. *Spectrochim. Acta A* **2012**,*99*, 62–68.
46. De, A.; Monal, N.; Samanta, A. Hole Transfer Dynamics from Photoexcited Cesium Lead Halide Perovskite Nanocrystals: 1-Aminopyrene as Hole Acceptor *J. Phys. Chem. C* **2018***, 122,* 13617−13623.
47. Roy, P.; Yadav, K. K. Dasgupta, J. Pillai, P. P. Bright, Stable, and Active: Surface Engineered Blue-Emitting InP Quantum Dots for Photoinduced Charge Separation in Water. *J. Phys. Chem. Lett.* **2025**, *16*, 9346−9352.
48. Lakowicz, J. R. Principles of Fluorescence Spectroscopy *Springer*: New York, **2006**.
49. Morgan, D. P.; Kelley, D. F. What Does the Transient Absorption Spectrum of CdSe Quantum Dots Measure? *J. Phys. Chem. C* **2020**, *124*, 15, 8448–8455.
50. Nirmal, M.; Brus, L. Luminescence Photophysics in Semiconductor Nanocrystals. *Acc. Chem. Res.* **1999**, 32, 5, 407–414.
51. Palato, S.; Seiler, H.; McGovern, L.; Mack, T. G.; Jethi, L.; Kambhampati, P. Electron Dynamics at the Surface of Semiconductor Nanocrystals. *J. Phys. Chem. C* **2017**, *121*, 26519−26527.
52. Kambhampati, P. Unraveling the Structure and Dynamics of Excitons in Semiconductor Quantum Dots. *Acc. Chem. Res.* 2011, 44, 1, 1–13.
53. Mondal, N.; Samanta, A. Ultrafast Charge Transfer and Trapping Dynamics in a Colloidal Mixture of Similarly Charged CdTe Quantum Dots and Silver Nanoparticles. *J. Phys. Chem. C* **2016**, *120*, 650−658.

54. Rawalekar, S.; Kaniyankandy, S.; Verma, S.; Ghosh, H. N. Ultrafast Charge Carrier Relaxation and Charge Transfer Dynamics of CdTe/CdS Core-Shell Quantum Dots as Studied by Femtosecond Transient Absorption Spectroscopy. *J. Phys. Chem. C* **2010,** *114,* 1460–1466.

55. Xavier, J. A. M.; Devatha, G.; Roy, S.; Rao, A.; Pillai P. P. Electrostatically Regulated Photoinduced Electron Transfer in Cationic Eco-friendly CuInS2/ZnS Quantum Dots in Water. *J. Mater. Chem. A* **2018**, *6*, 22248-22245.

Thesis Summary and Future Perspective

This thesis investigates how interfacial engineering—through ionic liquids (ILs) and organic J-aggregates—can modulate exciton dynamics, enhance stability, and control energy/charge-transfer processes in halide perovskite nanocrystals (PNCs) and chalcogenide quantum dots (QDs). Although these nanomaterials exhibit tunable optical properties and strong excitonic behaviour, their performance is often constrained by surface traps, structural instability, and inefficient exciton transport. The work presented here addresses these challenges through the systematic design of hybrid systems.

The first section demonstrates that imidazolium-based ILs significantly improve the photophysical properties of $CsPbX_3$ PNCs by suppressing trap-assisted recombination, removing surface Pb-adatoms, and enhancing resistance to moisture and continuous irradiation. These treatments yield higher photoluminescence (PL) intensity and prolonged exciton lifetimes, confirmed at ensemble and single-particle levels. Subsequently, an IL-directed antisolvent precipitation strategy is developed to synthesize phase-pure Cs_4PbBr_6 microdisks at room temperature. The IL not only governs crystal morphology but also enables strong green emission with large exciton-binding energy and pronounced exciton–phonon coupling. Spatial PL mapping reveals heterogeneous trap distributions across individual microstructures.

The hybrid studies explore excitonic coupling and charge-transfer phenomena. In CdTe@ZnS QD–J-aggregate assemblies, highly efficient Förster resonance energy transfer (FRET) produces tunable valley splitting in QD emission without external fields, introducing a new approach to exciton manipulation through nanoscale hybridization. The final section examines photoinduced electron transfer (PET) in QD–IL systems using pyridinium-based mono- and dicationic ILs. Ultrafast transient absorption and time-resolved PL reveal IL-structure-

dependent charge separation on femtosecond–nanosecond timescales, offering mechanistic insight into how ILs regulate exciton dissociation and interfacial electronic coupling.

Overall, this thesis provides a unified understanding of how ILs and organic aggregates serve as effective interfacial modulators, enabling improved stability, controlled exciton transfer, and emergent optical functionalities in semiconductor nanostructures.

Future Perspective

Future work may focus on the molecular design of ILs with tailored binding motifs to achieve stronger defect suppression, enhanced charge mobility, and long-term stability in nanocrystals. The IL-mediated synthesis of zero-dimensional perovskites can be expanded to scalable or greener routes, aiding the ongoing investigation into the intrinsic origin of their emission. The discovery of FRET-induced valley splitting opens pathways toward hybrid excitonic and valleytronic platforms, potentially applicable in polarization-controlled photonic devices. Additionally, ILs with tunable polarity, viscosity, or embedded redox functionalities could be engineered to guide directional charge transfer for improved photovoltaic or photocatalytic performance. Translating these hybrid nanomaterials into device architectures—such as LEDs, photodetectors, and light-harvesting systems—remains a promising avenue to bridge fundamental photophysics with functional technologies.